3-29-2016

Hard QCD Processes in the Nuclear Medium

Adam Freese
Florida International University, afree008@fiu.edu

DOI: 10.25148/etd.FIDC000229

FLORIDA INTERNATIONAL UNIVERSITY

Miami, Florida

HARD QCD PROCESSES IN THE NUCLEAR MEDIUM

A dissertation submitted in partial fulfillment of the

requirements of the degree of

DOCTOR OF PHILOSOPHY

in

PHYSICS

by

Adam Freese

2016

To: Dean Michael R. Heithaus
College of Arts, Sciences and Education

This dissertation, written by Adam Freese, and entitled Hard QCD Processes in the Nuclear Medium, having been approved in respect to style and intellectual content, is referred to you for judgment.

We have read this dissertation and recommend that it be approved.

Werner Boeglin

Lei Guo

Mirroslav Yotov

Misak M. Sargsian, Major Professor

Date of Defense: March 29, 2016

The dissertation of Adam Freese is approved.

Dean Michael R. Heithaus
College of Arts, Sciences and Education

Andrés G. Gil
Vice President for Research and Economic Development
and Dean of the University Graduate School

Florida International University, 2016

DEDICATION

I would like to dedicate this dissertation to Juan Alberto-sensei and Cedric Capestany-sensei, who in teaching me the art of Aikido imparted onto me the virtues of Bushido, including respect and temperance. 先生、ありがとうございました！

ACKNOWLEDGMENTS

I would like to acknowledge many of the people who made my graduate school experience enjoyable and fruitful.

First of all, the members of my dissertation committee all deserve acknowledgment: Mirroslav Yotov for helping me to appreciate the depths of pure mathematics, especially of complex analysis; Werner Boeglin for repeatedly demonstrating the virtue of clarity in explanations; Lei Guo for organizing and leading graduate student discussions; and most of all, my adviser, Misak Sargsian, for teaching me the difference between being a science student and being a scientist, and putting in so much work to transform me into the latter.

I wish to acknowledge the graduate program director, Brian Raue, as well as many of the past and present secretaries of the FIU physics department, including Elizabeth Bergano-Smith, Omar Tolbert, Maria Martinez, Ofelia Adan-Fernandez, and Robert Brown for helping me navigate the bureaucratic aspects of the graduate student experience.

I additionally acknowledge Rafael Badui, Jason Bono, Wim Cosyn, Jose Gonzalez, Francisco Muller, and Ricardo Leante for the absolutely fascinating physics and mathematics discussions that I have had with them.

I too must acknowledge my parents for their support and encouragement: my mom especially for her moral support, and my dad for his incessant nagging.

This research would not have been possible without financial support. I would like to acknowledge the Department of Energy for providing the grant that supported my research assistantship.

Lastly, I acknowledge the Panther Aikido sports club and its members for providing a venue for de-stressing, and for keeping myself grounded in social reality.

ABSTRACT OF THE DISSERTATION

HARD QCD PROCESSES IN THE NUCLEAR MEDIUM

by

Adam Freese

Florida International University, 2016

Miami, Florida

Professor Misak Sargsian, Major Professor

The environment inside the atomic nucleus is one of the most fascinating arenas for the study of quantum chromodynamics (QCD). The strongly-interacting nature of the nuclear medium affects the nature of both QCD processes and the quark-gluon structure of hadrons, allowing several unique aspects of the strong nuclear force to be investigated in reactions involving nuclear targets. The research presented in this dissertation explores two aspects of nuclear QCD: firstly, the partonic structure of the nucleus itself; and secondly, the use of the nucleus as a micro-laboratory in which QCD processes can be studied.

The partonic structure of the nucleus is calculated in this work by deriving and utilizing a convolution formula. The hadronic structure of the nucleus and the quark-gluon structure of its constituent nucleons are taken together to determine the nuclear partonic structure. Light cone descriptions of short range correlations, in terms of both hadronic and partonic structure, are derived and taken into account. Medium modifications of the bound nucleons are accounted for using the color screening model, and QCD evolution is used to connect nuclear partonic structure at vastly different energy scales. The formalism developed for calculating nuclear partonic structure is applied to inclusive dijet production from proton-nucleus collisions at LHC kinematics, and novel predictions are calculated and presented for the dijet cross section.

The nucleus is investigated as a micro-laboratory in vector meson photoproduction reactions. In particular, the deuteron is studied in the break-up reaction $\gamma d \to Vpn$, for both the $\phi(1020)$ and J/ψ vector mesons. The generalized eikonal approximation is utilized, allowing unambiguous separation of the impulse approximation and final state interactions (FSIs). Two peaks or valleys are seen in the angular distribution of the reaction cross

section, each of which is due to a FSI between either the proton and neutron, or the produced vector meson and the spectator nucleon. The presence and size of the latter FSI valley/peak contains information about the meson-nucleon interaction, and it is shown that several models of this interaction can be distinguished by measuring the angular distribution for the deuteron breakup reaction.

TABLE OF CONTENTS

CHAPTER PAGE

1 Introduction . . . 1
1.1 QCD structure of the nucleus . . . 3
1.2 The nucleus as a microlab . . . 8

2 Inclusive reactions . . . 10
2.1 General formalism . . . 11
2.2 Deep inelastic scattering from nuclei . . . 17
2.3 The nuclear light cone fraction distribution . . . 24
2.4 Short range correlations . . . 32
2.5 Medium modifcations . . . 63
2.6 Evolution of nuclear PDFs . . . 71
2.7 Dijet production in proton-nucleus collisions . . . 88
2.8 Summary . . . 109

3 Exclusive reactions . . . 110
3.1 General formalism . . . 110
3.2 Formalism for vector meson production with deuteron breakup . . . 116
3.3 Photoproduction of $\phi(1020)$ mesons . . . 139
3.4 Photoproduction of J/ψ mesons . . . 147
3.5 Summary . . . 159

4 Conclusions . . . 161

Bibliography . . . 164

Vita . . . 172

LIST OF FIGURES

FIGURE PAGE

1.1 Cartoon of QCD evolution 6

2.1 Spacetime diagram for DIS 11
2.2 Spacetime diagram for DIS in parton model 15
2.3 Feynman diagram for hadronic current in parton model 16
2.4 Cut diagram for LCFD 27
2.5 Feynman diagram for hadronic current of mean field 30
2.6 Cut diagram for two-nucleon SRC 36
2.7 Plot of LCFD with 2N SRCs 41
2.8 Feynman diagram for hadronic current of two-nucleon SRC 42
2.9 Cut diagrams for three-nucleon SRC 47
2.10 Plot of LCFD with 3N SRCs 59
2.11 Feynman diagram for hadronic current of three-nucleon SRC 60
2.12 Plot of EMC ratio with no medium modifications 65
2.13 Plot of EMC ratio with x shifted 68
2.14 Plot of EMC ratio using the color screening model 72
2.15 Plot of evolution computation with different x meshes 82
2.16 Plot of evolution computation with different $\log(Q^2)$ step sizes 83
2.17 Comparison plot of LO and NLO evolution 84
2.18 Plot of evolution of medium modifications 85
2.19 Plot of evolution trajectories 87
2.20 Feynman diagram for $pA \to \text{dijet} + X$ 90
2.21 Plot of LO calculation for $pp \to$ dijet against experimental data 97
2.22 Plot of dependence of x_A on η_4 101
2.23 Plots of $pA \to \text{dijet} + X$ cross section without medium modifications 102

2.24 Plots of $pA \to \text{dijet} + X$ cross section in the color screening model 103
2.25 Plots of $pA \to \text{dijet} + X$ cross section compared to FS81 model 103
2.26 Plots of $pA \to \text{dijet} + X$ cross section without medium modifications 105
2.27 Plots of $pA \to \text{dijet} + X$ cross section using the color screening model . . . 106

3.1 Geometry of $\gamma d \to Vpn$ 117
3.2 Angular distribution of final state momenta 121
3.3 Feynman diagram for PWIA contribution to $\gamma d \to Vpn$ 123
3.4 Feynman diagram for single rescattering contributions to $\gamma d \to Vpn$ 124
3.5 Feynman diagram for double rescattering contributions to $\gamma d \to Vpn$ 131
3.6 Angular distribution of $\gamma d \to \phi(1020)pn$ (single resc. approx.) 142
3.7 Angular distribution of $\gamma d \to \phi(1020)pn$ (double resc. approx.) 144
3.8 Ratio of angular distributions of $\gamma d \to \phi(1020)pn$ 145
3.9 Ratio of angular distributions of $\gamma d \to J/\psi pn$ 151
3.10 Angular distribution of $\gamma d \to J/\psi pn$ 152
3.11 Ratio of angular distribution of $\gamma d \to J/\psi pn$ (multiple $\sigma_{\Psi N}$) 153
3.12 Plot of Fermi momentum needed to effect subthreshold J/ψ production . . 155
3.13 Angular distributions of $\gamma d \to J/\psi pn$ below threshold 156
3.14 Angular distributions of $\gamma d \to J/\psi pn$ at high energies 158

CHAPTER 1

Introduction

Quantum chromodynamics (QCD) is believed to be the fundamental theory of strong nuclear interactions. QCD is a non-Abelian quantum field theory with a group structure $\mathrm{SU}(3,\mathbb{C})$. It postulates that nuclear matter is made of two fundamental kinds of fields. The first are the quark fields, which transform under the defining representation of $\mathrm{SU}(3,\mathbb{C})$. Quarks come in six flavors—up (u), down (d), strange (s), charm (c), bottom (b), and top (t)—and each flavor has a corresponding anti-quark, which transforms under the anti-defining representation of $\mathrm{SU}(3,\mathbb{C})$. The three-state internal degree of freedom possessed by each quark flavor is called color, in analogy to RGB color space, and anti-quarks are considered to have an "anti-color," *e.g.*, the anti-quark of a red u quark would be an anti-red $\bar{u}$ anti-quark. Secondly, there are gluons, which transform under the adjoint representation of $\mathrm{SU}(3,\mathbb{C})$. Because of this, the gluon has a $3^2 - 1 = 8$-state internal degree of freedom, which is also called the color of the gluon.

Physical hadrons are postulated to be colorless mixtures of quarks, anti-quarks, and gluons. In particular, every known hadron transforms under a trivial (singlet) representation of $\mathrm{SU}(3,\mathbb{C})$. The basic known hadrons are categorized into two groups: baryons, which consist of three valence quarks, which have a color state of:

$$\frac{1}{\sqrt{6}}\left(|\, rgb\rangle + |\, gbr\rangle + |\, brg\rangle - |\, bgr\rangle - |\, grb\rangle - |\, rbg\rangle\right), \tag{1.1}$$

and mesons, which consist of a quark and an anti-quark in their valence states, having a color state of:

$$\frac{1}{\sqrt{3}}\left(|\, r\bar{r}\rangle + |\, g\bar{g}\rangle + |\, b\bar{b}\rangle\right). \tag{1.2}$$

Anti-baryons, consisting of three valence anti-quarks, also exist as the anti-particles of baryons.

The only known stable baryon is the proton, which has valence quark flavor content uud. Its anti-particle, the anti-proton (with valence quark content $\bar{u}\bar{u}\bar{d}$) is likewise the only

stable anti-baryon. The neutron (valence quark content udd) is an unusually long-lived baryon, with a mean lifetime of 15 minutes; all other known baryons have lifetimes on the order of microseconds or less.

Protons and neutrons are able to form stable bound states called nuclei. In particular, Z protons and $(A - Z)$ neutrons bound together form a nucleus with charge number Z and mass number A. Typically, theoretical and experimental studies of nuclei are based on nuclear structure in terms of its nucleonic degrees of freedom. One postulates that nucleons interact via a phenomenological potential, or the exchange of certain mesons, and proceeds to calculate nuclear properties in terms of various models. Under a mean field approximation, in which each nucleon is treated as moving independently under the average influence of the other $(A-1)$ nucleons, the distances between nucleons are larger than both the size of the nucleon, and the distance scales at which QCD descriptions have successfully been applied. Accordingly, descriptions of the nucleus in terms of QCD often amount to treating the nucleus as a collection of quasi-free nucleons, each of which is individually described using QCD.

The premise explored in this dissertation is that the nucleus is not just a collection of nucleons, and that QCD effects unique to the nuclear environment can be observed. There are several uniquely nuclear aspects to QCD that can be explored. Firstly, the structure of the protons and neutrons making up the nucleus is expected to be modified by the nucleons' immersion in a strongly-interacting environment. There is already strong experimental evidence for this in the EMC effect, named after the European Muon Collaboration which first observed the effect [1]. Additionally, the nature of various QCD processes, such as vector meson production and hadron-hadron scattering, may also be changed within the nuclear environment.

In light of these two aspects, the dissertation is divided into two major chapters. Chapter 2 explores how the QCD structure of nuclei can be theoretically explicated by developing a formalism that accounts for the latest phenomenology of high-energy, short-distance-scale experiments using nuclear targets. This is accomplished by looking at inclusive reactions where minimal constraints are placed on the final states, with a particular focus to inclusive

dijet production in proton-nucleus collisions. Chapter 3 explores how the nucleus can be used as a micro-laboratory in which to study specific QCD processes. This chapter instead looks at exclusive reactions, where the final state is fully specified, and focuses particularly on incoherent vector meson photoproduction from the deuteron.

1.1 QCD structure of the nucleus

QCD is notoriously difficult to apply at low energies. This happens for several reasons. Firstly, renormalized QCD has a coupling strength that depends on the energy resolution scale Q^2: it decreases at large Q^2—a property called asymptotic freedom—allowing perturbative QCD to be applied at high energy scales, but it also grows without bound for low Q^2, diverging logarithmically at an infrared energy scale, Λ_{QCD}. Secondly, the theory contains infrared divergences corresponding to emission of soft and collinear gluonic radiation. Collinear divergences are traditionally dealt with in field theories by recognizing that the asymptotic free states of real experiments do not correspond to the "bare" particles that appear as lines in Feynman diagrams. In QCD in particular, the asymptotic free states are not quarks and gluons at all, but are instead colorless (color singlet state) hadrons. Accordingly, proper application of perturbative QCD requires the input of several non-perturbative quantities, corresponding to the probability that quarks and gluons entering into a pQCD reaction are found within the initial-state hadrons, and the probability that quarks and gluons emerging from this reaction form into the final-state hadrons.

Perturbative QCD thus proceeds through a scheme called factorization in which a hadronic cross section is decomposed into three parts:

1. A universal parton distribution function (PDF) that describes the quark and gluon makeup of a hadron.
2. A hard (*i.e.*, high-Q^2) perturbative QCD cross section for quarks and gluons.
3. A fragmentation function (FF), which describes how a scattered parton forms into a shower of observable hadrons.

Parton distribution functions and fragmentation functions are manifestly non-perturbative quantities, and it is currently unknown how to calculate them from first principles. Parametriza-

tion of both FFs and PDFs for the free proton exist based on extensive experimental data. Through this factorization scheme, peturbative QCD has achieved a great amount of experimental success (see for instance the Handbook of Perturbative QCD [2] and the Review of Particle Physics [3]).

1.1.1 Parton distribution functions

The parton distribution function is a function of two parameters: a light cone momentum fraction x, and an energy resolution scale μ. The momentum fraction x conventionally ranges from 0 to 1, and for sufficiently fast hadrons (*i.e.*, in the infinite momentum frame), it describes the fraction of the hadron's fast, longitudinal momentum carried by the parton. The energy resolution scale μ characterizes how exactly factorization is done. Roughly, QCD processes that occur below the energy μ are considered part of the hadron's nonperturbative structure, while processes above the energy μ are calculated within perturbative QCD using the Feynman rules.

The PDF for the proton is fairly well-known for a wide range of x and μ. However, the PDFs of atomic nuclei are not especially well-known. A naive guess would suggest that the PDF of a nucleus can be obtained by convoluting the proton and neutron PDFs with their individual momentum distributions, but this does not account for modification of the protons and neutrons inside the nucleus.

The fact that protons and neutrons are modified, and that this modification is significant, can be seen in the EMC effect [1, 4]. The EMC effect is that the deep inelastic scattering cross section for a bound nucleon within a heavy nucleus is not equal to the DIS cross section for a free nucleon, and instead their ratio is a function of the momentum fraction x of the struck parton. In particular, for x from 0.3 to 0.8, DIS from the bound nucleon is suppressed, whereas for x above this it is enhanced. A myriad of models have been proposed for account for this effect [5, 6], but they have mostly proved inconclusive. In particular, models based on the Fermi motion and binding energy of a single nucleon can only partially account for the effect.

There is increasing evidence that the EMC effect can be related to multinucleon short range correlations (SRCs) [7]. It is possible to obtain $x > 1$, since the parton that was struck could have been shared between nucleons. Moreover, the cross section ratio at $x > 1$ becomes a sequence of plateaus, in line with predictions made on the basis of SRCs [8].

Accounting for SRCs is necessary for describing nuclear modification at low μ. The nuclear PDF at low energy resolutions can indeed be accounted for using a composition of the nucleonic PDF and the nuclear density, if the nuclear density is modified to include the effects of SRCs. At high energy resolutions, however, this is not enough. One of the main focuses of this dissertation is obtaining high-μ nuclear PDFs using the latest phenomenology of SRCs, the EMC effect, and QCD evolution. This is done in Chapter 2.

1.1.2 QCD evolution

The QCD evolution equation relates the PDF at different energy resolution scales. By evolving the PDF from a low μ to a high μ one considers many low-energy processes to now be part of the hadron's structure. At the same time, one is describing the hadron's structure at finer distance scales since these correspond to larger energy scales.

Within renormalized QCD quarks and gluons are not structureless, but instead contain more partons at smaller distance scales (higher energy scales). It is possible to redefine the boundary between the partons' structure and their interactions, so that what was previously considered a quark can instead be considered a quark with a cloud of gluons and quark-antiquark pairs surrounding it. The boundary is defined by the experimental scenario: there is an energy scale Q characterizing how hard a particular kinematic scenario is, and this scale is chosen as the energy resolution scale for factorization. Changing the energy resolution scale by performing a harder scattering process removes some of the cloud of gluons and quark-antiquark pairs from the dressed parton and considers it as being part of the hadron containing the parton instead. This is illustrated in the cartoon in Fig. 1.1.

This higher-resolution parton invariably has a smaller light cone momentum fraction x than the lower-resolution parton. As can be seen in Fig. 1.1b, some of the low-μ parton's momentum is carried away by gluons, leaving the high-μ parton with less momentum,

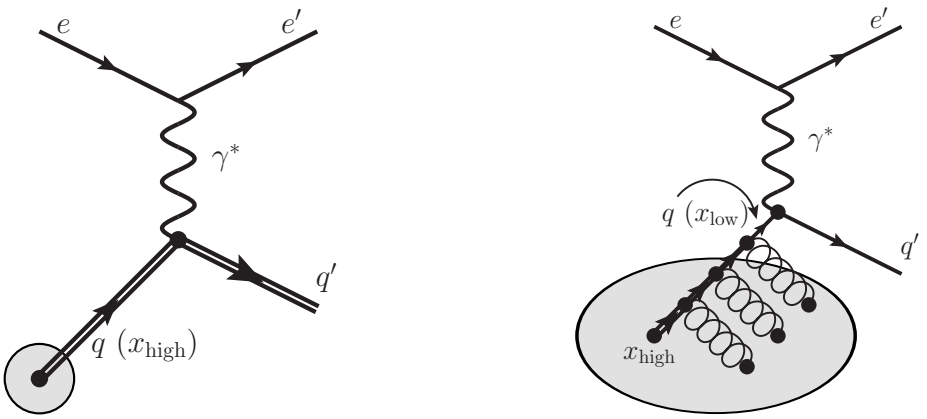

(a) Scattering at low μ

(b) Scattering at high μ

Figure 1.1: Cartoon illustration of QCD evolution. Higher μ moves structure from the parton to the hadron.

and thus a smaller momentum fraction. Conversely, if one sees a parton with a small (or moderate) momentum fraction x at a high energy resolution, it may have been contained within a fast (high x) quark at low resolution.

This fact is especially pertinent to the study of nuclear modifications. This is easiest to see when considering that x can be greater than 1 for reactions involving nuclei. If $x > 1$, this suggests that the probed parton carried two nucleons' share of the longitudinal momentum, and thus was likely to have been shared between overlapping nucleons in a short range correlation. Likewise, $x > 2$ suggests the parton was shared between three nucleons, and so on.

1.1.3 Short range correlations on the light cone

It is possible to obtain the observed $x > 1$ through high-density fluctuations of multiple nucleons into short range correlations [8]. Therefore, it is necessary to develop a model of SRCs to describe nuclear PDFs. This dissertation improves upon a model of SRCs using light cone dynamics [9]. We describe two-nucleon correlations using the two-nucleon light cone wave function, and correlations between three or more nucleons as arising from a sequence of two-nucleon correlations. This model describes nucleons with low light cone

momentum fractions as existing within a mean field, and nucleons with high momentum fractions as existing within multinucleon correlations. The model developed to account for multinucleon short range correlations is given in Section 2.4.

1.1.4 QCD evolution of nuclear parton distributions

Jefferson Lab currently measures parton distribution functions at low Q^2 and high x, and these measurements will be extended into the $x > 1$ region for nuclear targets. Using QCD evolution, we will make numerical predictions for nuclear PDFs at very large Q^2, on the order of $Q^2 = 10000$ GeV^2, at intermediate values of x. These calculations will provide input for deep inelastic scattering experiments at the EIC, as well as for heavy ion collisions at the LHC.

A complication that arises here is that, at low energy resolution scales, the masses of heavy quarks (such as c and b) are not negligible compared to the resolution scale. The most commonly used renormalization scheme for QCD, the modified minimal subtraction scheme or $\overline{\text{MS}}$, neglects quark masses. Conventionally, one compensates for this by turning quarks off when dealing with energy resolutions below the quark mass, and turning them on at higher energy scales. This quark mass scheme, due to Collins and Tung [10], shall be used in this work.

A detailed description of how QCD evolution is adapted to nuclear partonic structure, together with a computational algorithm for performing this evolution, is given in Section 2.6.

1.1.5 Inclusive jet production

After the hard pQCD scattering reaction occurs, the parton will hadronize—that is, it will fragment into an observable shower of closely spaced hadrons, called a jet. If specific hadrons are looked for in the final state, then it is necessary to introduce a fragmentation function to calculate the cross section. However, for the inclusive cross section—that is, with all possible final hadronic states summed over—fragmentation functions are unnecessary. Since fragmentation functions are an additional complication, it is desirable to avoid them

if possible when they are not the object of study, and therefore to look at inclusive jet production.

This dissertation examines inclusive jet production at high-energy kinematics as a means of studying nuclear PDFs. In particular, this dissertation demonstrates that inclusive jet production at high energy can be used to observe the presence of shared quarks and gluons within the nucleus at high energy resolutions. This is something that can be accomplished at the LHC in proton-nucleus collisions by looking at inclusive two-jet production.

A jet is characterized by two kinematic variables: its rapidity, which is a measure of the jet's speed in the heavy ion beam direction, and its momentum in the plane transverse to the beam direction. The transverse momentum in particular serves as the characteristic energy resolution scale in proton-nucleus collisions.

Large $x > 1$ can be obtained by looking at large rapidity and large transverse momentum in the jets. However, since the high-μ partons obtained by QCD evolution have a smaller momentum fraction than their low-μ parents, it should be sufficient to look at moderate $x < 1$ to see the effects of SRCs. This can be accomplished by looking at high-p_T jets with moderate rapidity, which are easier to measure at the LHC. Using QCD evolution and the light cone description of SRCs, I have made predictions for inclusive two-jet production at the LHC based on these kinematics.

An explication of the dijet formalism together with the cross section predictions can be found in Section 2.7.

1.2 The nucleus as a microlab

For many purposes, experiments involving proton targets are adequate for studying the nature of QCD interactions. However, there are problems for which the proton cannot serve as an adequate target. Such an example is in studying the nature of J/ψ scattering from the nucelon. J/ψ is a vector meson composed of a charm quark and its antiquark. The J/ψ meson has a short lifetime, and the cross section for its production is small enough that making a J/ψ beam is not feasible. However, using nuclear targets in photo- and

electroproduction experiments provides a means of studying J/ψ scattering from a nucleon. The deuteron in particular is a promising candidate.

The rationale behind this is that, in hard photoproduction reactions, the deuteron can function as a microlab in which a J/ψ produced from one nucleon can be studied as though it is rescattering from the other (spectator) nucleon. In hard reactions in particular, it is possible to use an effective Feynman rule formalism: the amplitude for the process can be described using the amplitudes for isolated two-body interactions occurring in turn. Photoproduction of J/ψ occurs from either the proton or the neutron within the deuteron, and then the three final-state hadrons (two nucleons and the produced J/ψ) may afterwards interact with one-another. In particular, the J/ψ may scatter from the spectator to the initial production reaction, which produces a distinct peak or dip in the differential cross section. The size and shape of this peak provides a means of studying the J/ψ-nucleon interaction, just as the magnitude and shape of differential cross sections in ordinary macrolabs allows one to study the nature of scattering reactions.

Chapter 3 of this dissertation explores the use of vector meson photoproduction in a deuteron breakup reaction in using the nucleus as a micro-lab for studying both the nature of photoproduction reactions, and of meson-nucleon scattering reactions. This reaction is analyzed in the framework of the generalized eikonal approximation, and a formalism developed in Section 3.2 is applied to both $\phi(1020)$ production in Section 3.3 and J/ψ production in Section 3.4.

CHAPTER 2

Inclusive reactions

The easiest reactions to study in nuclear physics are fully inclusive reactions, where the probe (usually an electron) that is scattered from a proton or nuclear target is the only particle detected in the final state. Theoretically, inclusive reactions are characterized by a summation over all possible final states. This allows the use of completeness relations, meaning knowledge of the final state is not necessary to calculate scattering cross sections. Accordingly, scattering cross sections depend only on the structure of the target and its interaction with the probe.

By considering a pointlike probe that interacts through a well-understood mechanism (*e.g.*, an electron that interacts *via* photon exchange), the cross section for the reaction can be used to study the structure of a hadronic target. The target will tend to be a proton or a nucleus, although the formalism for inclusive scattering is typically given in terms of a proton target. In what follows, the standard formalism for inclusive electron scattering from a proton will be described (in Sec. 2.1), and subsequently the changes in the formalism necessary for a nuclear target and their consequences will be explained (in Sec. 2.2).

The physical meaning of the "structure" of a hadron can be interpreted in terms of constituents making up the hadron. These constituents are called partons, and in an inclusive scattering reaction the probe can be understood as scattering from one constituent parton. The partons making up a hadron target are mostly the quarks, anti-quarks and gluons of QCD, although it is also believed that other elementary particles such as photons make up a small part of a hadron's partonic structure [11]. The distribution of these partons in terms of light cone variables, quantified by the so-called parton distribution functions (PDFs), can be related to the structure functions F_1 and F_2: firstly, in the quark-parton model, which treats the constituents of the hadronic target as free and pointlike; and secondly, in a perturbative correction to the quark-parton model that accounts for interactions among partons. The main consequence of interactions among partons is that the parton distribution functions must be regularized to deal with infrared divergences, and

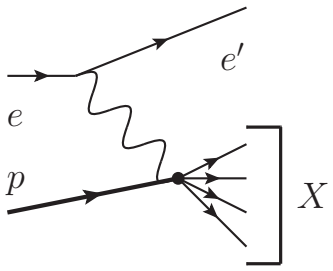

Figure 2.1: Diagram for $ep \to e'X$.

as a result, they obtain dependence on the energy/momentum resolution scale at which the hadron is probed. This resolution scale dependence is given by a set of evolution equations called the Dokshitzer-Gribov-Lipatov-Altarelli-Parisi (DGLAP) equations [12–14].

The study of inclusive scattering on nuclear targets in particular allows one to examine how conventional nuclear structure, namely the composition of the nucleus in terms of protons and neutrons, interplays with the structure of nucleons in terms of partons to produce the partonic structure of the nucleus. This interplay is described by a convolution formula for nuclear PDFs, which is derived in Secs. 2.3.4, 2.4.5, and 2.4.9. The interplay works two ways. Firstly, the partonic structure of the nucleus originates in part from the motion of nucleons within the nucleus, which is described by the light cone fraction distribution, the definition and formalism of which are given in Sec. 2.3; Secondly, the fact that the nucleons making up the nucleus are immersed in a strongly-interacting medium causes their structure (in the form of nucleonic PDFs) to be modified. This is described in Sec. 2.5.

After the nuclear PDF formalism is developed, I will explore an application of it to high-energy proton-nucleus collisions in Sec. 2.7.

2.1 General formalism

The most straightforward reaction that can be used to study the structure of a proton or nuclear target is inclusive electron scattering. This reaction proceeds at the leading order by exchange of a single photon, as depicted in Fig. 2.1.

2.1.1 Kinematics

The reaction is characterized by the following kinematic variables:

- l (l') is the initial (final) electron four-momentum.
- $q = l - l'$ is the four-momentum transfer.
- p is the target four-momentum.
- p_X is the four-momentum of the unknown hadronic final state X.
- $s = (p + l)^2$ is the total center-of-mass energy squared.
- $W^2 = (p + q)^2 = p_X^2$ is the invariant mass of the state X.
- $x_B = \frac{-q^2}{2(p \cdot q)}$ is the Bjorken scaling variable.
- $\nu = \frac{(p \cdot q)}{M}$ is the photon energy in the lab frame (target rest frame).
- $Q^2 = -q^2 > 0$ is the scalar momentum transfer.
- $y = \frac{(p \cdot q)}{(p \cdot l)}$ is the inelasticity of the scattering.

2.1.2 Hadronic tensor and structure functions

Let λ (λ') denote the helicity of the initial (final) electron, σ the helicity of the target, and $\{\lambda_{X,i}\}$ the internal degrees of freedom of the N_X particles in the state X. The momentum-space Feynman rules give a matrix element for inclusive electron scattering of

$$\mathcal{M} = \frac{e^2}{-q^2} \bar{u}^{\lambda'}(l') \gamma_\mu u^{\lambda}(l) \langle X \mid J^\mu(0) \mid p, \sigma \rangle, \tag{2.1}$$

where $J^\mu(0)$ is the hadronic current operator that characterizes the transition $p + \gamma^* \to X$, the exact form of which depends on the particular final state X[1]. Final states with different numbers of particles will add incoherently, and even have different phase space elements, so summation over possible X should await calculation of the cross section. Use of the relation

$$d\sigma = \sum_X \frac{\overline{|\mathcal{M}|^2}}{\Phi} d\mathcal{Q}_X \tag{2.2}$$

[1] The hadronic current is defined to be an argument of the spacetime point x, but in the momentum-space representation one uses the operator evaluated at $x = 0$.

for the unpolarized cross section element $d\sigma$, together with the flux $\Phi = 4(l \cdot p)$ and the phase space element

$$d\mathcal{Q}_X = (2\pi)^4 \delta^{(4)}(p + q - p_X) \frac{d^3\mathbf{l}'}{2E'_e(2\pi)^3} \prod_{j=1}^{N_X} \frac{d^3\mathbf{p}_{X,j}}{2E_{X,j}(2\pi)^3},$$

gives

$$\frac{E'_e d\sigma}{d^3\mathbf{l}'} = \frac{\alpha_{\mathrm{EM}}^2}{4\pi(l \cdot p)} L_{\mu\nu}(l, l') \int dX (2\pi)^4 \delta^{(4)}(p + q - p_X) \frac{1}{2} \sum_{\sigma} \langle p, \sigma \mid J^\mu(0) \mid X \rangle \langle X \mid J^\nu(0) \mid p, \sigma \rangle, \tag{2.3}$$

where

$$\int dX = \sum_X \int \prod_{j=1}^{N_X} \frac{d^3\mathbf{p}_{X,j}}{2E_{X,j}(2\pi)^3} \sum_{\{\lambda_{X,j}\}} \tag{2.4}$$

is shorthand for summation and integration over all hadronic states X, and where $L_{\mu\nu}(k, k')$ is the leptonic tensor, given by

$$L_{\mu\nu}(l, l') = \frac{1}{2} \sum_{\lambda,\lambda'} \bar{u}^\lambda(l) \gamma_\mu u^{\lambda'}(l') \bar{u}^{\lambda'}(l') \gamma_\nu u^\lambda(l) = 2 \left(l_\mu l'_\nu + l'_\mu l_\nu - (l \cdot l') g_{\mu\nu} \right). \tag{2.5}$$

In analogy to the leptonic tensor, a hadronic tensor $W^{\mu\nu}(p, q)$ is also defined:

$$W^{\mu\nu}(p, q) = \frac{1}{4\pi M} \int dX (2\pi)^4 \delta^{(4)}(p + q - p_X) \frac{1}{2} \sum_{\sigma} \langle p, \sigma \mid J^\mu(0) \mid X \rangle \langle X \mid J^\nu(0) \mid p, \sigma \rangle. \tag{2.6}$$

Since all the degrees of freedom associated with the final hadronic state X are summed, it is a function of just p and q. The hadronic tensor is symmetric in its indices since any anti-symmetric contributions will disappear when contracted with $L_{\mu\nu}$, and it is Hermitian since exchanging the indices in Eq. (2.6) is equivalent to complex conjugation. Thus, it is

a real-valued function. It is possible to rewrite $W^{\mu\nu}(p,q)$ as

$$W^{\mu\nu}(p,q) = \frac{1}{4\pi M}\int d^4x e^{iq\cdot x}\frac{1}{2}\sum_\sigma \langle p,\sigma \mid J^\mu(x)J^\nu(0)\mid p,\sigma\rangle, \tag{2.7}$$

which is found by using the Fourier transform $\delta^{(4)}(p+q-p_X) = \int d^4x e^{i\cdot(p+q-p_X)}$, and the fact that $J^\mu(0)$ transforms under the Poincare group as $J^\mu(0) = e^{i\hat{P}\cdot x}J^\mu(0)e^{-i\hat{P}\cdot x}$. Eq. (2.7) can be used as the starting point of the operator product expansion, which allows a great deal of knowledge about proton or nuclear structure to be determined from general principles such as symmetries. It can also be used to see that current conservation, *i.e.*, $\partial_\mu J^\mu(x) = 0$ implies $q_\mu W^{\mu\nu}(p,q) = 0$. The index exchange symmetry of $W^{\mu\nu}(p,q)$, along with this current conservation condition, means that the most general possible form that the hadronic tensor can take is

$$W^{\mu\nu}(p,q) = \left(-g^{\mu\nu}+\frac{q^\mu q^\nu}{q^2}\right)W_1(p,q)+\left(p^\mu-\frac{(p\cdot q)q^\mu}{q^2}\right)\left(p^\mu-\frac{(p\cdot q)q^\mu}{q^2}\right)\frac{W_2(p,q)}{M^2}. \tag{2.8}$$

The structure functions $W_1(p,q)$ and $W_2(p,q)$ are functions of just the scalar invariants q^2 and $(p\cdot q)$, or equivalently of the momentum transfer $Q^2 = -q^2$ and the Bjorken scaling variable $x_B = \frac{Q^2}{2(p\cdot q)}$. Typically, one uses rescaled structure functions that are redefined to be unitless (*n.b.* $W_{1/2}(p,q)$ have units of inverse energy):

$$F_1(x_B,Q^2) = MW_1(p,q) \tag{2.9}$$

$$F_2(x_B,Q^2) = \frac{(p\cdot q)}{M}W_2(p,q) = \nu W_2(p,q). \tag{2.10}$$

Since the hadronic tensor depends on these two structure functions alone, likewise does the cross section. It is possible to derive from Eq. (2.3), and the definitions of the leptonic tensor and structure functions:

$$\frac{d\sigma}{dE_e' d\Omega} = \frac{\alpha_{\rm EM}^2}{4E_e^2\sin^4\frac{\theta}{2}}\left[\frac{1}{\nu}F_2(x_B,Q^2)\cos^2\frac{\theta}{2}+\frac{2}{M}F_1(x_B,Q^2)\sin^2\frac{\theta}{2}\right], \tag{2.11}$$

where θ is the angle between the incident and scattered electron momenta.

Spacetime diagram for DIS in parton model

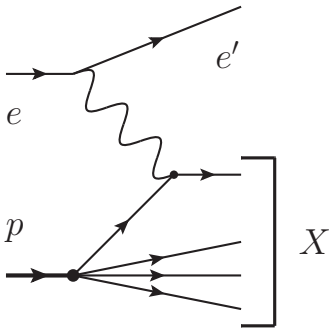

Figure 2.2: The reaction $ep \to e'X$ at a partonic level.

2.1.3 The parton model

The quark-parton model, originally proposed by J. D. Bjorken [15] and R. P. Feynman [16], postulates that hadrons are made up of pointlike, structureless parts called "partons". According to this model, deep inelastic electron scattering occurs by exchange of a highly virtual photon with a charged parton. A spacetime picture of such a process is depicted in Fig. 2.2. The applicability of such a picture requires the interaction time to be extremely short, in particular much shorter than the characteristic interaction times within the hadron. This is achieved by (1) using the light cone formalism, where the light cone "time" is given by $x^+ = ct + z$, and (2) going to the infinite momentum frame, *i.e.*, taking the limit $p^+ = E + p_z \to \infty$, so that the light cone time x^+ becomes infinitely dilated and the partonic structure of the target becomes frozen. This is an idealization, but a decent approximation in high-energy experiments, and one for which corrections can be calculated since the nature of the partonic interactions (*i.e.*, QCD) is known.

The parton model assumes a collinear approximation: in a frame of reference where the composite hadron is moving extremely fast in the forward light cone direction, the partons are assumed to be collinear with the target. Moreover, this approximation neglects the masses of the partons, which are assumed to be small compared to the energy and momentum transfer scales that characterize reactions where partons can be seen.

The quark-parton model is understood in the light cone framework, and the hadronic tensor $W^{\mu\nu}(p, q)$ is calculated using light cone perturbation theory. Since this formalism is

Feynman diagram for hadronic current in parton model

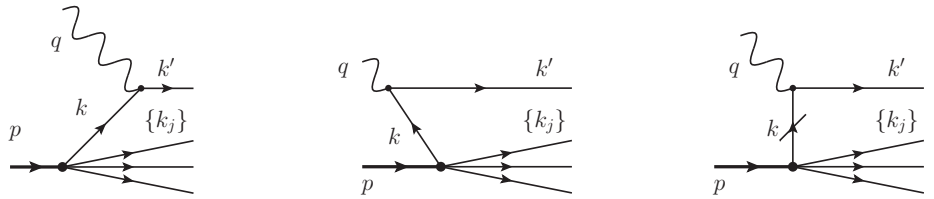

(a) Parton from hadron (b) Parton from photon (c) Contact term

Figure 2.3: Feynman diagrams for $\langle X \mid J^\mu(0) \mid p, \sigma \rangle$ in the parton model.

"time"-order dependent, there are three diagrams for matrix element $\langle X \mid J^\mu(0) \mid p, \sigma \rangle$, depicted in Fig. 2.3. By appropriate choice of coordinates, namely with $q^+ = 0$, the diagrams of Fig. 2.3b (in which the photon splits) and Fig. 2.3c (in which the parton is "simultaneously" [in light cone time] present at both the photon and inside the hadron) can be made to vanish [17]. Thus only Fig. 2.3a needs to be calculated.

Because of the collinearity of the quark-parton model, the component $J^-(0)$ of the hadronic current decouples from the DIS reaction, meaning $W^{--}(p,q) = W^{+-}(p,q) = W^{-+}(p,q) = 0$ [17]. Calculating $W^{++}(p,q)$ allows one to relate the parton distribution function, defined by the formula [17]

$$f_{i/p}(x_B) = \sum_{\mathcal{F}} \int \frac{dx d^2\mathbf{k}_\perp}{2x(2\pi)^3} \prod_{j=1}^{n_s} \frac{dx_j d^2\mathbf{k}_{j\perp}}{2x_j(2\pi)^3} 2(2\pi)^3 \delta^{(1)}\left(1 - x - \sum_{j=1}^{n_s} x_j\right) \delta^{(2)}\left(\mathbf{k}_\perp + \sum_{j=1}^{n_s} \mathbf{k}_{j\perp}\right)$$
$$\delta^{(1)}(x - x_B) \overline{\left|\psi_{i,\mathcal{F}/p}(x, \mathbf{k}_\perp; \{x_j\}, \{\mathbf{k}_{j\perp}\})\right|^2}, \tag{2.12}$$

to the structure function $F_2(x_B, Q^2)$. Here, $\psi_{i,\mathcal{F}/p}(x, \mathbf{k}_\perp; \{x_j\}, \{\mathbf{k}_{j\perp}\})$ is the light cone wave function of the parton within the hadron (*cf.* [18]). The relationship, given by [17]:

$$F_2(x_B) = \sum_i e_i^2 x_B f_{i/p}(x_B), \tag{2.13}$$

can be derived from the general form of $W^{\mu\nu}(p,q)$ within the quark-parton model.

The lack of dependence of F_2 on Q^2 in Eq. (2.13) is called Bjorken scaling [15, 19] and is a consequence of neglecting interactions between partons. It is an imperfect description

of experimental data for $F_2(x_B, Q^2)$, which include logarithmic Q^2 dependence known as "scaling violations." Several authors (see [12–14]) derived the so-called DGLAP evolution equations, which introduce the requisite logarithmic Q^2 dependence into $f_{i/p}(x_B, Q^2)$ by using the known forms of QCD interactions. Currently, a wide range of experimental data agree to great precision with the predictions of DGLAP evolution [3].

In summary, the quark-parton model and DGLAP evolution are known to explain the internal structure of the proton with great success. It is the purpose of the present work to import this legacy to nuclear physics, and to describe nuclear structure in terms of its partonic degrees of freedom. This possibility will be explored for the remainder of the chapter.

2.2 Deep inelastic scattering from nuclei

It is in principle possible to perform deep inelastic scattering of electrons from any hadronic target, and use experimental data about the reaction to determine the partonic structure of this target. Nuclei may accordingly be targets in such experiments. The formalism developed previously for proton targets may thus be applied directly to nuclei, with merely changes of notation: p_A and M_A will notate the four-momentum and mass of the nucleus, $W_A^{\mu\nu}(p_A, q)$ the nuclear hadronic tensor, $F_{1/2}^{(A)}(x_A, Q^2)$ the nuclear structure functions, *etc.* The biggest change of notation arises from the conventional definition of the nuclear Bjorken scaling variable; one defines, for nuclear DIS:

$$x_A = A\frac{Q^2}{2(p_A \cdot q)} = A\frac{Q^2}{2\nu M_A}, \tag{2.14}$$

with ν being the energy transfer from the lepton to the nucleus in the lab frame.

Direct application of the DIS formalism to a nuclear target, without any additional development, would leave us back at the beginning: the wave function of the nucleus, in terms of its partonic structure, cannot be calculated from first principles, and one would need to determine the partonic structure of each nucleus separately from DIS experiments. However, it is a the goal of further theoretical development to avoid this. Previously-

obtained knowledge of the partonic structure of nucleons, together with knowledge about the conventional nuclear structure of nuclei in terms of protons and neutrons, should be combined in order to determine the partonic structure of nuclei. Once the nuclear parton distribution functions (nPDFs) are theoretically obtained in this way, predictions for cross sections can be compared to experiment.

For a very crude example of how nuclear and nucleonic partonic structure might be related—with a conceptual justification for the factor of A present in the definition of x_A—consider what the partonic structure of nuclei would look like if a nucleus with mass number A and charge number Z consisted of Z protons and $(A-Z)$ neutrons, all non-interacting and all at rest in the lab frame. If $f_{i/p}$, $f_{i/n}$, and $f_{i/A}$ denote the PDFs of the proton, neutron, and nucleus respectively, then one would have

$$f_{i/A}(x_B, Q^2) = Z f_{i/p}(x_B, Q^2) + (A-Z) f_{i/n}(x_B, Q^2), \tag{2.15}$$

in the approximation $m_p \approx m_n \equiv m_N$. In such a scenario, the lepton probe scatters from one of the nucleons, and the contributions add incoherently. $x_B \equiv \frac{Q^2}{2\nu m_N}$[2] is the proper scaling variable, since the *de facto* target was one of the nucleus's constituent nucleons, which was at rest. However, x_B is the fraction of the nucleon's forward momentum carried by the struck parton, rather than that of the nucleus. The fraction of the nucleus's forward momentum carried by the struck parton is instead

$$\frac{k^+}{p_A^+} = \frac{k^+}{p_N^+}\frac{p_N^+}{p_A^+} = x_B \frac{m_N}{M_A} = \frac{Q^2}{2\nu m_N}\frac{m_N}{M_A} = \frac{Q^2}{2\nu M_A} = \frac{x_A}{A}.$$

In other words, $\frac{x_A}{A}$ is the actual fraction of the nucleus's light cone momentum carried by the parton; however, $x_B \approx x_A$ (with the approximation being inexact owing to the binding energy of the nucleus, *i.e.* the fact that $M_A \neq A m_N$) is the scaling variable in the "free nucleon" approximation. Accordingly, x_B or x_A is used in the comparison of nuclear to nucleonic DIS data and predictions, since differences between the structure functions for

[2] Bjorken x_B is always defined with the nucleonic mass, rather than the target mass.

the nucleon and nucleus at a fixed x_A (where $x_A = x_B$ in the special case $A = 1$) indicate nuclear structure.

Another significant indication of nuclear structure comes from the possibility that $x_A > 1$. This is kinematically possible, since the upper limit of x_A comes (kinematically) from $(p_A + q)^2 = p_X^2 \geq M_A^2$, which entails $\frac{Q^2}{2(p_A \cdot q)} \leq 1$.

In particular, $x_A > 1$ indicates motion of the struck nucleon. Although the upper limit of the momentum fraction $x_N = \frac{k^+}{p_N^+}$ is 1, if the nucleon is bound and in motion relative to the lab frame then $x_N \neq x_B$. In situations where $x_N < x_B$, since $x_N = 1$ at most, one can have $x_B > 1$. Since this is purely an effect of nuclear structure, it is worth exploring scenarios where $x_B > 1$ (and $x_A > 1$) will occur.

2.2.1 Nuclear hadronic tensor, structure functions, and parton distributions

The nuclear hadronic tensor $W_A^{\mu\nu}(p_A, q)$ is defined in strict analogy to the proton's hadronic tensor, namely

$$W_A^{\mu\nu}(p_A, q) = \frac{1}{4\pi M_A} \int dX (2\pi)^4 \delta^{(4)}(p_A + q - p_X) \\ \frac{1}{2} \sum_{s_A} \langle p_A, s_A \mid J^\mu(0) \mid X \rangle \langle X \mid J^\nu(0) \mid p_A, s_A \rangle. \tag{2.16}$$

Just as with the hadronic tensor of the proton, the nuclear hadronic tensor decomposes into a sum of scalar functions of p_A and q, namely

$$W_A^{\mu\nu}(p_A, q) = \left(-g^{\mu\nu} + \frac{q^\mu q^\nu}{q^2} \right) W_1^{(A)}(p_A, q) \\ + \left(p_A^\mu - \frac{(p_A \cdot q) q^\mu}{q^2} \right) \left(p_A^\mu - \frac{(p_A \cdot q) q^\mu}{q^2} \right) \frac{W_2^{(A)}(p_A, q)}{M_A^2}, \tag{2.17}$$

and moreover structure functions $F_1^{(A)}(x_A, Q^2)$ and $F_2^{(A)}(x_A, Q^2)$ are defined in terms of these as

$$F_1^{(A)}(x_A, Q^2) = M_A W_1^{(A)}(p_A, q) \tag{2.18}$$

$$F_2^{(A)}(x_A, Q^2) = \frac{(p_A \cdot q)}{M_A} W_2^{(A)}(p_A, q) = \nu W_2^{(A)}(p_A, q). \tag{2.19}$$

One can find $F_2^{(A)}(x_A, Q^2)$ by looking specifically at the $++$ component of the nuclear hadronic tensor; one finds

$$W_A^{++}(p_A, q) = \frac{(p_A^+)^2}{M_A(q \cdot p_A)} F_2^{(A)}(x_A, Q^2). \tag{2.20}$$

With Eq. (2.20), we are in a position to find the relationship between $F_2^{(A)}(x_A, Q^2)$ and the nuclear PDF.

The derivation of the nuclear PDF is given now. In particular, we find the expression for $W_A^{++}(p_A, q)$ in terms of the nuclear PDF by first evaluating the matrix element $\langle X \mid J^+(0) \mid p_A, s_A \rangle$. The final state X in this derivation is characterized by the flavor i of the struck parton, since a hard probe will knock the struck parton far from the rest of the target, causing flavor to be added incoherently, and the Fock component $\mathcal{F}$ of partons making up the nucleus. Realistically, in nuclear DIS reactions, one or a few nucleons are removed and just one of the nucleons is destroyed, leaving the others, as well as a nuclear remnant, intact. However, owing to quark-hadron duality, we can express a general final state (including *e.g.*, states where just one nucleon is removed and destroyed and the remaining $(A-1)$ nucleons are left in an excited bound state) in terms of quark and gluon degrees of freedom, and a sum over all such partonic degrees of freedom is equivalent to a sum over all possible hadronic final states. Therefore, we proceed in this section by considering the final hadronic state as $\mid X\rangle = \mid i, \mathcal{F}\rangle$. Later in this chapter, scenarios with more specific final states (in terms of nucleonic degrees of freedom) will be considered, and comparing the result of this derivation to that of subsequent calculations will be used to relate the nuclear PDF to the nucleonic degrees of freedom of the nucleus.

Bearing these considerations in mind, we have

$$\langle i, \mathcal{F} \mid J^+(0) \mid p_A, s_A \rangle = \bar{u}_i^{\lambda'}(k') e_i \gamma^+ \frac{\sum_\lambda u_i^\lambda(k) \bar{u}_i^\lambda(k) \Theta(k^+)}{k^+ \mathcal{D}(k^-)} \left[\prod_{j=1}^{n_s} \bar{u}_{i_j}^{\lambda_j}(k_j) \right] \Gamma_{\mathcal{F}/A} u_A^{s_A}(p_A), \tag{2.21}$$

where here $u_A^{s_A}(p_A)$ denotes the part of the nuclear wave function that transforms under an irreducible representation of the Lorentz group[3]. The denominator factor, $\mathcal{D}(k^-)$ is given by

$$\mathcal{D}(k^-) = p_A^- - k^- - \sum_{i=1}^{n_s} k_i^- = \frac{1}{p_A^+} \left(M_A^2 - \frac{m_i^2 + \mathbf{k}_\perp^2}{x/A} - \sum_{j=1}^{n_s} \frac{m_{i_j}^2 + \mathbf{k}_{j\perp}^2}{x_j/A} \right), \tag{2.22}$$

where $x = A\frac{k^+}{p_A^+}$ and $x_i = A\frac{k_i^+}{p_A^+}$, since we consistently adopt the convention of scaling momentum fractions by A as long as x_A is going to be scaled as such. Except for the factor of $\frac{1}{p_A^+}$, this is the denominator of the light cone wave function [18], give by:

$$\psi_{i,\mathcal{F}/A}^{(\lambda,\{\lambda_j\};s_A)}(x, \mathbf{k}_\perp; \{x_j\}, \{\mathbf{k}_{j\perp}\}; p_A) = \frac{\left[\prod_{j=1}^{n_s} \bar{u}_{i_j}^{\lambda_j}(k_j)\right] \bar{u}_i^\lambda(k) \Gamma_{\mathcal{F}/A} u_A^{s_A}(p_A)}{M_A^2 - \frac{m_i^2 + \mathbf{k}_\perp^2}{x/A} - \sum_{j=1}^{n_s} \frac{m_{i_j}^2 + \mathbf{k}_{j\perp}^2}{x_j/A}}. \tag{2.23}$$

Using this and the spinor relation $\bar{u}^{\lambda'}(k')\gamma^+ u^\lambda(k) = 2\sqrt{k^+ k'^+}\delta_{\lambda\lambda'}$ gives

$$\langle i, \mathcal{F} \mid J^+(0) \mid p_A, s_A \rangle = e_i 2p_A^+ \psi_{i,\mathcal{F}/A}^{(\lambda,\{\lambda_j\};s_A)}(x, \mathbf{k}_\perp; \{x_j\}, \{\mathbf{k}_{j\perp}\}; p_A). \tag{2.24}$$

Therefore we have, for the ++ component of the nuclear hadronic tensor,

$$W_A^{++}(p_A, q) = \frac{1}{4\pi M_A} \sum_{i,\mathcal{F}} \int \frac{dk'^+ d^2\mathbf{k}'_\perp}{2k'^+(2\pi)^3} \prod_{j=1}^{n_s} \frac{dk_j^+ d^2\mathbf{k}_{j\perp}}{2k_j^+(2\pi)^3} \left[(2\pi)^4 \delta^{(4)} \left(p_A + q - k' - \sum_{j=1}^{n_s} k_j \right) \right.$$
$$\left. 4(p_A^+)^2 \overline{\left| \psi_{i,\mathcal{F}/A}(x, \mathbf{k}_\perp; \{x_j\}, \{\mathbf{k}_{j\perp}\}) \right|^2} \right]. \tag{2.25}$$

[3] For instance, if the nucleus is spin-half, u_A is just a Dirac spinor; if the nucleus is spin-zero, u_A is a constant; if the nucleus is spin-one, u_A is a polarization four-vector; and so on.

We work with three particular approximations when using the quark-parton model: (1) the collinear approximation, in which the transverse momentum of the partons is set to zero prior to scattering; (2) the massless quark approximation; and (3) the Bjorken limit, in which Q^2 is much larger than other energy scales involved, but Q^2/ν is fixed. Within these approximations, the four-dimensional delta function evaluates to

$$\delta^{(4)}\left(p_A+q-k'-\sum_{j=1}^{n_s}k_j\right)=\frac{x_A}{(q\cdot p_A)}\delta^{(1)}\left(x-x_A\right)\\ \delta^{(1)}\left(1-\frac{x}{A}-\sum_{j=1}^{n_s}\frac{x_j}{A}\right)\delta^{(2)}\left(\mathbf{k}_\perp+\sum_{j=1}^{n_s}\mathbf{k}_{j\perp}\right). \tag{2.26}$$

Next, we need to employ the definition of a parton distribution, but must be careful that the formal definition will be given in terms of a scaled momentum fraction. If a prototypical nuclear PDF is given in terms of an unscaled momentum fraction $\tilde{x}_A = x_A/A$ as

$$\tilde{f}_{i/A}(\tilde{x}_A)=\sum_{\mathcal{F}}\int\frac{d\tilde{x}d^2\mathbf{k}_\perp}{2\tilde{x}(2\pi)^3}\prod_{j=1}^{n_s}\frac{d\tilde{x}_j d^2\mathbf{k}_{j\perp}}{2\tilde{x}_j(2\pi)^3}2(2\pi)^3\delta^{(1)}\left(1-\tilde{x}-\sum_{j=1}^{n_s}\tilde{x}_j\right)\delta^{(2)}\left(\mathbf{k}_\perp+\sum_{j=1}^{n_s}\mathbf{k}_{j\perp}\right)\\ \delta^{(1)}(\tilde{x}-\tilde{x}_A)\,\overline{\left|\psi_{i,\mathcal{F}/p}(\tilde{x},\mathbf{k}_\perp;\{\tilde{x}_j\},\{\mathbf{k}_{j\perp}\})\right|^2}\,, \tag{2.27}$$

i.e., if the ordinary definition of a PDF in terms of the true momentum fraction is used, then because the ordinary sum rules are obeyed for integrations over $\tilde{x}_A$, *e.g.*

$$\int_0^1 d\tilde{x}_A\left[\tilde{f}_{u/A}(\tilde{x}_A)-\tilde{f}_{\bar{u}/A}(\tilde{x}_A)\right]=N_u=2Z+(A-Z) \tag{2.28}$$

$$\sum_i\int_0^1 d\tilde{x}_A\tilde{x}_A\tilde{f}_{i/A}(\tilde{x}_A)=1, \tag{2.29}$$

we have for the scaled fraction x_A the relations

$$\int_0^A dx_A\left[\tilde{f}_{u/A}(x_A)-\tilde{f}_{\bar{u}/A}(x_A)\right]=AN_u=2AZ+A(A-Z) \tag{2.30}$$

$$\sum_i\int_0^A dx_A x_A\tilde{f}_{i/A}(x_A)=A^2. \tag{2.31}$$

This is not the correct normalization for the nPDF, since integration over the chosen momentum fraction should yield N_u for the valence quark sum rule and A for the momentum sum rule (rather than 1, since the scaling of x_A by A means the total amount of forward momentum in fractional units is A). Thus, the correct definition of the nPDF in terms of x_A is $f_{i/A} = \frac{1}{A}\tilde{f}_{i/A}$, or

$$f_{i/A}(x_A) = \sum_{\mathcal{F}} \int \frac{dx d^2\mathbf{k}_\perp}{2x(2\pi)^3} \prod_{j=1}^{n_s} \frac{dx_j d^2\mathbf{k}_{j\perp}}{2x_j(2\pi)^3} 2(2\pi)^3 \delta^{(1)}\left(1 - \frac{x}{A} - \sum_{j=1}^{n_s} \frac{x_j}{A}\right) \delta^{(2)}\left(\mathbf{k}_\perp + \sum_{j=1}^{n_s} \mathbf{k}_{j\perp}\right)$$
$$\delta^{(1)}(x - x_A) \overline{\left|\psi_{i,\mathcal{F}/p}(x, \mathbf{k}_\perp; \{x_j\}, \{\mathbf{k}_{j\perp}\})\right|^2}, \tag{2.32}$$

where the factor of $\frac{1}{A}$ has been absorbed by the delta function $\delta^{(1)}(x - x_A)$. With this definition in hand, one finds that

$$W_A^{++}(p_A, q) = \frac{(p_A^+)^2}{M_A(p_A \cdot q)} \sum_i e_i^2 x_A f_{i/A}(x_A), \tag{2.33}$$

or in terms of the nuclear structure function,

$$F_2^{(A)}(x_A) = \sum_i e_i^2 x_A f_{i/A}(x_A). \tag{2.34}$$

Eq. (2.34) predicts scaling for nuclear DIS in the Bjorken limit. Scaling violations will however occur due to interactions between partons, and these violations are manifested in Q^2 evolution of the nuclear PDF.

While these formulas look identical in their form to those of the proton PDF, it was important to ensure that this identical form held in spite of the A-scaled definition of x_A. With these formulas in hand, it is possible to now relate the nuclear PDF to the nucleonic degrees of freedom of the nucleus, together with the partonic structure of the nucleons. To do this will require that a formalism be developed for describing the nucleonic degrees of freedom in a manner formally equivalent to the partonic degrees of freedom, *i.e.*, in terms of a light cone fraction distribution. This is done in the next section.

2.3 The nuclear light cone fraction distribution

To describe nuclear structure in the light cone momentum representation, we use a light cone fraction distribution (LCFD) $f_{N/A}(\alpha, \mathbf{p}_\perp)$. This essentially describes how nucleons of "flavor" $N = p$ and $N = n$ are distributed over various values of the (scaled) light cone momentum fraction

$$\alpha = A\frac{p_N^+}{P_A^+}, \tag{2.35}$$

as well as the nucleon transverse momentum $\mathbf{p}_\perp$. The LCFD is defined in analogy to the parton distribution function, but instead it describes the distribution of nucleons inside a nucleus. In particular, it is defined to satisfy sum rules, *viz.*

$$\int_0^A d\alpha \int d^2\mathbf{p}_\perp \left(f_{p/A}(\alpha, \mathbf{p}_\perp) - f_{\bar{p}/A}(\alpha, \mathbf{p}_\perp)\right) = Z \tag{2.36}$$

$$\int_0^A d\alpha \int d^2\mathbf{p}_\perp \left(f_{n/A}(\alpha, \mathbf{p}_\perp) - f_{\bar{n}/A}(\alpha, \mathbf{p}_\perp)\right) = (A - Z), \tag{2.37}$$

in analogy to the valence quark sum rules for the PDF of a proton, and a momentum conservation sum rule

$$\sum_N \int_0^A d\alpha \int d^2\mathbf{p}_\perp \frac{\alpha}{A} f_{N/A}(\alpha, \mathbf{p}_\perp) = 1. \tag{2.38}$$

Notice that Eqs. (2.36,2.37) state that (*e.g.*) the number of protons minus the number of anti-protons in the nucleus is fixed to Z, in analogy to the number of u quarks minus $\bar{u}$ antiquarks being fixed to 2 in the proton. This accounts for the possibility, in principle, of a proton and anti-proton being created within the nucleus, something that could happen (with a very tiny probability) if an evolution equation analogous to DGLAP were developed and applied to the hadronic structure of the nucleus. Developing an account of evolution in this way would be less straightforward than in the case of QCD, since conventional nuclear physics is not a fundamental theory describing pointlike objects. However, since nucleon masses are large in comparison to momentum transfer scales where conventional nuclear physics is applicable, the creation of nucleon-antinucleon pairs is extremely unlikely, and it

is reasonable to take $f_{\bar{p}/A}(\alpha, \mathbf{p}_\perp) = f_{\bar{n}/A}(\alpha, \mathbf{p}_\perp) = 0$. Accordingly, the baryon number sum rules are simplified to

$$\int_0^A d\alpha \int d^2\mathbf{p}_\perp f_{p/A}(\alpha, \mathbf{p}_\perp) = Z \tag{2.39}$$

$$\int_0^A d\alpha \int d^2\mathbf{p}_\perp f_{n/A}(\alpha, \mathbf{p}_\perp) = (A - Z). \tag{2.40}$$

2.3.1 Decomposition of the LCFD

For relativistic bound states, the meaning of such a quantity as the LCFD is best understood in terms of processes. Most straightforward to consider are scenarios where an impulse approximation works reasonably well; a hard probe collides with a single nucleon, producing some final state (by scattering elastically, destroying the nucleon, inducing production of specific hadrons, or something else), without any final state interactions with the remainder of the nucleus. The lack of final state interactions requires that the entire process occurs within a very small time and distance scale, requiring sufficiently large Q^2 and x_A. In particular, x_A should be considered well within the valence region of the nuclear PDF, so $x_A \gtrsim 0.2$, and one should take $Q^2 \gg m_N^2$ in order to avoid complications from higher-twist and target mass effects.

Even within the impulse approximation, it is possible to obtain final states with varying numbers of removed nucleons. Consider first the mean field approximation, which is is characterized by the assumption that each nucleon within the nucleus acts independently, under the influence of the force produced by the bulk of the nucleus (*i.e.* by the other $(A-1)$ nucleons). In other words, none of the $(A-1)$ spectators is specifically correlated with a nucleon that is removed in a nuclear reaction, and the missing momentum in *e.g.*, the quasi-elastic removal reaction $A(e, e'N)$ is shared entirely by the remaining $(A-1)$ nucleons, which remain in a bound state. In other nuclear processes (such as hadron production and inclusive DIS), the final state will be more complicated than $e' + N + (A-1)$, and the removed nucleon may even be destroyed (such as in the case of DIS), but the contribution

of the mean field to such a reaction will nonetheless include a remnant of $(A-1)$ nucleons in a bound, possibly excited state.

On the other hand, it is possible to have configurations where a small number of nucleons cluster at short distance, and balance each others' momenta. For instance, there are configurations where the probed nucleon has a large initial momentum in the nuclear center of momentum frame, $\gtrsim 250$ MeV or so, which is balanced almost entirely by a single nucleon. Such a configuration is called a short range correlation (SRC), and probing a nucleon in an SRC will remove not just the probed nucleon, but its correlated partners from the nucleus as well. This will be explained further in Sec. 2.4.

Since final states with different numbers of removed nucleons occupy far distant regions of phase space, the probabilities for processes which produce these final states will add incoherently. Accordingly, within the impulse approximation, the distributions describing scenarios which will result in these incoherently added final states can also be added incoherently. In other words, the LCFD can be decomposed into distributions of nucleons within the mean field (which will produce one removed nucleon) and within j-nucleon correlations (which will produce j removed nucleons). In equations, we have

$$f_{N/A}(\alpha, \mathbf{p}_\perp) = f^{(\mathrm{MF})}_{N/A}(\alpha, \mathbf{p}_\perp) + \sum_{j=2}^{A} f^{(j)}_{N/A}(\alpha, \mathbf{p}_\perp) = \sum_{j=1}^{A} f^{(j)}_{N/A}(\alpha, \mathbf{p}_\perp), \tag{2.41}$$

where $f^{(1)}_{N/A}(\alpha, \mathbf{p}_\perp)$ may be used to denote the mean field part of the LCFD (*i.e.* the part that contributes to the one nucleon removal cross section). Since $f_{N/A}(\alpha, \mathbf{p}_\perp)$ is normalized to the number of nucleons of "flavor" N in the nucleus (*e.g.* $f_{p/A}(\alpha, \mathbf{p}_\perp)$ is normalized to Z), $f^{(j)}_{N/A}(\alpha, \mathbf{p}_\perp)$ in general will not be normalized as such; instead, $f^{(j)}_{p/A}(\alpha, \mathbf{p}_\perp)$ will be normalized to the average number of protons in the mean field ($j = 1$) or in a j-nucleon SRC ($j \geq 2$). Likewise, $\frac{1}{Z} f^{(j)}_{p/A}(\alpha, \mathbf{p}_\perp)$ will indicate the probability of a single proton being in the mean field or a j-nucleon correlation.

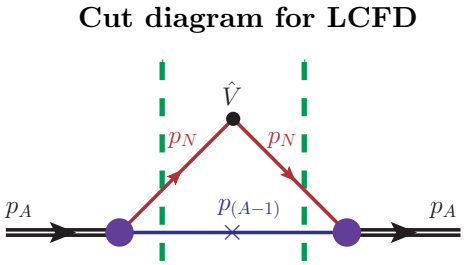

Figure 2.4: Cut diagram for finding the LCFD.

2.3.2 Diagrammatic rules for the LCFD

It is possible to find a set of diagrammatic rules for calculating the LCFD and derive relations involving it. There are obstacles to using the most straightforward methods such as the optical theorem, since nucleons are not elementary particles and the vertex factors involved in the process may contain poles in the complex plane in addition to the poles contained in the propagators, and since the final state particles will not necessarily all be nucleons, but will in general contain a bound state of $(A-1)$ or $(A-j)$ nucleons (depending on how many nucleons are removed in the relevant process).

In light of these concerns, one instead uses a cut diagram, an example of which is depicted in Fig. 2.4. In the cut diagram, spectator particles are placed on their light cone energy shells, while the interacting particle has an operator $\hat{V}_N(\alpha, \mathbf{p}_\perp; \alpha_N, \mathbf{p}_{N\perp})$, given by

$$\hat{V}_N(\alpha, \mathbf{p}_\perp; \alpha_N, \mathbf{p}_{N\perp}) = \sum_\sigma a_N^\dagger(p,\sigma)\frac{\alpha}{A}\delta^{(1)}(\alpha - \alpha_N)\delta^{(2)}(\mathbf{p}_\perp - \mathbf{p}_{N\perp})a_N(p,\sigma), \tag{2.42}$$

placed on its internal line.

The creation and annihilation operators satisfy the rules

$$\bar{u}_{N'}^{\sigma'}(p)a_N^\dagger(p,\sigma) = a_N(p,\sigma)u_{N'}^{\sigma'}(p) = \delta_{\sigma\sigma'}\delta_{NN'}.$$

Essentially, the operator $\hat{V}_N(\alpha, \mathbf{p}_\perp; \alpha_N, \mathbf{p}_{N\perp})$ fixes the light cone fraction and the transverse momentum of a probed nucleon to the fixed values α and $\mathbf{p}_\perp$, respectively, and ensures that the probed nucleon is of the correct "flavor" N. This does not involve a sum over

all nucleons, however. In Fig. 2.4, for instance, the final state is known to consist of a single nucleon and a bound state of $(A-1)$ nucleons. Accordingly, this diagram is used for calculating $\frac{1}{A\chi_N} f^{(MF)}_{N/A}(\alpha, \mathbf{p}_\perp)$ (where χ_N is the fraction of nucleons of "flavor" N, *i.e.* $\chi_p = \frac{Z}{A}$ and $\chi_n = \frac{(A-Z)}{A}$).

2.3.3 The LCFD for the mean field

Using Fig. 2.4, let us calculate the LCFD of the mean field using the rules of light cone perturbation theory. We have

$$\begin{aligned} f^{(MF)}_{N/A}(\alpha, \mathbf{p}_\perp) = \overline{\sum_{s_A}} \int \frac{d\alpha_s d^2\mathbf{p}_{s\perp}}{2\alpha_s(2\pi)^3} \Bigg[\bar{u}^{s_A}_A(p_A)\Gamma_{N/A} \frac{\sum_{\sigma_N} u^{\sigma_N}_N(p_N)\bar{u}^{\sigma_N}_N(p_N)}{p^+_N \mathcal{D}(p^-_N)} \\ \left(\sum_{\sigma_s} u^{\sigma_s}_{(A-1)}(p_s)\bar{u}^{\sigma_s}_{(A-1)}(p_s) \right) \hat{V}_N(\alpha, \mathbf{p}_\perp; \alpha_N, \mathbf{p}_{N\perp}) \\ \frac{\sum_{\sigma'_N} u^{\sigma'_N}_N(p_N)\bar{u}^{\sigma'_N}_N(p_N)}{p^+_N \mathcal{D}(p^-_N)} \Gamma_{N/A} u^{s_A}_A(p_A) \Bigg] \\ = \overline{\sum_{s_A}} \sum_{\sigma_N, \sigma_s} \frac{A}{\alpha_N \alpha_s} \left| \frac{1}{\sqrt{2(2\pi)^3}} \frac{\bar{u}^{\sigma_N}_N(p_N)\bar{u}^{\sigma_s}_{(A-1)}(p_s)\Gamma_{N/A} u^{s_A}_A(p_A)}{p^+_A \mathcal{D}(p^-_N)} \right|^2, \end{aligned} \tag{2.43}$$

where

$$p^+_A \mathcal{D}(p^-_N) = M^2_A - \frac{m^2_N + \mathbf{p}^2_{N\perp}}{\alpha_N/A} - \frac{M^2_{(A-1)} + \mathbf{p}^2_{N\perp}}{\alpha_s/A}.$$

The squared quantity between the $|\quad|$ in Eq. (2.43) takes roughly the form of a two-body wave function. However, a two-body light cone wave function is normalized to satisfy the relation

$$\int \frac{d\alpha_N d^2\mathbf{p}_{N\perp}}{\alpha_N(A-\alpha_N)} \overline{\left| \psi^{(MF)}_{N/A}(\alpha_N, \mathbf{p}_{N\perp}) \right|^2} = 1, \tag{2.44}$$

whereas the normalization of $f_{N/A}^{(MF)}(\alpha, \mathbf{p}_\perp)$ to $\chi_N A$ requires the right-hand side of Eq. (2.43) to be normalized as well to $\chi_N A$. In other words, the mean field wave function is given by

$$\psi_{N/A}^{(MF)(\sigma_N)}(\alpha_N, \mathbf{p}_{N\perp}) = \frac{1}{\sqrt{\chi_N}} \frac{1}{\sqrt{2(2\pi)^3}} \frac{\bar{u}_N^{\sigma_N}(p_N)\bar{u}_{(A-1)}^{\sigma_s}(p_s)\Gamma_{N/A}u_A^{s_A}(p_A)}{M_A^2 - \frac{m_N^2+\mathbf{p}_{N\perp}^2}{\alpha_N/A} - \frac{M_{(A-1)}^2+\mathbf{p}_{N\perp}^2}{\alpha_s/A}}, \tag{2.45}$$

and thus the LCFD is related to the wave function in the mean field by

$$f_{N/A}^{(MF)}(\alpha, \mathbf{p}_\perp) = \chi_N A \frac{1}{\alpha_N \alpha_s} \overline{\left|\psi_{N/A}^{(MF)}(\alpha_N, \mathbf{p}_{N\perp})\right|^2}. \tag{2.46}$$

With this, the baryon sum rule and the wave function normalization rule are simultaneously satisfied.

The mean field contribution to the nuclear wave function falls off rapidly above the Fermi momentum, which for a typical heavy nucleus is around 250 MeV [20]. Since $\frac{k_F^2}{m_N^2} \sim 0.005 \ll 1$, the non-relativistic limit is a valid approximation for these momenta, and relativistic corrections to a non-relativistic mean field model will at most be on the order one percent.

Constructing a non-relativistic mean field model requires relating the LCFD to the non-relativistic wave function. The non-relativistic wave function is different from the light cone wave function, since it is normalized in terms of different variables. Namely, it is normalized to satisfy $\int d^3\mathbf{p} \overline{\left|\psi_{N/A}^{(NR)}(\mathbf{p})\right|^2} = 1$, so must be related to the LCFD by $f_{N/A}^{(MF)}(\alpha, \mathbf{p}_\perp)d\alpha = \overline{\left|\psi_{N/A}^{(NR)}(\mathbf{p})\right|^2} dp_z$. In the non-relativistic limit, we have $dp_z \approx \frac{M_A}{A} d\alpha$, so the mean field LCFD is, in the non-relativistic limit:

$$f_{N/A}^{(MF)}(\alpha, \mathbf{p}_\perp) = \frac{M_A}{A} \overline{\left|\psi_{N/A}^{(NR)}(\mathbf{p})\right|^2}. \tag{2.47}$$

With Eq. (2.47), it is possible to perform numerical computations for the mean field contribution to the LCFD, and thus calculate cross sections for incoherent nuclear processes with one nucleon removed. Existing calculations of the mean field contribution have been done using Hartree-Fock approximations. For numerical computations, the mean field mo-

Feynman diagram for hadronic current of mean field

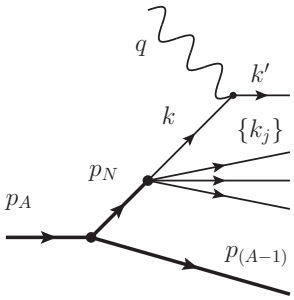

Figure 2.5: Diagram for $\langle X \mid J^+(0) \mid p_A, s_A \rangle$ in the mean field approximation.

mentum distributions calculated for ^{56}Fe and ^{208}Pb by Zverev and Saperstein [21] will be used in this dissertation.

2.3.4 Nuclear PDF in the mean field

The nuclear PDF within the mean field model of the nucleus can be related to the LCFD by the following convolution formula:

$$f_{i/A}^{(MF)}(x_A, Q^2) = \sum_{N=p,n} \int_{x_A}^{A} \frac{d\alpha}{\alpha} \int d^2\mathbf{p}_\perp f_{N/A}^{(MF)}(\alpha, \mathbf{p}_\perp) f_{i/N}^{(b,MF)}\left(\frac{x_A}{\alpha}, Q^2; \alpha, \mathbf{p}_\perp\right). \tag{2.48}$$

The function $f_{i/N}^{(b,MF)}\left(\frac{x_A}{\alpha}, Q^2; \alpha, \mathbf{p}_\perp\right)$ is the bound nucleon PDF for a parton with flavor i. The superscript b signifies that the nucleon is bound, which in general may alter its partonic structure. (See Sec. 2.5 for further discussion about this.) How the partonic structure of a bound nucleon is modified may depend on how strongly it is bound, which can depend on the kinematic parameters α and $\mathbf{p}_\perp$, which is why they are included as arguments. Here, I shall derive the convolution formula within the mean field approximation.

First, as before, the formula for $W_A^{++}(p_A, q)$ (given in Eq. (2.16)) is used. However, in evaluating the matrix element $\langle X \mid J^+(0) \mid p_A, s_A \rangle$ of the hadronic current, we characterize the final hadronic state X as consisting of (1) a (possibly excited) bound state of $(A-1)$

nucleons; (2) the Fock component $\mathcal{F}$ of the probed nucleon; (3) the "flavor" N of the probed nucleon[4]; and (4) the flavor i of the probed parton.

The diagram for the matrix element is given in Fig. 2.5, and the rules of light cone perturbation theory give

$$\begin{aligned}\langle X \mid J^+(0) \mid p_A, s_A\rangle = \bar{u}_i^{\lambda'}(k')e_i\gamma^+\frac{\sum_\lambda u_i^\lambda(k)\bar{u}_i^\lambda(k)}{k^+\mathcal{D}(k^-)}\left[\prod_{j=1}^{n_s}\bar{u}_{i_j}^{\lambda_j}(k_j)\right]\Gamma_{i,\mathcal{F}/N} \\ \frac{\sum_\lambda u_N^{\sigma_N}(p_N)\bar{u}_N^{\sigma_N}(p_N)}{p_N^+\mathcal{D}(p_N^-)}\bar{u}_{(A-1)}^{\sigma_s}(p_s)\Gamma_{N/A}u_A^{s_A}(p_A) \\ = 2p_A^+e_i\delta_{\lambda\lambda'}\psi_{i,\mathcal{F}/N}^{(\lambda,\{\lambda_j\};\sigma_N)}(x_N,\mathbf{k}_\perp,\{x_j,\mathbf{k}_{j\perp}\};\alpha_N,\mathbf{p}_{N\perp}) \\ \psi_{N/A}^{(\sigma_N,\sigma_s;s_A)(MF)}(\alpha_N,\mathbf{p}_{N\perp}),\end{aligned} \tag{2.49}$$

where $x_N = k^+/p_N^+$ and $x_j = k_j^+/p_N^+$ are the partons' light cone momentum fractions with respect to the nucleon's forward light cone momentum. It is worth noting that since the nucleon is in motion, the partonic wave function of the nucleon is given (in the lab frame) as a function of α_N and $\mathbf{p}_{N\perp}$ in addition to the partons' momenta.

In addition to the hadronic current matrix element, we must rewrite the four-dimensional delta function in $W_A^{++}(p_A,q)$. It decomposes in terms of light cone momenta as $\delta^{(4)}(\Delta p) = 2\delta^{(1)}(\Delta p^+)\delta^{(1)}(\Delta p^-)\delta^{(2)}(\Delta\mathbf{p}_\perp)$, with the "plus" and transverse components becoming statements of conservation rules within the nucleonic PDF, namely

$$\delta^+ = \delta^{(1)}\left(p_N^+ - k^+ - \sum_{j=1}^{n_s}k_j^+\right) = \frac{A}{\alpha_N p_A^+}\delta^{(1)}\left(1 - x_N - \sum_{j=1}^{n_s}x_j\right) \tag{2.50}$$

$$\delta^\perp = \delta^{(2)}\left(\mathbf{p}_{N\perp} - \mathbf{k}_\perp - \sum_{j=1}^{n_s}\mathbf{k}_{j\perp}\right), \tag{2.51}$$

and the "minus" delta function setting the momentum fraction x_N in terms of external observables; namely, in the collinear and massless quark approximations, with the Bjorken

[4] Since isospin is conserved in strong nuclear processes, the final states produced by a probed proton and neutron will be distinct.

limit taken, we have

$$\delta^- = p_A^+ \delta^{(1)}\left(2(q\cdot p_A) - \frac{AQ^2}{x_N \alpha_N}\right) = \frac{x_A p_A^+}{2(q\cdot p_A)\alpha_N}\delta^{(1)}\left(x_N - \frac{x_A}{\alpha_N}\right), \tag{2.52}$$

where we have defined $x_A = \frac{AQ^2}{2(q\cdot p_A)}$. This gives a nuclear hadronic tensor of

$$\begin{aligned} W_A^{++}(p_A,q) = \frac{(p_A^+)^2}{M_A(q\cdot p_A)} x_A \sum_i e_i^2 \sum_N \Bigg\{ \int \frac{d\alpha_N}{\alpha_N} d^2\mathbf{p}_{N\perp} \frac{A\chi_N \left|\psi_{N/A}^{(MF)}(\alpha_N,\mathbf{p}_{N\perp})\right|^2}{\alpha_N(A-\alpha_N)} \\ \int \frac{dx_N d^2\mathbf{k}_\perp}{2x_N(2\pi)^3} \prod_{j=1}^{n_s} \frac{dx_j d^2\mathbf{k}_{j\perp}}{2x_j(2\pi)^3} \Bigg[\left|\psi_{i,\mathcal{F}/N}(x_N,\mathbf{k}_\perp,\{x_j,\mathbf{k}_{j\perp}\};\alpha_N,\mathbf{p}_{N\perp})\right|^2 \\ 2(2\pi)^3\delta^{(1)}\left(1 - x_N - \sum_{j=1}^{n_s} x_j\right)\delta^{(2)}\left(\mathbf{p}_{N\perp} - \mathbf{k}_\perp - \sum_{j=1}^{n_s}\mathbf{k}_{j\perp}\right)\Bigg]\Bigg\} \\ = \frac{(p_A^+)^2}{M_A(q\cdot p_A)} x_A \sum_i e_i^2 \sum_N \int \frac{d\alpha_N}{\alpha_N} d^2\mathbf{p}_{N\perp} \Bigg[f_{N/A}^{(MF)}(\alpha_N,\mathbf{p}_{N\perp}) \\ f_{i/N}^{(b,1)}\left(\frac{x_A}{\alpha_N}, Q^2; \alpha_N, \mathbf{p}_{N\perp}\right)\Bigg]. \end{aligned} \tag{2.53}$$

Comparing this to Eq. (2.33), we have the convolution formula

$$f_{i/A}^{(MF)}(x_A,Q^2) = \sum_N \int_{x_A}^A \frac{d\alpha}{\alpha} \int d^2\mathbf{p}_\perp f_{i/N}^{(b,1)}\left(\frac{x_A}{\alpha}, Q^2; \alpha, \mathbf{p}_\perp\right) f_{N/A}^{(MF)}(\alpha,\mathbf{p}_\perp) \tag{2.54}$$

for the nPDF in the mean field. The lower limit of α in this integration is determined by the constraint that $x_N = x_A/\alpha \leq 1$.

2.4 Short range correlations

A short-range correlation (SRC) is a high-momentum, short-distance configuration of several nucleons within a nucleus. These stand in contrast to a mean field configuration, where each nucleon moves independently under the average influence of the $(A-1)$ other nucleons. In an SRC, by contrast, the nucleons within the short-distance configuration are strongly correlated with each other, and, owing to the short distance and the strength of the inter-nucleon force at short distances, nucleons in a j-nucleon SRC are predominantly influenced

by each other in their dynamics, with the influence of the $(A-j)$ remaining nucleons negligible in comparison.

2.4.1 The convolution formula

As discussed in Sec. 2.3.1, processes that involve different numbers of removed nucleons make contributions to the DIS cross section that are incoherently added. Since DIS from a short range correlation produces a different number of removed nucleons than mean field contributions—namely, j removed nucleons for a j-nucleon SRC—the mean field and j-nucleon SRCs add incoherently. This is encoded at the level of purely nucleonic physics by the decomposition of the LCFD in Eq. (2.41). A similar relation holds for the nuclear PDF, namely:

$$f_{i/A}(x_A, Q^2) = f_{i/A}^{(MF)}(x_A, Q^2) + \sum_{j=2}^{A} f_{i/A}^{(j)}(x_A, Q^2) = \sum_{j=1}^{A} f_{i/A}^{(j)}(x_A, Q^2). \tag{2.55}$$

The mean field contribution to the nPDF is related to the mean field part of the LCFD by Eq. (2.54). There is the question of whether a similar relation holds for the j-nucleon SRC contributions to the nPDF and their contributions to the LCFD. In fact, it will be demonstrated in this section that the following relation explicitly holds for $j = 2$ and $j = 3$-nucleon correlations:

$$f_{i/A}^{(j)}(x_A, Q^2) = \sum_{N=p,n} \int_{x_A}^{A} \frac{d\alpha}{\alpha} \int d^2\mathbf{p}_\perp f_{N/A}^{(j)}(\alpha, \mathbf{p}_\perp) f_{i/N}^{(b,j)}\left(\frac{x_A}{\alpha}, Q^2; \alpha, \mathbf{p}_\perp\right). \tag{2.56}$$

Here, $f_{i/N}^{(b,j)}\left(\frac{x_A}{\alpha}, Q^2; \alpha, \mathbf{p}_\perp\right)$ is the bound nucleon PDF, which differs from the free nucleon PDF due to immersion of the nucleon in the strongly-interacting nuclear medium. It is indexed by j since the form of the medium modification is likely to differ for a nucleon influenced primarily by the mean field and one whose dynamics are primarily influenced by a small number of correlated partners. Accordingly, the j-nucleon SRC contribution to the nPDF must be calculated by a separate convolution formula of the form Eq. (2.56) for each j, and then added, to obtain the total nPDF.

2.4.2 Motivation and evidence for two-nucleon SRCs

In the 1980s and 1990s a series of proton removal experiments that hinted at 2N SRCs were performed with hard electron probes. These experiments are summarized in Refs. [22–24]. Lapikas [25] found in an analysis of the 1980s proton removal experiments [22, 23] that only 60 to 70% of protons appear to occupy the valence orbitals generated by the mean internucleon potential. By contrast, Hartree-Fock calculations predict 90% occupancy for these orbitals [25], with the other 10% in orbitals above the Fermi level owing to long-range correlations. On the other hand, it has been found that calculations which include appreciable short range correlations induced by a tensor interaction can account for the missing 20 to 30% of protons. In other words, it was predicted on the basis of spectroscopic measurements that 20-30% of protons are in two-nucleon short-range correlations.

More recent experiments with high-energy electron and proton probes have more directly demonstrated the existence of two-nucleon SRCs through triple-coincidence measurements (*cf.* [26–28]). In these experiments, the probe and a removed proton are detected and their momenta measured, allowing the missing momentum to be calculated. When the removed proton is a member of a short-range nucleon pair, the missing momentum will be almost entirely carried by the proton's correlated partner, rather than shared by the bulk of the nucleus. If another nucleon is detected that carries all of the missing momentum, then a two-nucleon SRC was probed.

In addition to the existence of two-nucleon SRCs, such triple-coincidence experiments have also studied their properties. In particular, several experiments [26, 27, 29, 30] have demonstrated that the majority ($\gtrsim 90\%$) of 2N SRCs are proton-neutron pairs. This leads one to expect that the light cone fraction distribution for such an SRC should follow the high-momentum LCFD of the deuteron in its functional form. Additionally, several theoretical and experimental studies (see [30–33]) have found that the *pn* dominance of 2N SRCs increases the average momentum of a proton in neutron-rich nuclei, since fewer protons are present to be paired with neutrons into SRCs.

Another important property of two-nucleon SRCs has been studied by recent experiments, namely the universality of the high-momentum functional form of the momentum distribution. The universality is observed in low-Q^2 quasi-elastic electron scattering experiments, where the ratio

$$R(A, A') = \frac{A'}{A} \frac{\sigma_{eA}(x, Q^2)}{\sigma_{eA'}(x, Q^2)} \tag{2.57}$$

is measured, where the comparison nucleus A' has typically been either ^{2}H or ^{3}He.

The earliest experiments with evidence for two-nucleon correlations in cross section ratios were performed at SLAC. Frankfurt *et al.* [34] analyzed a series of electron-nucleus scattering experiments at SLAC and found that $Q^2 \gtrsim 0.9$ GeV^2 and $x_B \gtrsim 1.4$, the ratio $R(A, d)$ became roughly constant as a function of x_B at fixed Q^2, *i.e.*, this ratio formed a plateau. In the range $1.4 < x_B < 2$, Frankfurt *et al.* defined

$$a_2(A) = \frac{2}{A} \frac{\sigma_{eA}}{\sigma_{ed}}, \tag{2.58}$$

and extracted values of this factor for ^{3}He, ^{4}He, ^{12}C, ^{27}Al, ^{56}Fe, and ^{197}Au from the SLAC experiments. While $a_2(A)$ itself was taken as an experimentally constrained parameter, the existence of plataeus, as well as the functional form of the ratio $R(A, d)$ as a function of x, were predictions of [34] derived from their short-range correlation model. In their model, the light cone distribution of nucleons in a nucleus scales like the light cone distribution of a deuteron. $a_2(A)$ can be interpreted in this framework as a probability factor for two-nucleon SRCs.

Later experiments at Jefferson Lab, in particular a CLAS experiment by Kim Egiyan *et al.* [8, 35] and a Hall C experiment by Fomin *et al.* [36], measured electron scattering cross section ratios for a range of nuclei in the region $Q^2 \geq 1.4$ GeV^2 and $x_B > 1.5$. Both experiments found scaling plateaus, the former in the ratio $R(A, ^3\text{He})$ for ^{4}He, ^{12}C, and ^{56}Fe, and the latter in the ratio $R(A, d)$ for ^{3}He, ^{4}He, ^{9}Be, ^{12}C, ^{63}Cu, and ^{197}Au. Weinstein *et al.* [7] converted the $R(A, ^3\text{He})$ measurements of CLAS into $a_2(A)$ values using a calculated $R(^2\text{H}, ^3\text{He})$.

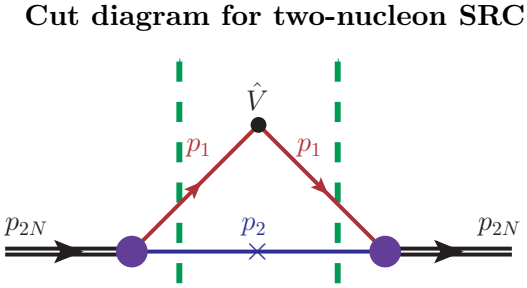

Figure 2.6: Cut diagram for the LCFD of a two-nucleon SRC.

In summary, there is a large body of evidence for the existence of two-nucleon short range correlations in nuclei, and a fair amount of experimental constraint on the properties of 2N SRCs. It is well-known that the majority of two-nucleon SRCs occur in proton-neutron pairs, and that the functional dependence of the momentum distribution follows the high-momentum part of the deuteron distribution. Moreover, for a range of nuclei, the scale factor $a_2(A)$ is well-known. These facts will constrain the theoretical analysis of two-nucleon SRCs to follow.

2.4.3 Light cone fraction distribution for $2N$ SRCs

The empirical evidence for two-nucleon SRCs described in Sec. 2.4.2 points to a strong dominance of NN pairs that both share the quantum numbers of the deuteron, *i.e.*, are spin-one and isospin zero, and share the functional form of the deuteron momentum distribution at high momentum. Accordingly, the LCFD of the two-nucleon SRC is modeled after the LCFD of the deuteron. In particular, the LCFD can be derived using light cone perturbation theory, applied to the cut diagram in Fig. 2.6. For the cut diagram, the operator $\hat{V}(\alpha, \mathbf{p}_\perp)$ given in Eq. (2.42) is placed on one of the internal nucleon lines.

First, the LCFD of the deuteron is derived, since the LCFD of 2N SRCs is modeled after it. Since the deuteron consists of one proton and one neutron, and is an isospin zero state, we should have $f_{p/d}(\alpha, \mathbf{p}_\perp) = f_{n/d}(\alpha, \mathbf{p}_\perp)$, each of these being normalized to $Z = (A - Z) = 1$. Using this normalization rule, together with the cut diagram of Fig. 2.6,

we have

$$f_{p/d}(\alpha,\mathbf{p}_\perp)=\overline{\sum_{s_d}}\int\frac{d\alpha_n d^2\mathbf{p}_{n\perp}}{2\alpha_n(2\pi)^3}\Bigg[\bar{u}_d^{s_d}(p_d)\Gamma_{dpn}\left(\sum_{\sigma_n}u_n^{\sigma_n}(p_n)\bar{u}_n^{\sigma_n}(p_n)\right)\frac{\sum_{\sigma_p}u_p^{\sigma_p}(p_p)\bar{u}_p^{\sigma_p}(p_p)}{p_p^+\mathcal{D}(p_p^-)}$$
$$\left(\sum_\sigma a_p^\dagger(p,\sigma)\frac{\alpha}{2}\delta^{(1)}(\alpha-\alpha_p)\delta^{(2)}(\mathbf{p}_\perp-\mathbf{p}_{p\perp})a_p(p,\sigma)\right)$$
$$\frac{\sum_{\sigma_p}u_p^{\sigma_p}(p_p)\bar{u}_p^{\sigma_p}(p_p)}{p_p^+\mathcal{D}(p_p^-)}\Gamma_{dpn}u_d^{s_d}(p_d)\Bigg]. \tag{2.59}$$

The rules for creation and annihilation operators are applied, and the delta functions eliminate the integrations with help of the momentum conservation relations $\alpha_p+\alpha_n=2$ and $\mathbf{p}_{p\perp}+\mathbf{p}_{n\perp}=\mathbf{p}_{d\perp}$. Additionally, it is noted that

$$\begin{aligned}p_p^+\mathcal{D}(p_p^-)&=\frac{\alpha_p}{2}p_d^+\left(p_d^--p_p^--p_n^-\right)=\frac{\alpha_p}{2}\left(M_d^2+\mathbf{p}_{d\perp}^2-\frac{m_p^2+\mathbf{p}_{p\perp}^2}{\alpha_p/2}-\frac{m_n^2+\mathbf{p}_{n\perp}^2}{\alpha_n/2}\right)\\&=\alpha_p\frac{1}{2}\left[M_d^2-4\left(m_N^2+\frac{(\alpha_p-1)^2m_N^2+\left[\mathbf{p}_{p\perp}-\frac{\alpha_p}{2}\mathbf{p}_{d\perp}\right]^2}{\alpha_p\alpha_n}\right)\right]\\&\equiv\alpha_p\frac{1}{2}\left[M_d^2-4\left(m_N^2+k^2\right)\right],\end{aligned} \tag{2.60}$$

where k^2 is written as a shorthand for

$$k^2=\frac{(\alpha_p-1)^2m_N^2+\left[\mathbf{p}_{p\perp}-\frac{\alpha_p}{2}\mathbf{p}_{d\perp}\right]^2}{\alpha_p\alpha_n}. \tag{2.61}$$

It should be noted that $k=|\mathbf{k}|$, where $\mathbf{k}$ is effectively the internal, relative momentum of the proton-neutron pair corresponding to the light cone momentum fraction α_p. In particular,

$$\mathbf{p}_\perp-\frac{\alpha}{2}\mathbf{p}_{d\perp}=\mathbf{k}_\perp \tag{2.62}$$

$$\alpha=2\frac{\sqrt{k^2+m_N^2}+k_z}{2\sqrt{k^2+m_N^2}}=1+\frac{k_z}{\sqrt{k^2+m_N^2}}, \tag{2.63}$$

and inverting these to find k^2 gives Eq. (2.61). The result of these considerations is

$$f_{p/d}(\alpha, \mathbf{p}_\perp) = \overline{\sum_{s_d}} \sum_{\sigma_p, \sigma_n} \frac{1}{\alpha(2-\alpha)} \left| \frac{1}{\sqrt{2}\sqrt{2(2\pi)^3}} \frac{\bar{u}_p^{\sigma_p}(p_p) \bar{u}_n^{\sigma_n}(p_n) \Gamma_{dpn} u_d^{s_d}(p_d)}{\frac{1}{2}\left[M_d^2 - 4\left(m_N^2 + k^2\right)\right]} \right|^2 . \tag{2.64}$$

Note that in this case $\mathbf{p}_{d\perp} = \mathbf{0}$, but we have left $\mathbf{p}_{d\perp}$ present in these formulas in order to obtain more general results. The deuteron light cone wave function is given by

$$\psi_{p/d}^{(\sigma_N, \sigma_s; s_{2N})}(\alpha_N, \mathbf{p}_{N\perp}) = \frac{1}{\sqrt{2}\sqrt{2(2\pi)^3}} \frac{\bar{u}_p^{\sigma_p}(p_p) \bar{u}_n^{\sigma_n}(p_n) \Gamma_{dpn} u_d^{s_d}(p_d)}{\frac{1}{2}\left[M_d^2 - 4\left(m_N^2 + k^2\right)\right]}, \tag{2.65}$$

which can be found by comparing to Eq. (2.45) with $\chi_p = \frac{Z}{A} = \frac{1}{2}$, so that the factor of $\sqrt{\chi_N} = \sqrt{1/2} = \sqrt{2}\frac{1}{2}$. This gives us

$$f_{p/d}(\alpha, \mathbf{p}_\perp) = \overline{\sum_{s_d}} \sum_{\sigma_p, \sigma_n} \frac{1}{\alpha(2-\alpha)} \left| \psi_{p/d}^{\sigma_p, \sigma_n; s_d}(\mathbf{k}) \right|^2 , \tag{2.66}$$

and due to the isospin symmetry, more generally,

$$f_{N/d}(\alpha, \mathbf{p}_\perp) = \frac{1}{\alpha(2-\alpha)} \overline{\left|\psi_{N/d}(k)\right|^2}. \tag{2.67}$$

It should be noted here that $\overline{\left|\psi_{N/d}(k)\right|^2}$ is the square of the light cone deuteron wave function. This is related to the non-relativistic deuteron wave function $\overline{|\psi_{NR}(k)|^2}$ through their respective normalizations. In particular, since the LCFD of the deuteron is normalized to 1 for either $N = p$ or $N = n$, and since the non-relativistic wave function is also normalized to 1,

$$\int \frac{d\alpha}{\alpha(2-\alpha)} d^2\mathbf{k}_\perp \overline{\left|\psi_{N/d}(k)\right|^2} = \int dk_z d^2\mathbf{k}_\perp \overline{|\psi_{NR}(k)|^2}. \tag{2.68}$$

One can show that $\frac{dk_z}{E_k} = \frac{d\alpha}{\alpha(2-\alpha)}$, and accordingly

$$\overline{\left|\psi_{N/d}(k)\right|^2} = \overline{|\psi_{NR}(k)|^2} E_k = \overline{|\psi_{NR}(k)|^2} \sqrt{m_N^2 + k^2}. \tag{2.69}$$

This relationship is useful for performing numerical computations, since several potentials exist for parameterizing the non-relativistic deuteron wave function.

With the LCFD of the deuteron in hand, it is necessary to relate it now to the LCFD of two-nucleon SRCs in a nucleus. The observation that the high-momentum part of the nuclear wave function behaves as a scaled version of the deuteron wave function requires, at least for large $k \gtrsim k_F$ (hence the step function), that one has

$$f^{(2)}_{N/A}(\alpha, \mathbf{p}_\perp) = C_N f_{N/d}(\alpha, \mathbf{p}_\perp)\Theta(k - k_F). \tag{2.70}$$

Since there are two C_N (C_p for the proton and C_n for the neutron), there are two independent quantities to be found. There are accordingly two constraints that fix their values. The first comes from experimental studies of the cross section ratio $R(x) = 2\sigma_{eA}(x)/A\sigma_{ed}(x)$, which for $x \gtrsim 1.4$ becomes a plateau with a nucleus-specific value $a_2(A)$. Since the wave functions of the nucleus and deuteron take the same form at high ($> k_F$) momenta, the fact that $\sigma_{eA} = \frac{A}{2}a_2(A)\sigma_{ed}$ suggests that (suppressing the step function for brevity)

$$f^{(2)}_{p/A} + f^{(2)}_{n/A} = \frac{A}{2}a_2(A)\left(f_{p/d} + f_{n/d}\right) = Aa_2(A)f_{N/d}. \tag{2.71}$$

The second constraint comes from the dominance of pn pairs in two-nucleon SRCs, and in fact fixes $C_p = C_n$. If we make an approximation where each 2N SRC is a pn pair, then every proton found in a two-nucleon SRC has a paired neutron, and vice-versa, so there must be an equal number of protons and neutrons in 2N SRCs. Since $f^{(2)}_{N/A}$ is normalized to the number of nucleons of "flavor" N in a two-nucleon SRC, we thus have that $f^{(2)}_{p/A}$ and $f^{(2)}_{n/A}$ are normalized to the same value, and therefore

$$f^{(2)}_{p/A}(\alpha, \mathbf{p}_\perp) = f^{(2)}_{n/A}(\alpha, \mathbf{p}_\perp) = \frac{Aa_2(A)}{2}f_{N/d}(\alpha, \mathbf{p}_\perp)\Theta(k - k_F). \tag{2.72}$$

It is worth noting that the equality of $f^{(2)}_{p/A}$ and $f^{(2)}_{n/A}$ comes from defining the LCFD to give the number of baryons of a particular flavor; *cf.* Eqs. (2.39,2.40). If instead one had defined densities normalized to 1, effectively dividing the LCFD we have by Z for $f^{(2)}_{p/A}$

and $(A-Z)$ for $f_{n/A}^{(2)}$, then these would instead be unequal, with $f_N^{(2)} = \frac{a_2(A)}{2\chi_N} f_{N/d}$ in both cases. This has the consequence that a greater proportion of protons than neutrons have high ($> k_F$) momentum in neutron-rich nuclei, and for increasingly asymmetric nuclei this momentum imbalance is greatly enhanced. The reader should refer to Refs. [30–33] for more information on momentum sharing in asymmetric nuclei.

It is important to note that while arbitrarily high k may contribute to the two-nucleon SRC part of the LCFD, the highest α that can contribute is 2. For a nucleon in the 2N SRC, the relationship between k and α is determined by Eq. (2.61), in which k grows arbitrarily large for α arbitrarily close to 2. The $\alpha > 2$ contributions to the nuclear LCFD can only come from correlations of more than two nucleons.

2.4.4 Numerical computations of $2N$ SRC distributions

Numerical computations are presented for the LCFD with and without contributions from two-nucleon SRCs. For these computations, mean field momentum distributions calculated by Zverev and Saperstein [21] are used, and the Paris potential is used for the non-relativistic deuteron wave function [37], in conjunction with Eqs. (2.67,2.69) in order to compute the two-nucleon SRC contribution to the LCFD.

When accounting for two-nucleon SRCs, the values $a_2(^{56}\text{Fe}) = 5.58$ (from [8,35]) and $a_2(^{208}\text{Pb}) = 5.6$ (a conservative estimate) are used to characterize their strengths. When two-nucleon SRCs are accounted for, in order that the LCFD for the proton and neutron be respectively normalized to Z and $(A-Z)$, the mean field contribution must be diluted by a factor of $a_1^{(N)}(A)$. It is found that for ^{56}Fe, 29% of protons and 25% of neutrons are in two-nucleon SRCs, so dilution factors of $a_1^{(p)}(^{56}\text{Fe}) = 0.71$ and $a_1^{(n)}(^{56}\text{Fe}) = 0.75$ are needed for the mean field. Using the conservative estimate of two-nucleon SRCs in lead, one finds 32% of protons and 21% of neutrons in ^{208}Pb are in two-nucleon SRCs, giving dilution factors of $a_1^{(p)}(^{208}\text{Pb}) = 0.68$ and $a_1^{(n)}(^{208}\text{Pb}) = 0.79$.

Plots of the computations can be seen in Fig. 2.7, where the LCFD *per nucleon*, with and without two-nucleon correlations, is presented. One can see that two-nucleon SRCs

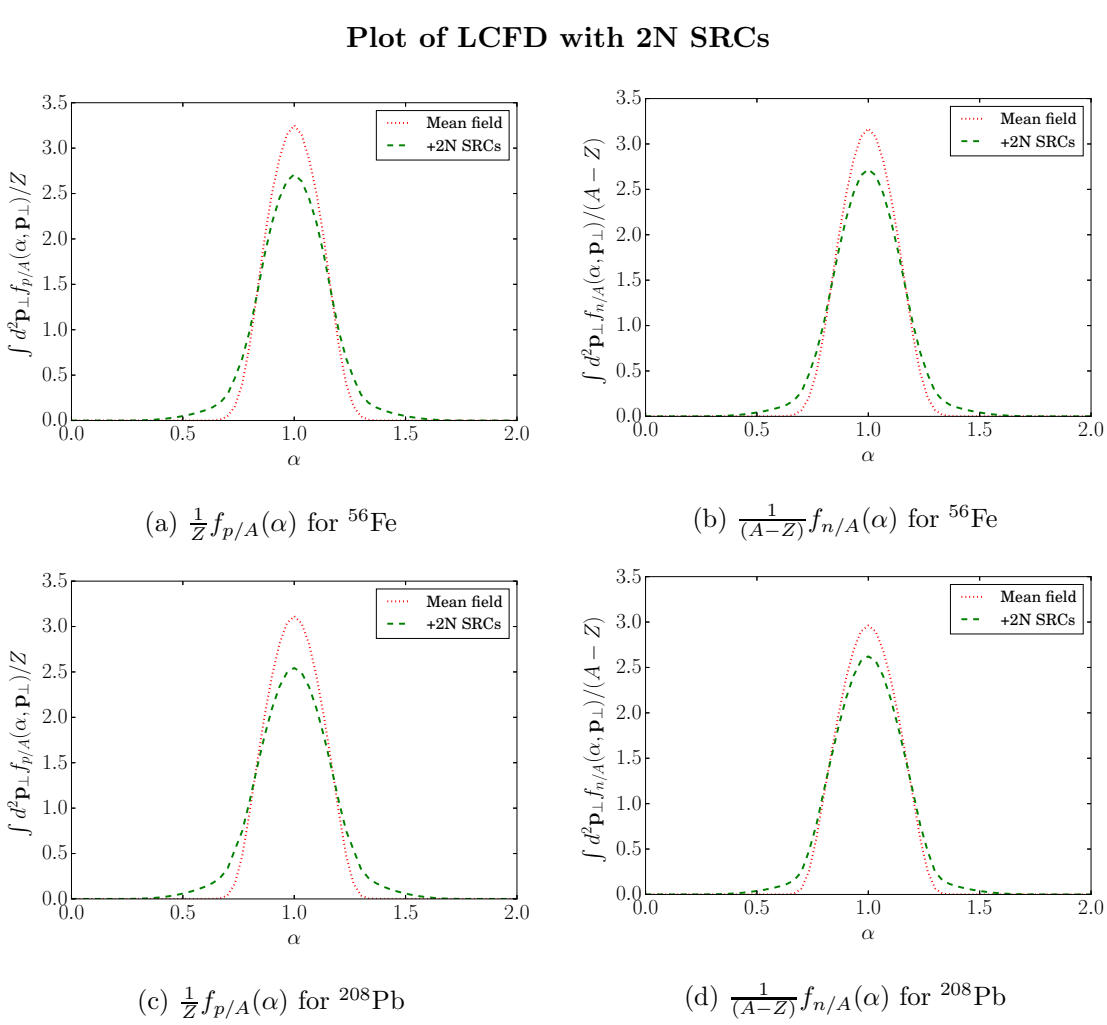

(a) $\frac{1}{Z} f_{p/A}(\alpha)$ for ^{56}Fe

(b) $\frac{1}{(A-Z)} f_{n/A}(\alpha)$ for ^{56}Fe

(c) $\frac{1}{Z} f_{p/A}(\alpha)$ for ^{208}Pb

(d) $\frac{1}{(A-Z)} f_{n/A}(\alpha)$ for ^{208}Pb

Figure 2.7: The *per nucleon* light cone fraction distribution $f_{N/A}(\alpha)$, with $\mathbf{p}_\perp$ integrated over.

Feynman diagram for hadronic current of two-nucleon SRC

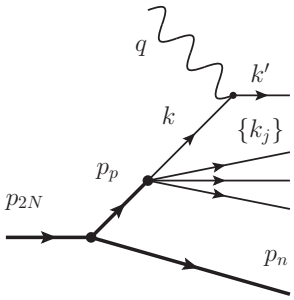

Figure 2.8: Diagram for $\langle X \mid J^+(0) \mid p_{2N}, s_{2N} \rangle$ given that a two-nucleon SRC was probed.

take away a slightly greater proportion of protons than neutrons from the mean field, and that 2N SRCs additionally enhance the LCFD in the $\alpha \gtrsim 1.2$ region.

2.4.5 Convolution formula for PDFs of $2N$ SRCs

The formula for the contribution of two-nucleon short range correlations to the nuclear PDF is derived here. The result will be a convolution formula, similar in form to the convolution formula for the mean field contribution to the nPDF (see Eq. (2.54)). Since the mean field and 2N SRC contributions to the nPDF will involve final states with different numbers of removed nucleons, their contributions will add incoherently, just like their contributions to the LCFD.

We proceed by finding the contribution that two-nucleon SRCs make to the nuclear hadronic tensor, namely

$$W_{2N}^{++}(p_A, q) = \frac{1}{4\pi M_A} \overline{\sum_{s_A}} \int dX (2\pi)^4 \delta^{(4)}(p_A + q - p_X) \langle p_A, s_A \mid J^+(0) \mid X \rangle \langle X \mid J^+(0) \mid p_A, s_A \rangle, \tag{2.73}$$

where for the 2N SRC contribution, the final hadronic state is restricted to one with two removed nucleons, one of which was destroyed. In particular, since 2N SRCs are dominated by the isospin-zero dominance hypothesis, there will be one proton and one neutron removed from the nucleus, and one of these two particles will be deeply probed by the incident virtual

photon (with the individual contribution of each adding incoherently). The center-of-mass motion of the pn pair is neglected, so the final hadronic state is characterized in this case by (1) whether the proton or neutron in the SRC was probed; (2) the flavor i of the probed parton; and (3) the Fock component $\mathcal{F}$ of the probed nucleon. With the SRC center-of-mass motion and the degrees of freedom of the $(A-2)$-nucleon remnant neglected, calculation of the SRC's contribution to the nPDF amounts to calculating the internal partonic structure of the SRC, and multiplying by the probability that a 2N SRC occurs. The diagram for calculating the matrix element $\langle X \mid J^+(0) \mid 2N\rangle$ of the hadronic current in such a case is given in Fig. 2.8. Since $\sigma_{eA} = \frac{Aa_2(A)}{2}\sigma_{ed}$ in the kinematic domain where 2N SRCs dominate, the appropriate probability weight is $\frac{Aa_2(A)}{2}$. This weight is accounted for by introducing a factor of $\sqrt{\frac{Aa_2(A)}{2}}$ into each 2N vertex. Moreover, the threshold constraint $\Theta(k-k_F)$ is introduced, since the short-range interaction is not considered to have occurred in this model unless the relative two-nucleon momentum passes the Fermi momentum threshold.

Using the diagram in Fig. 2.8 and the rules of light cone perturbation theory, we have

$$\begin{aligned}\langle X \mid J^+(0) \mid 2N\rangle = \bar{u}_i^{\lambda'}(k')e_i\gamma^+\frac{\sum_\lambda u_i^\lambda(k)\bar{u}_i^\lambda(k)}{k^+\mathcal{D}(k^-)}\left[\prod_{j=1}^{n_s}\bar{u}_{i_j}^{\lambda_j}(k_j)\right]\Gamma_{i,\mathcal{F}/N} \\ \frac{\sum_\lambda u_N^{\sigma_N}(p_N)\bar{u}_N^{\sigma_N}(p_N)}{p_N^+\mathcal{D}(p_N^-)}\bar{u}_s^{\sigma_s}(p_s)\sqrt{\frac{Aa_2(A)}{2}}\theta(k-k_F)\Gamma_{pn}u_{2N}^{s_{2N}}(p_{2N}) \\ = 2p_A^+e_i\sqrt{2(2\pi)^3}\psi_{i,\mathcal{F}/N}^{(\lambda',\{\lambda_j\};\sigma_N)}(x_N,\mathbf{k}_\perp,\{x_j,\mathbf{k}_{j\perp}\};\alpha_N,\mathbf{p}_{N\perp}) \\ \sqrt{\frac{Aa_2(A)}{2}}\theta(k-k_F)\psi_{N/2N}^{(\sigma_N,\sigma_s;s_{2N})}(\alpha_N,\mathbf{p}_{N\perp}),\end{aligned} \tag{2.74}$$

where $x_N = k^+/p_N^+$ and $x_j = k_j^+/p_N^+$ as in the mean field derivation, and the expression above was found using the two-nucleon bound state wave function given by Eq. (2.65).

The four-dimensional delta function is given by

$$\delta^{(4)}\left(p_A + q - k' - \sum_{j=1}^{n_s}k_j - p_s - p_{(A-2)}\right). \tag{2.75}$$

Since the "plus" and transverse components of the four-momentum are conserved at each step, these parts of the delta function are given by

$$\delta^+ = \frac{A}{\alpha_N p_A^+}\delta^{(1)}\left(1 - x_N - \sum_{j=1}^{n_s} x_j\right) \tag{2.76}$$

$$\delta^\perp = \delta^{(2)}\left(\mathbf{p}_{N\perp} - \mathbf{k}_\perp - \sum_{j=1}^{n_s}\mathbf{k}_{j\perp}\right), \tag{2.77}$$

and the "minus" component is found in the usual approximations (collinear, massless quarks in the Bjorken limit) to be

$$\delta^- = p_A^+\delta^{(1)}\left(2(q\cdot p_A) - \frac{AQ^2}{x_N\alpha_N}\right) = \frac{x_A p_A^+}{2(q\cdot p_A)\alpha_N}\delta^{(1)}\left(x_N - \frac{x_A}{\alpha_N}\right). \tag{2.78}$$

This gives a contribution to the nuclear hadronic tensor of

$$\begin{aligned} W_{2N}^{++}(p_A,q) = \frac{Aa_2(A)}{2}\frac{(p_A^+)^2}{M_A(q\cdot p_A)}x_A\sum_i e_i^2\sum_N\Bigg\{\int\frac{d\alpha_N}{\alpha_N}d^2\mathbf{p}_{N\perp}\frac{1}{\alpha_N\alpha_s}\,\overline{\left|\psi_{N/2N}(\alpha_N,\mathbf{p}_{N\perp})\right|^2} \\ \int\frac{dx_N d^2\mathbf{k}_\perp}{2x_N(2\pi)^3}\prod_{j=1}^{n_s}\frac{dx_j d^2\mathbf{k}_{j\perp}}{2x_j(2\pi)^3}\Bigg[\overline{\left|\psi_{i,\mathcal{F}/N}(x_N,\mathbf{k}_\perp,\{x_j,\mathbf{k}_{j\perp}\};\alpha_N,\mathbf{p}_{N\perp})\right|^2} \\ 2(2\pi)^3\delta^{(1)}\left(1 - x_N - \sum_{j=1}^{n_s}x_j\right)\delta^{(2)}\left(\mathbf{p}_{N\perp} - \mathbf{k}_\perp - \sum_{j=1}^{n_s}\mathbf{k}_{j\perp}\right)\Bigg]\Bigg\} \end{aligned} \tag{2.79}$$

$$\begin{aligned} = \frac{(p_A^+)^2}{M_A(q\cdot p_A)}x_A\sum_i e_i^2\sum_N\int\frac{d\alpha_N}{\alpha_N}d^2\mathbf{p}_{N\perp}\Bigg[f_{N/A}^{(2)}(\alpha_N,\mathbf{p}_{N\perp}) \\ f_{i/N}^{(b,2)}\left(\frac{x_A}{\alpha_N},Q^2;\alpha_N,\mathbf{p}_{N\perp}\right)\Bigg]. \end{aligned} \tag{2.80}$$

This produces a convolution formula of

$$f_{i/A}^{(2)}(x_A,Q^2) = \sum_N\int_{x_A}^2\frac{d\alpha}{\alpha}\int d^2\mathbf{p}_\perp f_{i/N}^{(b,2)}\left(\frac{x_A}{\alpha},Q^2;\alpha,\mathbf{p}_\perp\right)f_{N/A}^{(2)}(\alpha,\mathbf{p}_\perp) \tag{2.81}$$

for the two-nucleon SRC contribution to the nuclear PDF. Notice that the upper bound of the alpha integration is $\alpha = 2$. Accordingly, $x_A \leq 2$ for a parton that originated in a two-nucleon SRC.

2.4.6 Motivation and evidence for $3N$ SRCs

Nucleons with a light cone fraction $\alpha > 2$ and partons with a momentum fraction $x_A > 2$ cannot originate from two-nucleon SRCs, so instead must originate within SRCs of three or more nucleons. Short-range configurations of greater numbers of nucleons will become increasingly unlikely, so after 2N SRCs the next most significant contributions to the nuclear LCFD (and thus to the nPDF) will be from three-nucleon correlations. Already, three-nucleon SRCs have comparatively little evidence demonstrating their existence, and several experimental studies have conflicting results.

Three- and more-nucleon correlations were proposed as a possibility by Frankfurt and Strikman [9], who stipulated an exponential decay of the nuclear light cone density with $\alpha > 2$, with the parametrization based on a fit of $p + A \to p + X$ data with 400 GeV protons [38]. The ratio $\mathcal{R}(A, {}^4\text{He})$ was predicted by this model to monotonically increase at $x_B > 2$.

A contrasting model was proposed by Vary [39], called the quark cluster model, where the regions $1 < x_B < 2$, $2 < x_B < 3$, *etc.*, were dominated by six-quark, nine-quark, *etc.* clusters, respectively. The form of the partonic distributions (and thus of the structure functions) should scale with respect to nuclear mass number, and the ratio $\mathcal{R}(A, {}^4\text{He})$ should form a series of rising plateaus—*i.e.*, a staircase.

The first experimental data for cross sections at $x_B > 2$ came from SLAC in the late 1980s [40, 41]. Donal Day *et al.* measured the cross section ratio $\mathcal{R}({}^{56}\text{Fe}, {}^4\text{He})$, finding it to agree with the prediction of Frankfurt and Strikman [9, 42]: it did not show a staircase behavior, with only a 2N SRC plateau present in the region $1.4 < x_B < 2$.

Egiyan *et al.* reported measurements of electron scattering cross sections from CLAS at Jefferson Lab [8] extending into the $x_B > 2$ region, and did find a second, three-nucleon plateau was present in the ratio $\mathcal{R}(A, {}^3\text{He})$. Several values of $a_3(A)$, defined as

$$a_3(A) = \frac{3}{A}\frac{\sigma_{eA}}{\sigma_{e^3\text{He}}} \qquad\qquad x_B \gtrsim 2.25, \tag{2.82}$$

were extracted from the data, namely $a_3(^4\text{He}) = 2.33 \pm 0.12 \pm 0.19$, $a_3(^{12}\text{C}) = 3.05 \pm 0.14 \pm 0.21$, and $a_3(^{56}\text{Fe}) = 4.38 \pm 0.19 \pm 0.33$ [8].

Another Jefferson Lab experiment at Hall C [36] also measured the ratio $\mathcal{R}(^4\text{He}, ^3\text{He})$ for $x_B > 2$, but in contrast to the CLAS experiment did not find a three-nucleon SRC plateau. A note by Higinbotham and Hen [43] suggests that the finding of the CLAS experiment may have been the result of bin migration, due to the bin size for the $x_B > 2$ being smaller than the energy resolution allowed by CLAS.

The current status of three-nucleon SRCs is, therefore, ambiguous. It is not clear that experiments which have probed $x_B > 2$ have been performed at high enough momentum transfer that universality should be expected to set in. It is also not clear whether a staircase behavior in the cross section ratio $\mathcal{R}(A, ^3\text{He})$ (as predicted by Vary [39]) should be observed, or instead a monotonic increase (as predicted by Frankfurt and Strikman [9]).

In light of this ambiguity, the possibility of three-nucleon SRCs is explored here within a collinear framework, where the three-nucleon correlations are stipulated to occur *via* a sequence of two-nucleon interactions at short range. This model expands upon on a previous model by Frankfurt and Strikman [9], but is developed further. Moreover, this updated model of three-nucleon SRCs incorporates the latest data about two-nucleon SRCs in the description of the two-nucleon short-range interaction, in particular the *pn* dominance of two-nucleon pairs.

2.4.7 Light cone fraction distribution for $3N$ SRCs

Unlike the two-nucleon SRC, the LCFD for a three-nucleon SRC cannot be modeled after the LCFD of an $A = 3$ nucleus such as ^{3}He. The spin and isospin of the 3N SRC are not known, and moreover the SRC will only behave like a particular short-range configuration that makes up a small part of the total $A = 3$ nuclear LCFD (which will also have a mean field and a 2N SRC contribution). However, a LCFD of the particular 3N configuration, which we call $f_{3N}(\alpha, \mathbf{p}_\perp)$, is still defined and calculated using a cut diagram and light cone perturbation theory rules; all that is needed is a model for the generation of the 3N SRC and a normalization rule.

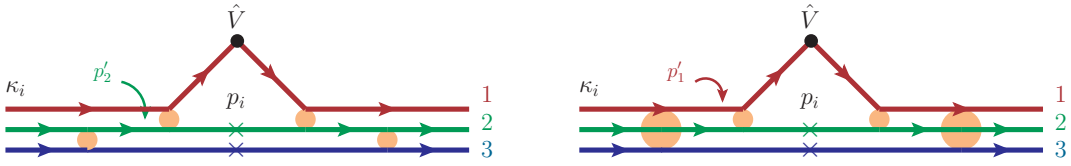

(a) *ppn* topology if p is probed. (b) *pnn* topology is p is probed.

Figure 2.9: Cut diagrams for calculating the short-range 3N LCFD.

There are two mechanisms which could potentially generate a three-nucleon SRC. The first is a sequence of two short-range two-nucleon interactions, and the second is an irreducible three-body interaction. The second mechanism results in a very high removal energy contribution to the nuclear spectral function [44], and since the LCFD involves an integral over removal energies, the contribution of this mechanism to the LCFD will be small. Accordingly, irreducible three-body interactions are neglected as the 3N SRC is modeled as arising from a sequence of two-body interactions. Such a model was originally developed in [9], but will be developed further here, in particular by accounting for the *pn* dominance for short-range two-nucleon interactions to predict a relationship between $a_2(A)$ and $a_3(A)$.

For definiteness, we will suppose that the nucleon probed within the 3N SRC is a proton, but the argument that follows is identical to that for a probed neutron if one simply performs the transposition $p \leftrightarrow n$. Owing to the *pn* dominance of the two-nucleon interactions at short distances, the 3N SRC will occur as a *ppn* or a *pnn* configuration. In particular, there are two diagrams describing how a 3N SRC can be generated, depicted in Fig. 2.9: Fig. 2.9a describes how a fast ($\alpha > 2$) proton can arise from a *ppn* configuration, and Fig. 2.9b describes how a fast proton can arise from a *pnn* configuration.

It will be shown that the functional forms of the LCFD contribution from each diagram in Fig. 2.9 are identical, aside from some *a priori* unknown overall constants. Accordingly, these constants can be factored out and combined, and then absorbed into one overall normalization constant. A normalization rule is imposed on the LCFD for the 3N configuration,

namely

$$\int_0^3 d\alpha \int d^2\mathbf{p}_\perp f_{3N}(\alpha, \mathbf{p}_\perp) = 1. \tag{2.83}$$

It should be noted that in a sense this normalization rule is somewhat artificial. The short range configuration described by $f_{3N}(\alpha, \mathbf{p}_\perp)$ is only significant for large α (or large $\mathbf{p}_\perp$), but the normalization rule involves integration over small α as well. However, Eq. (2.83) is a formal rather than a physical normalization rule. $f_{3N}(\alpha, \mathbf{p}_\perp)$ is itself a formal quantity that should be related to the physical LCFD of a three-nucleon SRC part of a particular nucleus. The relationship between $f_{3N}(\alpha, \mathbf{p}_\perp)$ and $f^{(3)}_{N/A}(\alpha, \mathbf{p}_\perp)$ is determined by two main constraints: (1) the vertex for a short-range two-nucleon interaction should contain a factor of $\sqrt{Aa_2(A)/2}$, since $Aa_2(A)/2$ is the probability weight for each two-nucleon interaction occurring, and (2) each short-range interaction should occur at an internal (relative) $k \geq k_F$. Formally, we write

$$f^{(3)}_{N/A}(\alpha, \mathbf{p}_\perp) = A\{a_2(A)\}^2 f_{3N}(\alpha, \mathbf{p}_\perp)\Theta_{3N}, \tag{2.84}$$

where $a_2(A)$ is squared because $\sqrt{a_2(A)}$ will appear four times in any diagram, and Θ_{3N} symbolically indicates that the momentum threshold constraint has been imposed on each interacting pair of nucleons. Internal momenta are functions of parameters that are integrated over, so Θ_{3N} does not signify a function that simply multiplies $f_{3N}(\alpha, \mathbf{p}_\perp)$. The factors of $1/\sqrt{2}$ associated with each short-range pn vertex, as well as one factor of A, are absorbed into the definition of $f_{3N}(\alpha, \mathbf{p}_\perp)$.

It should be noted that Eq. (2.84) is inexact, since it does not consider isospin effects. There will be corrections on the order of $1/A$ owing to isospin-dependent surface effects and the combinatorics of selecting multiple nucleons, but these can be neglected for large nuclei, and are neglected here.

Before proceeding to calculate the LCFD contributions from each topology in Fig. 2.9, the notation to be used and an approximation scheme will be established. Prior to the short-range two-nucleon interactions, all three nucleons in the configuration will be assumed to be collinear, with equal forward momentum. These initial four-momenta will be denoted κ_i, with $\kappa_i^+ = p_{3N}^+/3$, $\kappa_i^- = 3m_N^2/p_{3N}^+$, and $\kappa_{i\perp} = \mathbf{0}$. Their (scaled) momentum fractions will

be denoted $\beta_i = 3\kappa_i^+/p_{3N}^+ = 1$, and their helicities will be denoted ρ_i. Final state momenta (in the middle of the cut diagram) will be denoted p_i; momentum fractions will be denoted $\alpha_i = 3p_i^+/p_{3N}^+$; and helicities will be denoted σ_i. Intermediate states will use p, α, and σ with primes.

ppn topology

Applying the rules for light cone perturbation theory gives

$$
\begin{aligned}
A\left\{a_2(A)\right\}^2 f_{3N}^{(a)}(\alpha,\mathbf{p}_\perp) = \frac{1}{8}\sum_{\rho_1,\rho_2,\rho_3}\int \frac{dp_2^+ d^2\mathbf{p}_{2\perp}}{2p_2^+(2\pi)^3}\frac{dp_3^+ d^2\mathbf{p}_{3\perp}}{2p_3^+(2\pi)^3}\Bigg[& \bar{u}_p^{\rho_1}(\kappa_1)\bar{u}_n^{\rho_2}(\kappa_2)\bar{u}_p^{\rho_3}(\kappa_3) \\
& \left(\sqrt{\frac{Aa_2(A)}{2}}\Gamma_{pn}^{(2,3)}\right)\left(\sum_{\sigma_3} u_p^{\sigma_3}(p_3)\bar{u}_p^{\sigma_3}(p_3)\right)\frac{\sum_{\sigma_2'} u_n^{\sigma_2'}(p_2')\bar{u}_n^{\sigma_2'}(p_2')}{p_2'^+\mathcal{D}(p_2'^-)} \\
& \left(\sqrt{\frac{Aa_2(A)}{2}}\Gamma_{pn}^{(1,2)}\right)\left(\sum_{\sigma_2} u_n^{\sigma_2}(p_2)\bar{u}_n^{\sigma_2}(p_2)\right)\frac{\sum_{\sigma_1} u_p^{\sigma_1}(p_1)\bar{u}_p^{\sigma_1}(p_1)}{p_1^+\mathcal{D}(p_1^-)} \\
& \left(\sum_{\sigma} a_p^\dagger(p,\sigma)\frac{\alpha}{A}\delta^{(1)}(\alpha-\alpha_1)\delta^{(2)}(\mathbf{p}_\perp-\mathbf{p}_{1\perp})a_p(p,\sigma)\right) \\
& \frac{\sum_{\sigma_1'} u_p^{\sigma_1'}(p_1)\bar{u}_p^{\sigma_1'}(p_1)}{p_1^+\mathcal{D}(p_1^-)}\left(\sqrt{\frac{Aa_2(A)}{2}}\Gamma_{pn}^{(1,2)}\right)\frac{\sum_{\sigma_2''} u_n^{\sigma_2''}(p_2')\bar{u}_n^{\sigma_2''}(p_2')}{p_2'^+\mathcal{D}(p_2'^-)} \\
& \left(\sqrt{\frac{Aa_2(A)}{2}}\Gamma_{pn}^{(2,3)}\right)u_p^{\rho_1}(\kappa_1)u_n^{\rho_2}(\kappa_2)u_p^{\rho_3}(\kappa_3)\Bigg].
\end{aligned}
\tag{2.85}
$$

The intermediate state denominators $\mathcal{D}(p_2'^-)$ and $\mathcal{D}(p_1^-)$ are examined first. For the first of these, we have

$$
\begin{aligned}
\mathcal{D}(p_2'^-) &= (\kappa_1^- + \kappa_2^- + \kappa_3^-) - (\kappa_1^- + p_2'^- + p_3^-) \\
&= \frac{m_N^2}{\kappa_2^+} + \frac{m_N^2}{\kappa_3^+} - \frac{m_N^2+\mathbf{p}_{3\perp}^2}{p_2'^+} - \frac{m_N^2+\mathbf{p}_{3\perp}^2}{p_3^+},
\end{aligned}
\tag{2.86}
$$

where we used the fact that $\mathbf{p}_{2\perp}' = -\mathbf{p}_3\perp$ in the collinear approximation. We define a total momentum of the $(2,3)$ pair as

$$
p_{23}^+ = p_2'^+ + p_3^+ = \kappa_2^+ + \kappa_3^+,
\tag{2.87}
$$

and two relative light cone fractions

$$\gamma_2' = 2\frac{p_2'^+}{p_{23}^+} = 2 - \alpha_3 \tag{2.88}$$

$$\gamma_3 = 2\frac{p_3^+}{p_{23}^+} = \alpha_3 \tag{2.89}$$

for the (scaled by 2) fraction of the pair's forward light cone momentum carried by each nucleon. Naturally, these add to $\gamma_2' + \gamma_3 = 2$, and it is worth noting that $0 \leq \alpha_3 \leq 2$ is related to the ranges $0 \leq \gamma_2' \leq 2$ and $0 \leq \gamma_3 \leq 2$; the constraint on α_3 comes from the fact that, within the short-range configuration depicted in Fig. 2.9a, nucleon 3 only gets a kick from a short range interaction with nucleon 2, so can carry at most the total forward momentum of these two nucleons.

Now, within the collinear approximation where $\kappa_2^+/p_{23}^+ = \kappa_3^+/p_{23}^+ = 1/2$, we have

$$\begin{aligned}\mathcal{D}(p_2'^-) &= \frac{1}{p_{23}^+}\left(\frac{m_N^2}{1/2} + \frac{m_N^2}{1/2} - \frac{m_N^2 + \mathbf{p}_{3\perp}^2}{\gamma_2'} - \frac{m_N^2 + \mathbf{p}_{3\perp}^2}{\gamma_3}\right) \\ &= \frac{1}{p_{23}^+}\left(4m_N^2 - 4\left[\frac{m_N^2 + \mathbf{p}_{3\perp}^2}{\gamma_2'\gamma_3}\right]\right).\end{aligned} \tag{2.90}$$

The factor $\mathcal{D}(p_2'^-)$ is accompanied by $p_2'^+$ in the calculation of Eq. (2.85); multiplied together, they give

$$p_2'^+\mathcal{D}(p_2'^-) = \gamma_2'\frac{1}{2}\left(4m_N^2 - 4\left[\frac{m_N^2 + \mathbf{p}_{3\perp}^2}{\gamma_2'\gamma_3}\right]\right) \equiv \gamma_2'\tilde{\mathcal{D}}_{23}, \tag{2.91}$$

where $\tilde{\mathcal{D}}_{23}$ is part of the denominator of a two-nucleon wave function (see Eq. (2.65)), if we define a two-body relative light cone momentum (in analogy with Eq. (2.61)) for the nucleon pair (2,3) as

$$k_{23}^2 = \frac{(\gamma_2' - 1)^2 m_N^2 + \mathbf{p}_{3\perp}^2}{\gamma_2'\gamma_3} = \frac{(1-\alpha_3)^2 m_N^2 + \mathbf{p}_{3\perp}^2}{\alpha_3(2-\alpha_3)}. \tag{2.92}$$

For the other intermediate state denominator, one has

$$\begin{aligned}\mathcal{D}(p_1^-) &= (\kappa_1^- + \kappa_2^- + \kappa_3^-) - (p_1^- + p_2^- + p_3^-) \\ &= 9\frac{m_N^2}{p_{3N}^+} - \left(\frac{m_N^2 + \mathbf{p}_{1\perp}^2}{p_1^+} + \frac{m_N^2 + [\mathbf{p}_{1\perp} + \mathbf{p}_{3\perp}]^2}{p_2^+} + \frac{m_N^2 + \mathbf{p}_{3\perp}^2}{p_3^+}\right), \end{aligned} \tag{2.93}$$

where we have used the fact that $\mathbf{p}_{2\perp} = -(\mathbf{p}_{1\perp} + \mathbf{p}_{3\perp})$ in the collinear approximation. We introduce now the total forward light cone momentum of the nucleon pair (1,2)

$$p_{12}^+ = p_1^+ + p_2^+ = \kappa_1^+ + p_2'^+, \tag{2.94}$$

as well as relative light cone fractions for members of the pair:

$$\gamma_1 = 2\frac{p_1^+}{p_{12}^+} = 2\frac{\alpha_1}{3 - \alpha_3} \tag{2.95}$$

$$\gamma_2 = 2\frac{p_2^+}{p_{12}^+} = 2\frac{2 - \alpha_1 - \alpha_3}{3 - \alpha_3}. \tag{2.96}$$

Using these in the denominator factor $\mathcal{D}(p_1^-)$ and multiplying it by p_1^+ gives

$$\begin{aligned} p_1^+\mathcal{D}(p_1^-) &= \frac{\gamma_1}{2}\left\{\frac{p_{12}^+}{p_{3N}^+}\left(9m_N^2 - \frac{m_N^2 + \mathbf{p}_{3\perp}^2}{\alpha_3/3}\right)\left[-\mathbf{p}_{3\perp}^2 + \frac{m_N^2 + \mathbf{p}_{1\perp}^2}{\gamma_1/2} + \frac{m_N^2 + [\mathbf{p}_{1\perp} + \mathbf{p}_{3\perp}]^2}{\gamma_2/2}\right]\right\} \\ &= \frac{\gamma_1}{2}\left\{\left[4m_N^2 - 3\left(\alpha_3 + \frac{1}{\alpha_3} - 2\right)m_N^2 - \frac{3}{\alpha_3}\mathbf{p}_{3\perp}^2\right] - 4\left[\frac{m_N^2 + \left[\mathbf{p}_{1\perp} + \frac{\gamma_1}{2}\mathbf{p}_{3\perp}\right]^2}{\gamma_1\gamma_2}\right]\right\} \\ &= \frac{\gamma_1}{2}\left(m_{12}^2 - 4\left[m_N^2 + k_{12}^2\right]\right), \end{aligned} \tag{2.97}$$

where m_{12}^2 is the invariant mass squared of the (1,2) pair, given by

$$\begin{aligned} m_{12}^2 &= m_N^2\left(\frac{9p_{12}^+}{p_{3N}^+} - \frac{p_{12}^+}{p_3^+}\right) - \mathbf{p}_{3\perp}^2\left(\frac{p_{12}^+}{p_3^+} + 1\right) \\ &= m_N^2\left(9\frac{3 - \alpha_3}{3} - \frac{3 - \alpha_3}{3}\right) - \mathbf{p}_{3\perp}^2\frac{p_{3N}^+}{p_3^+} \\ &= \left[10 - 3\left(\alpha_3 + \frac{1}{\alpha_3}\right)\right]m_N^2 - \frac{3}{\alpha_3}\mathbf{p}_{3\perp}^2 \\ &= 4m_N^2 - \Delta. \end{aligned} \tag{2.98}$$

Here,

$$\Delta^{(a)} = 3\left[\alpha_3 + \frac{1}{\alpha_3} - 2\right] m_N^2 + \frac{3}{\alpha_3}\mathbf{p}_{3\perp}^2 \geq 0 \tag{2.99}$$

is the virtuality of the two-nucleon pair (1,2) in the intermediate state. It decreases the invariant mass of the two-body state. For small transverse momenta and $\alpha_3 \sim 1$, one has $m_{12}^2 \approx 4m_N^2$, which would allow Eq. (2.97) to be interpreted as the denominator of a two-nucleon wave function, with a relative light cone momentum of

$$\begin{aligned} k_{12}^2 &= \frac{(\gamma_1 - 1)^2 m_N^2 + \left[\mathbf{p}_{1\perp} + \frac{\gamma_1}{2}\mathbf{p}_{3\perp}\right]^2}{\gamma_1\gamma_2} \\ &= \frac{(3-\alpha_3)^2}{4}\left[\frac{\left(\frac{2\alpha_1}{3-\alpha_3} - 1\right)^2 m_N^2 + \left(\mathbf{p}_{1\perp} + \frac{\alpha_1}{3-\alpha_3}\mathbf{p}_{3\perp}\right)^2}{\alpha_1(3-\alpha_1-\alpha_3)}\right]. \end{aligned} \tag{2.100}$$

It is still possible to interpret Eq. (2.97) the denominator of a two-nucleon wave function even at moderately large $\Delta^{(a)}$, although to do so would require $k_{12}^2 \gg \Delta^{(a)}$, so that the difference between $4m_N^2 - 4(m_N^2 + k_{12}^2$ and $m_{12}^2 - 4(m_N^2 + k_{12}^2)$, which is Δ, is small relative to the momentum scale at which the wave function is evaluated. This smallness of Δ/k_{12}^2 would result in a small (and ideally negligible) error in the application of the 2N wave function. Within the domain where this calculation applies, namely the generation of 3N SRCs, one imposes the threshold condition $k_{12} \geq k_F$, which will guarantee k_{12} to be large enough for this interpretation of Eq. (2.97) to be valid. For smaller $k_{12} < k_F$ which do however appear in the normalization rule of Eq. (2.83), we simply neglect $\Delta^{(a)}$, since to do so is necessary for the construction of a two-nucleon wave function, and since $f_{3N}(\alpha, \mathbf{p}_\perp)$ is a formal definition for which the negligence of Δ is valid in the physically relevant domain.

With the results of these calculations applied to Eq. (2.85), and with off-diagonal ($\sigma_2' \neq \sigma_2''$) terms neglected because of their relative smallness, we have

$$\begin{aligned} f_{3N}^{(a)}(\alpha, \mathbf{p}_\perp) &= \int \frac{d\alpha_3 d^2\mathbf{p}_{3\perp}}{\alpha_1\alpha_2\alpha_3}\left\{\frac{\alpha_1}{\gamma_1\gamma_2'}\right\}^2 \overline{|\psi_{2N}(k_{12})|^2}\ \overline{|\psi_{2N}(k_{23})|^2} \\ &= \int \frac{d\alpha_3 d^2\mathbf{p}_{3\perp}}{\alpha_1\alpha_2\alpha_3}\left\{\frac{3-\alpha_3}{2(2-\alpha_3)}\right\}^2 \overline{|\psi_{2N}(k_{12})|^2}\ \overline{|\psi_{2N}(k_{23})|^2}. \end{aligned} \tag{2.101}$$

The factor in the curly brackets $\{\quad\}$ and its effect on the normalization of $f_{3N}(\alpha, \mathbf{p}_{3\perp})$ will be discussed following the derivation of $f_{3N}^{(b)}(\alpha, \mathbf{p}_\perp)$.

pnn **topology**

The rules of light cone perturbation theory are applied to the diagram in Fig. 2.9b, giving

$$\begin{aligned} A\left\{a_2(A)\right\}^2 f_{3N}^{(b)}(\alpha, \mathbf{p}_\perp) = \frac{1}{8}\sum_{\rho_1,\rho_2,\rho_3}\int \frac{dp_2^+ d^2\mathbf{p}_{2\perp}}{2p_2^+(2\pi)^3}\frac{dp_3^+ d^2\mathbf{p}_{3\perp}}{2p_3^+(2\pi)^3}\Bigg[\bar{u}_p^{\rho_1}(\kappa_1)\bar{u}_n^{\rho_2}(\kappa_2)\bar{u}_n^{\rho_3}(\kappa_3) \\ \left(\sqrt{\frac{Aa_2(A)}{2}}\Gamma_{pn}^{(1,3)}\right)\left(\sum_{\sigma_3} u_n^{\sigma_3}(p_3)\bar{u}_n^{\sigma_3}(p_3)\right)\frac{\sum_{\sigma_1''} u_p^{\sigma_1''}(p_1')\bar{u}_p^{\sigma_1''}(p_1')}{p_1'^+\mathcal{D}(p_1'^-)} \\ \left(\sqrt{\frac{Aa_2(A)}{2}}\Gamma_{pn}^{(1,2)}\right)\left(\sum_{\sigma_2} u_n^{\sigma_2}(p_2)\bar{u}_n^{\sigma_2}(p_2)\right)\frac{\sum_{\sigma_1} u_p^{\sigma_1}(p_1)\bar{u}_p^{\sigma_1}(p_1)}{p_1^+\mathcal{D}(p_1^-)} \\ \left(\sum_\sigma a_p^\dagger(p,\sigma)\frac{\alpha}{A}\delta^{(1)}(\alpha-\alpha_1)\delta^{(2)}(\mathbf{p}_\perp-\mathbf{p}_{1\perp})a_p(p,\sigma)\right) \\ \frac{\sum_{\sigma_1'} u_p^{\sigma_1'}(p_1)\bar{u}_p^{\sigma_1'}(p_1)}{p_1^+\mathcal{D}(p_1^-)}\left(\sqrt{\frac{Aa_2(A)}{2}}\Gamma_{pn}^{(1,2)}\right)\frac{\sum_{\sigma_1'''} u_p^{\sigma_1'''}(p_1')\bar{u}_p^{\sigma_1'''}(p_1')}{p_1'^+\mathcal{D}(p_1'^-)} \\ \left(\sqrt{\frac{Aa_2(A)}{2}}\Gamma_{pn}^{(1,3)}\right)u_p^{\rho_1}(\kappa_1)u_n^{\rho_2}(\kappa_2)u_n^{\rho_3}(\kappa_3)\Bigg]. \end{aligned} \tag{2.102}$$

We proceed by calculating the intermediate state denominators. Firstly, we have

$$\begin{aligned} \mathcal{D}(p_1'^-) &= (\kappa_1^- + \kappa_2^- + \kappa_3^-) - (p_1'^- + \kappa_2^- + p_3^-) = (\kappa_1^- + \kappa_3^-) - (p_1'^-) + p_3^-) \\ &= \left(\frac{m_N^2}{\kappa_1^+} + \frac{m_N^2}{\kappa_3^+}\right) - \left(\frac{m_N^2 + \mathbf{p}_{3\perp}^2}{p_1'^+} + \frac{m_N^2 + \mathbf{p}_{3\perp}^2}{p_3^+}\right). \end{aligned} \tag{2.103}$$

To proceed, we now define relative momentum fractions for nucleons within the short-range interaction. A superscript (b) is used to indicate that these fractions are defined for the topology in Fig. 2.9b, and these fractions are compared to quantities calculated for the topology of Fig. 2.9a (here indicated with a superscript (a)):

$$\gamma_1'^{(b)} = 2\frac{p_1'^+}{p_{13}^+} = 2 - \alpha_3 = \gamma_2^{(a)} \tag{2.104}$$

$$\gamma_3^{(b)} = 2\frac{p_3^+}{p_{13}^+} = \alpha_3 = \gamma_3^{(a)}. \tag{2.105}$$

With these momentum fractions, we have

$$p_1'^{+}\mathcal{D}(p_1'-) = \frac{\gamma_1'}{2}\left(4m_N^2 - 4\frac{m_N^2+\mathbf{p}_{3\perp}^2}{\gamma_1'^{(b)}\gamma_3^{(b)}}\right) = \frac{\gamma_1'}{2}\left(4m_N^2 - 4\left[m_N^2 + \left(k_{13}^{(b)}\right)^2\right]\right), \tag{2.106}$$

where

$$\left(k_{13}^{(b)}\right)^2 = \frac{(\gamma_1'^{(b)}-1)^2 m_N^2 + \mathbf{p}_{3\perp}^2}{\gamma_1'^{(b)}\gamma_3^{(b)}} = \frac{(1-\alpha_3)^2 m_N^2 + \mathbf{p}_{3\perp}^2}{\alpha_3(2-\alpha_3)} = \left(k_{23}^{(a)}\right)^2. \tag{2.107}$$

In other words, the factor $p_1'^{+}\mathcal{D}(p_1'^{-})$ in this topology is exactly equal to the factor $p_2'^{+}\mathcal{D}(p_2'^{-})$ in the other topology. As for the other intermediate state factor,

$$\mathcal{D}(p_1^-) = (\kappa_1^- + \kappa_2^- + \kappa_3^-) - (p_1^- + p_2^- + p_3^-) \tag{2.108}$$

is the same in both topologies. Consequently, we have $f_{3N}^{(b)}(\alpha, \mathbf{p}_\perp) = f_{3N}^{(a)}(\alpha, \mathbf{p}_\perp)$.

Formula and normalization of f_{3N}

The LCFD for a short-range three-nucleon cluster is given by $f_{3N}(\alpha, \mathbf{p}_\perp) = f_{3N}^{(a)}(\alpha, \mathbf{p}_\perp) = f_{3N}^{(b)}(\alpha, \mathbf{p}_\perp)$, which is

$$f_{3N}(\alpha, \mathbf{p}_\perp) = \int \frac{d\alpha_3 d^2\mathbf{p}_{3\perp}}{\alpha\alpha_3(3-\alpha-\alpha_3)}\left\{\frac{3-\alpha_3}{2(2-\alpha_3)}\right\}^2 \overline{|\psi_{2N}(k_{12})|^2}\ \overline{|\psi_{2N}(k_{23})|^2}, \tag{2.109}$$

where k_{12} and k_{23} are defined as in the Fig. 2.9a topology, namely by Eqs. (2.92,2.100). This equation is found numerically to satisfy the normalization condition of Eq. (2.83). While we cannot prove that this normalization condition is satisfied analytically, we can show that its satisfaction is close to exact. Consider the integral

$$\mathcal{I}_{3N} = \int f_{3N}(\alpha, \mathbf{p}_\perp) d\alpha d^2\mathbf{p}_\perp, \tag{2.110}$$

which is evaluated using the change of variables

$$\gamma_1 = \frac{2\alpha}{3-\alpha_3} \qquad \mathbf{k}_{12\perp} = \mathbf{p}_\perp + \frac{\alpha}{3-\alpha_3}\mathbf{p}_{3\perp}$$
$$\gamma_2' = 2-\alpha_3 \qquad \mathbf{k}_{23\perp} = -\mathbf{p}_{3\perp},$$

which has a Jacobian

$$\frac{d\alpha d^2\mathbf{p}_\perp}{\alpha}\frac{d\alpha_3 d^2\mathbf{p}_{3\perp}}{\alpha_3} = \frac{d\gamma_1 d^2\mathbf{k}_{12\perp}}{\gamma_1}\frac{d\gamma_2' d^2\mathbf{k}_{23\perp}}{2-\gamma_2'}.$$

Also note several additional factors transform as

$$\frac{1}{3-\alpha-\alpha_3} = \frac{1}{1+\gamma_2'}\frac{2}{2-\gamma_1}$$
$$\frac{3-\alpha_3}{2(2-\alpha_3)} = \frac{1+\gamma_2'}{2\gamma_2'},$$

so that

$$\begin{aligned}\mathcal{I}_{3N} &= \int d\gamma_1 d^2\mathbf{k}_{12\perp}\frac{\overline{|\psi_{2N}(k_{12})|^2}}{\gamma_1(2-\gamma_1)}\int d\gamma_2' d^2\mathbf{k}_{23\perp}\left\{\frac{1+\gamma_2'}{2\gamma_2'}\right\}\frac{\overline{|\psi_{2N}(k_{23})|^2}}{\gamma_2'(2-\gamma_2')} \\ &= 1+\int d\gamma_2' d^2\mathbf{k}_{23\perp}\left\{\frac{1-\gamma_2'}{2\gamma_2'}\right\}\frac{\overline{|\psi_{2N}(k_{23})|^2}}{\gamma_2'(2-\gamma_2')}, \end{aligned} \tag{2.111}$$

where the normalization rule for the light cone two-nucleon wave function was used. Exact normalization of $f_{3N}(\alpha, \mathbf{p}_\perp)$ fails by the average value of $\left\{\frac{1-\gamma_2'}{2\gamma_2'}\right\}$ within a short-range two-nucleon state, which is a small relativistic factor. Numerically, this correction is found to be 0.0028, which is negligible.

The factor $a_3(A)$

The factor $a_3(A)$ is defined in analogy to $a_2(A)$ for electron-nucleus scattering reactions, namely

$$a_3(A) = \frac{3}{A}\frac{\sigma_{eA}(x)}{\sigma_{e^3\mathrm{He}}(x)} \qquad 2.25 \lesssim x < 3, \tag{2.112}$$

supposing that this cross section ratio levels out into a plateau as Refs. [8,39] suggest. The plateau, if it exists, is present by virtue of the universality of 3N SRCs in various nuclei; in other words, the high light cone fraction ($2 < \alpha < 3$) part of the nuclear LCFD imitates the high-α part of the ^{3}He nuclear LCFD. The formula for the 3N SRC contribution to the LCFD, given by combining Eqs. (2.84,2.109), does not explicitly contain any factors of $a_3(A)$, but instead contains factors of $a_2(A)$. In particular,

$$f^{(3)}_{N/A}(\alpha, \mathbf{p}_\perp) = A \left\{a_2(A)\right\}^2 \int \frac{d\alpha_3 d^2\mathbf{p}_{3\perp}}{\alpha\alpha_3(3-\alpha-\alpha_3)} \left\{\frac{3-\alpha_3}{2(2-\alpha_3)}\right\}^2 \overline{|\psi_{2N}(k_{12})|^2}\ \overline{|\psi_{2N}(k_{23})|^2}\,. \tag{2.113}$$

Universality of the 3N SRC part of the LCFD entails

$$f^{(3)}_{p/A}(\alpha, \mathbf{p}_\perp) + f^{(3)}_{n/A}(\alpha, \mathbf{p}_\perp) = \frac{3a_3(A)}{A}\left(f^{(3)}_{p/^3\mathrm{He}}(\alpha, \mathbf{p}_\perp) + f^{(3)}_{n/^3\mathrm{He}}(\alpha, \mathbf{p}_\perp)\right), \tag{2.114}$$

which in turn gives us

$$a_3(A) = \left(\frac{a_2(A)}{a_2(^3\mathrm{He})}\right)^2. \tag{2.115}$$

Eq. (2.115) allows for the values of the scaling plateaus in $\mathcal{R}(A, ^3\mathrm{He})$ at $x \gtrsim 2.25$ to be calculated using the known values of $a_2(A)$. These values have been calculated and are presented in Table 2.1, where they are compared to the $a_3(A)$ values extracted from a CLAS experiment at Jefferson Lab [8]. There is a systematic discrepancy between the theoretical and experimental $a_3(A)$ values, with the former being consistently larger than the latter. This may partly be due to the theoretical calculation not accounting for surface effects, isospin asymmetry, or the combinatorics of selecting multiple nucleons—the last of which is expected to be especially pertinent for small nuclei such as ^{3}He and ^{4}He. However, these effects are expected to be small in large nuclei such as ^{56}Fe where the discrepancy persists.

Another possible explanation for the discrepancy is that the CLAS experiment did not observe genuine three-nucleon SRC plateaus. A later Jefferson Lab experiment at Hall C [36]

A	Theoretical	Experimental [8]
^{3}He	1	1
^{4}He	2.94 ± 0.18	2.33 ± 0.13
^{9}Be	3.47 ± 0.25	—
^{12}C	5.16 ± 0.36	3.18 ± 0.24
^{27}Al	6.37 ± 1.46	—
^{56}Fe	6.86 ± 1.03	4.63 ± 0.33
^{63}Cu	6.16 ± 0.53	—
^{197}Au	5.97 ± 0.54	—

Table 2.1: Values of $a_3(A)$ determined using Eq. (2.115) and the weighted averages of experimental $a_2(A)$ values from Refs. [8,34–36]. These are compared to the $a_3(A)$ values reported by CLAS [8]. There is a systematic discrepancy between theoretical and experimental values, which could be due either to experimental issues (*cf. e.g.*, [45] for instance) or to an incomplete theoretical description (such as isospin and selection combinatorics effects not being accounted for).

did not observe the three-nucleon plateau, and it has been reported that the plateaus seen by CLAS may have been an artifact of bin migration due to low energy resolution [45]. Ultimately, the status of three-nucleon SRCs and the value of $a_3(A)$ remain ambiguous.

2.4.8 Numerical computations of $3N$ SRC distributions

In section 2.4.4, numerical computations of the two-nucleon SRC contribution to the LCFD of ^{56}Fe and ^{208}Pb were presented. Here, three-nucleon SRCs are also accounted for. We use the model described above to account for three-nucleon correlations. Numerically, we find that three-nucleon SRCs are expected to constitute about 6-7% of the nuclear LCFD. Accordingly, the dilution factors for the mean field contribution to the LCFD change as such: For iron, $a_1^{(p)}(^{56}\text{Fe}) = 0.64$ and $a_1^{(n)}(^{56}\text{Fe}) = 0.68$; while for lead, $a_1^{(p)}(^{208}\text{Pb}) = 0.62$ and $a_1^{(n)}(^{208}\text{Pb}) = 0.73$.

In Fig. 2.10, plots of the numerical estimates are presented for $f_{p/A}(\alpha)$ (with $\mathbf{p}_\perp$ integrated over). Since the three-nucleon SRC contribution is quite small compared to even two-nucleon SRCs, log-scaled versions of the plots are also presented. In the log-scaled plots, one can see the 3N SRCs already contribute significantly around $\alpha \approx 1.6$-1.7, but are alone responsible for the survival of the LCFD beyond $\alpha > 2$ (as two-nucleon SRCs are kinematically forbidden from contributing to $\alpha > 2$ when center-of-mass motion is neglected). In the non-log-scaled plots, however, one can see that the three-nucleon SRCs "take away" nucleons from the mean field, in particular from $\alpha \sim 1$, where the LCFD is suppressed compared to the case when only the mean field and 2N SRCs contribute.

2.4.9 nPDF for $3N$ SRCs

The contribution to the nuclear PDF coming from 3N SRCs is now calculated. In this case, the final state is characterized by (1) the isospin of the destroyed nucleon (p or n), (2) the isospins of the other two removed nucleons (*e.g.*, pn or nn if the destroyed nucleon was p), (3) the flavor of the probed parton, and (4) the Fock component $\mathcal{F}$ of the destroyed nucleon. Recall that the *per nucleon* LCFD for a characteristic short-range three-nucleon configuration, $f_{3N}(\alpha, \mathbf{p}_\perp)$, was normalized to 1 and that different topologies for producing

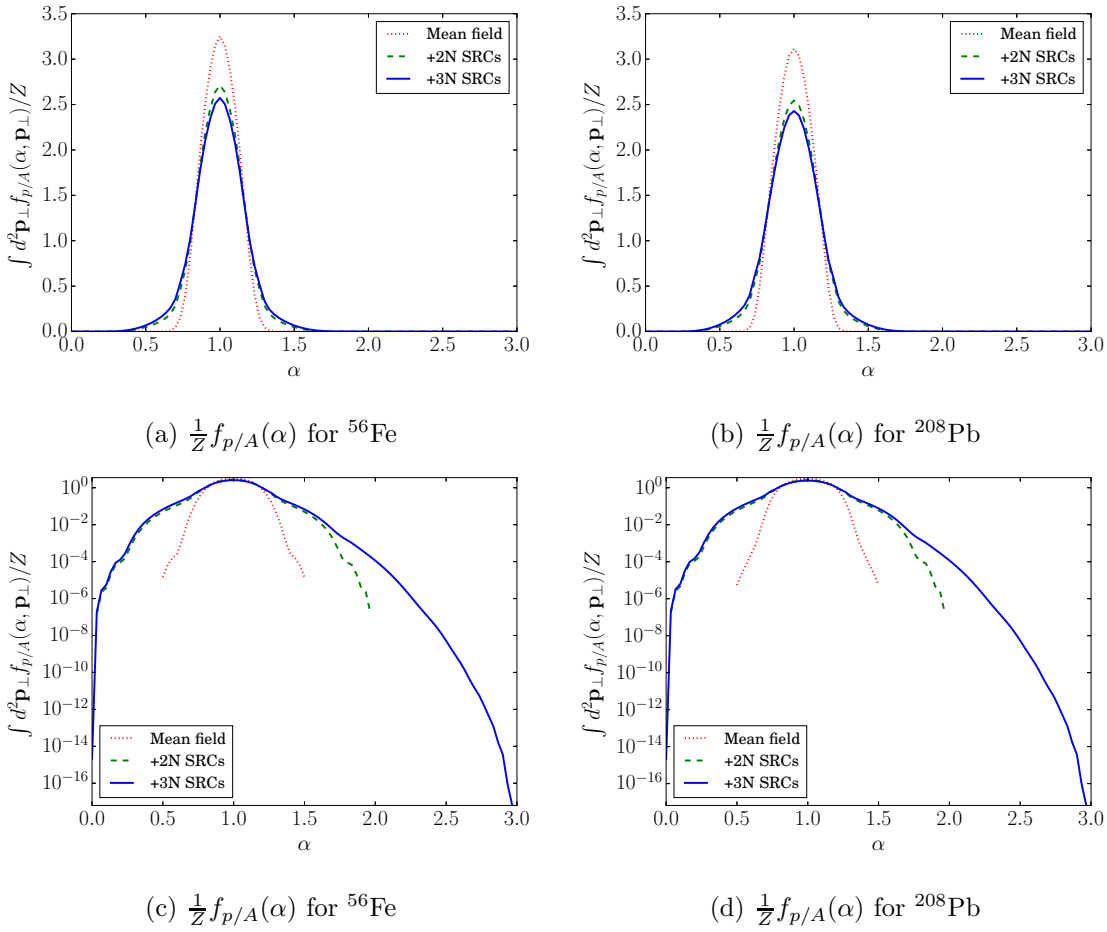

(a) $\frac{1}{Z} f_{p/A}(\alpha)$ for ^{56}Fe

(b) $\frac{1}{Z} f_{p/A}(\alpha)$ for ^{208}Pb

(c) $\frac{1}{Z} f_{p/A}(\alpha)$ for ^{56}Fe

(d) $\frac{1}{Z} f_{p/A}(\alpha)$ for ^{208}Pb

Figure 2.10: The *per nucleon* light cone fraction distribution $f_{p/A}(\alpha)$, with $\mathbf{p}_\perp$ integrated over.

Feynman diagram for hadronic current of three-nucleon SRC

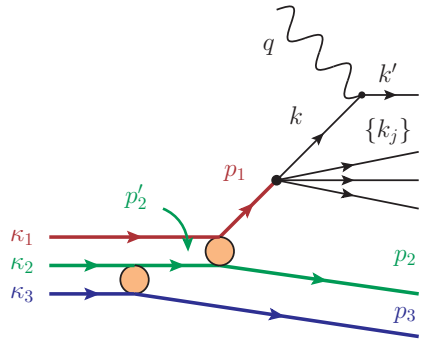

Figure 2.11: Diagram for the current $\langle X \mid J^+(0) \mid 3N \rangle$.

a 3N SRC (which have different removed nucleon content) produced the same functional form. The weight factors of $\sqrt{Aa_2(A)/2}$ present at each two-nucleon vertex are *overall* probability factors for short-range two-nucleon interactions to occur, and accordingly allow one to calculate the 3N SRC contribution to the LCFD or to the nPDF using a single diagram. In principle, since either topology can produce a 3N SRC, so each diagram should be weighted by a probability factor (the factors adding to 1); however, the fact that both topologies have the same dependence on external kinematics means only one diagram needs to be calculated in practice. Thus, we do not need to perform a sum over topologies for the 3N SRC contribution to the nuclear PDF.

Additionally, for concreteness, we will suppose that the probed nucleon was a proton; the total 3N SRC contribution to the nuclear hadronic tensor, $W_{3N}^{\mu\nu}$, is found by adding an otherwise identical term with the transposition $(p \leftrightarrow n)$ performed.

With this in mind, and continuing to use the same notion as before, the matrix element for the hadronic current is given by $\langle X \mid J^+(0) \mid 3N \rangle$, the diagram for which is depicted in

Fig. 2.11. Using the rules of light cone perturbation theory, the diagram evaluates to

$$\begin{aligned}\langle X \mid J^+(0) \mid 3N\rangle = \bar{u}_i^{\lambda'}(k')e_i\gamma^+\frac{\sum_\lambda u_i^\lambda(k)\bar{u}_i^\lambda(k)}{k^+\mathcal{D}(k^-)}\left[\prod_{j=1}^{n_s}\bar{u}_{i_j}^{\lambda_j}(k_j)\right]\Gamma_{i,\mathcal{F}/p}\frac{\sum_{\sigma_1}u_p^{\sigma_1}(p_1)\bar{u}_p^{\sigma_1}(p_1)}{p_1^+\mathcal{D}(p_1^-)}\\ \bar{u}_n^{\sigma_2}(p_2)\bar{u}_p^{\sigma_3}(p_3)\left(\sqrt{\frac{Aa_2(A)}{2}}\Gamma_{pn}^{(1,2)}\Theta(k_{12}-k_F)\right)\frac{\sum_{\sigma_2'}u_n^{\sigma_2'}(p_2')\bar{u}_n^{\sigma_2'}(p_2')}{p_2'^+\mathcal{D}(p_2'^-)}\\ \left(\sqrt{\frac{Aa_2(A)}{2}}\Gamma_{pn}^{(2,3)}\Theta(k_{23}-k_F)\right)u_p^{\rho_1}(\kappa_1)u_n^{\rho_2}(\kappa_2)u_p^{\rho_3}(\kappa_3)\\ =\frac{2e_ik^+}{x_N\gamma_1\gamma_2'}\sum_{\sigma_1,\sigma_2'}\Big\{\psi_{i,\mathcal{F}/p}^{(\lambda',\{\lambda_j\};\sigma_1)}(x_N,\mathbf{k}_\perp,\{x_j,\mathbf{k}_{j\perp}\};p_1)Aa_2(A)2(2\pi)^3\\ \psi_{2N}^{(\sigma_1,\sigma_2)}(\gamma_1,\mathbf{k}_{12\perp})\Theta(k_{12}-k_F)\psi_{2N}^{(\sigma_2',\sigma_3)}(\gamma_2',\mathbf{k}_{23\perp})\Theta(k_{23}-k_F)\Big\}.\end{aligned}$$

Since there are two sums (over σ_1 and σ_2') at the amplitude level, the square of this matrix element that will include off-diagonal interference terms. As before, we neglect these as small in comparison to the diagonal terms, and accordingly move the σ_1 and σ_2' sums outside the square.

The delta function that appears in $W_{3N}^{++}(p_A,q)$ is

$$\delta^{(4)}\left(p_A+q-k'-\sum_{j=1}^{n_s}k_j-p_2-p_3\right)=2\delta^+\delta^-\delta_\perp, \tag{2.116}$$

where

$$\delta^+=\delta^{(1)}\left(p_1^+-k^+-\sum_{j=1}^{n_s}k_j^+\right)=\frac{A}{\alpha p_A^+}\delta^{(1)}\left(1-x_N-\sum_{j=1}^{n_s}x_j\right) \tag{2.117}$$

$$\delta_\perp=\delta^{(2)}\left(\mathbf{p}_{1\perp}-\mathbf{k}_\perp-\sum_{j=1}^{n_s}\mathbf{k}_{j\perp}\right) \tag{2.118}$$

by virtue of conservation of the + and transverse components of momentum. The "minus" delta function is given, in the collinear, massless quark approximation, by

$$\delta^-=\delta^{(1)}\left(\frac{M_A^2}{p_A^+}+\frac{2(q\cdot p_A)}{p_A^+}-\frac{Q^2}{x_N\alpha p_A^+/A}-\frac{m_N^2+\mathbf{p}_{2\perp}^2}{p_2^+}-\frac{m_N^2+\mathbf{p}_{1\perp}^2}{p_1^+}\right), \tag{2.119}$$

which in the Bjorken limit becomes

$$\delta^- = \frac{x_A p_A^+}{2(q\cdot p_A)\alpha}\delta^{(1)}\left(x_N - \frac{x_A}{\alpha}\right). \tag{2.120}$$

Consequently, one has

$$\begin{aligned}
W_{3N}^{++}(p_A,q) = \frac{(p_A^+)^2}{M_A(q\cdot p_A)} x_A \sum_i e_i^2 \sum_{N=p,n}\int \frac{d\alpha}{\alpha} d^2\mathbf{p}_\perp \Bigg[\Bigg\{ A\left\{a_2(A)\right\}^2 \\
\int \frac{d\alpha_3 d^2\mathbf{p}_{3\perp}}{\alpha\alpha_3(3-\alpha-\alpha_3)}\Bigg(\left(\frac{3-\alpha_3}{2(2-\alpha_3)}\right)\overline{|\psi_{2N}(k_{12})|^2}\,\Theta(k_{12}-k_F) \\
\overline{|\psi_{2N}(k_{23})|^2}\,\Theta(k_{23}-k_F)\Bigg)\Bigg\} \\
\Bigg\{\int \frac{dx_N d^2\mathbf{k}_\perp}{2x_N(2\pi)^3}\left[\frac{dx_j d^2\mathbf{k}_{j\perp}}{2x_j(2\pi)^3}\right]\delta^{(1)}\left(x_N-\frac{x_A}{\alpha}\right)2(2\pi)^3\delta^{(1)}\left(1-x_N-\sum_{j=1}^{n_s}x_j\right) \\
\delta^{(2)}\left(\mathbf{p}_\perp-\mathbf{k}_\perp-\sum_{j=1}^{n_s}\mathbf{k}_{j\perp}\right)\overline{\left|\psi_{i,\mathcal{F}/N}(x_N,\mathbf{k}_\perp,\{x_j,\mathbf{k}_{j\perp}\};p\right|^2}\Bigg\}\Bigg] \\
= \frac{(p_A^+)^2}{M_A(q\cdot p_A)} x_A \sum_i e_i^2 \sum_{N=p,n}\int \frac{d\alpha}{\alpha} d^2\mathbf{p}_\perp \left[f_{i/N}^{(b,3)}\left(\frac{x_A}{\alpha},Q^2;\alpha,\mathbf{p}_\perp\right) f_{N/A}^{(3)}(\alpha,\mathbf{p}_\perp)\right],
\end{aligned} \tag{2.121}$$

where the two expressions in the big curly brackets $\left\{\ \right\}$ are the 3N SRC part of the LCFD, and the bound nucleon PDF. Therefore, we have

$$f_{i/A}^{(3)}(x_A,Q^2) = \sum_{N=p,n}\int_{x_A}^3 \frac{d\alpha}{\alpha}\int d^2\mathbf{p}_\perp\left[f_{i/N}^{(b,3)}\left(\frac{x_A}{\alpha},Q^2;\alpha,\mathbf{p}_\perp\right) f_{N/A}^{(3)}(\alpha,\mathbf{p}_\perp)\right]. \tag{2.122}$$

2.4.10 Concluding remarks

In this section, the existing experimental evidence for two- and three-nucleon short range correlations was reviewed, and information extracted from experiment was used in constructing a theoretical model of SRCs. The experimental status of three-nucleon SRCs is ambiguous, but a model for 3N SRCs was constructed based on the hypothesis that they arise from a sequence of short-range two-nucleon interactions, using the latest experimental

phenomenology of two-nucleon SRCs. Light cone fraction distributions were constructed for both the two- and three-nucleon SRC contributions to the nuclear LCFD, and convolution formulas were derived for the SRC contributions to the nuclear PDF. The convolution formula for the PDF of a j-nucleon correlation takes the same form as the formula for the mean field (with $j = 1$), namely that in Eq. (2.56).

2.5 Medium modifcations

The convolution formula of Eq. (2.56) allows for the nPDF contribution from processes with j removed nucleons to be calculated, provided that one has the light cone fraction distribution (LCFD) $f^{(j)}_{N/A}(\alpha, \mathbf{p}_\perp)$ and the bound nucleon PDF $f^{(b,j)}_{i/N}\left(\frac{x_A}{\alpha}, Q^2; \alpha, \mathbf{p}_\perp\right)$. In the previous section, the theoretical details necessary to construct the LCFD were developed, and numerical computations were performed. Now, we shall explore the issue of medium modifications, and determine how the bound nucleon PDF is to be calculated.

2.5.1 The unmodified PDF

The most straightforward, if naive, approach is to assume the bound nucleon PDF is equal to the free nucleon PDF, *i.e.*,

$$f^{(b,j)}_{i/N}\left(\frac{x_A}{\alpha}, Q^2; \alpha, \mathbf{p}_\perp\right) = f_{i/N}\left(\frac{x_A}{\alpha}, Q^2\right). \tag{2.123}$$

To do as much ignores that the fact that the nucleon is immersed in a strongly-interacting medium which can reasonably be expected to modify its dynamical properties. However, in parallel with all nPDF calculations that do account for medium modifications, the naive "no modifications" model of Eq. (2.123) shall be also be used as a point of comparison.

To begin, one can compare the no modifications model to experiment immediately, together with the LCFD developed previously and an experimental parametrization of the free nucleon PDF, in order to assess the importance of medium modifications. In particular,

we compare the ratio $R(A,d)$, given by

$$R(A,d) = \frac{2}{A}\frac{\sigma_{eA}(x,Q^2)}{\sigma_{ed}(x,Q^2)} \tag{2.124}$$

$$\approx \frac{2}{A}\frac{F_2^{(A)}(x,Q^2)}{F_2^{(d)}(x,Q^2)}. \tag{2.125}$$

One can use the relation

$$F_2(x,Q^2) = \sum_i e_i^2 f_i(x,Q^2) \tag{2.126}$$

to calculate $F_2(x,Q^2)$ from PDFs, or else use this relation to write a convolution formula for $F_2(x,Q^2)$ by placing it into Eq. (2.56). One finds that

$$F_2^{(A)}(x_A,Q^2) = \sum_{j=1}^{A}\sum_{N=p,n}\int_{x_A}^{A} d\alpha \int d^2\mathbf{p}_\perp f_{N/A}^{(j)}(\alpha,\mathbf{p}_\perp) F_2^{(N;b,j)}\left(\frac{x_A}{\alpha},Q^2;\alpha,\mathbf{p}_\perp\right), \tag{2.127}$$

where the superscript $(N;b,j)$ for the nucleonic structure function denotes that the nucleon is bound and in a j-nucleon correlation (or the mean field in the case $j=1$).

As it is, Eq. (2.127) is general; it can be simplified for the no modification model. In the absence of medium modifications, the PDF (and thus the structure function F_2) for a nucleon will not be different for a nucleon in the mean field and a nucleon in a j-nucleon correlation; these would only be different due to the nucleon experiencing different dynamical influences. Thus, without medium modifications, Eq. (2.127) factorizes to

$$F_2^{(A)}(x_A,Q^2) = \sum_{N=p,n}\int_{x_A}^{A} d\alpha \int d^2\mathbf{p}_\perp f_{N/A}(\alpha,\mathbf{p}_\perp) F_2^{(N)}\left(\frac{x_A}{\alpha},Q^2;\alpha,\mathbf{p}_\perp\right), \tag{2.128}$$

where the nuclear LCFD is decomposed as in Eq. (2.41).

In order to demonstrate the necessity of accounting for medium modifications, we use Eq. (2.128) to calculate the nuclear structure function $F_2^{(A)}(x_A,Q^2)$ and the deuteron structure function $F_2^{(d)}(x_A,Q^2)$, using an empirical parametrization of the free nucleon structure function given by Bodek *et al.* [46–48]. The values of $R(A,d)$ obtained from this parametrization is compared to experimental data from SLAC [4, 49] for ^{56}Fe in Fig. 2.12.

Plot of EMC ratio with no medium modifications

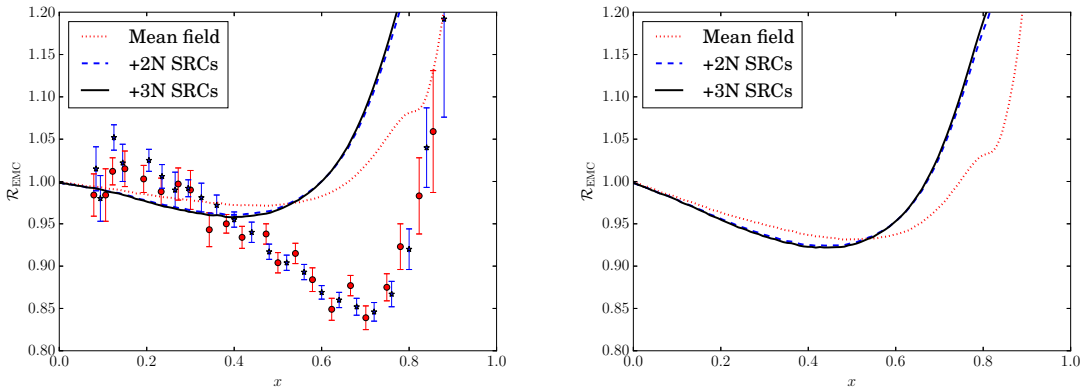

(a) EMC ratio for ^{56}Fe

(b) EMC ratio for ^{208}Pb

Figure 2.12: The EMC ratio at $Q^2 = 10$ GeV^2, calculated using the Bodek-Ritche parametrization of the free nucleon PDF [46–48] (no medium modifications present). Data are from SLAC experiments: Stars (blue) are from [4]; circles (red) are from [49]. No EMC ratio data currently exist for ^{208}Pb.

Additionally, the EMC ratio expected for ^{208}Pb in the convolution model without medium modifications is also presented in this figure.

As can be seen in Fig. 2.12, the experimental values of $R(A, d)$ fall well below the theoretical calculations. This demonstrates the necessity of accounting for medium modifications in calculating the nuclear PDF.

2.5.2 The EMC effect

The discrepancy between the no modifications model for the nuclear PDF and actual experimental results, as seen in Fig. 2.12, is known as the EMC effect, named after the European Muon Collaboration. The effect was first seen in 1983, when the EMC measured the ratio for muon scattering from iron and deuterium, expecting the ratio to be about 1 (with deviations at high x owing to Fermi smearing) [1, 50]. The effect has been confirmed and repeatedly measured by many other groups, such as by a Rochester-SLAC-MIT collaboration [51,52], SLAC [4,49], BCDMS [53,54], the EMC [55,56], the NMC [57–60], HERA [61], and Jefferson Lab [62,63].

The dip in the ratio $\mathcal{R}_{\mathrm{EMC}}$ and its shape are consistent throughout nuclei, and the strength of the EMC effect is typically characterized by the slope in the region $0.35 < x < 0.7$ [62]. This strength tends to increase with A, but roughly saturates at large A. Moreover, the EMC slope is roughly proportional to the local density of the nucleus being considered [62], already suggesting that the EMC effect is likely to be due to dynamics in the nuclear medium. Additionally, several theoretical works by Miller and Smith [64, 65] rigorously demonstrate that the dip in $\mathcal{R}_{\mathrm{EMC}}$ in the region $0.35 \leq x \leq 0.7$ cannot be accounted for by nucleonic motion alone, meaning that modifications of the quark and gluon degrees of freedom of the bound nucleons do indeed need to be accounted for.

There is a consensus that the EMC effect is due to medium modification, but not about how medium modification should be accounted for. A large number of differing theoretical models exist, due to different assumptions made about the nature of medium modification effects; for reviews of the EMC effect, *cf.* [5,6,66]. Several authors [67–69] have argued that the strength of the EMC effect for a bound nucleon should be proportional to the first-order approximation (in p^2/m^2) of the bound nucleon's kinetic energy, or more precisely to the off-shellness of the bound nucleon. Accordingly, higher-momentum nucleons are expected to be more highly-modified than lower-momentum nucleons, and short range correlations in particular are expected to be especially highly modified.

Recently, Weinstein *et al.* [7] noted a correlation between the strength of the EMC effect (as characterized by the slope of the EMC ratio in the region $0.35 < x < 0.7$) and the strength of two-nucleon SRCs (as characterized by $a_2(A)$). There appears to be a direct linear correlation between these quantities, and Weinstein *et al.* [7] have used this to make predictions for $a_2(A)$ for several nuclei. This correlation does lend credence to the expectation that short range correlations are highly modified by the nuclear medium.

Correctly defining x_A

Data from DIS experiments meant to measure the EMC ratio tend to plot the ratio $F_2^{(A)}(x_B, Q^2)/F_2^{(d)}(x_B, Q^2)$ against the kinematic Bjorken scaling variable,

$$x_B = \frac{Q^2}{2m_N\nu}, \tag{2.129}$$

where m_N is the mass of a free nucleon. However, this x_B is not the scaling variable that enters into the dynamics of QCD, including the convolution formulas of Eqs. (2.56,2.127). Instead, the correct dynamical momentum fraction is given by

$$x_A = \frac{AQ^2}{2M_A\nu}, \tag{2.130}$$

which, for fixed values of Q^2 and ν, gives different values for different nuclei. To find a structure function ratio that reflects nuclear dynamics, and not kinematic effects, one should evaluate $F_2^{(A)}(x_A, Q^2)$ and $F_2^{(d)}(x_d, Q^2)$ at the same values of x and Q^2, and to have $x_A = x_d$ one would need to perform the measurement with different lab-frame energy transfers ν for the deuteron and nuclear target.

However, in practice, experimental analyses are best done by using consistent binning for directly measured kinematic quantities such as the final electron energy E' and the electron scattering angle θ for both the nuclear and deuteron targets, in order to cancel out acceptance corrections. Accordingly, the ratio is most easily measured by using the same x_B value for both the nuclear and deuteron structure functions, so that $x_d \neq x_A$.

This means the ratio $\mathcal{R}_{\rm EMC}(x_B, Q^2)$ contains kinematic effects in addition to dynamical effects. The deuteron is a loosely-bound system, meaning x_d differs only slightly from x_B, whereas a heavy nucleus with a large binding energy per nucleon will have its x_A value shifted from x_B by a greater amount. Thus the ratio $\mathcal{R}_{\rm EMC}(x_B, Q^2)$ compares the structure functions of the deuteron and the heavy nucleus at different enough momentum fractions that a deviation from the "no modification" model plot in Fig. 2.12 can be expected.

Plot of EMC ratio with x shifted

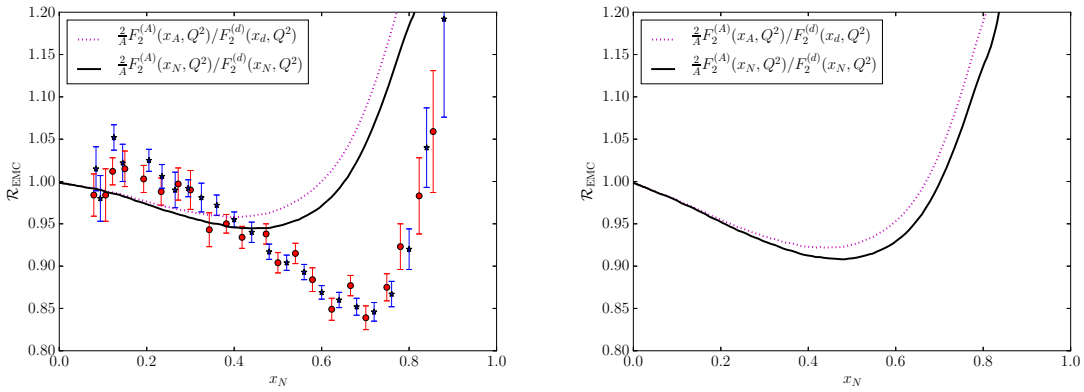

(a) EMC ratio for ^{56}Fe

(b) EMC ratio for ^{208}Pb

Figure 2.13: The EMC ratio at $Q^2 = 10$ GeV^2, calculated using the Bodek-Ritche parametrization of the free nucleon PDF [46–48] (no medium modifications present). 2N and 3N SRCs are accounted for in this calculation. Data are from SLAC experiments: Stars (blue) are from [4]; circles (red) are from [49].

The convolution formula for the nuclear PDF, in order to make the PDF a function of x_B, needs to be slightly modified. The nucleonic PDF requires x_A/α as its argument, and $x_A = \frac{Am_N}{M_A}x_B$, so

$$f_{i/A}^{\rm shift}(x_B,Q^2) = \sum_{j=1}^{A}\sum_{N=p,n}\int_{\frac{Am_N x_B}{M_A}}^{A}\frac{d\alpha}{\alpha}\int d^2\mathbf{p}_\perp f_{N/A}^{(j)}(\alpha,\mathbf{p}_\perp) f_{i/N}^{(b,j)}\left(\frac{Am_N x_B}{M_A\alpha},Q^2;\alpha,\mathbf{p}_\perp\right). \tag{2.131}$$

It has been observed by several authors [70, 71] that presenting the EMC ratio as a function of x_B (so that $x_A \neq x_d$) instead of a function of $x_A = x_d$ introduces an artificial dip in the ratio for $x_B \gtrsim 0.5$, partially explaining the EMC effect. This explanation is only partial, however; as can be seen in Fig. 2.13, where $\mathcal{R}_{\rm EMC}(x_B,Q^2)$ is compared to $\mathcal{R}_{\rm EMC}(x_{A/d},Q^2)$ as calculated within this work's LCFD model, the "shifted" ratio still falls far above the experimental data for the ratio. A dynamical account of medium modifications is still required.

The color screening model

In this dissertation, dynamical medium modifications are accounted for using the color screening model, which was first introduced by Frankfurt and Strikman [42, 67].

The color screening model is developed by considering that a nucleon does not have a sharply-determined "size." Its wave function is spread over a large number of possible configurations, where the quarks and gluons making up the nucleon are distributed in different ways. These include average-sized configuration (ASCs) where the radius of the nucleon is close to its mean value, but they also include point-like configurations (PLCs) where the partons making up the nucleon are compressed into a significantly smaller volume than average.

Since the nucleon is color-neutral, any strong interactions that occur between nucleons are due to higher-order moments (dipole, quadrupole, *etc.*), all of which become suppressed when the distance between color-charged constituents is decreased. Accordingly, PLCs interact more weakly than ASCs do. Since these configurations interact differently, their modification due to immersion in the nuclear medium should differ as well. In particular, the nucleon will tend to be in configurations that are more likely to bring the bound system into a lower-energy state, meaning that PLCs are expected to be suppressed for bound nucleons.

The change in probability has been estimated using non-relativistic perturbation theory by Frankfurt and Strikman [42, 67]. In particular, since the PLC contribution to the nucleonic PDF is expected to dominate when $x \gtrsim 0.6$, the PDF should be suppressed by a factor $\delta_A^{(j)}(k^2, x_N)$, which depends on the nucleon momentum (or off-shellness) k^2 as

$$\delta_A^{(j)}(k^2, x_N \gtrsim 0.6) = \frac{1}{(1+z^{(j)})^2} \qquad z^{(j)} = \frac{\frac{k^2}{m_N} + 2\epsilon_A^{(j)}}{\Delta E_A^{(j)}}, \tag{2.132}$$

where the superscript j denotes whether the nucleon is moving in the mean field ($j = 1$) or is in a j-nucleon SRC. Additionally, $\epsilon_A^{(j)}$ is the mean binding energy per nucleon and $\Delta E_A^{(j)}$ denotes the excitation energy of the nucleon in the nuclear medium.

For $x_N < 0.45$, it is supposed that no medium modification occurs, and for $0.45 < x_N < 0.6$, $\delta_A^{(j)}(k^2, x_N)$ is interpolated linearly:

$$\delta_A(k^2, 0.45 < x_N < 0.6) = 1 + \frac{x_N - 0.45}{0.15} \left\{ \delta_A(k^2, x_N \gtrsim 0.6) - 1 \right\}. \tag{2.133}$$

This neglects the enhancement of the bound nucleon PDF at small x, which can be seen in the data in Fig. 2.12, and which is implied by the baryon charge sum rule. However, the enhancement in this region owes to different dynamics than those at play at moderate and large x, and accordingly is beyond the scope of this dissertation. For a review of nuclear effects at low x, however, see Ref. [72].

The nucleon excitation energy $\Delta E_A^{(j)}$ is a dynamical parameter depending on local medium effects, in particular on the spin and isospin configurations of the interacting nucleons. Accordingly, it differs between a nucleon in the mean field and a nucleon in an SRC, which is a large part of why the mean field and j-nucleon SRCs are modified differently. For a nucleon in the mean field, the characteristic excitation energy is expected to be in the range 300-500 MeV, namely between the excitation energies of a Δ and an N^* resonance. The best fit to data occurs when $\Delta E_A^{(1)} \approx 500$ MeV, corresponding to the N^* resonance. However, for the deuteron, as well as for a nucleon in a two-nucleon SRC, the lowest excited state is expected to be a $\Delta\Delta$ configuration, giving $\Delta E_d = \Delta E_A^{(2)} \approx 600$ MeV. Since the three-nucleon SRC is generated through a sequence of two-nucleon SRCs, we also take $\Delta_A^{(3)} = 600$ MeV.

The binding energy in the mean field $\epsilon_A^{(1)}$ is taken to simply be the empirically-known binding energy per nucleon. For two- and three-nucleon correlations, the binding energy is neglected, since it is small compared to the kinetic energy of a nucleon in an SRC, which will dominate $z^{(j\geq 2)}$.

Lastly, the momentum k depends on whether the nucleon is in the mean field or a short range correlation. It corresponds to the light cone momentum of the bound nucleon relative to the center of mass of either the nucleus ($j = 1$) or with respect to the j-nucleon

cluster. In particular,

$$k_{j=1}^2 = (\alpha-1)^2 m_N^2 + \mathbf{p}_\perp^2 \tag{2.134}$$

$$k_{j=2}^2 = \frac{(\alpha-1)^2 m_N^2 + \mathbf{p}_\perp^2}{\alpha(2-\alpha)} \tag{2.135}$$

$$k_{j=3}^2 = 2\frac{(\alpha-1)^2 m_N^2 + \mathbf{p}_\perp^2}{\alpha(3-\alpha)}. \tag{2.136}$$

The $j=1$ and $j=3$ cases are approximations, and the $j=2$ case is exact. In particular, the $j=1$ case is the non-relativistic approximation, and the $j=3$ case assumes the relative momentum between the spectators in the 3N SRC is small.

In effect, with these values for the parameters in mind, the contribution to the bound nucleon PDF of processes that involve j removed nucleons is

$$f_{i/N}^{(b,j)}\left(x_N, Q^2; \alpha, \mathbf{p}_\perp\right) = f_{i/N}\left(x_N, Q^2\right) \delta^{(j)}\left(k^2(\alpha, \mathbf{p}_\perp), x_N\right). \tag{2.137}$$

If the artificial shift in x due to comparing nuclear and deuteron PDFs at a fixed x_B is to be accounted for, then x_N should be taken to be $\frac{Am_N}{M_A}\frac{x_B}{\alpha}$; otherwise, the argument should be $x_N = \frac{x_A}{\alpha}$.

The color screening model adequtely accounts for the EMC effect in ^{56}Fe, as can be seen in Fig. 2.14. It should be noted that this model has been developed to explain the EMC effect within a restricted range of Q^2, namely the region $2 \leq Q^2 < 200$ GeV^2, where the EMC effect has so far been experimentally explored. To account for the EMC effect at higher Q^2, it is necessary to consider the evolution equation in Q^2 for nuclear PDFs. This will be done in the following section.

2.6 Evolution of nuclear PDFs

In principle, the convolution formula Eq. (2.56) is valid at any Q^2 high enough that the impulse approximation can be applied. However, the bound nucleon PDFs are not known at high Q^2. Their form at low Q^2 can be parametrized using phenomenological models of the EMC effect in order to account for medium modification, but there is a limited amount

Plot of EMC ratio using the color screening model

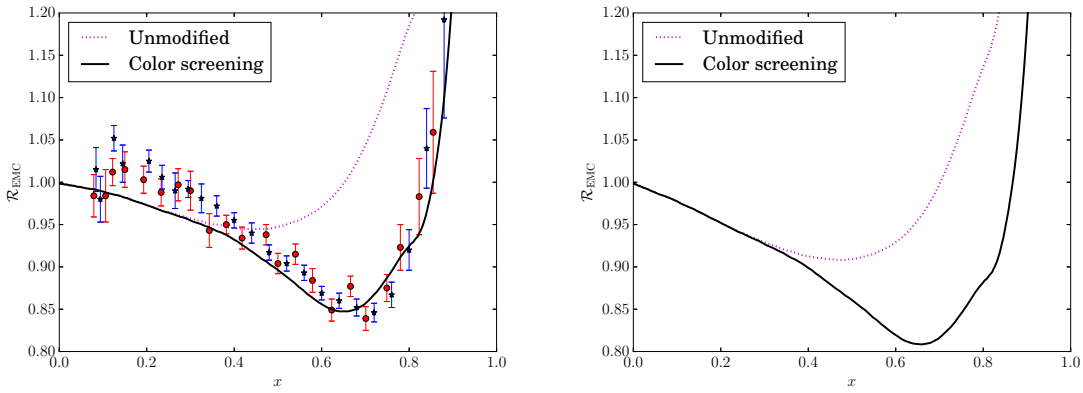

(a) EMC ratio for ^{56}Fe (b) EMC ratio for ^{208}Pb

Figure 2.14: The EMC ratio at $Q^2 = 10$ GeV^2, calculated using the Bodek-Ritche parametrization for the free nucleon PDF [46–48], with and without medium modifications accounted for by the color screening effect. 2N and 3N SRCs are accounted for in this calculation. Data are from SLAC experiments: Stars (blue) are from [4]; circles (red) are from [49].

of empirical data for the EMC effect at high Q^2. Experiments done at CERN in the 1980s measured the eA to ed cross section ratio at Q^2 up to 200 GeV^2, but with large errors on both Q^2 and the cross section ratio. At higher Q^2, such as those accessible at the LHC (going to 10^4 GeV^2 and beyond), the extent of medium modifications (as well as their x dependence) is unknown, and accordingly a simple application of the convolution formula is insufficient to find the nuclear PDF.

However, the nuclear PDFs at high Q^2 can be found from the low-Q^2 PDFs using DGLAP evolution [12–14]. In general, the DGLAP evolution equation describes the Q^2 dependence of a hadron's PDF through an integro-differential equation of the form

$$\frac{\partial f_{i/h}(x,Q^2)}{\partial \log(Q^2)} = \frac{\alpha(Q^2)}{2\pi} \sum_j \int_x^1 \frac{dy}{y} P_{ij}\left(\frac{x}{y}\right) f_{j/h}(y,Q^2). \tag{2.138}$$

Conceptually, the equation has the following interpretation: as one increases the momentum resolution scale with which the hadron is probed, one looks "inside" partons; the low-Q^2 partons are in a sense composite objects that are made up of high-Q^2 partons, and by increasing the resolution scale one sees deeper into the structure of the hadron and is able

to see more partons[5]. Conversely, a parton of flavor i that is seen at high Q^2 has some probability of having been found inside a low-Q^2 parton of flavor j, with the *splitting function* $P_{ij}(z)$ characterizing this probability.

The DGLAP evolution formula of Eq. (2.138) needs to be modified slightly for nuclei, since x now ranges up to A instead of 1. A simple guess would be that the upper limit of the integral should be A instead of 1, but this can be shown rigorously. Eq. (2.138) applies for the true momentum fraction $\frac{x_A}{A}$, and substituting this for x in Eq. (2.138) gives

$$\frac{\partial f_{i/A}(x_A, Q^2)}{\partial \log(Q^2)} = \frac{\alpha(Q^2)}{2\pi} \sum_j \int_{x_A/A}^1 \frac{dy}{y} P_{ij}\left(\frac{x_A}{Ay}\right) f_{j/A}(Ay, Q^2),$$

where the functional dependence of the nuclear PDF on its argument is scaled by A since the nuclear PDF conventionally takes A times the (true) momentum fraction as its argument. Defining $y_A = Ay$, one then has

$$\frac{\partial f_{i/A}(x_A, Q^2)}{\partial \log(Q^2)} = \frac{\alpha(Q^2)}{2\pi} \sum_j \int_{x_A}^A \frac{dy_A}{y_A} P_{ij}\left(\frac{x_A}{y_A}\right) f_{j/A}(y_A, Q^2). \tag{2.139}$$

Since this section concerns nuclear PDFs in particular, the subscript A will henceforth be omitted and it shall be understood that x and y are scaled momentum fractions.

For the sake of practical computations, it is often convenient to convert Eq. (2.139) with a change of variables. One uses $z = \frac{x}{y}$, in terms of which

$$\frac{\partial f_{i/A}(x, Q^2)}{\partial \log(Q^2)} = \frac{\alpha(Q^2)}{2\pi} \sum_j \int_{x/A}^1 \frac{dz}{z} P_{ij}(z) f_{j/A}\left(\frac{z}{x}, Q^2\right). \tag{2.140}$$

The convenience of this formulation comes from the fact that the splitting functions $P_{ij}(z)$ are actually distributions, and are defined in terms of how an integral of $P_{ij}(z)$ times a test function is evaluated. This will be described in depth in the next section.

[5] This interpretation is consistent with the modern view of the renormalization group, in which a quantum field theory at low momentum resolution scales is an effective field theory which integrates out unknown degrees of freedom [73].

2.6.1 Leading order splitting functions

At leading order, the splitting functions $P_{ij}(z)$ were found by several authors [12–14] to be (with $i, j \neq 0$):

$$P_{ij}(z) \equiv \delta_{ij} P_{qq}(z) = C_F \left[\frac{1+z^2}{(1-z)_+} + \frac{3}{2}\delta^{(1)}(1-z) \right] \tag{2.141}$$

$$P_{i0}(z) \equiv P_{qG}(z) = T_R \left[z^2 + (1-z)^2 \right] \tag{2.142}$$

$$P_{0j}(z) \equiv P_{Gq}(z) = C_F \left[\frac{1+(1-z)^2}{z} \right] \tag{2.143}$$

$$\begin{aligned} P_{00}(z) \equiv P_{GG}(z) = 2C_A &\left[\frac{z}{(1-z)_+} + \frac{1-z}{z} + z(1-z) \right] \\ &+ \left(\frac{11C_A - 4T_R N_f}{6} \right) \delta^{(1)}(1-z). \end{aligned} \tag{2.144}$$

Here, $C_F = \frac{N_c^2-1}{2N_c} = \frac{4}{3}$, $C_A = N_c = 3$, and $T_R = \frac{1}{2}$ are Casimir invariants of QCD. The quantity N_f denotes the number of active quark flavors. In particular, the splitting functions given above were derived in a massless quark approximation: the quark that is struck by a hard probe, as well as a parent quark which split into the probed quark, is assumed to be massless in comparison to the hard interaction scale Q^2. Quarks for which $m_q^2 > Q^2$ are "switched off," and are considered inactive. Essentially, N_f is the number of quark flavors for which Q^2 is greater than the quark mass squared. In this scheme, quarks may be "switched on" if Q^2 passes the square of the quark mass, so care must be taken in how this is dealt with; a quark mass prescription will be described in Sec. 2.6.2.

There are two distributions in the definitions of the splitting functions: the first is the familiar Dirac delta distribution, and the other is the "plus" distribution $\frac{1}{(1-z)_+}$ which was defined by Altarelli and Parisi as follows [14]: let $f(z)$ be a test function for which $(1-z)^{-1}\left(f(z) - f(1)\right)$ is integrable over the domain $[0,1]$. Then one defines:

$$\int_0^1 \frac{f(z)dz}{(1-z)_+} = \int_0^1 \frac{f(z) - f(1)}{1-z} dz. \tag{2.145}$$

Note that the lower integration limit in this definition is 0, while the lower integration limit in the DGLAP equation (2.140) is x/A. However, the definition of Eq. (2.145) is sufficient

to prescribe how the plus distribution times a test function will integrate with any lower limit. In particular, notice that

$$\begin{aligned}\int_x^1 \frac{f(z)dz}{(1-z)_+} &= \int_0^1 \frac{f(z)\Theta(z-x)dz}{(1-z)_+} = \int_0^1 \frac{f(z)\Theta(z-x) - f(1)\Theta(1-x)}{1-z}dz \\ &= \int_x^1 \frac{f(z)-f(1)}{1-z} - \int_0^x \frac{f(1)dz}{1-z} \\ \int_x^1 \frac{f(z)dz}{(1-z)_+} &= \int_x^1 \frac{f(z)-f(1)}{1-z} + f(1)\log(1-x). \end{aligned} \tag{2.146}$$

For a lower integration limit of $\frac{x}{A}$, one needs to substitute $x \mapsto \frac{x}{A}$ here, including in the logarithm.

2.6.2 Heavy quark scheme

Most of the formulas used in perturbative QCD, including the splitting functions $P_{ij}(z)$ in the DGLAP evolution equation, and the dependence of the running coupling strenth $\alpha(Q^2)$ on Q^2, are calculated in a massless quark approximation. In this approximation, the quarks that participate in a reaction are assumed to be massless, which is justified by the hard momentum transfer scaled Q^2 being much greater than m_q^2. This is always justified for the lightest three quarks, since the domain at which pQCD can be applied always involves Q^2 much greater than the squares of the up, down, and strange quark masses. However, pQCD can be applied (including in the present work) at Q^2 as low as a few GeV^2. The mass of the next-heaviest quark, the charm quark, is 1.29 GeV [3], meaning charm cannot always be treated as massless.

Additionally, when $m_q^2 \gg Q^2$, the momentum transfer is insufficient to create a heavy quark in the final state, and the (renormalized) heavy quark loop diagrams which contribute to the running of $\alpha(Q^2)$ are suppressed by powers of $\frac{m_q^2}{Q^2}$. Accordingly, quarks that are heavy compared to Q^2 are considered to be "inactive," and their small contributions to the running of the coupling strength and to DGLAP evolution, are neglected.

The regime where m_q^2 is comparable to Q^2 is in principle more complicated, but to a fair approximation, one can apply a scheme where the massless quark approximation is

used at all Q^2, but each quark flavor f is "switched on" when Q^2 reaches some threshold value Q_f^2. The condition that $\alpha(Q^2)$ be continuous across the thresholds imposes, at leading order, that $Q_f^2 = m_f^2$ [10]. Accordingly, the scheme that shall be used in this work is that given by Collins and Tung [10] in which a quark flavor is considered inactive for $Q^2 < m_f^2$ and active for $Q^2 > m_f^2$. N_f is the number of active quarks so, *e.g.*, for $Q^2 < (1.29\text{ GeV})^2$, $N_f = 3$, while for $(1.29\text{ GeV})^2 < Q^2 < (4.5\text{ GeV})^2$ (the mass of the bottom quark in the $\overline{\text{MS}}$ scheme), $N_f = 4$.

The quark mass prescription of [10] also has the parameter Λ_{QCD} appearing in the expression for the running coupling strength $\alpha(Q^2)$ as a function of N_f. This is required by continuity of the coupling strength across the heavy quark thresholds. The values given by the 2014 Particle Data Group [3] are:

$$\begin{aligned}
\Lambda_{\text{QCD}}^{(N_f=6)} &= (90.6 \pm 3.4)\text{ MeV} \\
\Lambda_{\text{QCD}}^{(N_f=5)} &= (214 \pm 7)\text{ MeV} \\
\Lambda_{\text{QCD}}^{(N_f=4)} &= (297 \pm 8)\text{ MeV} \\
\Lambda_{\text{QCD}}^{(N_f=3)} &= (340 \pm 8)\text{ MeV}
\end{aligned}$$

in the $\overline{\text{MS}}$ renormalization scheme.

2.6.3 Next-to-leading order corrections

The next-to-leading order splitting functions have a considerably more complicated form than the leading order splitting functions. They were first derived in Refs. [74, 75], but can also be found in Chapter 4 of [76] and the appendix of [77]. Just as with the leading order splitting functions, there are contributions from delta and plus distributions that must be properly accounted for.

The most significant challenge posed by NLO splitting functions is computational. At next-to-leading order, the splitting functions $P_{q_i q_j}$ for $i \neq j$ are non-zero; it is, for instance, possible to find an s quark inside a d quark because, at NLO, a d quark can radiate a gluon

that splits into an $s\bar{s}$ pair. Thus, the integro-differential DGLAP equations become highly coupled.

It is, however, possible to decouple the DGLAP equations by using appropriate (singlet and non-singlet) mixtures of quarks and anti-quarks, thus significantly reducing computation time. In particular, I employed Eqs. (4.97,4.98,4.99) of Ref. [76] in my code, evolved the singlet and non-singlet mixtures according to the computational algorithm given in Sec. 2.6.4 below, and then inverted these equations to obtain the evolved "physical" nPDFs.

It will be shown in the following section that NLO evolution makes a negligible correction to LO evolution within the kinematic regime that this dissertation is concerned with. It is for this reason that NLO is not described in depth here. NLO calculations were performed in this work only to demonstrate their negligibility in the domain of interest.

2.6.4 Computational algorithm

A computational algorithm was written for applying the DGLAP equations (2.140) to parameterizations of nuclear PDFs. The algorithm essentially takes a collection of functions $f_{i/A}(x, Q^2_{\text{ini}})$ representing the nuclear PDFs (for a set of flavors i) as functions of x at a given Q^2 value, as well as the initial Q^2 value and the target Q^2 value to which the PDFs should be evolved. The algorithm returns a collection of new functions $f_{i/A}(x, Q^2_{\text{fin}})$ of x at the final Q^2 value. The user may decide whether evolution is to be done at leading order or next-to-leading order.

The algorithm works as follows: first, an array of $(N+1)$ discrete x values $\{x_n | n = 0, \ldots, N\}$ is created, and a grid of PDFs defined at these discrete x values is constructed. The limiting values are chosen as $x_0 = x_{\text{min}}$ (which is a parameter that can be chosen by the user, but is set to 10^{-5} by default) and $x_N = A$. From the PDF grid, arrays for the singlet and non-singlet linear combinations of PDFs described in Sec. 2.6.3 are constructed, since their evolution can be performed much faster than for the "physical" PDFs.

The DGLAP equations (2.140) are then discretized. Special care must be taken when discretizing the splitting functions, since they are distributions. In general, a splitting function is a sum of three terms: an ordinary function, a Dirac delta distribution, and a

"plus" distribution:

$$P(z) = P_N(z) + P_\delta \delta^{(1)}(1-z) + \frac{P_+(z)}{(1-z)_+}. \tag{2.147}$$

Since the distributions are defined by how they integrate when multiplied by a test function, one should write out:

$$\begin{aligned}\int_{x/A}^1 \frac{dz}{z} P(z) f\left(\frac{x}{z}, Q^2\right) = &\int_{x/A}^1 \frac{dz}{z} P_N(z) f\left(\frac{x}{z}, Q^2\right) + P_\delta f(x, Q^2) \\ &+ \int_{x/A}^1 \frac{\frac{1}{z} P_+(z) f\left(\frac{x}{z}, Q^2\right) - P_+(1) f(x, Q^2)}{1-z} dz \\ &+ P_+(1) f(x, Q^2) \log\left(1 - \frac{x}{A}\right).\end{aligned} \tag{2.148}$$

Several of these terms can be directly evaluated, while the others require numerical integration. In particular, the grid of z values over which the integration is done is chosen to be identical to the x integration values, and a trapezoidal integration algorithm is applied, so, for instance,

$$\begin{aligned}\int_{x/A}^1 \frac{dz}{z} P_N(z) f\left(\frac{x}{z}, Q^2\right) \approx \frac{1}{2} \sum_{n=1}^{N} \Bigg[&\frac{P_N(z_n)}{z_n} f\left(\frac{x}{z_n}, Q^2\right) \\ &+ \frac{P_N(z_{n-1})}{z_{n-1}} f\left(\frac{x}{z_{n-1}}, Q^2\right) \Bigg] (z_n - z_{n-1}).\end{aligned} \tag{2.149}$$

While trapezoidal integration may seem crude, it was shown by Miyama and Kumano [77] that with a strategically-chosen mesh of x values based on the known functional behavior of the PDFs, trapezoidal integration produces an excellent approximation. The scheme chosen by Miyama and Kumano was to space x values logarithmically, in light of the well-known $f(x) \sim \frac{1}{x}$ behavior of the PDFs at small x. While the $\frac{1}{x}$ asymptotic form works well for $x \lesssim 0.1$, it does not describe the behavior of PDFs at larger x. Accordingly, the mesh of discrete x values used in the computational algorithm of the present work is different.

x mesh and interpolation algorithm

To construct the mesh of discrete x values used in numerically solving the DGLAP equations, the domain $[x_{\min}, A]$ (or $[x_{\min}, j]$ if only contributions of up to j-nucleon SRCs to the nPDF are considered) was partitioned into three regions. Based on the different approximate functional behavior of PDFs in these regions, the x values were spaced so that the PDF would be evaluated more frequently in regions where it undergoes the most rapid change. Firstly, in the region $x_{\min} < x < 0.1$, the discrete x values chosen to be in the x array were spaced logarithmically, with a greater density of x values closer to $x_{\min}$, in light of the $\frac{1}{x}$ asymptotic form at low x. Secondly, in the region $0.1 < x < 0.8$, since the PDF does not vary rapidly, x values were spaced uniformly. Lastly, in the region $0.8 < x < A$, since the PDF changes more rapidly at larger x (with an asymptotic form of $(A-x)^p$ for some power p), the discrete x values chosen for the x array were spaced logarithmically, with greater density towards $x = A$.

In formulas, the points making up the x mesh are chosen as follows:

$$x_n = x_{\min}\left(\frac{X_1}{x_{\min}}\right)^{n/\lfloor N/3\rfloor} \quad : \quad 0 \le n \le \lfloor N/3\rfloor \tag{2.150}$$

$$x_n = (X_2 - X_1)\frac{n - \lfloor N/3\rfloor}{2\lfloor N/3\rfloor} + X_1 \quad : \quad \lfloor N/3\rfloor \le n \le 2\lfloor N/3\rfloor \tag{2.151}$$

$$x_n = A + X_2 - X_2\left(\frac{A}{X_2}\right)^{(N-2\lfloor N/3\rfloor - n)/(N-2\lfloor N/3\rfloor)} \quad : \quad 2\lfloor N/3\rfloor \le n \le N \tag{2.152}$$

where $X_1 = 0.1$ and $X_2 = 0.8$ define the boundaries of the partitions, and where $\lfloor N/3\rfloor$ is the floor function of $N/3$, *i.e.*, the largest integer that is less than or equal to $N/3$.

In addition to the placement of discrete x values on the x mesh, the approximate asymptotic forms of the PDFs are used for defining an interpolation of $f_{j/A}(x, Q^2)$. This is a necessary ingredient for the computational algorithm, as the $\frac{x}{z_n}$ which the PDF takes as an argument in Eq. (2.149) will not in general lie on the mesh. In the following, suppose $x_a < x < x_b$, with x_a and x_b being neighboring points in the x mesh.

In the $x < 0.1$ region, the approximate asymptotic form is $f(x) \sim \frac{C}{x}$. However, with such an approximation, one has $x_b f(x_b) - x_a f(x_a) \approx 0$, and $xf(x)$ is known not to be

constant for actual PDFs. Instead, $xf(x)$ appears to be a slowly-varying function of $\log(x)$, as can be seen in PDF parameterizations for the proton extracted from experimental data. Accordingly, $xf(x)$ is interpolated as a function that is approximately linear in $\log(x)$, making the interpolation formula in the $x < 0.1$ region:

$$xf(x) = x_a f(x_a) \frac{\log(x/x_b)}{\log(x_a/x_b)} + x_b f(x_b) \frac{\log(x/x_a)}{\log(x_b/x_a)}. \tag{2.153}$$

In the $0.1 < x < 0.8$ region, linear interpolation is used, since the PDF does not vary greatly:

$$f(x) = \left(\frac{x - x_b}{x_a - x_b}\right) f(x_a) + \left(\frac{x - x_a}{x_b - x_a}\right) f(x_b). \tag{2.154}$$

Lastly, in the $0.8 < x$ region, the interpolation used is based on the $f(x) \sim (A - x)^p$ asymtptotic form. One has

$$\log(f(x_b)) - \log(f(x_a)) = \log\left(1 - \frac{x_b}{A}\right) - \log\left(1 - \frac{x_a}{A}\right) \approx -\frac{1}{A}(x_b - x_a),$$

i.e., the logarithm of the PDF is approximately linear in the $x \sim A$ region. Accordingly, geometric interpolation is used for $0.8 < x$:

$$\log(f(x)) = \left(\frac{x - x_b}{x_a - x_b}\right) \log(f(x_a)) + \left(\frac{x - x_a}{x_b - x_a}\right) \log(f(x_b)). \tag{2.155}$$

Evolving Q^2

The discretization of the integral in Eq. (2.140) has been described above; all that remains is to discuss the discretization of the derivative with respect to $\log(Q^2)$. While sophisticated schemes for numerically approximating the solutions of differential equations, such as the fourth-order Runge-Kutta method, are well-known, one can also apply the "crude" approximation

$$\frac{\partial f(x, Q^2)}{\partial \log(Q^2)} \approx \frac{f(x, Q_b^2) - f(x, Q_a^2)}{\log(Q_b^2) - \log(Q_a^2)}, \tag{2.156}$$

given $Q_b^2/Q_a^2 \approx 1$. If the given condition holds, then the full discretization of the DGLAP formula of Eq. (2.140) is

$$
\begin{aligned}
f_{i/A}(x_n, Q_b^2) = f_{i/A}(x_n, Q_a^2) + \frac{\alpha(Q_a^2)}{2\pi} \sum_j \Bigg\{ & P_{ij}^{(\delta)} f_{j/A}(x_n, Q^2) \\
& + P_{ij}^{(+)}(1) f_{j/A}(x_n, Q^2) \log\left(1 - \frac{x_n}{A}\right) \\
& + \frac{(z_l - z_{l-1})}{2} \sum_{l=n}^{N} \left[\frac{P_{ij}^{(N)}(z_l)}{z_l} f_{j/A}^{(\text{inter.})}\left(\frac{x_n}{z_l}, Q_a^2\right) + \frac{P_{ij}^{(N)}(z_{l-1})}{z_{l-1}} f_{j/A}^{(\text{inter.})}\left(\frac{x_n}{z_{l-1}}, Q_a^2\right) \right] \\
& + \frac{1}{2} \sum_{l=n}^{N} \Bigg(\frac{z_l - z_{l-1}}{1 - z_l} \left[\frac{P_{ij}^{(+)}(z_l)}{z_l} f_{j/A}^{(\text{inter.})}\left(\frac{x_n}{z_l}, Q_a^2\right) - P_{ij}^{(+)}(1) f_{j/A}\left(x_n, Q_a^2\right) \right] \\
& + \frac{z_l - z_{l-1}}{1 - z_{l-1}} \left[\frac{P_{ij}^{(+)}(z_{l-1})}{z_{l-1}} f_{j/A}^{(\text{inter.})}\left(\frac{x_n}{z_{l-1}}, Q_a^2\right) - P_{ij}^{(+)}(1) f_{j/A}\left(x_n, Q_a^2\right) \right] \Bigg) \Bigg\},
\end{aligned}
\tag{2.157}
$$

where the superscript (inter.) signifies that the interpolation scheme described in Sec. 2.6.4 should be used to find the value of the PDF at *e.g.* $\frac{x_n}{z_l}$. As written, Eq. (2.157) can be used to numerically evolve a PDF over a small Q^2 range.

For a $Q_{\text{fin}}^2 \gg Q_{\text{ini}}^2$, one should partition the domain of Q^2 values between the initial and final values into a mesh $\{Q_0^2, Q_1^2, \ldots, Q_M^2\}$ for which $Q_0^2 = Q_{\text{ini}}^2$ and $Q_M^2 = Q_{\text{fin}}^2$, and for which $Q_{m+1}^2/Q_m^2 \sim 1$ for all m. Then, evolution from Q_m^2 to Q_{m+1}^2 can be numerically performed using Eq. (2.157), and one can evolve a PDF from Q_{ini}^2 to Q_{fin}^2 by applying Eq. (2.157) M times, once for each interval in the Q^2 mesh.

Convergence of evolution for mesh sizes

The computational algorithm for numerically solving the DGLAP equation Eq. (2.140) through the discretization Eq. (2.157) has been fully described What remains is to choose the sizes of the x and Q^2 arrays in order to both optimize computation time and to produce accurate results.

The DGLAP equation was numerically solved for different values of two parameters: N, the number of intervals on the x mesh; and Q_{m+1}^2/Q_m^2, the geometric spacing between subsequent points in the Q^2 mesh. The discretized DGLAP equation (2.157) was

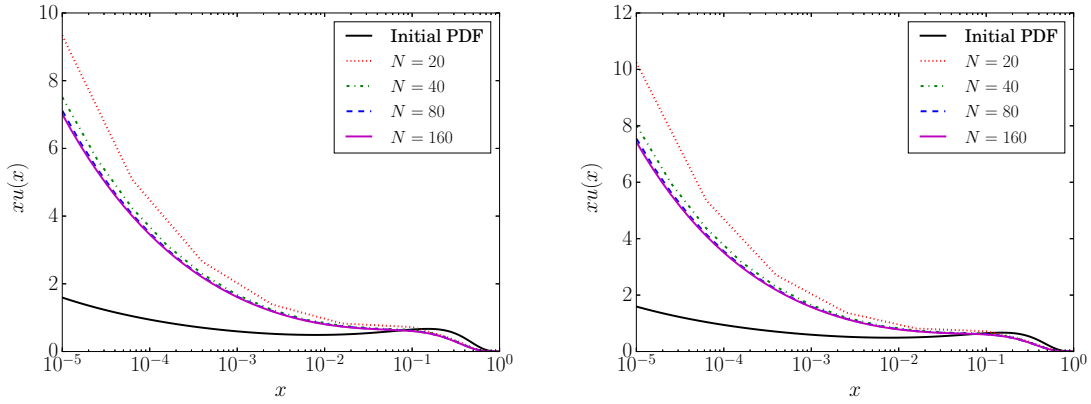

(a) $Q^2_{m+1}/Q^2_m = 5$ (b) $Q^2_{m+1}/Q^2_m = 2$

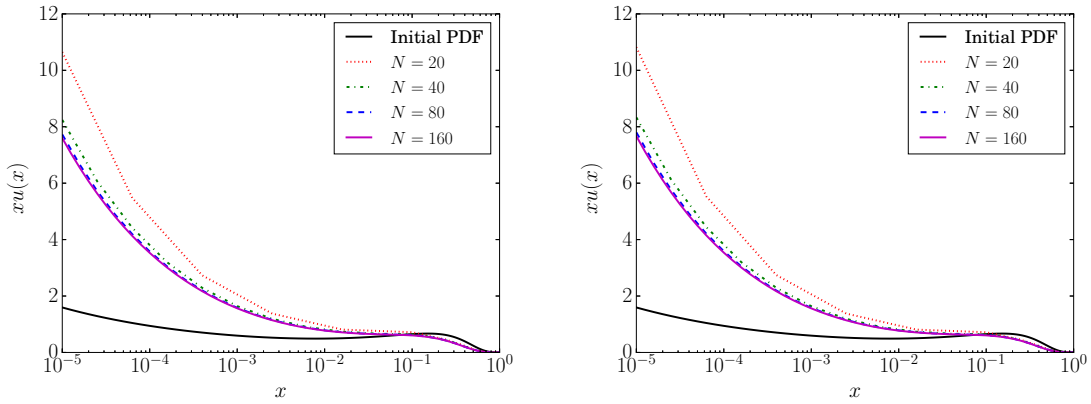

(c) $Q^2_{m+1}/Q^2_m = 1.4$ (d) $Q^2_{m+1}/Q^2_m = 1.2$

Figure 2.15: Comparison of evolution for different x mesh sizes for a given Q^2_{m+1}/Q^2_m. Initial Q^2 is 10 GeV^2, and final is 10^4 GeV^2. Evolution is NLO.

numerically evaluated by evolving the CT10 parametrization of the proton PDF [78] from $Q^2_{\text{ini}} = 10$ GeV^2 to $Q^2_{\text{fin}} = 10^4$ GeV^2 at next-to-leading order, using four different values of both N and Q^2_{m+1}/Q^2_m. The N values used were 20, 40, 80, and 160. The Q^2_{m+1}/Q^2_m values used were 5, 2, 1.4, and 1.2.

In Fig. 2.15, the results of numerical evolution of the proton PDF for different values of N at fixed Q^2_{m+1}/Q^2_m can be seen. It can be observed in this figure that the accuracy of the fit saturates around $N = 160$, so an x mesh with 160 intervals is sufficient for accurate solution of the DGLAP equation. In Fig. 2.16, the results of numerically evolving the proton PDF at different Q^2_{m+1}/Q^2_m values and a fixed N can be seen, and it can be observed that

Plot of evolution computation with different $\log(Q^2)$ step sizes

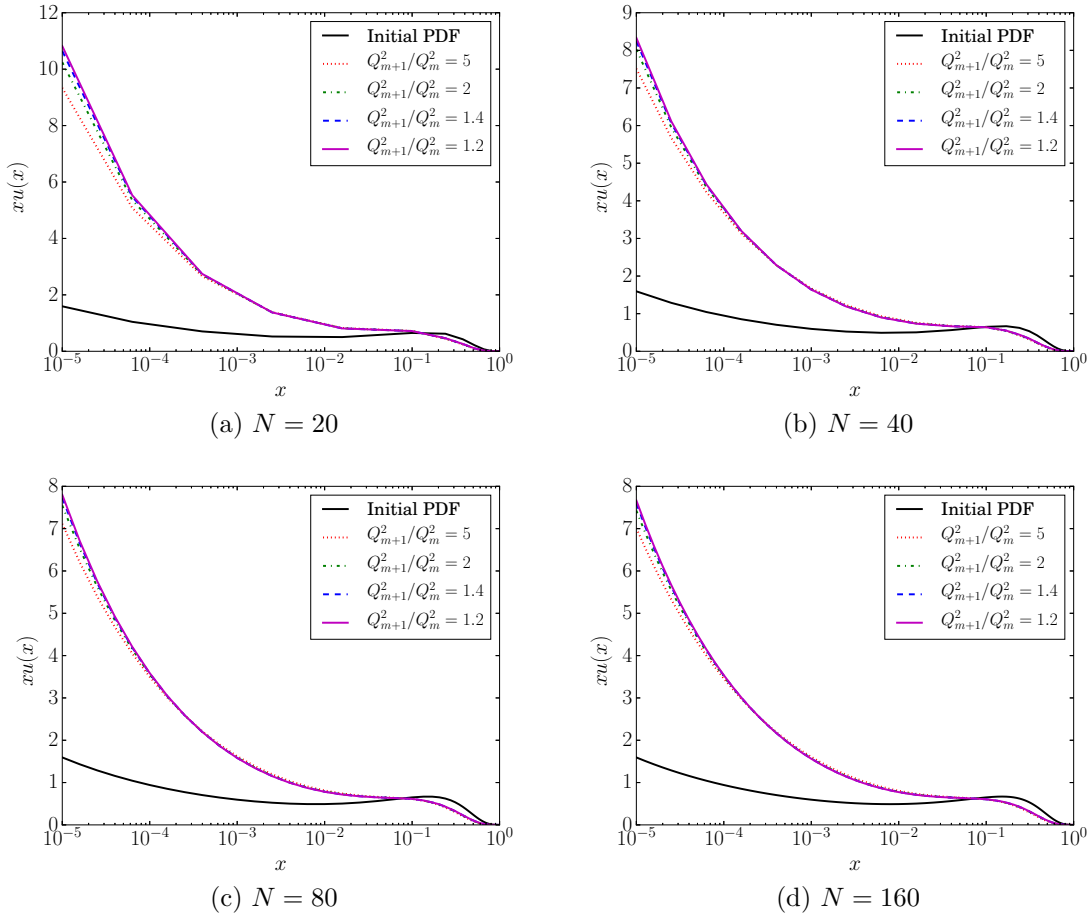

(a) $N = 20$ (b) $N = 40$

(c) $N = 80$ (d) $N = 160$

Figure 2.16: Comparison of evolution for different Q^2_{m+1}/Q^2_m values with a fixed x mesh size. Initial Q^2 is 10 GeV^2, and final is 10^4 GeV^2. Evolution is NLO.

the results converge for $Q^2_{m+1}/Q^2_m \approx 1.2$, which is a sufficiently small geometric spacing between discrete Q^2 values. Accordingly, the values $N = 160$ and $Q^2_{m+1}/Q^2_m = 1.2$ are used in the remainder of this dissertation for the evolution of nuclear PDFs.

2.6.5 Results of evolving nuclear PDFs

The nuclear PDFs obtained *via* the convolution formula (2.56) are obtained at $Q^2 = 10$ GeV^2. Now that the numerical DGLAP evolution algorithm has been developed, it can be used to evolve these nuclear PDFs to the higher Q^2 characteristic of high-energy experiments such as those at the EIC and LHC.

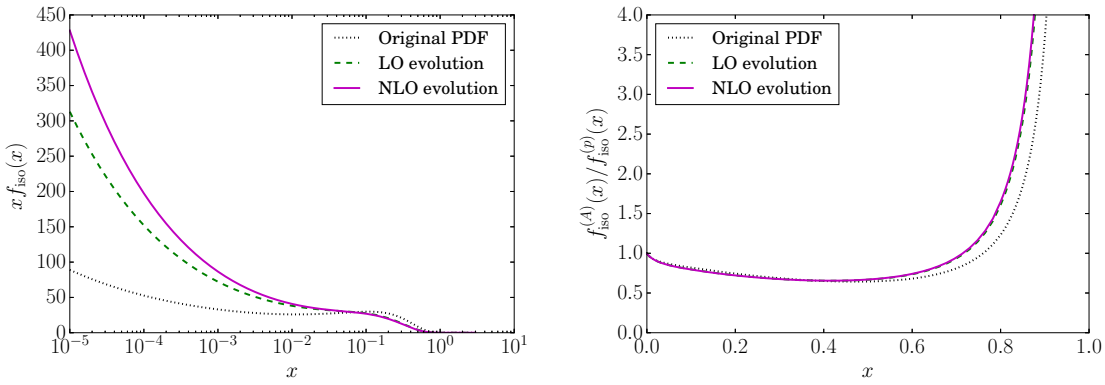

Figure 2.17: Comparison of LO and NLO evolution of nuclear PDFs for ^{56}Fe. $f_{\rm iso} = \frac{Z}{A}u(x) + \frac{A-Z}{A}d(x)$. $Q^2_{\rm ini} = 10$ GeV^2 and $Q^2_{\rm fin} = 10^4$ GeV^2. 2N and 3N SRCs are taken into account, and medium modifications are not.

Firstly, it should be emphasized that the scope of this dissertation is focused on moderate to large Bjorken x values, namely $x_A > 0.2$ where the dominant effects are medium modification and nucleonic motion. Because of this, leading order splitting functions are sufficient; next-to-leading order corrections are mainly significant at $x \lesssim 0.01$. The relative significance of NLO corrections to DGLAP evolution are shown for unmodified nuclear PDFs in Fig. 2.17. It can be seen that the leading order is sufficient in the x_A range of interest.

The evolution of medium modifications was also studied. The approach taken here is to define a ratio of the medium-modified nuclear PDF to the unmodified nuclear PDF, *viz.*

$$R_{i/A}^{(\rm mod.)}(x,Q^2) = \frac{f_{i/A}^{(\rm mod.)}(x,Q^2)}{f_{i/A}^{(\rm unmod.)}(x,Q^2)}. \tag{2.158}$$

In Fig. 2.18, this ratio is plotted for two values of Q^2. The difference in these curves demonstrates the extent to which medium modifications themselves evolve. If medium modifications did not evolve, then the convolution formula (2.56) could be applied with the same medium modification model at any Q^2, together with an empirical parametrization of the free nucleon PDF obtained at this Q^2. Since the ratio $R_{i/A}^{(\rm mod.)}(x,Q^2)$ does change with

Plot of evolution of medium modifications

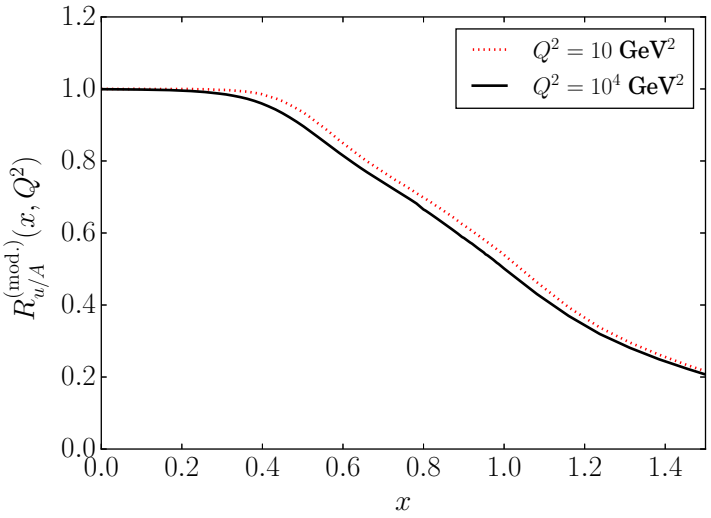

Figure 2.18: $R_{u/A}^{(\mathrm{mod.})}(x, Q^2)$ for ^{56}Fe, at two values of Q^2.

Q^2, we instead to apply DGLAP evolution to obtain high-Q^2 nuclear PDFs. It should be noted, however, that the evolution of medium modifications is a small effect. Nonetheless, for the sake of completeness, evolution will be used to connect the low-Q^2 region (where the form of the EMC effect is well-known) and the high-Q^2 region.

Evolution trajectories

DGLAP evolution describes how high-Q^2 partons are found within low-Q^2 partons. As one increases the momentum resolution scale with which a hadron is probed, the higher-Q^2 parent parton radiates away part of its forward momentum, so in general the evolved PDF is greater in the low-x and smaller in the high-x region, as can be seen for instance in Figs. 2.15, 2.16, and 2.17.

The fact that high-x partons migrate to the lower-x region with evolution has potential significance for high-Q^2 experiments. The empirically unconstrained high-x region can affect the evolution of PDFs in the moderate-to-low-x region. A high-x parton at *e.g.* $Q^2 \sim 10$ GeV^2 can become a moderate- or low-x parton at *e.g.* $Q^2 \sim 10^4$ GeV^2.

Conversely, at moderate- or low-x parton at $Q^2 \sim 10^4$ GeV^2 may have originated from a higher-x parton at $Q^2 \sim 10$ GeV^2. Evolution trajectories [72] quantitatively describe such a possibility. An evolution trajectory is a path through x-Q^2 parameter space that describes how much of a high-Q^2 PDF at low x originated from the evolution of higher-x, lower-Q^2 partons, as opposed to having primordially been present. It is defined first by choosing an initial high x_0 and low Q_0^2 at which the trajectory starts, and a cut-off PDF $\tilde{f}_{i/A}(x, Q^2; x_0, Q_0^2)$ given at $Q^2 = Q_0^2$ by

$$\tilde{f}_{i/A}(x, Q_0^2; x_0, Q_0^2) = f_{i/A}(x, Q_0^2)\Theta(x - x_0), \tag{2.159}$$

i.e., by cutting off the PDF at $x < x_0$. For $Q^2 > Q_0^2$, one obtains $\tilde{f}_{i/A}(x, Q^2; x_0, Q_0^2)$ by applying DGLAP evolution. While the cut-off PDF is initially zero at $x < x_0$, it will be non-zero at these low x after evolution, since the $x > x_0$ partons radiate away forward momentum when they evolve. Conversely, any partons with $x < x_0$ in the evolved cut-off PDF came entirely from evolution. With the cut-off PDF defined as in Eq. (2.159), one then defines a point $x' < x_0$, $Q^{2\prime} > Q_0^2$ as being on the evolution trajectory if

$$\tilde{f}_{i/A}(x', Q^{2\prime}; x_0, Q_0^2) = \frac{1}{2} f_{i/A}(x', Q^{2\prime}),$$

i.e., a point in x-Q^2 space is on the evolution trajectory when exactly half of the PDF at that point comes from evolution. Evolution trajectories, defined as such, allow one to determine how significant the contributions of higher-x partons are to the evolution of PDFs at lower x, and accordingly to determine whether precise knowledge of the high-x region of PDFs is necessary to predict the moderate- or low-x form of PDFs in different experimental scenarios.

Evolution trajectories were plotted in Fig. 2.19 to determine the importance of the high-x region of nuclear PDFs—especially the $x > 1$ region—to the form of PDFs at low and moderate x values. As can be seen, in the low-x region, a significant portion of the

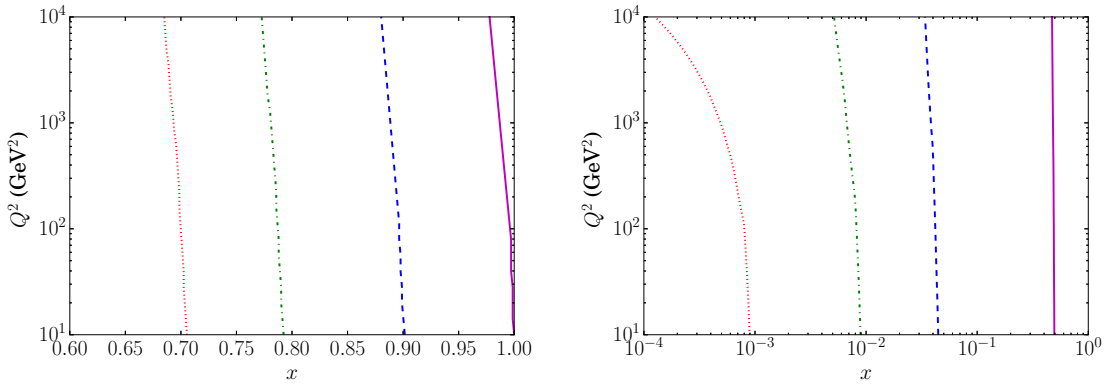

(a) (b)

Figure 2.19: Evolution trajectories for ^{56}Fe. 2N and 3N SRCs are taken into account, and medium modifications are not. Evolution is leading order.

PDFs are due to evolution[6], but in the moderate- and high-x regions, most of the partons are "primordially" present, rather than being due to the radiation of higher-x partons. The evolution trajectory which starts at $x_0 = 1$ and $Q_0^2 = 10$ GeV^2 does not even reach $x' = 0.9$ by the time $Q^{2\prime} = 10^4$ GeV^2. Accordingly, precise knowledge of the $x > 1$ region of nuclear PDFs is not necessary to describe the moderate-x region at high Q^2.

2.6.6 Summary

In this section, the evolution of nuclear PDFs obtained at low $Q^2 \sim 10$ GeV^2 was described. The necessity of applying DGLAP evolution to determine the high-Q^2 nuclear PDFs, rather than using a convolution approach directly, was demonstrated. A computational algorithm for numerically solving the DGLAP equations was elucidated, and the results of applying this algorithm to nuclear PDFs containing short range correlations and medium modifications were given. With high-Q^2 nuclear PDFs now obtained, they can be used to describe high-energy scattering reactions, as will be described in the following section.

[6] In fact, since the evolution was performed at leading order, at for $x \lesssim 0.01$ NLO contributions are significant, the trajectories will be more extreme in this region with NLO corrections.

2.7 Dijet production in proton-nucleus collisions

The majority of experiments probing the existence and properties of multi-nucleon short range correlations (SRCs), as well as medium modification *via* the EMC effect, occur at low Q^2 where quasi-elastic contributions are significant. At $x > 1$ especially, where the cross section is due almost entirely SRCs, quasi-elastic contributions at low Q^2 completely dominate over inelastic contributions that would allow the nuclear parton distribution functions (nPDFs) to be directly probed. It is possible to study nuclear PDFs at low Q^2 by using a model of quasi-elastic scattering and subtracting off the quasi-elastic contribution, but this procedure is highly model-dependent. Moreover, even when the inelastic cross section is obtained in this fashion, it will contain higher-twist and target mass effects which become significant at low Q^2. Target mass effects are theoretically well-understood within the context of the operator product expansion [79,80] but their framing in the quark-parton model is problematic, and the exact procedure is debated (see [80] for a review of such efforts). Higher-twist effects are less understood, and are often phenomenologically fit to data.

It would be a more ideal state of affairs to study SRCs and the EMC effect at large Q^2 where these concerns become negligible. Large Q^2 at $0.5 \leq x_A \leq 3$ in electron-scattering experiments is difficult to achieve, since

$$W^2 - M_A^2 = Q^2 \left(\frac{A}{x_A} - 1 \right), \tag{2.160}$$

meaning that a large center-of-mass energy needs to be achieved in order to probe such kinematics. For instance, to study $x_A \sim 1$ for ^{56}Fe at $Q^2 = 100$ GeV^2, one needs center-of-mass energies exceeding 240 GeV, which is not realistically achievable for an electron beam incident on a fixed target.

The most feasible way to attain high Q^2, and thus to probe the deep structure of nuclei and study nuclear PDFs, is to attain high center-of-mass energy, which can be accomplished using beam collision experiments. The proposed Electron Ion Collider (EIC) is one method of doing this. Another method, which can be accomplished using currently available devices,

is proton-nucleus collisions. This section of the dissertation is concerned with the second method. In particular, I demonstrate that nuclear PDFs can be studied using inclusive dijet production in proton-nucleus collisions, and investigate whether information about the EMC effect and SRCs can be extracted from this reaction. Special focus is given to p-^{208}Pb collisions at the kinematics of the Large Hadron Collider (LHC).

2.7.1 Formalism

The idea of using proton-nucleus collisions to study nuclear PDFs depends on an important theoretical assumption which has not been rigorously proven [81], but has nonetheless been found to be an invaluable guiding principle for hadronic collision experiments: namely, that the hadron-hadron cross section factorizes in terms of universal parton distribution functions, in the same way that deep inelastic scattering and Drell-Yan processes are known to factorize [81].

In particular, the factorization formula for a hadron-hadron collision (between two hadrons h_1 and h_2) is postulated to be [76]

$$\sigma_{h_1 h_2} = \sum_{ij} \int_0^{x_{h_1}^{\max}} dx_{h_1} \int_0^{x_{h_2}^{\max}} dx_{h_2} f_{i/h_1}(x_{h_1}, Q^2) f_{j/h_2}(x_{h_2}, Q^2) \hat{\sigma}_{ij}(\hat{s}, \hat{t}, \hat{u}; Q^2), \tag{2.161}$$

where i and j are flavors of partons within the hadrons, and $\hat{\sigma}_{ij}(\hat{s}, \hat{t}, \hat{u}; Q^2)$ is a hard partonic cross section (with $\hat{s}$ *etc.* being parton-level Mandelstam variables) that can be calculated using perturbative QCD. The Q^2 dependence of this cross section comes from the running of the QCD coupling strength $\alpha_{\mathrm{QCD}}(Q^2)$.

The dijet production reaction in particular can be stated as

$$p + A \to \text{dijet} + X, \tag{2.162}$$

where the kinematics of the two outgoing jets are fully determined. At the leading order (LO) in pQCD, the contributing QCD processes are two-parton to two-parton reactions of the form $ij \to kl$, where i, j, k, l are parton flavors. The specific reactions allowed and their

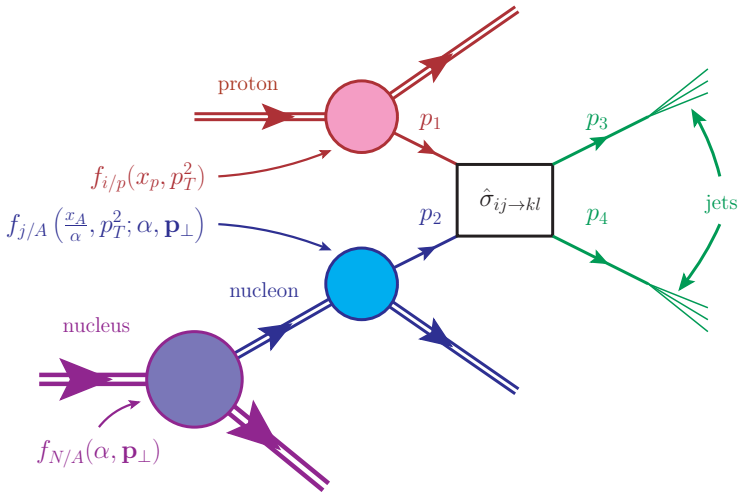

Figure 2.20: Diagram of $p + A \to \text{dijet} + X$ within the convolution formalism.

parton-level cross sections are given in Sec. 2.7.1. Since the subprocesses that contribute to the dijet cross section at LO are all two-body scattering reactions, it is possible to extract the light cone fractions x_p and x_A of the initial partons from measured jet kinematics, as will be shown in Sec. 2.7.1. Since this procedure depends on being able to treat the reaction as occurring through a two-body scattering subprocess, and this depends on the leading order approximation, the use of leading order is justified in Sec. 2.7.1.

Jet kinematics

The analysis is done in the collider rest frame, since this is the frame in which detector specifications such as resolution and acceptance are best known. The proton is considered to move in the $+z$ direction and the nucleus in the $-z$ direction. Both of these have energies far exceeding their masses, allowing their masses to be neglected; thus the only non-zero components of p_p and p_A are p_p^+ and p_A^-. The energy per proton for both initial hadrons is a fixed quantity E_0, which was given by $E_0 = 4$ TeV for the LHC prior to its shutdown, and will reach a maximum value of $E_0 = 7$ TeV in its current run. Accordingly, $p_p^+ = 2E_0$ and $p_A^- = 2ZE_0$. Computations are performed with both of these energy values.

The total center-of-mass energy squared is given by the Mandelstam variable $s_{pA} = p_p^+ p_A^-$, but results from proton-nucleus collision experiments are typically given in terms of the average center-of-mass energy per nucleon, $\sqrt{s_{NN}^{\text{avg.}}}$, where $s_{NN}^{\text{avg.}} = s_{pA}/A$. For a ^{208}Pb nucleus and $E_0 = 4$ TeV, $\sqrt{s_{NN}^{\text{avg.}}} \approx 5.02$ TeV, while for $E_0 = 7$ TeV with the same nucleus, $\sqrt{s_{NN}^{\text{avg.}}} \approx 8.8$ TeV. In what follows, formulas will be stated in terms of $\sqrt{s_{NN}^{\text{avg.}}}$ rather than E_0 or s_{pA}, since this is conventional. In particular, it should be noted that

$$p_p^+ = \sqrt{\frac{A}{Z} s_{NN}^{\text{avg.}}} \tag{2.163}$$

$$p_A^- = \sqrt{AZ s_{NN}^{\text{avg.}}}. \tag{2.164}$$

It should also be noted that while $\sqrt{s_{NN}^{\text{avg.}}}$ is a fixed quantity given E_0 and a particular nucleus, $\sqrt{s_{NN}}$ is variable since it depends on the momentum of whichever nucleon within the nucleus participates in the dijet production reaction.

At leading order, the pA collision results in an interaction between two partons, one each from the proton and the nucleus. Their respective four-momenta are labeled p_1 and p_2. Within the collinear framework, the partons have zero transverse momentum and are massless, and each move collinearly with their parent hadron, meaning

$$p_1 = \left(p_1^+, 0; \mathbf{0}\right) = \left(x_p p^+, 0; \mathbf{0}\right) \tag{2.165}$$

$$p_2 = \left(0, p_2^-; \mathbf{0}\right) = \left(0, \frac{x_A}{A} p_A^-; \mathbf{0}\right), \tag{2.166}$$

where the light cone momentum fractions are given by

$$x_p = \frac{p_1^+}{p_p^+} = \sqrt{\frac{Z}{A}} \frac{p_1^+}{\sqrt{s_{NN}^{\text{avg.}}}} \tag{2.167}$$

$$x_A = A \frac{p_2^-}{p_A^-} = \sqrt{\frac{A}{Z}} \frac{p_2^-}{\sqrt{s_{NN}^{\text{avg.}}}}. \tag{2.168}$$

x_A is given in terms of the "minus" component of the four-momenta involved rather than the plus component, since $p_A^+ = 0$ and p_A^- is large. Essentially, for the nucleus one should

interpret p_A^+ as the "energy" and p_A^- as the "forward momentum," which amounts to exchanging + and − components of all four-vectors in the light cone treatment of the nucleus. Accordingly, we define $\alpha = A\frac{p_N^-}{p_A^-}$ in this case.

The parton momentum fractions, besides kinematics of the initial state, depend on p_1^+ and p_2^-. These can both be obtained from four-momentum conservation. In particular, the two jets produced in the reaction (2.162) are generated at leading order by the fragmentation of the two final state partons, which are ascribed four-momenta p_3 and p_4. In particular, p_3 is the momentum of a jet in the central or proton-beam direction, while p_4 is the momentum of a jet in the nucleus-beam direction. Four-momentum conservation gives

$$p_1 + p_2 = p_3 + p_4 \tag{2.169}$$

$$p_1^+ = p_3^+ + p_4^+ \tag{2.170}$$

$$p_2^- = p_3^- + p_4^- . \tag{2.171}$$

What remains is to characterize $p_{3/4}^{\pm}$. Jet kinematics can be expressed in terms of two quantities: the the transverse momentum $\mathbf{p}_T$ of the jet, and the rapidity y, given by

$$y = \frac{1}{2}\log\left(\frac{p^+}{p^-}\right). \tag{2.172}$$

This relation can be inverted to give

$$\frac{p^+}{p^-} = e^{-2y}. \tag{2.173}$$

Given that the jet has a mass m, one has

$$p^+p^- - p_T^2 = m^2 \tag{2.174}$$

$$p^{\pm} = \frac{m^2 + p_T^2}{p^{\mp}}, \tag{2.175}$$

which can be used to eliminate either of $p^{\pm}$ from Eq. (2.173). Defining the transverse mass $m_T = \sqrt{m^2 + p_T^2}$, one has

$$p^{\pm} = m_T e^{\pm y}. \tag{2.176}$$

In practice, one typically has experimental access not to the rapidity y and transverse momentum p_T, but to the pseudo-rapidity η and transverse energy E_T, given by

$$\eta = -\log\tan(\theta/2) \tag{2.177}$$

$$E_T = E\sin\theta, \tag{2.178}$$

with θ being the angle between the beam direction and the jet, which is directly measured. Moreover, it is E_T rather than p_T which is measured by hadron calorimeters. However, in the limit that the jet mass goes to zero, we clearly have $E_T = p_T$, and

$$y = \frac{1}{2}\log\left(\frac{p+p_z}{p-p_z}\right) = \frac{1}{2}\log\left(\frac{1+\cos\theta}{1-\cos\theta}\right) = \log\left(\cot(\theta/2)\right) = \eta. \tag{2.179}$$

Since, at leading order, the jets in the considered reaction are generated by fragmenting partons, and the partons are massless, the jet masses can be taken to zero and the relations $E_T = p_T$ and $y = \eta$ can be used. Accordingly, $p^{\pm}$ can be given in terms of quantities directly measured in a collision experiment, namely the angle of the jet with respect to the beam, and the energy measured by a hadron calorimeter. The relation is

$$p^{\pm} = p_T e^{\pm\eta} = E_T\cot(\theta/2) = E\cos(\theta/2). \tag{2.180}$$

Quantities in what follows will be given in terms of p_T and η, since these are the conventional quantities in terms of which collider experiment results are given. Since the initial partons are collinear with the beams, $\mathbf{p}_{3\perp} = -\mathbf{p}_{4\perp} = \mathbf{p}_T$, so we have $p_{3/4}^{\pm} = p_T e^{\pm\eta_{3/4}}$, and thus

$$p_1^+ = p_T\left(e^{+\eta_3} + e^{+\eta_4}\right) \tag{2.181}$$

$$p_2^- = p_T\left(e^{-\eta_3} + e^{-\eta_4}\right). \tag{2.182}$$

Putting this result into Eqs. (2.167,2.168), we obtain

$$x_p = \sqrt{\frac{Z}{A}} \frac{p_T}{\sqrt{s_{NN}^{\text{avg.}}}} \left(e^{+\eta_3} + e^{+\eta_4}\right) \tag{2.183}$$

$$x_A = \sqrt{\frac{A}{Z}} \frac{p_T}{\sqrt{s_{NN}^{\text{avg.}}}} \left(e^{-\eta_3} + e^{-\eta_4}\right). \tag{2.184}$$

The primary objective here is to look at large x_A, either in the region $x_A \gtrsim 0.6$ or $x_A > 1$, so that the EMC effect or SRCs can respectively be studied at the high Q^2 characterizing LHC kinematics. Eq. (2.184) suggests three conditions be looked at for maximizing x_A:

1. Large p_T.
2. Small or negative η_3.
3. Small or negative η_4.

In order to distinguish the jets from their parent hadron of origin, and in order to allow for easier detection of one of the jets, the best configuration to look at involves one forward jet and one central jet, *i.e.* one jet should be confined to $|\eta| \leq 2.5$, and the other to $3 < |\eta| < 5$. We take η_3 to be the pseudo-rapidity of the central jet, and η_4 to be the forward jet. To satisfy the condition that both pseudo-rapidities be "small or negative," one should look for jets with $-5 < \eta_4 < -3$. This corresponds to a jet that is forward in the direction of the nucleus beam.

Another important kinematic quantity is the Q^2 of the reaction, which doubles as a factorization scale used in the PDFs, and the renormalization scale used in the running of the QCD coupling strength. The choice of Q^2 that minimizes NLO contributions is $-\hat{t}$, which is given by

$$-\hat{t} = -(p_1 - p_3)^2 = 2(p_1 \cdot p_3) = p_1^+ p_3^- = p_T^2 \left(1 + e^{-\eta_3 + \eta_4}\right) \approx p_T^2, \tag{2.185}$$

with the last step holding due to the highly negative value of η_4. (This approximation may be inadequate, on the other hand, for processes involving two central jets, or for two jets

that are collinear in the same direction.) Therefore, we take $Q^2 = p_T^2$ as the factorization and renormalization scales.

Dijet cross section

For reaction (2.162), the factorization formula of Eq. (2.161) becomes

$$\sigma_{pA} = \sum_{ijjk} \int_0^1 dx_p \int_0^A dx_A f_{i/p}(x_p, p_T^2) f_{j/A}(x_A, p_T^2) \hat{\sigma}_{ij\to jk}. \tag{2.186}$$

In terms of differential cross sections, this means leaving out the integration. The parton-level differential cross section is given by

$$\hat{\sigma}_{ij\to jk} = \frac{1}{4(p_1 \cdot p_2)} \frac{\overline{|\mathcal{M}_{ij\to kl}|^2}}{1+\delta_{kl}} (2\pi)^4 \delta^{(4)}(p_1 + p_2 - p_3 - p_4) \frac{d^3\mathbf{p}_3}{2E_3(2\pi)^3} \frac{d^3\mathbf{p}_4}{2E_4(2\pi)^3}, \tag{2.187}$$

where $\mathcal{M}_{ij\to kl}$ is the invariant Feynman amplitude for the $ij \to kl$ process, and the factor of $1+\delta_{kl}$ is a statistical factor to prevent double-counting when the two final-state partons are the same flavor.

The delta function in Eq. (2.187) can be rewritten

$$2\delta^{(1)}(p_1^+ - p_3^+ - p_4^+)\delta^{(1)}(p_2^- - p_3^- - p_4^-)\delta^{(2)}(\mathbf{p}_{3\perp} + \mathbf{p}_{4\perp}),$$

the transverse component of which can be integrated out using the $\mathbf{p}_{4\perp}$ integration. The remaining components are equal to

$$\frac{2A}{p_p^+ p_A^-} \delta^{(1)}\left(x_p - \frac{p_3^+ + p_4^+}{p_p^+}\right) \delta^{(1)}\left(x_A - A\frac{p_3^- + p_4^-}{p_A^-}\right).$$

These can be integrated out by the x_p and x_A integrations in Eq. (2.186), giving

$$\sigma_{pA} = \sum_{ijkl} \frac{1}{16\pi} \frac{2A}{p_p^+ p_A^-} \frac{1}{4(p_1 \cdot p_2)} f_{i/p}(x_p, p_T^2) f_{j/A}(x_A, p_T^2) \frac{\overline{|\mathcal{M}_{ij\to kl}|^2}}{1+\delta_{kl}} \frac{dp_{3z}}{E_3} \frac{dp_{4z}}{E_4} dp_T^2. \tag{2.188}$$

Next, one can use $d\eta = dp_z/E$ and $2(p_1 \cdot p_2) = \frac{x_p x_A}{A} p_p^+ p_A^-$ to obtain

$$\sigma_{pA} = \sum_{ijkl} \frac{1}{16\pi} \left(\frac{A}{p_p^+ p_A^-} \right) \frac{f_{i/p}(x_p, p_T^2)}{x_p} \frac{f_{j/A}(x_A, p_T^2)}{x_A} \frac{\overline{|\mathcal{M}_{ij\to kl}|^2}}{1+\delta_{kl}} \frac{dp_{3z}}{E_3} \frac{dp_{4z}}{E_4} dp_T^2, \tag{2.189}$$

and using the average center-of-mass energy per nucleon, $\sqrt{s_{NN}^{\text{avg.}}}$, we have

$$\frac{d^2\sigma}{d\eta_3 d\eta_4 dp_T^2} = \sum_{ijkl} \frac{1}{16\pi (s_{NN}^{\text{avg.}})^2} \frac{f_{i/p}(x_p, p_T^2)}{x_p} \frac{f_{j/A}(x_A, p_T^2)}{x_A} \frac{\overline{|\mathcal{M}_{ij\to kl}|^2}}{1+\delta_{kl}}. \tag{2.190}$$

Hard subprocesses and justification for LO

At leading order, an exhaustive list of partonic processes that can contribute to dijet production in hadron collisions, along with their squared Feynman amplitudes, is given by Combridge [82]. Each process involves partons of flavors i and j originating from the proton and the nucleus, respectively, and partons of flavors k and l that fragment into the observed jets. The partons can be either a quark, an anti-quark, or a gluon, but the processes that can occur are limited by flavor conservation.

At next-to-leading order (NLO), a dijet can be associated with either two or three partons in the final state. This can occur if two of the partons are roughly collinear, having very small differences in their rapidities and azimuthal angles; in particular, if $\Delta\eta^2 + \Delta\phi^2 < R^2$, where R is the cone radius used for defining jets, then the two partons will constitute a single jet. It is necessary to account for jets with finite radius in performing NLO calculations, since three-parton dijets are needed to cancel infrared divergences in the two-parton to two-parton Feynman amplitudes at NLO [83]. However, this would spoil the kinematic relations Eqs. (2.183,2.184) that allow the light cone fractions of the initial partons to be determined with jet observables.

Accordingly, it is necessary to verify the adequacy of the leading order approximation. This can be done by performing a leading order calculation of the reaction (2.162) in the case $A = 1$, *i.e.* for dijet production in a pp collision. The result of the calculation can then be compared to experiment. In Fig. 2.21, a calculation of the two-fold differential cross

Plot of LO calculation for $pp \to$ dijet against experimental data

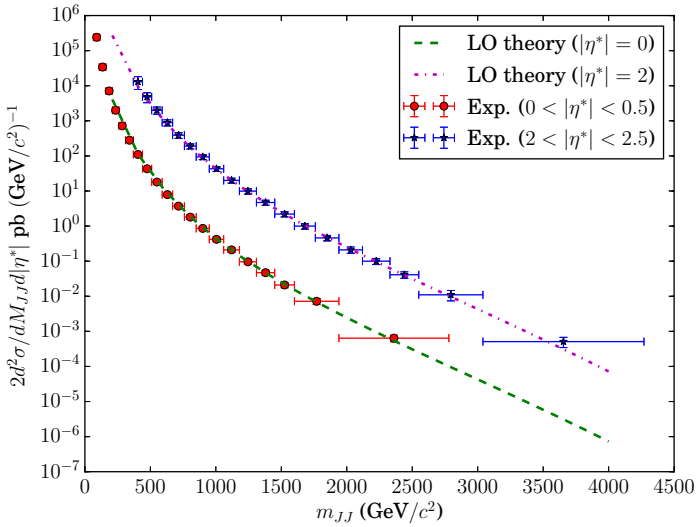

Figure 2.21: Comparison of leading-order (LO) calculation of the two-fold differential cross section using Eq. (2.196) to experimental data from ATLAS [84]. Proton PDF used is CT10 [78].

section $d^2\sigma/dm_{JJ}d|y^*|$ (calculated below) to experimental data from ATLAS [84] is given. The tight correspondence between LO theory and data justifies the use of the leading order in the pA collision calculation.

The ATLAS data are given in terms of the rapidity y, but at leading order, where the jets are massless, $y = \eta$, so these will be used interchangeably here. Let us now define the rapidity of the dijet as a whole $\bar{\eta}$ and the relative rapidity of the jets η^*, which is the rapidity of either jet in the dijet center-of-mass frame, which are used by the ATLAS data instead of η_3 and η_4. They are given by

$$\bar{\eta} = \frac{\eta_3 + \eta_4}{2} \tag{2.191}$$

$$\eta^* = \frac{\eta_3 - \eta_4}{2}. \tag{2.192}$$

The Jacobian for transforming between the jet rapidities and these new rapidities is $d\eta_3 d\eta_4 = 2d\bar{\eta}d\eta^*$. Additionally, the ATLAS data are given in terms of the dijet mass m_{JJ}, which is

given by

$$m_{JJ}^2 = (p_3 + p_4)^2 = 4p_T^2 \cosh^2(\eta^*) \tag{2.193}$$

$$m_{JJ} = 2p_T \cosh(\eta^*). \tag{2.194}$$

The overall Jacobian for the transformation from (η_3, η_4, p_T^2) to $(\bar{\eta}, \eta^*, m_{JJ})$ is given by

$$dp_T^2 d\eta_3 d\eta_4 = \frac{2p_T}{\cosh(\eta^*)} dm_{JJ} d\bar{\eta} d\eta^*, \tag{2.195}$$

and the two-fold differential cross section with respect to η^* and m_{JJ} is found by integrating over $\bar{\eta}$. Thus,

$$\frac{2d^2\sigma}{dm_{JJ}d\eta^*} = \frac{4p_T}{\cosh(\eta^*)} \int d\bar{\eta} \frac{d^3\sigma}{d\eta_3 d\eta_4 dp_T^2}, \tag{2.196}$$

where the three-fold cross section is given in Eq. (2.190).

2.7.2 The nuclear PDF

In order to calculate the cross section as given in Eq. (2.190), one needs the proton and nuclear PDFs. One can use a phenomenological parametrization of the proton PDF; here, the CT10 parametrization [78] is used. The nuclear PDF, especially for $x_A > 1$, must be determined theoretically, although the same CT10 parametrization is used as an input as the "free proton PDF." One similarly obtains a "free neutron PDF" by using the same phenomenological parametrization, but transposing the u and $\bar{u}$ with the d and $\bar{d}$ distributions, respectively.

The nuclear PDF can be obtained from a nucleon PDF by using the decomposition into mean field and SRC contributions, Eq. (2.55), and finding each contribution with the convolution formula Eq. (2.56) (which also holds for the mean field if we take $j = 1$ to signify it). However, Eq. (2.56) takes the *bound* nucleon PDF, rather than the free nucleon PDF, as its input. The modified PDF can be obtained from the free PDF by using a model of medium modification, as described in Sec. 2.5. Since the models of medium modification that currently exist are made to account for low-Q^2 data, one must apply the modification

at these low Q^2, and then evolve the nuclear PDF that is obtained to high Q^2 using DGLAP evolution (which is described in Sec. 2.6). At last, this nuclear PDF can be used in Eq. (2.190 to obtain a differential cross section.

Several of these steps are model-dependent, so different models of the nuclear PDF will be employed in the numerical estimates of this dissertation. The models will all follow the light cone convolution formalism that we have developed, but selectively account for specific phenomena within the formalism in order to gauge their relative significance. In particular, the nuclear PDF will be found (1) with and without two- and three-nucleon SRCs present, and (2) with and without medium modifications accounted for by the color screening model of the EMC effect. I will additionally compare these results to a calculation using a model by Frankfurt and Strikman [9][7] in order to compare my predictions to those of a different model of nuclear dynamics.

With these caveats in mind, we can now proceed to estimate the dijet production cross section, as will be done in the next subsection.

2.7.3 Numerical estimates

Here, I present numerical estimates for the cross section of dijet production in proton-nucleus collisions. The nucleus considered here is ^{208}Pb, which is used in nucleus beam experiments at the Large Hadron Collider. Particular focus is placed on superfast partons, namely partons with $x_A > 1$, a condition which can be checked using measurable jet kinematics and calculating x_A *via* Eq. (2.184). It is necessary to elaborate on the kinematics considered in light of this.

After elaborating on kinematics, numerical estimates of the three-fold differential cross section (*cf.* Eq. (2.190)) will be presented for several models of the nuclear PDF, and for beam energies of 4 and 7 TeV per proton. Afterwards, numerical estimates of partially and fully integrated cross sections will be given for a variety of nPDF models, and estimates of expected yields for x_A bins will be presented.

[7] See Eq. (5.11) of [9].

Kinematics considered

Large x_A is a primary goal of this study, and accordingly kinematics which tend to maximize x_A are considered. As discussed above, this is accomplished by considering (1) large p_T, (2) small η_3, and (3) highly negative η_4. The latter two conditions mean that the jet originating from the proton will be a central jet, and the jet originating from the nucleus will be a forward jet. The particular rapidity ranges considered are

$$-2.5 < \eta_3 < 2.5 \tag{2.197}$$

$$3 < -\eta_4 < 5. \tag{2.198}$$

There are two reasons for using a central jet from the proton rather than a backwards jet, even though Eq. (2.184) tells us that a highly negative η_3 would increase x_A. First, there is a larger cross section for production of central than backwards jets. Second, it is easier to detect central jets. On the other hand, once one of the detected jets is fixed to be a central jet, the other must be highly forward in the nucleus beam direction in order for x_A to be large. This is demonstrated graphically in Fig. 2.22.

The range of transverse jet momenta considered is broadly 40 GeV to 300 GeV. The cross section falls very rapidly with p_T, but the larger E_0 (and thus $\sqrt{s_{NN}^{\text{avg.}}}$) gets, the larger p_T will have to be while keeping η_3 and η_4 fixed to maintain a given x_A. Two values of E_0 are considered in these estimates: $E_0 = 4$ TeV, corresponding to $\sqrt{s_{NN}^{\text{avg.}}} = 5.02$ TeV, and $E_0 = 7$ TeV, corresponding to $\sqrt{s_{NN}^{\text{avg.}}} = 8.8$ TeV.

Three-fold differential cross section

The three-fold differential cross section can be calculated using Eq. (2.190). As discussed above, a collection of different models of the nuclear PDF are considered in carrying out the calculation. In particular, we estimate the three-fold dijet cross section by using the convolution formalism for the nPDF developed in this chapter. In all the models considered,

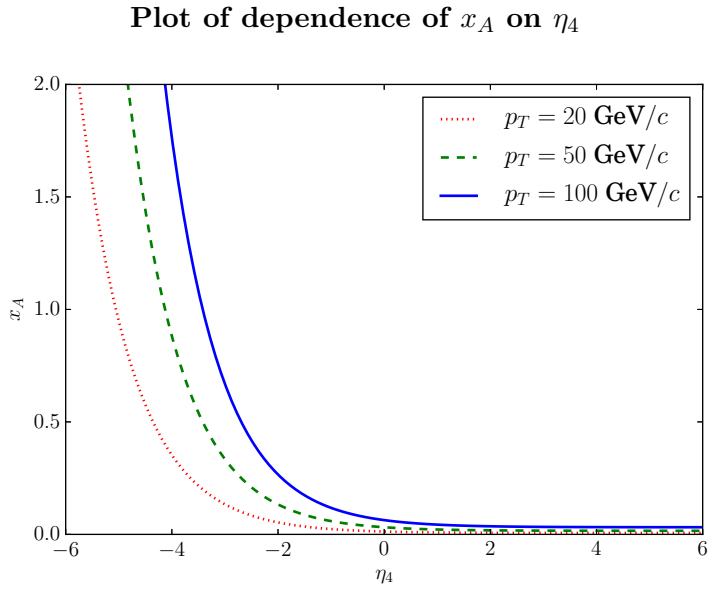

Figure 2.22: Dependence of x_A on the rapidity η_4 of the parton from nucleus, for several transverse jet momenta. $\eta_3 = 0$ and $\sqrt{s_{NN}^{\text{avg.}}} = 5.02$ TeV in this plot.

the nuclear PDF decomposes into mean field and SRC parts according to Eq. (2.55), and each contribution to the nPDF follows the convolution formula Eq. (2.56).

First, we consider the models of the mean field and SRC LCFD developed in this chapter, but estimate the dijet cross section in the absence of any medium modifications. This allows us to gauge the relative importance of the mean field versus SRC contributions. In Fig. 2.23, the cross section (sans medium modifications) is plotted for three cases: a purely mean field model of the nPDF, a model that includes 2N SRCs in addition, and a model that includes 2N and 3N correlations. Fig. 2.23a shows the result of this computation with a beam energy per proton of 4 TeV, and Fig. 2.23b for a beam energy of 7 TeV per proton.

In Fig. 2.23, the cross section has only been plotted within the range $3 < -\eta_4 < 5$, which limits the range of possible x_A values, although in a p_T-dependent way (see Eq. (2.184) for the dependence). In particular, the range of x_A values allowed will be proportional to p_T, since the lower and upper limits (corresponding to $-\eta_4 = 3$ and $-\eta_4 = 5$, respectively) are

Plots of $pA \to \text{dijet} + X$ cross section without medium modifications

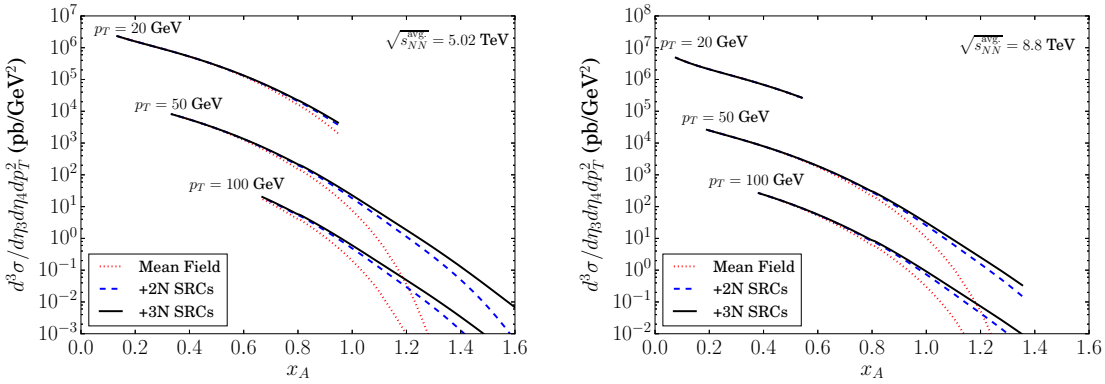

(a) $\sqrt{s_{NN}^{\text{avg.}}} = 5.02$ TeV ($E_0 = 4$ TeV) (b) $\sqrt{s_{NN}^{\text{avg.}}} = 8.8$ TeV ($E_0 = 7$ TeV)

Figure 2.23: Three-fold differential dijet cross section, in the absence of medium modifications.

both proportional to p_T. This is why the fixed-p_T curves are plotted for limited segments of x_A, and why these segments are smaller at smaller p_T.

The most significant takeaway from Fig. 2.23 is that starting already at $x_A \sim 1$, and for $x_A > 1$, the differential dijet cross section is dominated by contributions from two- and three-nucleon short range correlations. Accordingly, if one restricts their attention to kinematics for which $x_A \gtrsim 1$, the effects of short range nuclear phenomena will certainly be visible in the dijet production reaction.

Next, we account for nuclear medium modifications using the color screening model, and compare the three-fold differential cross section calculated with medium modification to the prior calculation done without medium effects. This allows us to gauge the importance of medium modifications to the dijet cross section. Both two- and three-nucleon correlations are accounted for in this calculation. The result of the computations can be seen in Fig. 2.24. The color screening effect results in an expected suppression of the differential cross section that becomes significant at larger x_A, but which still leaves the differential cross section larger than what would result from an unmodified mean field.

Plots of $pA \to \text{dijet} + X$ cross section in the color screening model

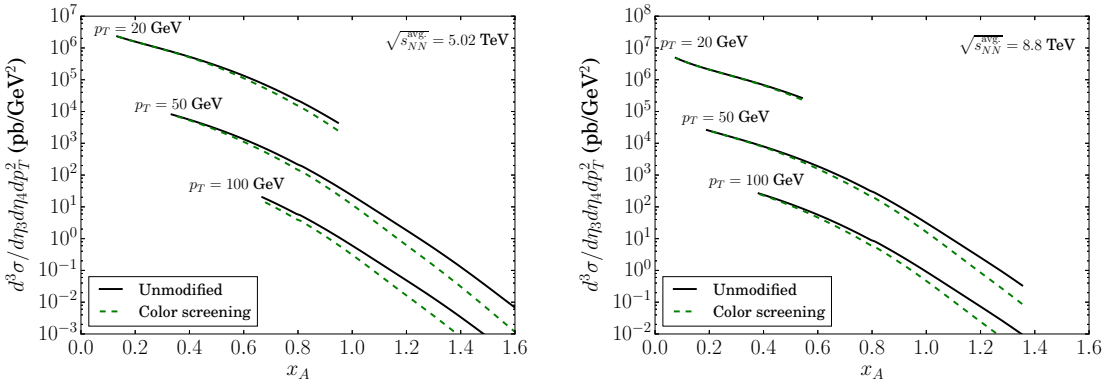

(a) $\sqrt{s_{NN}^{\text{avg.}}} = 5.02$ TeV ($E_0 = 4$ TeV) (b) $\sqrt{s_{NN}^{\text{avg.}}} = 8.8$ TeV ($E_0 = 7$ TeV)

Figure 2.24: Three-fold differential dijet cross section, with two- and three-nucleon SRCs accounted for.

Plots of $pA \to \text{dijet} + X$ cross section compared to FS81 model

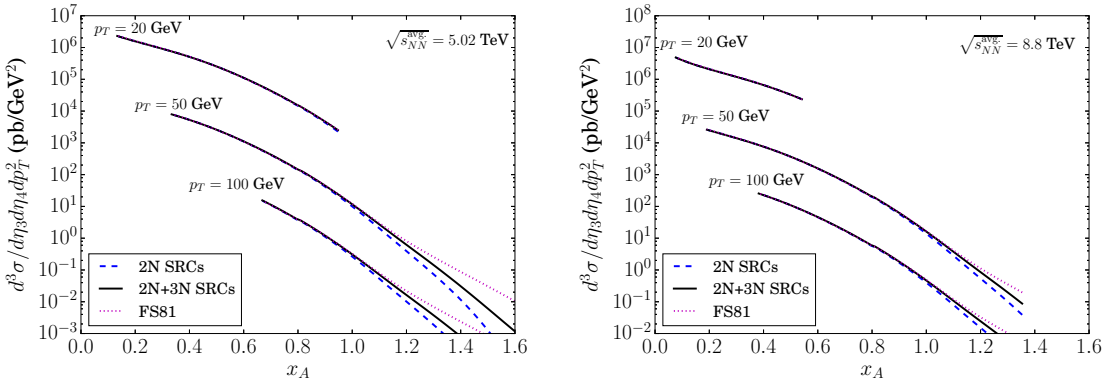

(a) $\sqrt{s_{NN}^{\text{avg.}}} = 5.02$ TeV ($E_0 = 4$ TeV) (b) $\sqrt{s_{NN}^{\text{avg.}}} = 8.8$ TeV ($E_0 = 7$ TeV)

Figure 2.25: Three-fold differential dijet cross section, with medium modifications accounted for by the color screening model.

Lastly, we compare the three-fold cross section calculated using the LCFD of this dissertation to the LCFD of the FS81 model[8]. The FS81 model contains a degenerate Fermi gas model of the mean field, an explicit model of two-nucleon correlations based on the light cone density of the deuteron, and an exponential fall off for the light cone distribution at high α which implicitly includes correlations between three, four, and more nucleons. Since this model accounts for two-nucleon explicitly, as well as three- and more-nucleon correlations implicitly, I compare its predictions for the diject cross section to the predictions of this work's LCFD. This comparison can be seen in Fig. 2.25. Most significantly, the FS81 prediction tracks the 2N+3N prediction a little while longer than it does the 2N-only prediction, but then diverges from both predictions and remains high, likely owing to the implicit inclusion of many-nucleon correlations. In particular, the FS81 prediction follows a straight line on the logarithmically-scaled plot, characteristic of exponential decay.

Partially and fully integrated cross sections

The three-fold differential cross section for reaction (2.162) becomes quite small at kinematics corresponding to $x_A > 1$, so it may be effective to integrate over pseudo-rapidities η_3 and η_4 in order to obtain a one-fold differential cross section, $d\sigma/dp_T$. Statistics may be too low to resolve a three-fold differential cross section, but by counting events over a range of rapidities, there may be enough events to resolve SRCs in the dijet cross section.

The ranges integrated over are as follows: η_3 is the rapidity of a central jet, so the range $-2.5 < \eta_3 < 2.5$ is used; and η_4 is the rapidity of a forward jet in the nucleus beam direction, meaning $-5 < \eta_4 < -3$. The one-fold differential cross section is thus

$$\frac{d\sigma}{dp_T} = \int_{-2.5}^{2.5} d\eta_3 \int_{-5}^{-3} d\eta_4 \frac{2p_T d^3\sigma}{d\eta_3 d\eta_4 dp_T^2}. \tag{2.199}$$

This integration will include superfast ($x_A > 1$) nuclear partons, but it will also involves partons with $x_A < 1$. However, one can define a one-fold differential cross section for $x_A > 1$ events, since whether $x_A > 1$ can be determined through measurable jet kinematics

[8] See Eq. (5.11) of [9].

Plots of $pA \to \text{dijet} + X$ cross section without medium modifications

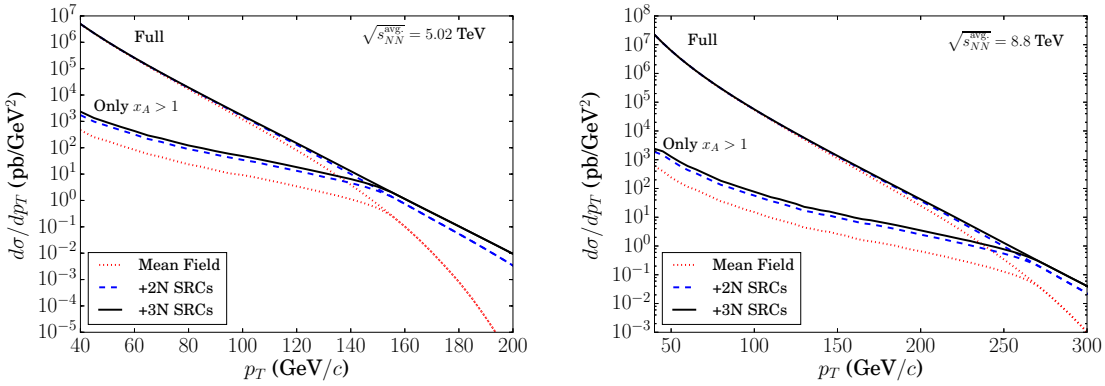

(a) $\sqrt{s_{NN}^{\text{avg.}}} = 5.02$ TeV ($E_0 = 4$ TeV) (b) $\sqrt{s_{NN}^{\text{avg.}}} = 8.8$ TeV ($E_0 = 7$ TeV)

Figure 2.26: One-fold dijet differential cross section, without medium modifications accounted for.

via Eq. (2.184. One simply has to count all the events in the considered pseudo-rapidity ranges, and select for events corresponding to $x_A > 1$, namely

$$\frac{d\sigma(x_A > 1)}{dp_T} = \int_{-2.5}^{2.5} d\eta_3 \int_{-5}^{-3} d\eta_4 \frac{2p_T d^3\sigma}{d\eta_3 d\eta_4 dp_T^2} \Theta(x_A - 1). \tag{2.200}$$

By comparing the one-fold differential cross sections of Eqs. (2.199,2.200), one can see the range of p_T where the cross section is dominated by superfast partons. In particular, if the cross section is nearly identical for both calculations in some p_T range, it means that p_T range is dominated by superfast partons, and thus extremely sensitive to short-range nuclear phenomena.

Just as with the three-fold differential cross section, we proceed by comparing the contributions made to the one-fold differential cross section by different nuclear and partonic phenomena. We begin by gauging the relative significance of the mean field and two- and three-nucleon SRCs by comparing cross sections results that selectively account for just the mean field, or 2N and 3N correlations in addition, and for the time being neglect contributions from medium modification effects. The result of this calculation can be seen in Fig. 2.26.

Plots of $pA \to \text{dijet} + X$ cross section using the color screening model

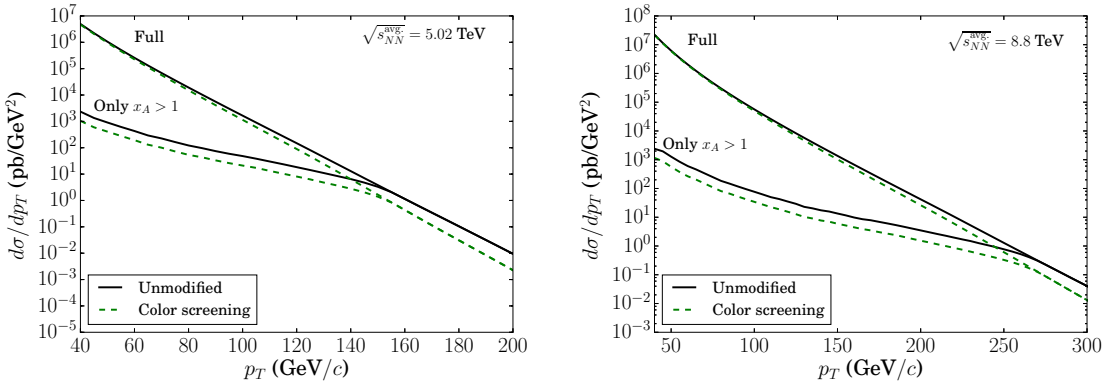

(a) $\sqrt{s_{NN}^{\text{avg.}}} = 5.02$ TeV ($E_0 = 4$ TeV) (b) $\sqrt{s_{NN}^{\text{avg.}}} = 8.8$ TeV ($E_0 = 7$ TeV)

Figure 2.27: One-fold dijet differential cross section, with two- and three-nucleon SRCs accounted for.

As would be expected, the cross section is for the most part dominated by partons with $x_A < 1$. For most of the p_T range considered, excluding $x_A < 1$ events results in the differential cross section decreasing by several orders of magnitude. However, the gap between the total differential cross section and the superfast-partons-only cross section decreases with increasing p_T, eventually becoming zero. At $p_T \approx 150$ GeV for the $E_0 = 4$ TeV cross section, or $p_T \approx 260$ GeV for the $E_0 = 7$ TeV cross section, $x_A > 1$ events make up almost all of the one-fold differential cross section. Accordingly, one can study superfast partons by specifically looking for jets above these transverse momenta.

Next, we gauge the importance of medium modification effects by again calculating the one-fold differential cross section, but now accounting for medium modifications *via* the color screening model. Two- and three-nucleon correlations, because they are significant in the high-p_T region, are accounted for. The result of this calculation is compared against the previous unmodified calculation in Fig. 2.27. As in the case of the three-fold cross section, medium modifications suppress the differential cross section, and this occurs primarily at large p_T. It is worth noting that at smaller p_T, there is comparatively little suppression of the total differential cross section, but the one-fold cross section for $x_A > 1$ events is heavily suppressed even at small p_T.

	Unmodified	Modified (no SRCs)	Modified (SRCs)	FS81 (modified)
$\sqrt{s_{NN}^{\text{avg.}}} = 5.02$ TeV ($E_0 = 4$ TeV)				
All x_A	7.4 μb	6.4 μb	6.6 μb	6.5 μb
$0.6 < x_A < 0.7$	0.93 μb	0.67 μb	0.74 μb	0.72 μb
$0.7 < x_A < 0.8$	0.37 μb	0.23 μb	0.26 μb	0.26 μb
$0.8 < x_A < 0.9$	0.12 μb	0.06 μb	0.08 μb	0.08 μb
$0.9 < x_A < 1$	37 nb	12 nb	20 nb	21 nb
$1 < x_A$	14 nb	2.0 nb	6.2 nb	6.8 nb
$\sqrt{s_{NN}^{\text{avg.}}} = 8.8$ TeV ($E_0 = 7$ TeV)				
All x_A	58 μb	55 μb	55 μb	56 μb
$0.6 < x_A < 0.7$	1.7 μb	1.2 μb	1.3 μb	1.3 μb
$0.7 < x_A < 0.8$	0.60 μb	0.37 μb	0.43 μb	0.42 μb
$0.8 < x_A < 0.9$	0.20 μb	0.11 μb	0.13 μb	0.13 μb
$0.9 < x_A < 1$	59 nb	20 nb	33 nb	34 nb
$1 < x_A$	21 nb	3.0 nb	9.3 nb	10 nb

Table 2.2: Estimates of integrated cross sections, for different bins of x_A. Calculations include two- and three-nucleon SRCs (except where otherwise stated).

In addition to one-fold differential cross sections, one can compute the fully integrated cross section. Moreover, one can impose threshold constraints such as $x_A > 1$, or on the other hand $x_{\text{min}} < x_A < x_{\text{max}}$ for some x_{min} and x_{max}. For instance, we may ask how much of the cross section comes from nuclear partons with $0.6 < x < 0.7$, in order to see whether medium modifications or short range correlations, for instance, have a big influence on partons in this region.

In Table 2.2 I present a table of integrated cross sections in x_A bins, as well as fully integrated cross sections with all x_A accounted for. Four models are considered in order to gauge the relative importance of SRCs and medium modifications. First, the cross section is calculated with the full LCFD, including short range correlations, but without medium modification effects. Second, the cross section is calculated with medium modifications but not SRCs accounted for. Third, modifications and SRCs are both accounted for: this column is in effect *the* prediction of this dissertation. This prediction is compared to a similar prediction made using the FS81 model for the nuclear light cone density, which has been used with nuclear medium modifications accounted for.

As can be seen in Table 2.2, medium modifications suppress the expected cross section, especially at high x_A; at $x_A > 1$, the cross section decreases by as much as a factor of 2. This is consistent with the expectations that (1) the EMC effect increases with the off-shellness of the bound nucleon (which itself increases with the nucleon's momentum), and (2) the EMC effect is felt most strongly by nucleons in short range correlations. In particular, the $x_A > 1$ region is dominated by short range correlations, and this is where the EMC effect most strongly suppresses the cross section.

There is lastly the question of whether these cross sections can expected to be realistically measurable in light of the luminosities that the LHC is capable of. The integrated luminosity for the one-month lead-proton collision run in 2013 was 35.5 nb^{-1} at CMS; this will be used as the reference luminosity for yield estimates. For a beam energy per proton of $E_0 = 4$ TeV, there are about 200 expected $x_A > 1$ dijet events, while for $E_0 = 7$ TeV, about 326 $x_A > 1$ events are expected to occur. Both of these numbers are fairly small, so when experimental resolution is taken into account, it may not be feasible to see evidence of superfast quarks at the LHC. On the other hand, one can still use dijet production in lead-proton collisions to study medium modifications of nuclei. $x_A > 0.6$ is the classical region of the EMC effect, and as many as 39000 events for $E_0 = 4$ TeV, or 69000 events for $E_0 = 7$ TeV, can be expected. This makes the reaction under investigation an extremely promising avenue for future studies of the EMC effect at very high Q^2.

2.7.4 Conclusions concerning dijet production

In this section, dijet production in proton-nucleus collisions was investigated as a means of studying nuclear QCD. In particular, the effects of short-range nuclear structure in the form of both short-range nuclear correlations and medium modifications of bound nucleons on the reaction cross section were investigated, and both phenomena were found to be significant in the production rates for dijets with one central and one forward (in the nucleus beam direction) jet. The effects were most pronounced when p_T was large, namely around 150 GeV for a beam energy per proton of 4 TeV, or 250 GeV for a beam energy per proton of 7 TeV. It is ambiguous whether superfast quarks in the nucleus (*i.e.*, with $x_A > 1$) can be

realistically be expected to be resolved, but around 200 or 326 (for beam energy per proton of 4 TeV or 7 TeV, respectively) events corresponding to x_A can be expected. On the other hand, dijet production in proton-nucleus collisions is an extremely promising avenue for new studies of the EMC effect at high $Q^2 = p_T^2$, since the expected yields in the region $x_A > 0.6$ are significant (39000 or 69000 events for $E_0 = 4$ TeV or $E_0 = 7$ TeV, respectively).

2.8 Summary

In this chapter, inclusive reactions were explored as a means of probing nuclear structure. The exploration focused on two particular aspects of nuclear structure: firstly, whether inclusive reactions could be used to indicate the presence of short range correlations between the nucleons composing the nucleus, thereby elucidating the conventional, hadronic structure of the nucleus; and secondly, whether inclusive reactions could study medium modifications of the bound nucleons making up the nucleus at a QCD level.

In order to explore these possibilities, a formalism for constructing nuclear parton distribution functions was derived. Nucleonic motion, including motion within short range correlations, is accounted for using a light cone fraction distribution (LCFD), the construction of which is made in analogy to the PDF of a hadron. The LCFD of two-nucleon correlations was made to account for the latest phenomenology of 2N SRCs, and a LCFD for three-nucleon correlations was developed based on the hypothesis that 3N SRCs arise from a sequence of short-range two-nucleon interactions.

This formalism was applied, together with a model for medium modifications and a modified DGLAP evolution equation, to make predictions for dijet production cross sections in proton-nucleus collisions at the LHC. It was found that the presence of short range correlations, as well as of medium modifications, made distinct predictions from the mean field and no-modifications models for the high transverse momentum cross section. Therefore, we conclude that inclusive reactions, particularly dijet production in p-A collisions, are a viable means of studying nuclear structure.

CHAPTER 3

Exclusive reactions

Exclusive reactions are preferred to inclusive reactions when studying the specific mechanisms responsible for the production of particular hadrons, and when performing searches for new particles, resonances, and bound states. For example, one may study the production mechanism for a vector meson by looking for final states exclusively containing such a vector meson and the target. Likewise, if it is possible to create a beam of vector mesons, one could use an exclusive reaction of the form $V + p \to V + p$ to study both the interaction mechanism between the meson V and the proton, and the possibility of any meson-baryon bound states that these particles form.

Realistically, experiments with heavy quarkonium (*e.g.*, J/ψ) beams are not possible, owing to the short lifetimes of the particles. However, it is with such short-lived particles that the idea of the nucleus as a micro-laboratory can be utilized. J/ψ can, for instance, be produced by a photon incident on a nucleon target. If such a photo-produced J/ψ then scatters from another nearby nucleon, information about the J/ψ-nucleon interaction could be extracted. Within a nucleus, both a nucleonic target for photoproduction and a nearby nucleonic target for J/ψ scattering are present.

In this chapter, vector meson production from a deuteron target will be explored as a possible venue for studying meson-nucleon interactions. The deuteron target is chosen for its relative simplicity as a nucleus, and for the fact that it is a loosely-bound system. In particular, the reaction $\gamma + d \to V + p + n$, *i.e.*, incoherent vector meson production, accompanied by breakup of the target will be studied. This reaction is chosen because a variety of recent experimental and theoretical studies have demonstrated the presence of a rescattering peak due to final state interactions (FSIs), *cf.* [85–92].

3.1 General formalism

In order to theoretically describe incoherent vector meson production from the deuteron, several prerequisites need to be addressed. One of these is the form of the sub-reaction

(*e.g*, photoproduction from a constituent nucleon, meson scattering from the spectator) amplitudes, which shall be addressed in Sec. 3.1.1. Another is the establishment of a kinematic regime where the contributions of these sub-reactions to the overall cross section can be unambiguously isolated. This regime is the eikonal regime, as a great deal of recent experimental and theoretical work has establish, *cf.* [87, 89–96]. The generalized eikonal approximation (GEA) is briefly discussed in Sec. 3.1.2. Lastly, it is necessary to give the form of the relativistic deuteron wave function in such a regime, where energies may be too low for the light cone formalism to apply. The virtual nucleon approximation (VNA) for the deuteron wave function is used, which is discussed in Sec. 3.1.3.

After these prerequisites are addressed, the formalism for the reaction $\gamma+d \to V+p+n$ is developed at length in Sec. 3.2. Subsequently, the formalism is applied to investigates of $\phi(1020)$ production in Sec. 3.3, and J/ψ production in Sec. 3.4.

3.1.1 The diffractive scattering amplitude

The optical theorem is a vital relationship for parameterizing the scattering amplitudes in phenomenological descriptions. It relates the total cross section for a collision between two incident particles, A and B, to the imaginary part of the forward scattering amplitude. It is a consequence of the unitarity of the S-matrix [97] and the form it takes for the Feynman amplitude $\mathcal{M}$ is:

$$\frac{\Phi}{2}\sigma_{\text{tot.}} = \text{Im}(\mathcal{M}_{ii}), \tag{3.1}$$

where $\Phi = (2E_A)(2E_B)|\mathbf{v}_A - \mathbf{v}_B|$ is the flux of the initial state, which can also be written

$$\begin{aligned}
\Phi &= (2E_A)(2E_B)|\mathbf{v}_A - \mathbf{v}_B| && (3.2)\\
&= 4\sqrt{(p_A \cdot p_B)^2 - m_A^2 m_B^2} && (3.3)\\
&= \sqrt{[s-(m_A-m_B)^2][s-(m_A+m_B)^2]} && (3.4)\\
&= 4\sqrt{s}|\mathbf{p}_i|. && (3.5)
\end{aligned}$$

In the last equation, $\mathbf{p}_i$ denotes the initial momentum in the center-of-mass frame.

For diffractive scattering applications, it is useful to utilize a scattering amplitude $f(s,t)$ normalized so that, for forward scattering,

$$\mathrm{Im}\big(f(s,t=0)\big) = \sigma_{\mathrm{tot.}}(s). \tag{3.6}$$

From Eq. (3.1), it can be seen that

$$\mathcal{M}(s,t) = \frac{\Phi}{2} f(s,t). \tag{3.7}$$

The amplitude $f(s,t)$ is called the diffractive scattering amplitude. It can be related for a two-particle to two-particle process $AB \to CD$ to the one-fold differential cross section $\frac{d\sigma}{dt}$ by:

$$\frac{d\sigma}{dt} = \frac{|f(s,t)|^2}{16\pi}. \tag{3.8}$$

This makes relating the diffractive scattering amplitude to measured differential cross sections especially straightforward, thus further simplifying their parametrization and usage.

The diffractive scattering amplitude $f(s,t)$ is especially useful for scenarios where $|t| \ll s$, where its parametrization has a simple form [98, 99]:

$$f(s,t) = A(s)(i + \alpha(s)) \exp\left(\frac{B(s)}{2} t + \frac{C(s)}{2} t^2\right), \tag{3.9}$$

where A, B, C, and α are real-valued functions of s. The factors of $\frac{1}{2}$ are present in the exponent of Eq. (3.9) because, when Eq. (3.8) is used, one obtains a parametrization of the differential cross section in the form

$$\frac{d\sigma}{dt} = \frac{[A(s)]^2(1 + [\alpha(s)]^2)}{16\pi} \exp(B(s)t + C(s)t^2). \tag{3.10}$$

The approximation $C(s) = 0$ is commonly used, often because the precision and t range of experimental data available don't allow for an accurate extraction of C [98]. Often, experimental data for the diffractive regime do, however, match Eq. (3.10) with $C = 0$. Since experimental values for $\frac{d\sigma}{dt}$ are often plotted with a log-scaled y-axis against $-t$, the

parameter $B(s)$ (for a given value of s) appears in plots as the downward slope of the data points. Accordingly, $B(s)$ is called the slope factor for the reaction being measured.

This form of the diffractive scattering amplitude is largely justified by experimental data, but there is some theoretical foundation for the form of Eq. (3.9) found within Regge theory; *cf.* Ref. [99] for further information.

The parameter $\alpha(s)$ can in principle be calculated using dispersion theory [99]. However, in this dissertation, estimates will be taken from experimental measurements.

In the special case that a reaction of the form $AB \to AB$ is being parametrized, $A(s) = \sigma_{\text{tot.}}(s)$ in Eqs. (3.9,3.10). For other cases, such as photoproduction of vector mesons, models exist for predicting the form of $A(s)$, often with the help of experimental parameters. Specific models for meson photoproduction shall be discussed in the following sections.

3.1.2 The generalized eikonal approximation

The generalized eikonal approximation (GEA) is a method of calculating amplitudes for multiple scatterings from a nuclear target using an effective Feynman diagram approach. It was developed early on by Gribov [100] and Bertocchi [101], and later expanded by other authors [85, 86, 95, 102] as a generalization of an earlier non-relativistic model by Glauber [103] that treated the constituent nucleons as stationary targets. The eikonal approximation, by contrast, conserves all four components of the total four-momentum, and accounts for relativistic kinematics, making it well-suited for high-energy processes.

Achievement of the eikonal regime establishes several vital features that are necessary to the present investigation. Firstly, it allows resolution of the deuteron target into two constituent nucleons [90,101], one of which is directly struck by the incident probe. Secondly, it allows interactions which occur after this initial probing of the struck nucleon—that is, final state interactions—to be described as cleanly-separated rescatterings that occur in sequence, each between two of the particles that appear in the final state [85, 86, 95, 102]. Thirdly, it allows for intermediate-state particles (other than the struck nucleon prior to its being probed) to be treated as real, on-mass-shell particles [101]. Lastly, in the eikonal

regime, there is a reduction theorem, due to Sargsian [86], which states that the same two particles will not rescatter from one-another more than once.

In the case of deuteron disintegration, these properties of the eikonal regime allow for the virtual nucleon approximation (VNA) of the deuteron wave function to be used [90,101], and for the vector meson production amplitude to be fully given by diagrams involving no more than two rescatterings. Moreover, the placement of intermediate particles on their mass shells permits use of completeness relations for the numerators of intermediate-state propagators, allowing for intermediate states to be given by Dirac spinors, polarization vectors, *etc.* that are absorbed into on-shell sub-reaction amplitudes. It is this specific feature of the generalized eikonal approximation which is pertinent to the present investigation, since it means that the on-shell $VN \to VN$ amplitude appears in the amplitude for V rescattering diagrams.

Establishment of the eikonal regime in the present reaction requires momentum transfer at the $\gamma N \to \gamma N$ vertex on the order of $-t \geq 1$ GeV^2. This occurs when just one of the nucleons in deuteron disintegration emerges with a momentum > 1 GeV. This necessity shall be kept in mind when the $\gamma + d \to V + p + n$ reaction is investigated in the following section.

3.1.3 Deuteron wave function in the virtual nucleon approximation

It is necessary to give a relativistic description of the deuteron wave function to describe exclusive reactions at kinematics relevant to high-precision fixed target experiments, such as those at Jefferson Lab. For this reason, we use the virtual nucleon approximation (VNA) for describing the deuteron wave function.

The VNA treats the deuteron as consisting of a proton and a neutron, neglecting higher Fock components. Accordingly, its domain of applicability extends up to about 700 MeV Fermi momentum [90]. It applies in situations where the generalized eikonal approximation can be used, so that one of the two nucleons is struck by the internal probe, with the other as a spectator. The VNA functions by placing the spectator on its positive-energy mass shell. In the plane wave impulse approximation (PWIA), where the spectator

already emerges from the deuteron on its mass shell, this placement is exact. For corrections to the PWIA involving final state interactions, the VNA proceeds by evaluating the integral over the zeroth component of the spectator's four-momentum (the off-shell energy) as:

$$\int_{-\infty}^{\infty} \frac{dp_0}{(2\pi)i} \frac{f(p_0)}{p^2 - m^2 + i\epsilon} = \frac{f(E_{\text{on}})}{2E_{\text{on}}}, \tag{3.11}$$

where $E_{\text{on}} = \sqrt{m^2 + \mathbf{p}^2}$ is the on-shell energy of the particle, and $f(p_0)$ represents other p_0-dependent functions present within the Feynman amplitude $\mathcal{M}$.

Since the spectator nucleon is placed on its positive-energy mass shell, the completeness relation $\not{p} + m = \sum_\lambda u^\lambda(\mathbf{p})\bar{u}^\lambda(\mathbf{p})$ is exact for this nucleon, and can be applied to the numerator of its propagator. For the virtual nucleon, this completeness relation may be used as an approximation, and will be used as an approximation in this work, but calculations exist where the off-shell contributions to $\not{p} + m$ are also accounted for in specific interactions (*cf.* [90] for an example in electrodisintegration of the deuteron).

The VNA deuteron wave function is given by [90]

$$\psi_{\text{VNA}}^{(\lambda_1,\lambda_2;\lambda_d)}(\mathbf{k}) = \frac{\bar{u}_1^\lambda(\mathbf{k})\bar{u}^{\lambda_2}(-\mathbf{k})\Gamma_{dpn}\chi^{\lambda_d}}{\sqrt{(2E_\mathbf{k})2(2\pi)^3}M_d(2E_\mathbf{k} - M_d)}, \tag{3.12}$$

where χ_d^λ is the polarization vector of the deuteron, Γ_{dpn} is the deuteron-to-nucleons transition vertex (due to Blankenbecler and Cook, cf. [104]), and $\mathbf{k} = \frac{\mathbf{p}_1 - \mathbf{p}_2}{2}$ is the internal, relative momentum of the nucleons.

Alternatively, if the struck nucleon momentum is labeled p_1 and the spectator momentum p_2, then the VNA wave function can be written

$$\psi_{\text{VNA}}^{(\lambda_1,\lambda_2;\lambda_d)}\left(\frac{\mathbf{p}_1 - \mathbf{p}_2}{2}\right) = \frac{\bar{u}_1^\lambda(\mathbf{p}_1)\bar{u}^{\lambda_2}(\mathbf{p}_2)\Gamma_{dpn}\chi^{\lambda_d}}{\sqrt{(2E_2)2(2\pi)^3}(m_N^2 - p_1^2)}. \tag{3.13}$$

It is the form of Eq. (3.13) that is most helpful for reading the deuteron wave function from Feynman diagram calculations. The equivalence of Eqs. (3.12,3.12) can be seen by noting

$$m_N^2 - p_1^2 = m_N^2 - (p_d - p_2)^2 = 2(p_d \cdot p_2) - M_d^2 = M_d(2E_2 - M_d). \tag{3.14}$$

The normalization of the VNA deuteron wave function is [90]:

$$\sum_{\lambda_1,\lambda_2} \int d^3\mathbf{k} \left|\psi_{\rm VNA}^{(\lambda_1,\lambda_2;\lambda_d)}(\mathbf{k})\right|^2 \frac{2(M_d - E_{\mathbf{k}})}{M_d} = 1. \tag{3.15}$$

For the sake of numerical calculations, since the non-relativistic deuteron wave function is normalized to 1, the relationship

$$\psi_{\rm VNA}^{(\lambda_1,\lambda_2;\lambda_d)}(\mathbf{k}) = \sqrt{\frac{M_d}{2(M_d - E_{\mathbf{k}}}}\psi_{\rm NR}^{(\lambda_1,\lambda_2;\lambda_d)}(\mathbf{k}) \tag{3.16}$$

is used, with a numerical parametrization given for $\psi_{\rm NR}^{(\lambda_1,\lambda_2;\lambda_d)}(\mathbf{k})$. In this work, the Paris potential is used in parameterizing the non-relativistic deuteron wave function [37].

3.2 Formalism for vector meson production with deuteron breakup

Vector meson photoproduction from a deuteron target is an especially promising avenue for investigating nuclear QCD, with a view to the nucleus as a micro-laboratory. In particular, the breakup reaction

$$\gamma + d \to V + p + n \tag{3.17}$$

is investigated as a means of studying vector meson-nucleon interactions. This reaction can serve as a substitute for elastic vector meson scattering, *e.g.* $VN \to VN$, in the absence of vector meson beams. This is accomplished by a "rescattering" contribution to the reaction (3.17), *viz.* the vector meson is photo-produced from one of the deuteron's constituent nucleons, and then subsequently scatters from the other nucleon. Characteristics of the meson-nucleon interaction can be investigated by measuring the deviation of the deuteron breakup cross section from the plane wave impulse approximation (PWIA). This will be explained in more depth below.

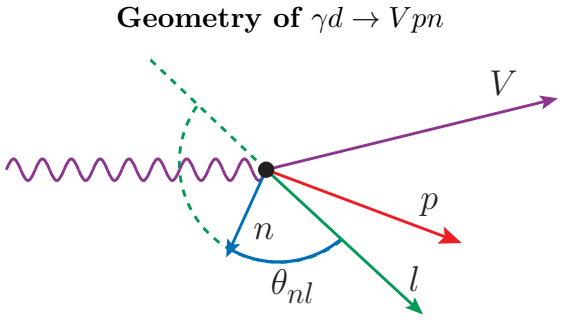

Figure 3.1: Geometry of the reaction $\gamma d \to Vpn$.

3.2.1 Kinematics and validity of eikonal approximation

The four-momenta of the deuteron, photon, vector meson, (final-state) proton, (final-state) neutron are respectively denoted $p_d = (E_d, \mathbf{p}_d)$, $q = (q_0, \mathbf{q})$, $p_V = (E_V, \mathbf{p}_V)$, $p_p = (E_p, \mathbf{p}_p)$, and $p_n = (E_n, \mathbf{p}_n)$. The initial four-momenta of the proton and neutron while they're inside the deuteron are denoted with a prime symbol, *i.e.* they are p'_p and p'_n. The four-momentum transfer to the deuteron is defined as

$$l = (l_0, \mathbf{l}) = (q_0 - E_V, \mathbf{q} - \mathbf{p}_V)\,, \tag{3.18}$$

with the invariant momentum transfer being $t = l^2$. The direction of outgoing particles will be characterized by the angle they make with respect to the vector momentum transfer $\mathbf{l}$, *i.e.* θ_{Xl} for any final-state particle X. The angle θ_{nl} characterizing the direction of the final-state neutron, for instance, is illustrated in Fig. 3.1.

This reaction will be considered in the lab frame, where the deuteron is at rest, so $p_d = (m_d, \mathbf{0})$. Kinematics where the proton emerges with a large momentum ($|\mathbf{p}_p| > 1$ GeV) and the neutron emerges with a small momentum will in particular be considered. Within the plane wave impulse approximation, this means that the proton was almost certainly struck by the incident photon, since the probability of the spectator having a momentum > 1 GeV in the deuteron rest frame is vanishingly small. These kinematics also establish the eikonal regime.

The goal of using the reaction (3.17) to study the meson-nucleon interaction can only be accomplished if it is possible to cleanly separate vertices for the photoproduction (*i.e.*, $\gamma N \to VN$) and meson-nucleon scattering ($VN \to VN$) reactions. This can be accomplished within the generalized eikonal approximation (GEA) [87, 89–96], which is justified when the final momenta of the rescattered hadrons are on the order of a GeV or above.

A major advantage of the eikonal approximation is that the pole values of propagators in rescattering amplitudes can be taken, *i.e.* the intermediate-state hadrons can be taken to be on their mass shells. This allows rescattering vertices for meson-nucleon or proton-neutron scattering to be expressed through the amplitudes for real pn or VN scattering. In the former case, well-known parameterizations of the proton-neutron scattering amplitude can be used to make the problem more tractable. In the latter case, it is the scattering amplitude for meson-nucleon scattering that is to be investigated, so being able to express the cross section for reaction (3.17) in terms of this quantity is necessary.

The validity of the eikonal regime for reaction (3.17) is established by concentrating on kinematics where the subprocess $\gamma N \to VN$ has large momentum transfer, and where exactly one of the nucleons emerges with a large momentum $\gtrsim 1$ GeV. Within the plane wave impulse approximation, this nucleon was the one upon which the vector meson was photoproduced. One has to show, for a choice of kinematics, that the condition $|\mathbf{p}_p| \gtrsim 1$ GeV.

There are five independent kinematic parameters in this reaction: there are 12 components of four-momentum for the three final-state particles, together with 4 constraints from four-momentum conservation and 3 more constraints from the mass shell condition. We consider the coplanar case for simplicity; this fixes two of the five parameters. For the remaining three, we fix the magnitude of the final neutron momentum $|\mathbf{p}_n|$, the angle θ_{nl} between the neutron and the momentum transfer $\mathbf{l}$, and the invariant four-momentum transfer $t = l^2$.

Experimentally, the neutron is the least likely particle to be detected; however, for the sake of theoretical analysis, this is the most useful particle to fix the momentum of. If the proton was struck, then the neutron was the spectator, and accordingly the neutron

momentum is opposite and equal to the initial proton momentum in the plane wave impulse approximation (PWIA).

The remaining kinematic parameters can be determined from the givens as follows. First, $|\mathbf{l}|$ can be found by taking the four-momentum conservation formula,

$$p_d + q = p_p + p_n + p_V$$
$$p_d + l = p_p + p_n,$$

and then isolating the p_p term on one side and squaring, using $p_p^2 = m_N^2$[1] to eliminate explicit p_p dependence. This gives

$$\begin{aligned}
&(p_d + l - p_n)^2 = p_p^2 \\
&M_d^2 + t + m_N^2 + 2E_d l_0 - 2E_d E_n - 2l_0 E_n + 2\mathbf{p}_n \cdot \mathbf{l} = m_N^2 \\
&(2E_n - 2E_d) l_0 = 2|\mathbf{p}_n||\mathbf{l}| \cos\theta_{pl} + (t + M_d^2 - 2E_d E_n).
\end{aligned}$$

This is an equation of the form

$$aE = 2b|\mathbf{p}| - c, \tag{3.19}$$

$$a = 2E_n - 2E_d \tag{3.20}$$
$$b = 2|\mathbf{E}_n| \cos\theta_{nl} \tag{3.21}$$
$$c = t + M_d^2 - 2E_d E_n. \tag{3.22}$$

To solve Eq. (3.19), both sides are squared, and the result is rearranged into a quadratic equation.

$$\begin{aligned}
&a^2(t + |\mathbf{p}|^2) = 4b^2|\mathbf{p}|^2 - 4bc|\mathbf{p}| + c^2 \\
&(a^2 - 4b^2)|\mathbf{p}|^2 + 4bc|\mathbf{p}| + (a^2 t - c^2) = 0,
\end{aligned} \tag{3.23}$$

[1] We take $m_p \approx m_n \equiv m_N$.

Solutions of Eq. (3.23) with *positive* $|\mathbf{p}|$ are physically valid, and up to two may exist. A closed form of the solution will not shed conceptual light on the kinematics, but one can use Eq. (3.23), together with Eqs. (3.20,3.21,3.22), to compute $|\mathbf{l}|$. With this, one also has $l_0 = \sqrt{t + \mathbf{l}^2}$, $E_V = q_0 - l_0$, and θ_{Vq} from

$$\mathbf{l}^2 = \mathbf{q}^2 + \mathbf{p}_V^2 - 2\mathbf{q}\cdot\mathbf{p}_V = q_0^2 + E_V^2 - m_V^2 - 2q_0\sqrt{E_V^2 - m_V^2}\cos\theta_{Vq}, \tag{3.24}$$

thus giving all components of the four-vector p_V. One also has $l = q - p_V$ as a result, and can determine $\cos\theta_{nq}$ from the angle addition formula

$$\cos\theta_{nq} = \cos\theta_{nl}\cos\theta_{ql} + \sin\theta_{nl}\cos\theta_{ql}\cos(\phi_{nl} - \phi_{ql}). \tag{3.25}$$

In order to understand the ϕ terms in the coplanar case, one must define the orientation of the reaction plane. If the reaction plane is called the xz-plane, and the photon beam direction the z-axis, then we define the x direction to be the direction in which the vector meson travels. With this definition, $\phi_{Vq} = 0$. For any other particle, $\phi_{Xq} = 0$ means the particle is moving in the positive x direction (*i.e.*, the same direction as the vector meson), and $\phi_{Xq} = \pi$ means it is moving in the negative x direction. The equation $l = q - p_V$ will naturally produce $\phi_{lq} = \pi$, and we take $\phi_{nl} = 0$. With θ_{nq}, one now has $\mathbf{p}_n$, and the remaining proton momentum can be determined through momentum conservation.

Now that all kinematic parameters can be determined, we can investigate the values of p_n, θ_{nl}, and t for which both the GEA, and the neglect of PWIA from the neutron can be justified. In Fig. 3.2, the dependence of the proton and vector meson momentum on these parameters is given for $\phi(1020)$ and $J\Psi$. For J/ψ, at the threshold value (as calculated for a stationary proton target) of $-t = 2.23$ GeV^2, the approximation is justified at high spectator momenta. For $\phi(1020)$, even at fairly high values of the invariant momentum transfer (*e.g.* $-t = 1.2$ GeV^2), one must be careful when considering high spectator momenta; at $p_n = 600$ MeV and small θ_{nl}, one cannot distinguish between the spectator and the struck nucleon at the PWIA level.

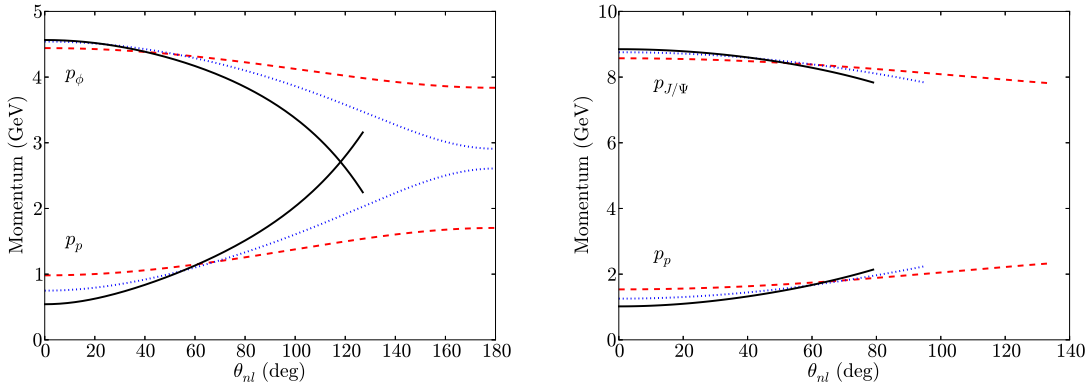

(a) (b)

Figure 3.2: Dependence of the final-state momenta of the proton and vector meson on the momenta and direction of the recoil neutron. Dashed (red), dotted (blue), and solid (black) curves correspond to neutron momenta of 200, 400, and 600 MeV. (a) $\phi(1020)$, with $q_0 = 5$ GeV and $t = -1.2$ GeV^2. (b) J/ψ, with $q_0 = 10$ GeV and $t = -2.23$ GeV^2.

3.2.2 Calculation of the amplitude and cross section

For the exclusive reaction (3.17), the cross section element is given by

$$d\sigma = \frac{\overline{|\mathcal{M}|^2}}{4(q \cdot p_d)}(2\pi)^4 \delta^{(4)}(q + p_d - p_V - p_p - p_n) \frac{d^3\mathbf{p}_V}{2E_V(2\pi)^3} \frac{d^3\mathbf{p}_p}{2E_p(2\pi)^3} \frac{d^3\mathbf{p}_n}{2E_n(2\pi)^3}, \tag{3.26}$$

where initial polarizations are averaged over and final polarizations summed over; *i.e.* the unpolarized case is considered. In the GEA framework, the matrix element $\mathcal{M}$ is expanded in terms of the number of hadronic rescatterings. By the reduction theorem of Ref. [86], the any pair of hadrons is vanishingly unlikely to interact more than once, so the expansion can be made in up to two rescatterings, *viz.*

$$\mathcal{M} = \mathcal{M}_0 + \mathcal{M}_1 + \mathcal{M}_2, \tag{3.27}$$

where $\mathcal{M}_0$, $\mathcal{M}_1$, and $\mathcal{M}_2$ are the PWIA and single- and double-rescattering amplitudes, respectively. These amplitudes shall be calculated in detail below.

Since the neutron is difficult to detect, its presence in the final state will likely be inferred from missing mass, while the proton and vector meson will be detected. Accordingly, we integrate out the neutron momentum in Eq. (3.26). This gives:

$$d\sigma = \frac{\overline{|\mathcal{M}|^2}}{2(s_d - M_d^2)}(2\pi)\delta((p_d + q - p_V - p_p)^2 - m_N^2)\frac{d^3\mathbf{p}_V}{(2E_V)(2\pi)^3}\frac{d^3\mathbf{p}_p}{(2E_p)(2\pi)^3}. \tag{3.28}$$

The remaining delta function is eliminated by integrating over the magnitude of the proton momentum. This gives us

$$\frac{d^5\sigma}{d^3\mathbf{p}_V d\Omega_p} = \frac{\overline{|\mathcal{M}|^2}}{2(s_d - M_d^2)}\frac{1}{(2\pi)^5}\frac{1}{8E_V E_p E_n}\frac{p_p^3}{|\mathbf{p}_p \cdot (\mathbf{v}_p - \mathbf{v}_n)|}, \tag{3.29}$$

where the outgoing velocities are given by the relativistic relation $\mathbf{v} = \frac{\mathbf{p}}{E}$.

Plane wave impulse approximation

In the plane wave impulse approximation (PWIA), the reaction (3.17) is assumed to proceed by the photoproduction of the vector meson V from a single nucleon within the deuteron. The particles participating in the reaction are treated as plane waves, and final state interactions between the hadrons are neglected. This is represented pictorially in Fig. 3.3. The invariant matrix element $\mathcal{M}_0$ can be calculated using effective Feynman diagram rules (*cf.* [86]), which give:

$$\begin{aligned}\mathcal{M}_0^{(\lambda_V\lambda_p\lambda_n;\lambda_\gamma\lambda_d)} = &-\bar{u}^{\lambda_p}(\mathbf{p}_p)\bar{u}^{\lambda_n}(\mathbf{p}_n)\phi^{\dagger\,\lambda_V}_{\nu}(\mathbf{p}_V)\Gamma^{\mu\nu}_{\gamma N\to VN}\epsilon_\mu^{\lambda_\gamma}(q)\\ &\frac{\not{p}'_p + m_N}{p_p'^2 - m_N^2 + i\epsilon}\Gamma_{dpn}\chi_d^{\lambda_d}(\mathbf{p}_d).\end{aligned} \tag{3.30}$$

Here, Γ_{dpn} and $\Gamma^{\mu\nu}_{\gamma N\to VN}$ are the covariant interaction vertices for the transitions $d \to pn$ and $\gamma N \to VN$. The spin wave functions of the deuteron, nucleons, photon and vector meson are denoted χ_d, u, ϵ_μ, and ϕ_ν, respectively. The spin degree of freedom of each particle is identified by a superscript.

Since we are working within the virtual nucleon approximation (VNA), only the positive-energy pole is taken for the bound nucleon propagator. Moreover, the approxi-

Feynman diagram for PWIA contribution to $\gamma d \to Vpn$

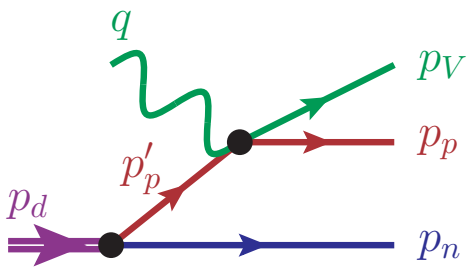

Figure 3.3: Effective Feynman diagram for the PWIA contribution to reaction (3.17).

mation completeness relation $\not{p}'_p + m_N \approx \sum_{\lambda'_p} u^{\lambda'_p}(\mathbf{p}'_p)\bar{u}^{\lambda'_p}(\mathbf{p}'_p)$ is used, although the four-momentum of the bound proton is off-shell and defined through momentum conservation, *i.e.* $p'_p = p_d - p_n$. This enables us to use the VNA deuteron wave function of Eq. (3.12), allowing us to gather the terms

$$\psi_d^{(\lambda_d;\lambda'_p,\lambda_n)}(\mathbf{p}_n) = -\frac{\bar{u}^{\lambda'_p}(\mathbf{p}'_p)\bar{u}^{\lambda_n}(\mathbf{p}_n)}{p'^2_p - m_N^2}\frac{\Gamma_{dpn}\chi_d^{\lambda_d}(\mathbf{p}_d)}{\sqrt{2(2\pi)^3 2E_n}} \tag{3.31}$$

together. Additionally, we use the invariant matrix element for vector meson photoproduction from the struck nucleon,

$$\mathcal{M}_{\gamma N\to VN}^{(\lambda_V\lambda_p;\lambda_\gamma\lambda'_p)}(s_{\gamma N^*}, t_{\gamma N^*}) = \bar{u}^{\lambda_p}(\mathbf{p}_p)\phi^{\dagger\lambda_V}_{\nu}(\mathbf{p}_V)\Gamma^{\mu\nu}_{\gamma N\to VN}\epsilon_\mu(q)u^{\lambda'_p}(\mathbf{p}'_p), \tag{3.32}$$

where $s_{\gamma N^*}$ and $t_{\gamma N^*}$ are the Mandelstam variables at the $\gamma N \to VN$ vertex. Note that this photoproduction amplitude is half-off-shell (*i.e.* the initial proton is off-shell), but we use an on-shell spinor for the bound proton, accounting for off-shell effects only kinematically. Earlier estimates [90] demonstrated this to be a valid approximation to be valid when $\frac{|\mathbf{p}'_p|}{\sqrt{-t}} \ll 1$ and $\frac{|\mathbf{p}'_p|}{\sqrt{s}} \ll 1$, both of which are satisfied for the kinematics considered.

With these caveats in mind, using the $\gamma N \to VN$ amplitude and the VNA deuteron wave function give the invariant PWIA amplitude, when inserted into Eq. (3.30), as

$$\mathcal{M}_0^{(\lambda_V\lambda_p\lambda_n;\lambda_\gamma\lambda_d)} = \sqrt{2(2\pi)^3 2E_n}\sum_{\lambda'_p}\mathcal{M}_{\gamma N\to VN}^{(\lambda_V\lambda_p;\lambda_\gamma\lambda'_p)}(s_{\gamma N^*}, t_{\gamma N^*})\Psi_d^{(\lambda_d;\lambda'_p\lambda_n)}(\mathbf{p}_n). \tag{3.33}$$

Single rescattering correction

In the GEA framework, there are up to four single rescattering diagrams to consider. These are depicted in Fig. 3.4. The processes can be separated into two groups: one where the proton receives its large momentum at the photoproduction vertex (Figs. 3.4a,3.4b) and one where photoproduction occurs from the neutron, but the proton receives a large momentum transfer due to the $VN \to VN$ rescattering (Figs. 3.4c,3.4d).

Feynman diagram for single rescattering contributions to $\gamma d \to Vpn$

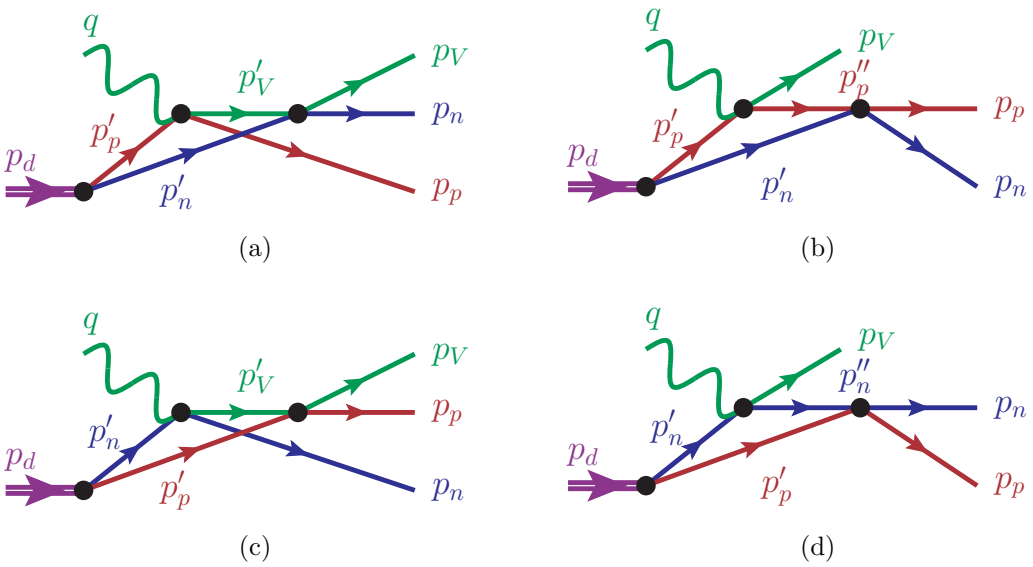

Figure 3.4: Effective Feynman diagrams for the single rescattering contributions to reaction (3.17).

The rescattering contributions will appreciably contribute to $\mathcal{M}$ only when one of the hadronic vertices is hard and the other soft; two hard vertices will produce a negligible scattering amplitude, since in the eikonal regime the t-dependence for scattering goes as $e^{-b|t|}$. A one-hard, one-soft scenario can be realized for the first three diagrams easily: for Figs. 3.4a,3.4b, the hard vertex is the photoproduction vertex, and the soft the rescattering vertex, while for Fig. 3.4c, the hard vertex is the rescattering vertex and the soft the photoproduction vertex. For Fig. 3.4d, however, both vertices need to be hard in order to produce high momenta for both the proton and the vector meson in the final state.

In principle, a one-hard, one-soft scenario can be realized for Fig. 3.4d *via* a charge interchange reaction, but this contribution will be negligible at the high s_{pn} in the present scenario. Ref. [90] contains a detailed discussion of final state interactions, including the charge interchange reaction, for $d(e,e'N)N$, and discusses the domain in which this contribution is kinematically significant.

Due to the antisymmetry of the deuteron wave function, the diagrams of Figs. 3.4a,3.4c enter with opposite signs. However, the contribution of Fig. 3.4c will be suppressed for near-threshold production of heavy vector mesons, such as J/ψ, since the large $-t_{\rm thr.}$ will make the photoproduction vertex hard, producing a two-hard-vertices scenario. However, at high energies, and for light vector mesons, the contributions of Figs. 3.4a,3.4c will largely cancel, entirely canceling in the limit of very high energies. Accordingly, sensitivity of reaction (3.17) to the meson-nucleon scattering vertex will only be possible to see in the near-threshold limit.

Since the diagram of Fig. 3.4d is negligible, the Feynman amplitudes for Figs. 3.4(a-c) will be calculated. These diagrams are calculated using effective Feynman rules. The contributions of these diagrams to $\mathcal{M}_1$ are denoted $\mathcal{M}_{1a}$, $\mathcal{M}_{1b}$ and $\mathcal{M}_{1c}$, and are in full:

$$\mathcal{M}_{1a}^{(\lambda_V,\lambda_p,\lambda_n;\lambda_\gamma,\lambda_d)} = -\bar{u}^{\lambda_p}(\mathbf{p}_p)\bar{u}^{\lambda_n}(\mathbf{p}_n)\phi_\pi^{\lambda_V}(\mathbf{p}_V)\int\frac{d^4p'_n}{(2\pi)^4 i}\left[\Gamma^{\rho\pi}_{VN\to VN}\frac{G_{\nu\rho}(p'_V)}{(p'_V)^2-m_V^2+i\epsilon}\right.$$
$$\left.\Gamma^{\mu\nu}_{\gamma N\to VN}\epsilon_\mu^{\lambda_\gamma}\frac{\not{p}'_p+m_N}{(p'_p)^2-m_N^2+i\epsilon}\frac{\not{p}'_n+m_N}{(p'_n)^2-m_N^2+i\epsilon}\Gamma_{dpn}\chi_d^{\lambda_d}\right] \tag{3.34}$$

$$\mathcal{M}_{1b}^{(\lambda_V,\lambda_p,\lambda_n;\lambda_\gamma,\lambda_d)} = -\bar{u}^{\lambda_p}(\mathbf{p}_p)\bar{u}^{\lambda_n}(\mathbf{p}_n)\phi_\pi^{\lambda_V}(\mathbf{p}_V)\int\frac{d^4p'_p}{(2\pi)^4 i}\left[\Gamma_{pn\to pn}\frac{\not{p}''_p+m_N}{(p''_p)^2-m_N^2+i\epsilon}\right.$$
$$\left.\frac{\not{p}'_n+m_N}{(p'_n)^2-m_N^2+i\epsilon}\Gamma^{\mu\nu}_{\gamma N\to VN}\epsilon_\mu^{\lambda_\gamma}\frac{\not{p}'_p+m_N}{(p'_p)^2-m_N^2+i\epsilon}\Gamma_{dpn}\chi_d^{\lambda_d}\right] \tag{3.35}$$

$$\mathcal{M}_{1c}^{(\lambda_V,\lambda_p,\lambda_n;\lambda_\gamma,\lambda_d)} = -\bar{u}^{\lambda_p}(\mathbf{p}_p)\bar{u}^{\lambda_n}(\mathbf{p}_n)\phi_\pi^{\lambda_V}(\mathbf{p}_V)\int\frac{d^4p'_p}{(2\pi)^4 i}\left[\Gamma^{\rho\pi}_{VN\to VN}\frac{G_{\nu\rho}(p'_V)}{(p'_V)^2-m_V^2+i\epsilon}\right.$$
$$\left.\Gamma^{\mu\nu}_{\gamma N\to VN}\epsilon_\mu^{\lambda_\gamma}\frac{\not{p}'_p+m_N}{(p'_p)^2-m_N^2+i\epsilon}\frac{\not{p}'_n+m_N}{(p'_n)^2-m_N^2+i\epsilon}\Gamma_{dpn}\chi_d^{\lambda_d}\right], \tag{3.36}$$

where $G_{\mu\nu}(p_V)=g_{\mu\nu}-p_{V,\mu}p_{V,\nu}/m_V^2$ is the numerator of the propagator of the intermediate vector meson. The notation for the momentum of intermediate states is given in Fig. 3.4.

From here, the derivations follow the prescriptions of the virtual nucleon approximation. First, the spectator nucleon to the photoproduction subreaction is placed on its mass shell by taking only the positive-energy pole in the integration over the intermediate spectator energy, *viz.*

$$\int \frac{dp'^0_{p/n}}{p'^2_{p/n} - m_N^2 + i\epsilon} = -i\frac{2\pi}{2E'_{p/n}} \tag{3.37}$$

where $E'_{p/n} = +\sqrt{m_N^2 + \mathbf{p}'^2_{p/n}}$. Since this integration places the spectator on its mass shell, the completeness relation $\not{p}'_{p/n} + m_N = \sum_{\lambda'_{p/n}} u^{\lambda'_{p/n}}(\mathbf{p}'_{p/n})\bar{u}^{\lambda'_{p/n}}(\mathbf{p}'_{p/n})$ is exact for the intermediate spectator (within the VNA prescription). For the other intermediate-state nucleon, the completeness relation remains an approximation, but the approximation is used as it is reasonable within the high-momentum transfer, high-energy regime, as discussed above. In particular, introducing this approximate completeness relation for the off-shell nucleon propagator (but leaving the numerator of the vector meson propagator alone for now) allows the VNA deuteron wave function to be introduced into the invariant amplitudes, giving:

$$\begin{aligned}
\mathcal{M}_{1a}^{(\lambda_V,\lambda_p,\lambda_n;\lambda_\gamma,\lambda_d)} &= -\bar{u}^{\lambda_p}(\mathbf{p}_p)\bar{u}^{\lambda_n}(\mathbf{p}_n)\phi_\pi^{\lambda_V}(\mathbf{p}_V)\sum_{\lambda'_p,\lambda'_n}\int \frac{d^3\mathbf{p}'_n}{(2\pi)^3}\Bigg[\sqrt{\frac{2(2\pi)^3}{2E'_n}}\Gamma^{\rho\pi}_{VN\to VN} \\
&\quad u^{\lambda'_n}(\mathbf{p}'_n)\frac{G_{\nu\rho}(p'_V)}{(p'_V)^2 - m_V^2 + i\epsilon}\Gamma^{\mu\nu}_{\gamma N\to VN}\epsilon_\mu^{\lambda_\gamma}u^{\lambda'_p}(\mathbf{p}'_p)\Psi_d^{(\lambda'_p,\lambda'_n;\lambda_d)}(\mathbf{p}'_n)\Bigg] \qquad (3.38)\\
\mathcal{M}_{1b}^{(\lambda_V,\lambda_p,\lambda_n;\lambda_\gamma,\lambda_d)} &= -\bar{u}^{\lambda_p}(\mathbf{p}_p)\bar{u}^{\lambda_n}(\mathbf{p}_n)\phi_\pi^{\lambda_V}(\mathbf{p}_V)\int \frac{d^3\mathbf{p}'_n}{(2\pi)^3}\Bigg[\sqrt{\frac{2(2\pi)^3}{2E'_n}}\Gamma_{pn\to pn} \\
&\quad u^{\lambda'_n}(\mathbf{p}'_n)\frac{\not{p}''_p + m_N}{(p''_p)^2 - m_N^2 + i\epsilon}\Gamma^{\mu\nu}_{\gamma N\to VN}\epsilon_\mu^{\lambda_\gamma}u^{\lambda'_p}(\mathbf{p}'_p)\Psi_d^{(\lambda'_p,\lambda'_n;\lambda_d)}(\mathbf{p}'_n)\Bigg] \qquad (3.39)\\
\mathcal{M}_{1c}^{(\lambda_V,\lambda_p,\lambda_n;\lambda_\gamma,\lambda_d)} &= +\bar{u}^{\lambda_p}(\mathbf{p}_p)\bar{u}^{\lambda_n}(\mathbf{p}_n)\phi_\pi^{\lambda_V}(\mathbf{p}_V)\int \frac{d^3\mathbf{p}'_p}{(2\pi)^3}\Bigg[\sqrt{\frac{2(2\pi)^3}{2E'_p}}\Gamma^{\rho\pi}_{VN\to VN} \\
&\quad u^{\lambda'_p}(\mathbf{p}'_p)\frac{G_{\nu\rho}(p'_V)}{(p'_V)^2 - m_V^2 + i\epsilon}\Gamma^{\mu\nu}_{\gamma N\to VN}\epsilon_\mu^{\lambda_\gamma}u^{\lambda'_n}(\mathbf{p}'_n)\Psi_d^{(\lambda'_n,\lambda'_p;\lambda_d)}(\mathbf{p}'_p)\Bigg]. \qquad (3.40)
\end{aligned}$$

The plus sign in Eq. (3.40) comes from the antisymmetry of the deuteron wave function under a p-n swap, *i.e.*, must have the opposite sign of Eq. (3.38).

There is a remaining propagator denominator (*i.e.*, factor of the form $p^2 - m^2 + i\epsilon$) in each amplitude: from the vector meson propagator in $\mathcal{M}_{1a}$ and $\mathcal{M}_{1c}$, and from the proton propagator in $\mathcal{M}_{1b}$. In each case, the four-momentum transferred at the rescattering vertex is introduced as $K = p_n - p'_n$, and the propagator is rewritten in terms of K.

For the propagator in $\mathcal{M}_{1a}$, we find

$$\begin{aligned}(p'_V)^2 - m_V^2 + i\epsilon &= (p_V + p_n - p'_n)^2 - m_V^2 + i\epsilon = (p_V + K)^2 - m_V^2 + i\epsilon \\ &= 2p_{V,z}\left(\Delta_{1a} - K_z + i\epsilon\right), \end{aligned} \tag{3.41}$$

where

$$\Delta_{1a} = \frac{K^2 + 2K_0 E_V - 2\mathbf{K}_\perp \cdot \mathbf{p}_V}{2p_{V,z}}. \tag{3.42}$$

To proceed with the integration, a key feature of eikonal scattering is used: the rescattering amplitude is soft and dominated by small-angle scattering, *i.e.* $K_z^2 \ll \mathbf{K}_\perp^2$, meaning that K_0 and K^2 are approximately equal to their $K_z = 0$ values. Additionally, $\frac{\partial \Delta_{1a}}{\partial K_z} \sim \frac{K_z}{p_{V,z}} \ll 1$, so we may take Δ_{1a} to be independent of K_z in the eikonal regime. Ultimately, this has the effect of linearizing the propagator denominator: the term $2p_{V,z}\left(\Delta_{1a} - K_z + i\epsilon\right)$ in Eq. (3.41) is now linear in K_z. Additionally, the integration over $\mathbf{p}'_n$ in Eq. (3.38) can be rewritten as an integration over $\mathbf{K}$, the z-component of which can be integrated using the identity

$$\int \frac{f(z)dz}{\Delta - z + i\epsilon} = -i\pi f(\Delta) + \mathcal{P}\int \frac{f(z)dz}{\Delta - z}, \tag{3.43}$$

where the symbol $\mathcal{P}$ indicates that the Cauchy principal value of the integral is to be taken.

In applying the decomposition of Eq. (3.43) to $\mathcal{M}_{1a}$, we are separating $\mathcal{M}_{1a}$ into on-shell and off-shell parts. The condition $\Delta_{1a} = K_z$ imposed by the delta function in the decomposition corresponds to the on-mass-shell condition for the intermediate vector meson, since it this equality occurs when $(p'_V)^2 = m_V^2$. This term in the composition shall henceforth be called the pole term, with the other being called the principal value term. Because the pole term corresponds to the intermediate vector meson being on its mass shell, the completeness relation $G_{\nu\rho}(p'_V) = \sum_{\lambda'_V} \phi_\nu{}^{(\lambda'_V)}(\mathbf{p}'_V)\phi^{*(\lambda'_V)}_\rho(\mathbf{p}'_V)$ can be used for the pole

term contribution to $\mathcal{M}_{1a}$. With this relation in use, spin wave functions can be gathered into invariant amplitudes for the $\gamma N \to VN$ and $VN \to VN$ subprocesses, giving

$$\mathcal{M}^{(\lambda_V,\lambda_p,\lambda_n;\lambda_\gamma,\lambda_d)}_{1a,\text{pole}} = \frac{i}{4p_{V,z}} \sum_{\lambda'_V,\lambda'_p,\lambda'_n} \int \frac{d^2\mathbf{K}_\perp}{(2\pi)^2} \left[\sqrt{\frac{2(2\pi)^3}{2E'_n}} \mathcal{M}^{(\lambda_V,\lambda_n;\lambda'_V,\lambda'_n)}_{VN\to VN}(s_{VN}, t_{VN}) \right.$$
$$\left. \mathcal{M}^{(\lambda'_V,\lambda_p;\lambda_\gamma,\lambda'_p)}_{\gamma N\to VN}(s_{\gamma N^*}, t_{\gamma N^*}) \Psi_d^{(\lambda'_p,\lambda'_n;\lambda_d)}(p_{n,z} - \Delta_{1a}, \mathbf{p}_{n,\perp} - \mathbf{K}_\perp) \right] \quad (3.44)$$

for the pole term. Here, as in the PWIA amplitude, the invariant amplitudes appearing on the right-hand side are functions of the Mandelstam variables for their respective transitions.

For the other two rescattering amplitudes, similar decompositions of the remaining propagators are possible. For $\mathcal{M}_{1b}$, we have

$$(p'_p)^2 - m_N^2 + i\epsilon = (p_p + p_n - p'_n)^2 - m_N^2 + i\epsilon = (p_p + K)^2 - m_N^2 + i\epsilon$$
$$= 2p_{p,z}\left(\Delta_{1b} - K_z + i\epsilon\right), \quad (3.45)$$

where

$$\Delta_{1b} = \frac{K^2 + 2K_0E_p - 2\mathbf{K}_\perp \cdot \mathbf{p}_p}{2p_{p,z}}, \quad (3.46)$$

giving a pole part of the amplitude equal to

$$\mathcal{M}^{(\lambda_V,\lambda_p,\lambda_n;\lambda_\gamma,\lambda_d)}_{1b,\text{pole}} = \frac{i}{4p_{p,z}} \sum_{\lambda'_p,\lambda''_p,\lambda'_n} \int \frac{d^2\mathbf{K}_\perp}{(2\pi)^2} \left[\sqrt{\frac{2(2\pi)^3}{2E'_n}} \mathcal{M}^{(\lambda_p,\lambda_n;\lambda''_p,\lambda'_n)}_{pn\to pn}(s_{pn}, t_{pn}) \right.$$
$$\left. \mathcal{M}^{(\lambda_V,\lambda''_p;\lambda_\gamma,\lambda'_p)}_{\gamma N\to VN}(s_{\gamma N^*}, t_{\gamma N^*}) \Psi_d^{(\lambda'_p,\lambda'_n;\lambda_d)}(p_{n,z} - \Delta_{1b}, \mathbf{p}_{n,\perp} - \mathbf{K}_\perp) \right]. \quad (3.47)$$

For $\mathcal{M}_{1c}$, we have

$$(p'_V)^2 - m_V^2 + i\epsilon = (q + p'_n - p_n)^2 - m_V^2 + i\epsilon = (q - K)^2 - m_V^2 + i\epsilon$$
$$= 2q_0\left(K_z - \Delta_{1c} + i\epsilon\right), \quad (3.48)$$

where

$$\Delta_{1c} = \frac{m_V^2 - K^2}{2q_0} + K_0, \quad (3.49)$$

giving a pole part of the amplitude equal to

$$\mathcal{M}^{(\lambda_V,\lambda_p,\lambda_n;\lambda_\gamma,\lambda_d)}_{1c,\text{pole}} = -\frac{i}{4q_0}\sum_{\lambda'_V,\lambda'_p,\lambda'_n}\int\frac{d^2\mathbf{K}_\perp}{(2\pi)^2}\Bigg[\sqrt{\frac{2(2\pi)^3}{2E'_p}}\mathcal{M}^{(\lambda_V,\lambda_p;\lambda'_V,\lambda'_p)}_{VN\to VN}(s_{VN},t_{VN})$$
$$\mathcal{M}^{(\lambda'_V,\lambda_n;\lambda_\gamma,\lambda'_n)}_{\gamma N\to VN}(s_{\gamma N^*},t_{\gamma N^*})\Psi_d^{(\lambda'_n,\lambda'_p;\lambda_d)}(-p_{n,z}+\Delta_{1c},-\mathbf{p}_{n,\perp}+\mathbf{K}_\perp)\Bigg]. \quad (3.50)$$

For the principal value (PV) parts of each amplitude, the notation is simplified by introducing half-off-shell amplitudes for the $VN\to VN$ and $pn\to pn$ subprocesses, allowing us to write the following:

$$\mathcal{M}^{(\lambda_V,\lambda_p,\lambda_n;\lambda_\gamma,\lambda_d)}_{1a,\text{PV}} = \frac{1}{2p_{V,z}}\sum_{\lambda'_V,\lambda'_p,\lambda'_n}\int\frac{d^2\mathbf{K}_\perp}{(2\pi)^2}\mathcal{P}\int\frac{dK_z}{2\pi}\Bigg[\sqrt{\frac{2(2\pi)^3}{2E'_n}}\mathcal{M}^{(\lambda_V\lambda_n;\lambda'_V\lambda'_n)}_{V^*N\to VN}(s_{V^*N},t_{V^*N})$$
$$\mathcal{M}^{(\lambda'_V\lambda_p;\lambda_\gamma\lambda'_p)}_{\gamma N^*\to VN}(s_{\gamma N^*},t_{\gamma N^*})\frac{\Psi_d^{(\lambda'_p,\lambda'_n;\lambda_d)}(p_{n,z}-\Delta_{1a},\mathbf{p}_{n,\perp}-\mathbf{K}_\perp)}{K_z-\Delta_{1a}}\Bigg] \quad (3.51)$$

$$\mathcal{M}^{(\lambda_V,\lambda_p,\lambda_n;\lambda_\gamma,\lambda_d)}_{1b,\text{PV}} = \frac{1}{2p_{p,z}}\sum_{\lambda'_V,\lambda'_p,\lambda'_n}\int\frac{d^2\mathbf{K}_\perp}{(2\pi)^2}\mathcal{P}\int\frac{dK_z}{2\pi}\Bigg[\sqrt{\frac{2(2\pi)^3}{2E'_n}}\mathcal{M}^{(\lambda_p\lambda_n;\lambda''_p\lambda'_n)}_{p^*n\to pn}(s_{p^*n},t_{p^*n})$$
$$\mathcal{M}^{(\lambda_V\lambda_{p'\prime};\lambda_\gamma\lambda'_p)}_{\gamma N^*\to VN}(s_{\gamma N^*},t_{\gamma N^*})\frac{\Psi_d^{(\lambda'_p,\lambda'_n;\lambda_d)}(p_{n,z}-\Delta_{1b},-\mathbf{p}_{n,\perp}+\mathbf{K}_\perp)}{K_z-\Delta_{1b}}\Bigg] \quad (3.52)$$

$$\mathcal{M}^{(\lambda_V,\lambda_p,\lambda_n;\lambda_\gamma,\lambda_d)}_{1c,\text{PV}} = -\frac{1}{2q_0}\sum_{\lambda'_V,\lambda'_p,\lambda'_n}\int\frac{d^2\mathbf{K}_\perp}{(2\pi)^2}\mathcal{P}\int\frac{dK_z}{2\pi}\Bigg[\sqrt{\frac{2(2\pi)^3}{2E'_p}}\mathcal{M}^{(\lambda_V\lambda_p;\lambda'_V\lambda'_p)}_{V^*N\to VN}(s_{V^*N},t_{V^*N})$$
$$\mathcal{M}^{(\lambda'_V\lambda_n;\lambda_\gamma\lambda'_n)}_{\gamma N^*\to VN}(s_{\gamma N^*},t_{\gamma N^*})\frac{\Psi_d^{(\lambda'_n,\lambda'_p;\lambda_d)}(-p_{n,z}+\Delta_{1c},\mathbf{p}_{n,\perp}-\mathbf{K}_\perp)}{K_z-\Delta_{1c}}\Bigg]. \quad (3.53)$$

The notation V^* and p^* signify that these particles are off-shell in their intermediate states. The amplitudes are estimated numerically by simply using the on-shell counter-parts for the subreaction amplitudes, but using off-shell kinematics in the computation. In any case, it is important to note that the approach of using reaction (3.17) to study the on-shell meson-nucleon scattering amplitude can only be used if the PV parts of the rescattering amplitudes are neglected.

Double rescattering correction

Lastly, in the GEA framework, there are up to four double rescattering diagrams to consider. These are depicted in Fig. 3.5.

Like with the single rescattering diagrams, these are split into two categories. Firstly, Figs. 3.5a,3.5b correspond to processes with hard meson photoproduction from the proton, followed by two rescatterings of the hadrons in the final state. They differ only in that in Fig. 3.5a, the meson-proton rescattering occurs before the proton-neutron rescattering, while the opposite occurs in Fig. 3.5b. These diagrams will make a significant contribution to the overall matrix element $\mathcal{M}$ only when the two rescattering vertices are soft.

On the other hand, Figs. 3.5c,3.5d are essentially copies of Figs. 3.5a,,3.5b respectively, but with the proton and neutron swapped. Since the kinematic situation under consideration corresponds to a fast proton and a slow neutron in the final state, one of the scattering vertices involving the proton must be a hard sub-reaction. In particular, in order that the neutron end up slow in the final state, the proton-meson rescattering in particular must be hard. In order to achieve a scenario where this is the only hard vertex (as two or more hard vertices will suppress the amplitude considerably), the vector meson must be light, or the energies considered high. Therefore, for photoproduction of heavy vector mesons as threshold kinematics, Fig. 3.5c is suppressed. However, for light vector mesons or high photon energies, Fig. 3.5c will be appreciable, and will largely cancel Fig. 3.5a in the high energy limit. This is due, just as in the single-rescattering case, to the antisymmetry of the deuteron wave function under a proton-neutron swap. On the other hand, Fig. 3.5d is suppressed at all energy scales. Since there is a slow proton-neutron pair, the relative momentum of which is integrated over, the application of a closure relation is warranted as an approximation, meaning Fig. 3.5d does not make any appreciable contribution to the invariant amplitude beyond the contribution that Fig. 3.4d makes, which is already negligible.

The derivation follows the steps of the GEA, as before. Firstly, the full amplitude is written out using effective Feynman diagram rules. Secondly, the energy of the spectator

Feynman diagram for double rescattering contributions to $\gamma d \to Vpn$

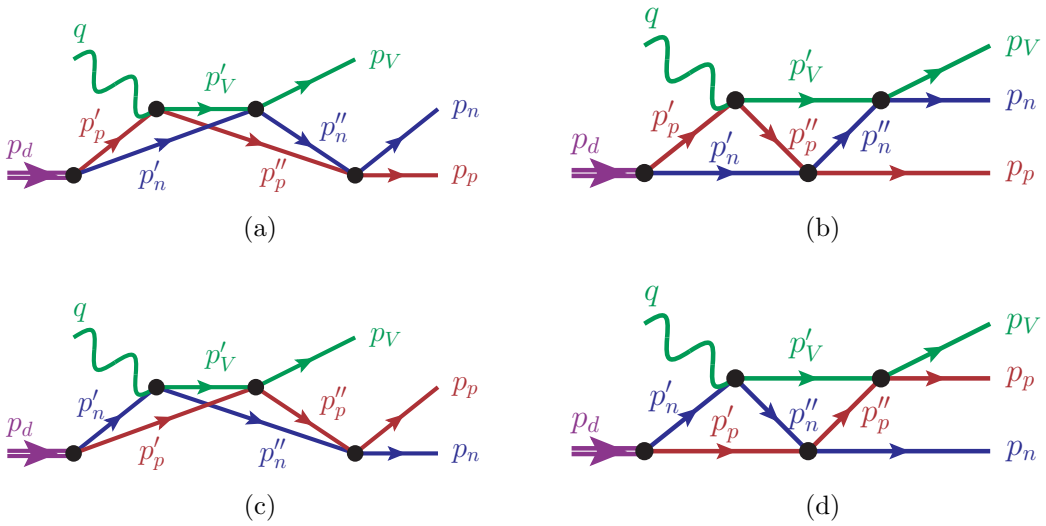

Figure 3.5: Effective Feynman diagrams for the double rescattering contributions to reaction (3.17).

nucleon is integrated over, and the positive energy pole is taken. This allows completeness relations to be used for the intermediate states of the spectator, and at the same time, an approximate completeness relation is used for the struck nucleon, allowing terms to be gathered into the VNA deuteron wave function. The remaining propagator is decomposed into pole and principal value parts, as in Eq. (3.43), after the propagator is (approximately) linearized through a change of variables. Due to the fact that already $\mathcal{M}_2 \ll \mathcal{M}_1$, and principal value parts of integrals are suppressed relative th the pole parts, only the pole terms for the double rescattering amplitudes will be considered here. Lastly, completeness relations are used for the remaining intermediate states, justified by the fact that the pole terms place these states on their mass shells, and the remaining terms are gathered into subprocess amplitudes.

First, using the effective Feynman rules for Fig. 3.5a, we have

$$\mathcal{M}_{2a}^{(\lambda_V,\lambda_p,\lambda_n;\lambda_\gamma,\lambda_d)} = -\bar{u}^{\lambda_p}(\mathbf{p}_p)\bar{u}^{\lambda_n}(\mathbf{p}_n)\phi_\pi^{*\,\lambda_V}(\mathbf{p}_V)\int\frac{d^4p'_n}{(2\pi)^4 i}\int\frac{d^4p''_n}{(2\pi)^4 i}\Bigg[\Gamma_{pn\to pn}$$
$$\frac{\not{p}''_p + m_N}{(p''_p)^2 - m_N^2 + i\epsilon}\frac{\not{p}''_n + m_N}{(p''_n)^2 - m_N^2 + i\epsilon}\Gamma^{\rho\pi}_{VN\to VN}\frac{G_{\rho\nu}(p'_V)}{(p'_V)^2 - m_V^2 + i\epsilon}$$
$$\Gamma^{\mu\nu}_{\gamma N\to VN}\epsilon_\mu^{\lambda_\gamma}(q)\frac{\not{p}'_p + m_N}{(p'_p)^2 - m_N^2 + i\epsilon}\frac{\not{p}'_n + m_N}{(p'_n)^2 - m_N^2 + i\epsilon}\Gamma_{dpn}\chi^{\lambda_d}\Bigg], \tag{3.54}$$

where the momenta are as notated in the figure. Next, integration over $p_n'^0$ and $p_n''^0$ is used to put the neutron on its positive-energy mass shell, and exact completeness relations are subsequently used for the intermediate neutron states. This gives:

$$\mathcal{M}_{2a}^{(\lambda_V,\lambda_p,\lambda_n;\lambda_\gamma,\lambda_d)} = -\bar{u}^{\lambda_p}(\mathbf{p}_p)\bar{u}^{\lambda_n}(\mathbf{p}_n)\phi_\pi^{*\,\lambda_V}(\mathbf{p}_V)\sum_{\lambda'_n\lambda''_n}\int\frac{d^3\mathbf{p}'_n}{(2\pi)^3}\int\frac{d^3\mathbf{p}''_n}{(2\pi)^3}\Bigg[\frac{1}{2E'_n}\frac{1}{2E''_n}$$
$$\Gamma_{pn\to pn}u^{\lambda''_n}(\mathbf{p}''_n)\bar{u}^{\lambda''_n}(\mathbf{p}''_n)\frac{\not{p}''_p + m_N}{(p''_p)^2 - m_N^2 + i\epsilon}\Gamma^{\rho\pi}_{VN\to VN}\frac{G_{\rho\nu}(p'_V)}{(p'_V)^2 - m_V^2 + i\epsilon}$$
$$u^{\lambda'_n}(\mathbf{p}'_n)\Gamma^{\mu\nu}_{\gamma N\to VN}\epsilon_\mu^{\lambda_\gamma}(q)\frac{\not{p}'_p + m_N}{(p'_p)^2 - m_N^2 + i\epsilon}\bar{u}^{\lambda'_n}(\mathbf{p}'_n)\Gamma_{dpn}\chi^{\lambda_d}\Bigg]. \tag{3.55}$$

Next, the approximate completeness relation $\not{p}'_p + m_N \approx \sum_{\lambda'_p} u^{\lambda'_p}(\mathbf{p}'_p)\bar{u}^{\lambda'_p}(\mathbf{p}'_p)$ is used for the struck proton, so terms can be gathered into the VNA deuteron wave function. This gives

$$\mathcal{M}_{2a}^{(\lambda_V,\lambda_p,\lambda_n;\lambda_\gamma,\lambda_d)} = -\bar{u}^{\lambda_p}(\mathbf{p}_p)\bar{u}^{\lambda_n}(\mathbf{p}_n)\phi_\pi^{*\,\lambda_V}(\mathbf{p}_V)\sum_{\lambda'_p\lambda'_n\lambda''_n}\int\frac{d^3\mathbf{p}'_n}{(2\pi)^3}\int\frac{d^3\mathbf{p}''_n}{(2\pi)^3}\Bigg[\sqrt{\frac{2(2\pi)^3}{2E'_n}}\frac{1}{2E''_n}$$
$$\Gamma_{pn\to pn}u^{\lambda''_n}(\mathbf{p}''_n)\bar{u}^{\lambda''_n}(\mathbf{p}''_n)\frac{\not{p}''_p + m_N}{(p''_p)^2 - m_N^2 + i\epsilon}\Gamma^{\rho\pi}_{VN\to VN}\frac{G_{\rho\nu}(p'_V)}{(p'_V)^2 - m_V^2 + i\epsilon}$$
$$u^{\lambda'_n}(\mathbf{p}'_n)\Gamma^{\mu\nu}_{\gamma N\to VN}\epsilon_\mu^{\lambda_\gamma}(q)u^{\lambda'_p}(\mathbf{p}'_p)\Psi_d^{(\lambda'_p,\lambda'_n;\lambda_d)}(\mathbf{p}'_n)\Bigg]. \tag{3.56}$$

Next, the integration variable is changed, with the purpose of allowing the remaining propagator denominators to be linearized. We define

$$K = p_n - p''_n \tag{3.57}$$

$$K' = p''_n - p'_n. \tag{3.58}$$

For the remaining proton propagator (*i.e.*, the one not absorbed into the VNA wave function),

$$\begin{aligned}(p_p'')^2 - m_N^2 + i\epsilon &= (p_p + p_n - p_n'')^2 - m_N^2 + i\epsilon = (p_p + K)^2 - m_N^2 + i\epsilon \\ &= K^2 + 2E_p K_0 - \mathbf{p}_p \cdot \mathbf{K}_\perp - p_{p,z} K_z + i\epsilon \\ &= 2p_{p,z}(\Delta_{2a} - K_z + i\epsilon),\end{aligned} \tag{3.59}$$

where we have

$$\Delta_{2a} = \frac{K^2 + 2E_p K_0 - 2\mathbf{p}_p \cdot \mathbf{K}_\perp}{2p_{p,z}}. \tag{3.60}$$

For the vector meson propagator,

$$\begin{aligned}(p_V')^2 - m_V^2 + i\epsilon &= (p_V + p_n'' - p_n')^2 - m_V^2 + i\epsilon = (p_V + K')^2 - m_V^2 + i\epsilon \\ &= (K')^2 + 2E_V K_0' - \mathbf{p}_V \cdot \mathbf{K}_\perp' - p_{V,z} K_z' + i\epsilon \\ &= 2p_{V,z}(\Delta_{2a}' - K_z' + i\epsilon),\end{aligned} \tag{3.61}$$

where in this case

$$\Delta_{2a}' = \frac{(K')^2 + 2E_V K_0' - 2\mathbf{p}_V \cdot \mathbf{K}_\perp'}{2p_{V,z}}. \tag{3.62}$$

Just as in the single rescattering case, these are (approximately) linearizations of the propagator denominators, because $\Delta_{2a}^{(\prime)}$ has a weak dependence on $K_z^{(\prime)}$, *i.e.* a nearly zero derivative. Thus we may evaluate $\Delta_{2a}^{(\prime)}$ when $K_z^{(\prime)}$ is zero, and then set $K_z^{(\prime)} = \Delta_{2a}^{(\prime)}$ for the pole part of the decomposition (3.43). As discussed above, the principal value parts of both denominators are neglected as small compared to an already small correction, so the pole values are used for both propagators. This justifies use of completeness relations for the

remaining propagator numerators, giving

$$\mathcal{M}_{2a}^{(\lambda_V,\lambda_p,\lambda_n;\lambda_\gamma,\lambda_d)} = -\frac{1}{4p_{p,z}p_{V,z}} \sum_{\lambda'_p\lambda'_n\lambda''_p\lambda''_n\lambda'_V} \int \frac{d^2\mathbf{K}_\perp}{(2\pi)^2} \int \frac{d^2\mathbf{K}'_\perp}{(2\pi)^2} \Bigg[\sqrt{\frac{2(2\pi)^3}{2E'_n}} \frac{1}{2E''_n}$$
$$\bar{u}^{\lambda_p}(\mathbf{p}_p)\bar{u}^{\lambda_n}(\mathbf{p}_n)\Gamma_{pn\to pn}u^{\lambda''_n}(\mathbf{p}''_n)u^{\lambda''_p}(\mathbf{p}''_p)$$
$$\bar{u}^{\lambda''_n}(\mathbf{p}''_n)\phi_\pi^{*\,\lambda_V}(\mathbf{p}_V)\Gamma^{\rho\pi}_{VN\to VN}\phi_\nu^{*\,\lambda'_V}(\mathbf{p}'_V)u^{\lambda'_n}(\mathbf{p}'_n)$$
$$\bar{u}^{\lambda''_p}(\mathbf{p}''_p)\phi_\rho^{\lambda'_V}(\mathbf{p}'_V)\Gamma^{\mu\nu}_{\gamma N\to VN}\epsilon_\mu^{\lambda_\gamma}(q)u^{\lambda'_p}(\mathbf{p}'_p)$$
$$\Psi_d^{(\lambda'_p,\lambda'_n;\lambda_d)}(p_{n,z}-\Delta_{2a}-\Delta'_{2a};\mathbf{p}_{n,\perp}-\mathbf{K}_\perp-\mathbf{K}'_\perp)\Bigg]. \tag{3.63}$$

Finally, terms are gathered into sub-reaction amplitudes, giving

$$\mathcal{M}_{2a}^{(\lambda_V,\lambda_p,\lambda_n;\lambda_\gamma,\lambda_d)} = -\frac{1}{4p_{p,z}p_{V,z}} \sum_{\text{spins}} \int \frac{d^2\mathbf{K}}{(2\pi)^2} \int \frac{d^2\mathbf{K}'}{(2\pi)^2} \Bigg[\sqrt{\frac{2(2\pi)^3}{2E'_n}}$$
$$\frac{1}{2E''_n}\mathcal{M}_{pn\to pn}^{(\lambda_p,\lambda_n;\lambda''_p,\lambda''_n)}(p_p,p_n;p''_p,p''_n)$$
$$\mathcal{M}_{VN\to VN}^{(\lambda_V,\lambda''_n;\lambda'_V,\lambda'_n)}(p_V,p''_n;p'_V,p'_n)\mathcal{M}_{\gamma N\to VN}^{(\lambda'_V,\lambda''_p;\lambda_\gamma,\lambda'_p)}(p'_V,p''_p;p_\gamma,p'_p)$$
$$\Psi_d^{(\lambda'_p,\lambda'_n;\lambda_d)}(p_{n,z}-\Delta_{2a}-\Delta'_{2a};\mathbf{p}_{n,\perp}-\mathbf{K}_\perp-\mathbf{K}'_\perp)\Bigg]. \tag{3.64}$$

Next, Fig. 3.5b is evaluated. The effective Feynman rules give

$$\mathcal{M}_{2b}^{(\lambda_V,\lambda_p,\lambda_n;\lambda_\gamma,\lambda_d)} = -\bar{u}^{\lambda_p}(\mathbf{p}_p)\bar{u}^{\lambda_n}(\mathbf{p}_n)\phi_\pi^{*\,\lambda_V}(\mathbf{p}_V) \int \frac{d^4p'_n}{(2\pi)^4 i} \int \frac{d^4p''_n}{(2\pi)^4 i} \Bigg[\Gamma^{\rho\pi}_{VN\to VN}$$
$$\frac{\not{p}''_n + m_N}{(p''_n)^2 - m_N^2 + i\epsilon} \frac{G_{\rho\nu}(p'_V)}{(p'_V)^2 - m_V^2 + i\epsilon} \Gamma_{pn\to pn} \frac{\not{p}''_p + m_N}{(p''_p)^2 - m_N^2 + i\epsilon}$$
$$\Gamma^{\mu\nu}_{\gamma N\to VN}\epsilon_\mu^{\lambda_\gamma}(q) \frac{\not{p}'_p + m_N}{(p'_p)^2 - m_N^2 + i\epsilon} \frac{\not{p}'_n + m_N}{(p'_n)^2 - m_N^2 + i\epsilon} \Gamma_{dpn}\chi^{\lambda_d}\Bigg], \tag{3.65}$$

where the momenta are as depicted in Fig. 3.5b. From here, integration over p''^0_n and p''^0_n places the neutron on its mass shell in its intermediate states, which also allows application of the completeness relation. An approximate completeness relation is also used for the struck proton, so terms can be absorbed into the deuteron VNA wave function. The two remaining propagator denominators—for the proton (with four-momentum p''_p) and the

vector meson—are dealt with, as before, by (approximately) linearizing the denominator. The following intermediate four-momenta are defined:

$$K = p_n - p_n'' \tag{3.66}$$

$$K' = p_n'' - p_n'. \tag{3.67}$$

For the intermediate vector meson state, this gives us

$$\begin{aligned}(p_V')^2 - m_V^2 + i\epsilon &= (p_V + K)^2 - m_V^2 + i\epsilon \\ &= K^2 + 2K_0E_V - 2K_z p_{V,z} - 2\mathbf{K}_\perp \cdot \mathbf{p}_{V,\perp} + i\epsilon \\ &= 2p_{V,z}(\Delta_{2b} - K_z + i\epsilon),\end{aligned} \tag{3.68}$$

where

$$\Delta_{2b} = \frac{K^2 + 2K_0E_V - 2\mathbf{K}_\perp \cdot \mathbf{p}_{V,\perp}}{2p_{V,z}}. \tag{3.69}$$

For the intermediate proton state, we have

$$\begin{aligned}(p_p'')^2 - m_N^2 + i\epsilon &= (p_p + K')^2 - m_N^2 + i\epsilon \\ &= (K')^2 + 2K_0'E_p - 2K_z' p_{p,z} - 2\mathbf{K}_\perp' \cdot \mathbf{p}_{p,\perp} + i\epsilon \\ &= 2p_{p,z}(\Delta_{2b}' - K_z' + i\epsilon),\end{aligned} \tag{3.70}$$

where

$$\Delta_{2b}' = \frac{(K')^2 + 2K_0'E_p - 2\mathbf{K}_\perp' \cdot \mathbf{p}_{p,\perp}}{2p_{p,z}}. \tag{3.71}$$

The Delta terms are evaluated when $K_z^{(\prime)} = 0$, since they are approximately independent of $K_z^{(\prime)}$. With the denominators effectively linearized, the propagators are decomposed into pole and principal value parts, the latter of which are neglected as comparatively small. The pole parts put the intermediate particles on their mass shells, and accordingly completeness

relations are used. Finally, terms are gathered into sub-reaction amplitudes. The result of applying all these operations is

$$\begin{aligned}\mathcal{M}_{2b}^{(\lambda_V,\lambda_p,\lambda_n;\lambda_\gamma,\lambda_d)} = -\frac{1}{4p_{p,z}p_{V,z}}\sum_{\text{spins}}\int\frac{d^2\mathbf{K}}{(2\pi)^2}\int\frac{d^2\mathbf{K}'}{(2\pi)^2}\Bigg[\sqrt{\frac{2(2\pi)^3}{2E'_n}} \\ \frac{1}{2E''_n}\mathcal{M}_{VN\to VN}^{(\lambda_V,\lambda_p;\lambda'_V,\lambda''_p)}(p_V,p_p;p'_V,p''_p) \\ \mathcal{M}_{pn\to pn}^{(\lambda_p,\lambda''_n;\lambda''_p,\lambda'_n)}(p_p,p''_n;p''_p,p'_n)\mathcal{M}_{\gamma N\to VN}^{(\lambda'_V,\lambda''_p;\lambda_\gamma,\lambda'_p)}(p'_V,p''_p;p_\gamma,p'_p) \\ \Psi_d^{(\lambda'_p,\lambda'_n;\lambda_d)}(p_{n,z}-\Delta_{2b}-\Delta'_{2b};\mathbf{p}_{n,\perp}-\mathbf{K}_\perp-\mathbf{K}'_\perp)\Bigg].\end{aligned} \tag{3.72}$$

Lastly, Fig. 3.5c is evaluated. The effective Feynman rules give

$$\begin{aligned}\mathcal{M}_{2c}^{(\lambda_V,\lambda_p,\lambda_n;\lambda_\gamma,\lambda_d)} = -\bar{u}^{\lambda_p}(\mathbf{p}_p)\bar{u}^{\lambda_n}(\mathbf{p}_n)\phi_\pi^{*\,\lambda_V}(\mathbf{p}_V)\int\frac{d^4p'_p}{(2\pi)^4 i}\int\frac{d^4p''_n}{(2\pi)^4 i}\Bigg[\Gamma_{pn\to pn} \\ \frac{\not{p}''_p+m_N}{(p''_p)^2-m_N^2+i\epsilon}\frac{\not{p}''_n+m_N}{(p''_n)^2-m_N^2+i\epsilon}\Gamma_{VN\to VN}^{\rho\pi}\frac{G_{\rho\nu}(p'_V)}{(p'_V)^2-m_V^2+i\epsilon} \\ \Gamma_{\gamma N\to VN}^{\mu\nu}\epsilon_\mu^{\lambda_\gamma}(q)\frac{\not{p}'_p+m_N}{(p'_p)^2-m_N^2+i\epsilon}\frac{\not{p}'_n+m_N}{(p'_n)^2-m_N^2+i\epsilon}\Gamma_{dpn}\chi^{\lambda_d}\Bigg],\end{aligned} \tag{3.73}$$

where the four-momenta are as depicted in Fig. 3.5c. The integration is over p'_p rather than p'_n, due to the proton being the spectator to the photon-nucleon interaction in this diagram. The energy integrations performed for this diagram are over p'^0_p and p''^0_n, which put the proton in the pre-photoproduction intermediate state and the neutron in the post-photoproduction intermediate state on their mass shells. With these hadrons on their mass shells, exact completeness relations can be used. An approximate completeness relation is additionally used for the struck neutron, so terms can be absorbed into the VNA deuteron wave function. It is important to note that for this diagram, a minus sign will be picked up, due to the proton-neutron swap relative to Fig. 3.5a. Next, the remaining intermediate hadron propagators—the proton state after meson-proton rescattering, with four-momentum p''_p and the vector meson—can be approximately linearized by using

a change of momentum variables. We define

$$K = p_n - p_n'' \tag{3.74}$$

$$K' = p_n' - p''. \tag{3.75}$$

The denominator for the remaining proton propagator is

$$\begin{aligned}(p_p'')^2 - m_N^2 + i\epsilon &= (p_p + K)^2 - m_N^2 + i\epsilon \\ &= K^2 + 2K_0 E_p - 2K_Z p_{p,z} - 2\mathbf{K}_\perp \cdot \mathbf{p}_{p,\perp} + i\epsilon \\ &= 2p_{p,z}(\Delta_{1c} - K_z + i\epsilon),\end{aligned} \tag{3.76}$$

where

$$\Delta_{1c} = \frac{K^2 + 2K_0 E_p - \mathbf{K}_\perp \cdot \mathbf{p}_{p,\perp}}{2p_{p,z}}. \tag{3.77}$$

The denominator for the intermediate vector meson propagator is

$$\begin{aligned}(p_V')^2 - m_V^2 + i\epsilon &= (q + K')^2 - m_V^2 + i\epsilon \\ &= (K')^2 + q_0 K_0 - q_0 K_z - m_V^2 + i\epsilon \\ &= 2q_0(\Delta_{1c}' - K_z + i\epsilon),\end{aligned} \tag{3.78}$$

where

$$\Delta_{1c}' = \frac{(K')^2 - m_V^2}{2q_0} + K_0. \tag{3.79}$$

As above, $\Delta_{1c}^{(\prime)}$ is approximately independent of $K_z^{(\prime)}$, and accordingly can be evaluated when $K_z^{(\prime)} = 0$, thus linearizing the denominators. Eq. (3.43) is then used to decompose each propagator into a pole and PV part, the latter of which is neglected as small. Finally, for the pole part, the mass shell relations are valid, making completeness relations exact;

these are used, and terms are gathered into sub-reaction amplitudes, and we have

$$\mathcal{M}_{2c}^{(\lambda_V,\lambda_p,\lambda_n;\lambda_\gamma,\lambda_d)} = +\frac{1}{4q_0 p_{p,z}} \sum_{\text{spins}} \int \frac{d^2\mathbf{K}}{(2\pi)^2} \int \frac{d^2\mathbf{K}'}{(2\pi)^2} \Bigg[\sqrt{\frac{2(2\pi)^3}{2E'_p}} \\ \frac{1}{2E''_n} \mathcal{M}_{pn\to pn}^{(\lambda_p,\lambda_n;\lambda''_p,\lambda''_n)}(p_p, p_n; p''_p, p''_n) \\ \mathcal{M}_{VN\to VN}^{(\lambda_V,\lambda''_p;\lambda'_V,\lambda'_p)}(p_V, p''_p; p'_V, p'_p) \mathcal{M}_{\gamma N\to VN}^{(\lambda'_V,\lambda''_p;\lambda_\gamma,\lambda'_p)}(p'_V, p''_n; p_\gamma, p'_n) \\ \Psi_d^{(\lambda'_n,\lambda'_p;\lambda_d)}(-p_{n,z} + \Delta_{2a} + \Delta'_{2a}; -\mathbf{p}_{n,\perp} + \mathbf{K}_\perp + \mathbf{K}'_\perp) \Bigg]. \tag{3.80}$$

Considerations for numerical estimates

In the following two sections, the formalism developed here will be applied to diffractive photoproduction of $\phi(1020)$ and J/ψ accompanied by deuteron breakup. Before proceeding to specific applications of the formalism, however, some considerations should be explored regarding how numerical estimates should be performed and presented.

To begin, while the formulas derived for $\mathcal{M}_0$, $\mathcal{M}_{1a}$, *etc.* are presented in terms of sub-reaction amplitudes such as $\mathcal{M}_{\gamma N\to VN}$ and so on, it is most useful to parametrize reactions in terms of the diffractive scattering amplitude $f(s,t)$. After Eq. (3.7), we write

$$\mathcal{M}_{AB\to CD}^{(\lambda_C,\lambda_D;\lambda_A,\lambda_B)}(s,t) = \frac{\Phi_{AB}}{2} f_{AB\to CD}^{(\lambda_C,\lambda_D;\lambda_A,\lambda_B)}(s,t), \tag{3.81}$$

where Φ_{AB} is as given in Eqs. (3.2-3.5). The diffractive amplitude is useful in particular because it is normalized so that $\text{Im}(f(s,0)) = \sigma_{\text{tot.}}$. Thus, for the special case $A = C$ and $B = D$, we can, assuming helicity conservation, parametrize the diffractive amplitude in the form

$$f_{AB\to CD}^{(\lambda_C,\lambda_D;\lambda_A,\lambda_B)}(s,t) = \sigma_{AB}^{\text{tot.}}(s)[i + \alpha(s)] \exp\left(\frac{b(s)}{2} t\right) \delta_{\lambda_A\lambda_C} \delta_{\lambda_B\lambda_D}. \tag{3.82}$$

For the case of the $pn \to pn$ sub-reaction, existing data is used to parametrize the diffractive scattering amplitude. Values for $\sigma_{\text{tot.}}(s)$, $\alpha(s)$, and $b(s)$ are extracted from SAID data [105] for low energies and from Particle Data Group data [106] at high energies, with the region between connected by a cubic spline.

For the case of the $VN \to VN$ sub-reaction, since the vector meson-nucleon interaction is the object of study in this work, the parametrization of Eq. (3.82) is used in numerical computations with varied values of the slope factor b_{VN} and the total cross section $\sigma_{VN}^{\text{tot.}}$ in order to study the sensitivity of the overall $\gamma d \to Vpn$ cross section on these parameters.

Finally, for the $\gamma N \to VN$ sub-reaction, existing parameterizations of the photoproduction amplitude are used. The forms of these parameterizations will be elaborated on in the specific $\phi(1020)$ and J/ψ sections.

Besides the parametrization of sub-reaction amplitudes, another consideration to bear in mind is the presentation of the computations. This will be geared towards being useful for experimental searches. Absolute cross sections are notoriously difficult to measure, so ratios of cross sections will be presented in addition to absolute cross sections. While it is theoretically enlightening to present ratios of the form

$$\frac{\sigma_{\text{full}}}{\sigma_{\text{PWIA}}},$$

(where σ is shorthand for the five-fold differential cross section of Eq. (3.29)) it is impossible in real experiments to turn off higher-order diagrams and measure only the PWIA cross section to feed into such a ratio. Instead, estimates will be presented in the form of ratios

$$R = \frac{\sigma\left(p_n^{(2)}\right)}{\sigma\left(p_n^{(1)}\right)}, \tag{3.83}$$

i.e. between the five-fold cross section measured at two different values of the spectator (neutron) momentum.

3.3 Photoproduction of $\phi(1020)$ mesons

Photoproduction of $\phi(1020)$ from nuclear targets has attracted a great deal of interest due to the large ϕ-N cross sections measured in these reactions; *cf.* Refs. [107, 108] for example. Specifically, these experiments measured the $\gamma A \to \phi A$ cross section and analyzed the

reaction in a Glauber model framework in order to extract the ϕ-N cross section, finding values varying between 16-70 mb [109].

These large ϕ-N cross sections are interesting because they contradict the predictions of the vector meson dominance (VMD) model. VMD considers the physical (as opposed to the bare) photon to be in a superposition of different hadronic states with the quantum numbers of the bare photon, *i.e.* the photon has a probability of being found to be various odd-parity, neutral vector mesons. VMD predicts a relationship between the $\gamma N \to VN$ and $VN \to VN$ differential cross sections, namely of the form

$$\left(\frac{d\sigma}{dt}\right)_{\gamma N \to VN} = \frac{e^2}{f_{VN}^2}\left(\frac{d\sigma}{dt}\right)_{VN \to VN}, \tag{3.84}$$

where f_{VN} is a coupling constant for the V-N interaction. (See Refs. [98, 110] for more details about VMD.) The prediction for the ϕ-N cross section from vector meson dominance is $\sigma_{\phi N} \approx 11$ mb [111], significantly less than the values found from rescattering in nuclear target experiments. The variety of values measured for $\sigma_{\phi N}$ has led to speculation about medium modifications of the ϕ meson, and thus variation of $\sigma_{\phi N}$ within the nuclear medium [109].

In recent years, several experiments have measured phi photoproduction from a deuteron target specifically [96, 109, 112, 113]. Ref. [112] studied both incoherent and coherent ϕ photoproduction, in the reactions $d(\gamma, pK^+K^-)n$ and $d(\gamma, K^+K^-)d$ respectively. Incoherent production in the photon energy range $E_\gamma = 1.65$-3.59 GeV suggested a ϕ-N cross section in excess of 20 mb. Coherent production also showed the presence of ϕ-N rescattering, with measured cross sections in excess of the PWIA prediction, but could not decide between the VMD model (with $\sigma_{\phi N} \approx 10$ mb) and the larger cross section measurements. In particular, choosing the slope factor to be a large value (*e.g.*, $B_{\phi N} \approx 10$ GeV^{-2} [88]) in addition to the total ϕ-N cross section gave coherent $\gamma d \to \phi d$ cross sections consistent with the predictions of VMD [96, 112].

We show, however, that the breakup reaction $\gamma + d \to \phi + p + n$ is sensitive enough to the ϕ-N interaction to distinguish between these models. In order to demonstrate this,

the formalism of Sec. 3.2 is applied to photoproduction of $\phi(1020)$ in particular, for both models of the ϕ-N interaction. The formalism is applied in the energy range that coherent production was explored in a JLab experiment [96], and the $\gamma N \to \phi N$ photoproduction amplitude is parametrized based on a Pomeron exchange model from Ref. [98][2], namely:

$$f_{\gamma N\to\phi N}(s,t) = \left(\frac{s}{1\ \mathrm{GeV}^2}\right)^{\alpha_{\mathrm{R}}(t)-1} A(i+\alpha(s)) \exp\left(\frac{1}{2}\left(Bt + Ct^2\right)\right), \tag{3.85}$$

where $\alpha_R(t) = 1.14 + (0.27\ \mathrm{GeV}^{-2})t$ is the Regge trajectory predicted by the model, and the parameters $A = 0.372\ \mathrm{GeV}^{-2}$, $B = 4.8\ \mathrm{GeV}^{-2}$, and $C = 1.7\ \mathrm{GeV}^{-4}$ are taken as constants. (*n.b.* that, according to Ref. [98], different sets of ϕ photoproduction data from proton targets can only be made consistent by taking into account a non-zero quadratic coefficient C.) Additionally, the factor $\alpha(s) = -0.5$ is taken from Ref. [98].

The vector meson dominance model models $f_{\phi N\to\phi N}(s,t)$ after $f_{\gamma N\to\phi N}(s,t)$ as contained in Eq. (3.85), but with the normalization set so that $\mathrm{Im}(f_{\phi N\to\phi N}(s,0)) = 10$ mb, in accordance with the optical theorem and the VMD prediction for the ϕ-N cross section. By contrast, in the "30-10" model of Laget [88] (named for $\sigma_{\phi N} = 30$ mb and $B_{\phi N} = 10\ \mathrm{GeV}^{-2}$), we use a simpler parametrization for the ϕ-N diffractive amplitude:

$$f_{\phi N\to\phi N}(s,t) = \sigma_{\phi N}(i-\alpha(s)) \exp\left(\frac{1}{2}Bt\right), \tag{3.86}$$

with $\alpha = -0.5$ taken in this case too.

With the prerequisites for modeling the sub-reactions in hand, we first proceed to produce numerical estimates for ϕ photoproduction from the deuteron in the plane wave impulse approximation, and with the contributions of $\mathcal{M}_{1a}$ (ϕ-neutron rescattering) and $\mathcal{M}_{1b}$ (proton-neutron rescattering) taken into account. Such estimates are presented in Fig. 3.6, for an incident photon energy of $q_0 = 5$ GeV and momentum transfer $-t = 1.2\ \mathrm{GeV}^{-2}$, for three values of the spectator neutron momentum ($p_n = 100$, 200, and 400 MeV). Here, σ is notational shorthand for the differential cross section $\sigma \equiv d^5\sigma/d^3\mathbf{p}_V d\Omega_p$ as given in

[2] *cf.* Eqs. (3.85b,3.85c) of *ibid.*

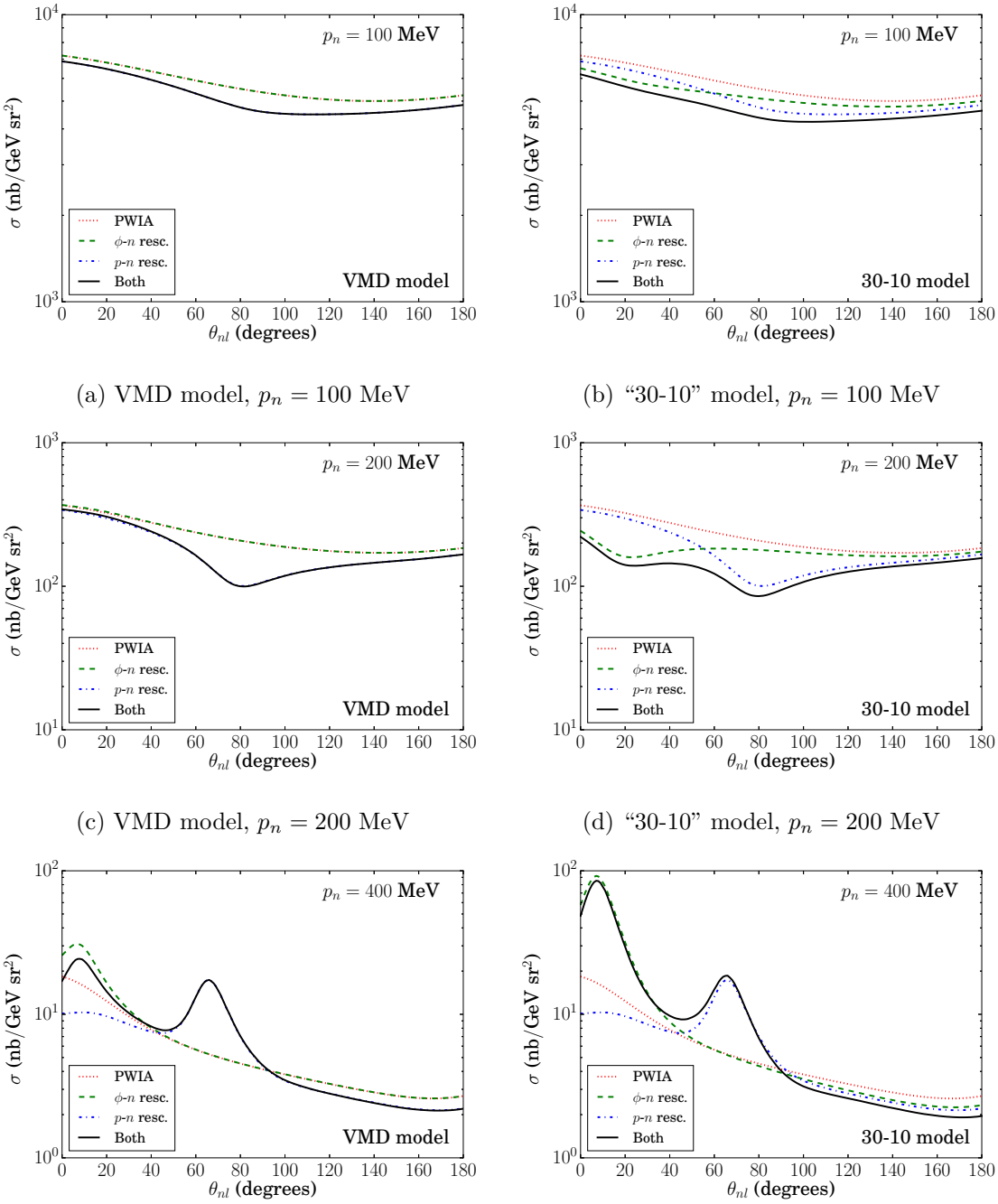

(a) VMD model, $p_n = 100$ MeV

(b) "30-10" model, $p_n = 100$ MeV

(c) VMD model, $p_n = 200$ MeV

(d) "30-10" model, $p_n = 200$ MeV

(e) VMD model, $p_n = 400$ MeV

(f) "30-10" model, $p_n = 400$ MeV

Figure 3.6: Angular dependence of the ϕ photoproduction cross section at different neutron momenta, for both the VMD and "30-10" models of the ϕ-N interaction. These plots consider the contributions due to rescattering of the proton and the ϕ from the spectator neutron. $q_0 = 5$ GeV and $-t = 1.2$ GeV^2.

Eq. (3.29). Figs. 3.6a,3.6c,3.6e employ the vector meson dominance model to describe the ϕ-n interaction, while Figs. 3.6b,3.6d,3.6f employ the "30-10" model of Laget.

Two features of these plots are immediately striking: the first is that, depending on the neutron momentum, there are valleys (for $p_n = 200$ MeV) or peaks (for $p_n = 400$ MeV) in the angular distribution of the cross section, due to the ϕ-n and p-n rescatterings. The small-angle ($\theta_{nl} \approx 10^\circ$) valley/peak is due to the ϕ-n rescattering, whereas the larger-angle ($\theta_{nl} \approx 70^\circ$) valley/peak is due to the p-n FSI. The second striking feature is that the size of the ϕ-n rescattering peak differs between the models, with the "30-10" model predicting a significantly larger rescattering peak.

The distinction between the 200 MeV valleys and the 400 MeV peaks is due to the single rescattering contribution entering with an overall opposite sign from the PWIA contribution. At low neutron momenta (*e.g.*, $p_n = 100$ MeV), the rescattering contribution is too small for the destructive interference to be visible. At moderate neutron momenta (*e.g.*, $p_n = 200$ MeV), the destructive interference manifests as two valleys in the differential cross section—one due to the ϕ-N rescattering contribution, and one due to p-n rescattering. At high neutron momenta (*e.g.*, $p_n = 400$ MeV), the single rescattering contribution becomes so large that the cross section is increased overall at specific kinematics, despite the destructive interference between the PWIA and rescattering contributions. This results in peaks at $p_n = 400$ MeV at θ_{nl} values where $p_n = 200$ MeV saw valleys.

The particular locations of the valleys and peaks can be understood in terms of the reaction geometry, as seen in Fig. 3.1. Rescattering of a particle from the spectator produces the largest contribution when the scattered hadron is roughly perpendicular to the scatterer. Since the proton has a greater momentum than the neutron, this means the p-n rescattering peak or valley should occur between $45^\circ < \theta_{nl} < 90^\circ$; for $|\mathbf{p}_p| \gtrsim 2|\mathbf{p}_n|$, for instance, the peak should occur at about $\theta_{nl} \gtrsim 60^\circ$, where a rescattering peak can be clearly seen. The presence of a p-n rescattering peak at this angle is also well-known from deuteron electrodisintegration [85–87, 89–92].

Deuteron breakup accompanied by meson photoproduction, by contrast, contains a second valley or peak at a smaller value of θ_{nl}. This is due to meson-nucleon rescattering.

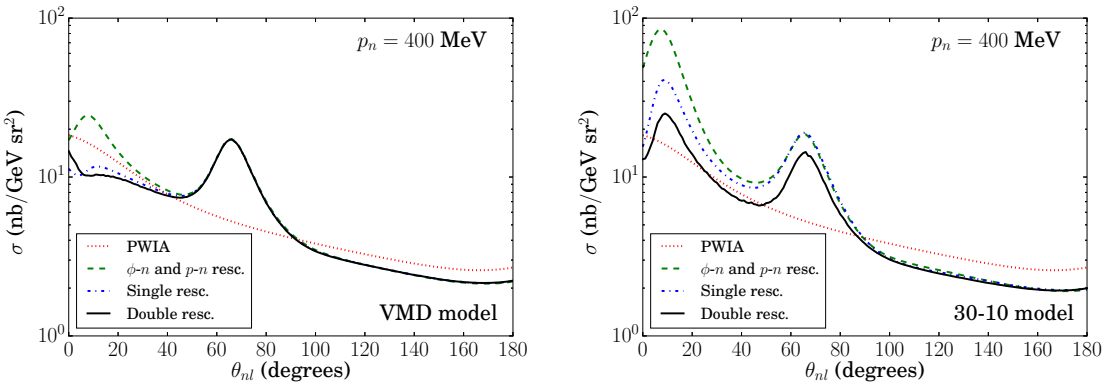

(a) VMD model, $p_n = 400$ MeV

(b) "30-10" model, $p_n = 400$ MeV

Figure 3.7: Angular dependence of the ϕ photoproduction cross section at $p_n = 400$ MeV, for both the VMD and "30-10" models of the ϕ-N interaction. These plots compare the PWIA against cross sections with single- and double-rescattering contributions. $q_0 = 5$ GeV and $-t = 1.2$ GeV^2.

As can be seen in Fig. 3.1, the meson-nucleon rescattering peak is expected to occur at smaller values of θ_{nl} than the p-n rescattering peak. This feature is present in Fig. 3.6, and was previously found to exist by a previous theoretical calculation [88].

Next, we explore the contribution of $\mathcal{M}_{1c}$ to the $\phi(1020)$ production amplitude, as well as the contribution of double rescatterings. Numerical estimates can be seen in Fig. 3.7. $\mathcal{M}_{1c}$ is the amplitude for the ϕ meson to be produced from the slow-moving neutron, and then to subsequently rescatter from the proton, giving the latter a large "kick" to a high-momentum state. Its contribution, when added to the contributions of the other single-rescattering amplitudes, can be seen in the dash-dotted (blue) lines of Fig. 3.7. Due to the antisymmetry of the deuteron wave function, $\mathcal{M}_{1c}$ has an opposite sign from $\mathcal{M}_{1a}$, and accordingly partially or fully cancels the valley or peak produced by the former. The double rescattering amplitudes, additionally, enter with an overall opposite sign from the single rescattering amplitudes, thus partially canceling the latter's contribution.

As discussed in Sec. 3.2.2, it is conducive to the purpose of studying ϕ-N rescattering to look at ratios of the differential cross section at different spectator momenta (*cf.* Eq. (3.83)). Since, as can be seen in Fig. 3.6, there are rescattering peaks in the cross

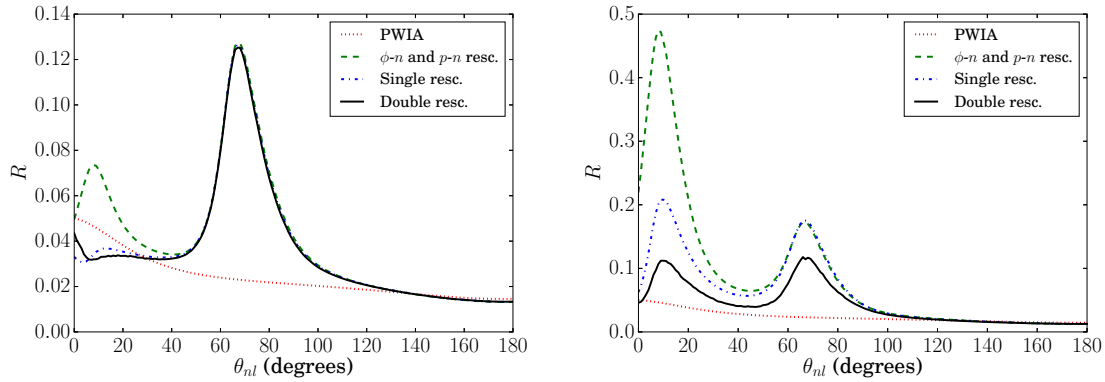

(a) VMD model

(b) "30-10" model

Figure 3.8: Angular dependence of the ratio defined in Eq. (3.87), for two models of the ϕ-N interaction. $q_0 = 5$ GeV and $-t = 1.2$ GeV^2.

section at $p_n = 400$ MeV and valleys at $p_n = 200$ MeV, taking the ratio

$$R_\phi = \frac{\sigma(p_n = 400 \text{ MeV})}{\sigma(p_n = 200 \text{ MeV})} \tag{3.87}$$

will enhance the visibility of the rescattering peaks.

In Fig. 3.8, numerical estimates of R_ϕ (as defined in Eq. (3.87) are presented for both the VMD and the "30-10" models of the ϕ-N interaction. Fig. 3.8a employs vector meson dominance, whereas Fig. 3.8b uses the "30-10" model.

It can be seen that these two models predict starkly different behavior for the ratio R_ϕ. Even qualitatively, vector meson dominance predicts no ϕ-N rescattering peak, due to the contributions from $\mathcal{M}_{1a}$ (Fig. 3.4a) and $\mathcal{M}_{1c}$ (Fig. 3.4c) canceling almost perfectly; however, in the "30-10" model, the cancellation is imperfect, and the ϕ-N scattering peak survives. Quantitatively, the "30-10" model predicts a cross section ratio that is about an order of magnitude greater at $\theta_{nl} \approx 10^\circ$ than VMD.

It is worth discussing why the cancellation between $\mathcal{M}_{1a}$ and $\mathcal{M}_{1c}$ are (nearly) perfect for one model and imperfect for the other. The nearly perfect cancellation in the VMD model is due to the photoproduction and ϕ rescattering amplitude having the same t dependence as the photoproduction amplitude (as is an assumption of vector meson dominance).

Moreover, whereas for Fig. 3.4a, one has

$$t_{\gamma N\to\phi N} = (p_p - p'_p)^2$$
$$t_{\phi N\to\phi N} = (p_n - p'_n)^2,$$

the formulas for t for the contribution of Fig. 3.4c are instead

$$t_{\gamma N\to\phi N} = (p_n - p'_n)^2$$
$$t_{\phi N\to\phi N} = (p_p - p'_p)^2.$$

In other words, the formulas for t are switched between the sub-reactions. Since in the VMD model, the t dependence of both sub-reactions is the same, the t dependence of $\mathcal{M}_{1a}$ and $\mathcal{M}_{1c}$ is identical in VMD, and these amplitudes enter with a relative minus sign due to the isospin asymmetry of the deuteron wave function. Therefore, nearly perfect cancellation occurs between these contributions.

By contrast, the "30-10" model of the ϕ-N interaction predicts different t dependence for the ϕ photoproduction and rescattering sub-reactions. Accordingly, the cancellation is imperfect, at least at the relatively low energy range considered here. At specific kinematics, the cancellation will still be perfect. Firstly, if the proton and neutron are produced with equal momenta on opposite sides of the scattering plane (making $\mathbf{l}$ parallel to the z axis), then the kinematic symmetry would result in perfect cancellation. Secondly, at sufficiently large photon energies, the kinematic constraints which guarantee a one-hard, one-soft vertex scenario are not present, so $t_{\gamma N\to\phi N}$ and $t_{\phi N\to\phi N}$ will take on similar values, resulting in near-perfect cancellation between $\mathcal{M}_{1a}$ and $\mathcal{M}_{1c}$.

To conclude this section, the breakup reaction (3.17) for $V = \phi$ is able to effectively discriminate between two models of the ϕ-N scattering interaction at low energies. Accordingly, we suggest that it be used to complement other methods of studying the ϕ-N interaction, especially at near-threshold energies.

3.4 Photoproduction of J/ψ mesons

Photoproduction of J/ψ in deuteron breakup reactions will be studied here in three different kinematic regimes: firstly, for near- (but above-) threshold kinematics, in Sec. 3.4.1; secondly, for below-threshold kinematics in Sec. 3.4.2; and lastly, for extremely high-energy kinematics in Sec. 3.4.3. Examining J/ψ photoproduction in these different kinematic regimes will allow different features of the eikonal dynamics of final state interactions to manifest. In particular, for near-threshold kinematics, the rescattering peaks and valleys seen in Sec. 3.3 for $\phi(1020)$ production will be visible for J/ψ production as well. For below-threshold kinematics, the requisite kinematic conditions for J/ψ production will suppress FSIs and render their effects invisible. Lastly, for extremely high energies, different rescattering mechanisms (*i.e.*, from Figs. 3.4a,3.4a) will cancel each other out near-perfectly, resulting in the absence of a J/ψ-N rescattering peak at these energies.

3.4.1 Near-threshold J/ψ production

Near-threshold photoproduction of J/ψ is especially pertinent to Jefferson Lab in light of the 12 GeV energy upgrade [114]. The threshold for photoproduction is defined as on a proton target, and occurs when the J/ψ meson and the target proton are both at rest in the center-of-mass frame. Accordingly, $s_{\text{thr.}} = (m_p + m_\Psi)^2$. In the lab frame, where the proton is initially at rest, a threshold s value entails $(p_\gamma + p_p)^2 = m_p^2 + 2m_p E_\gamma = (m_p + m_\Psi)^2$, making the formula for the threshold photoproduction energy

$$E_{\text{thr.}} = \frac{m_\Psi^2 + 2m_p m_\Psi}{2m_p} \approx 8.2 \text{ GeV}, \tag{3.88}$$

given a J/ψ mass of $m_\Psi = 3.09$ GeV. J/ψ photoproduction in particular is a worthwhile subject of study at near-threshold kinematics because such kinematics guarantee the applicability of the generalized eikonal approximation. In particular, at threshold, one has a

large $|t|$ value. Since, in the center-of-mass frame, $E_\gamma = \frac{s-m_p^2}{2\sqrt{s}}$ and $E_\Psi = \frac{s+m_\Psi^2-m_p^2}{2\sqrt{s}}$, we have

$$\begin{aligned} t_{\text{thr}} = (q - p_\Psi)^2 &= m_\Psi^2 - 2\frac{(s_{\text{thr.}} - m_p^2)(s_{\text{thr.}} + m_\Psi^2 - m_p^2)}{4s_{\text{thr.}}} \\ &= m_\Psi^2 - \frac{(2m_p m_\Psi + m_\Psi^2)(2m_p m_\Psi)}{2(m_p + m_\Psi)^2} \\ &= -\frac{m_\Psi^2 m_p}{m_p + m_\Psi} \approx -2.23 \text{ GeV}^{-2}. \end{aligned} \tag{3.89}$$

Above but close to the production threshold, a range of t values will be available, but as long as the photon energy is kept close to 8.2 GeV, the minimum $|t|$ value will be large and the eikonal regime will be established. $|t_{\text{thr.}}|$ is sufficiently high for J/ψ that the perturbative expansion of QCD is applicable, allowing multi-gluon exchange models to be explored as a photoproduction or rescattering mechanism. By contrast, using Eq. (3.89) with the $\phi(1020)$ mass in place of the J/ψ mass produces a threshold t value closer to -0.5 GeV^{-2}.

Near-threshold J/ψ production is studied here as a means of exploring the J/ψ-N interaction, the nature and strength of which are currently not well-understood. The vector meson dominance model suggests a total J/ψ-N cross section of around 1 mb [115] at high energies, but similar to the case of $\phi(1020)$, experimental data suggest a higher cross section, on the order of 3.5 mb [116]. On the theoretical side, different models of J/ψ production based on perturbative QCD make different predictions for the cross section's energy dependence. For instance, leading-twist pQCD calculations using a two-gluon exchange mechanism [117] predict a monotonically increasing energy dependence that asymptotically approaches a fixed high-energy value, thus suggesting a low J/ψ-N cross section for near-threshold kinematics. On the other hand, other models attempt to account for non-perturbative effects and make yet larger predictions for the low-energy J/ψ-N cross section, one estimate going as large as 17 mb [118].

To ascertain the sensitivity of the breakup reaction (3.17) to the strength and nature of the J/ψ-N interaction, we use a cross section ratio, just as in the case of $\phi(1020)$ production. Since the higher J/ψ mass allows for higher spectator momenta to be explored while still maintaining the requirements of the eikonal regime (*cf.* Fig. 3.2b), we take the ratio this

time to be

$$R_\Psi = \frac{\sigma(p_n = 600 \text{ MeV})}{\sigma(p_n = 200 \text{ MeV})}. \tag{3.90}$$

The larger value of p_n is chosen in the numerator in order to maximize the rescattering effects.

Since the sub-reaction amplitudes for J/ψ production from a constituent nucleon and J/ψ rescattering from the spectator do not factorize, care must be taken in treating the $\gamma N \to J/\psi N$ amplitude, which may be strongly energy-dependent near threshold. For this reason, two models of J/ψ photoproduction, from Ref. [119], are examined and used in our numerical estimates.

The first model considers photoproduction to be dominated by the leading-twist, two-gluon exchange contribution [119]. Eq. (3) from *ibid.* parametrizes the differential cross section based on this model as

$$\frac{d\sigma}{dt} = \frac{\mathcal{N}_{2g}^2}{16\pi} \frac{(1-x)^2}{e}^{Bt}, \tag{3.91}$$

where we have taken the liberty of absorbing several constants from Eq. (3) of Ref. [119] into the overall normalization constant $\mathcal{N}_{2g}^2$ (which has been squared and divided by 16π so that it is a linear constant in the scattering amplitude), and to evaluating the phase space factor. In [119], x was taken to be

$$x = \frac{2m_p m_\Psi + m_\Psi^2}{s - m_p^2} = \frac{s - s_{\text{thr.}}}{s - m_p^2} \tag{3.92}$$

and we take the same value of x here, giving

$$\frac{d\sigma}{dt} = \mathcal{N}_{2g}^2 \left(\frac{s - s_{\text{thr.}}}{s - m_p^2} \right)^2 e^{Bt}. \tag{3.93}$$

This allows the diffractive scattering amplitude parametrization of Eq. (3.9) to be used, with $C = 0$ and

$$A_{2g}(s) = \mathcal{N}_{2g} \left(\frac{s - s_{\text{thr.}}}{s - m_p^2} \right). \tag{3.94}$$

We find that a normalization constant of $\mathcal{N}_{2g} = 1.35$ GeV^{-2} gives an accurate fit to existing J/ψ photoproduction data from SLAC [120]. The slope factor B is given a slight t dependence in the form

$$B_{\text{eff.}}(t) = \frac{4}{1 \text{ GeV}^2 - t}. \tag{3.95}$$

as suggested by a theoretical study of the nucleon's two-gluon form factor [121]. A low-energy slope factor of $B = 1.25$ GeV^{-2} was measured in a Cornell experiment [122], although with threshold value of $t_{\text{thr.}} = -2.23$ GeV^{-2}, one has $B_{\text{eff.}}(t_{\text{thr.}}) \approx 1.24$ GeV^{-2}, thus reproducing the required low-energy form.

In addition to a two-gluon exchange model, Ref. [119] considered a possible dominance of a three-gluon exchange mechanism in the photoproduction of J/ψ. Near threshold, after all, the phase space is very limited, and this may favor a coherent interaction of all three valence quarks in the nucleon with the charmonium state. For this model, we take Eq. (4) of Ref. [119], as before absorbing constants into the overall normalization factor and evaluating the phase space factor to get:

$$\frac{d\sigma}{dt} = \frac{\mathcal{N}_{3g}^2}{16\pi} e^{Bt}. \tag{3.96}$$

Comparison with Eq. (3.9) gives $C = 0$ as before, and

$$A_{3g}(s) = \mathcal{N}_{3g}, \tag{3.97}$$

where a normalization constant of $\mathcal{N}_{3g} = 0.35$ GeV^{-2} fits the Cornell data [122] for J/ψ photoproduction. Since the three-gluon form factor of the nucleon is not well-known, we adopt the constant value $B = 1.25$ GeV^{-2} determined by *ibid.*

In Fig. 3.9, predictions for the ratio R_Ψ as defined in Eq. (3.90) are given for both the two- and three-gluon exchange mechanisms. For both models, the diffractive J/ψ-N scattering amplitude is parametrized in the form of Eq. (3.9), with $\sigma_{\Psi N} = 5$ mb and $B = 1.25$ GeV-2. As in the $\phi(1020)$ case, there are two rescattering peaks, with the peak at $\theta_{nl} \gtrsim 60^\circ$ due to proton-neutron rescattering and that at $\theta_{nl} \approx 30^\circ$ due to J/ψ-nucleon rescattering.

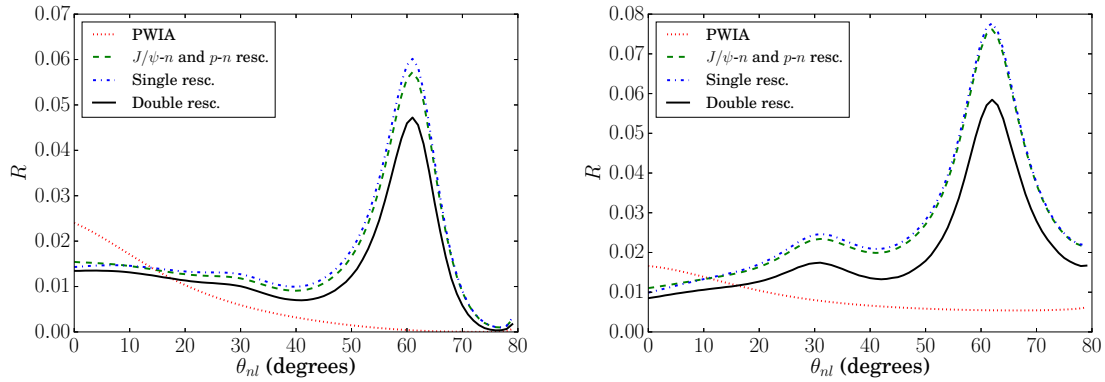

(a) Two-gluon mechanism

(b) Three-gluon mechanism

Figure 3.9: Angular dependence of the ratio defined in Eq. (3.90), for the (a) two- and (b) three-gluon exchange models of J/ψ photoproduction. Assumes $\sigma_{\Psi N} = 5$ mb. $q_0 = 10$ GeV and $t = t_{\text{thr.}} = -2.23$ GeV^2.

Fig. 3.9 demonstrates that the reaction (3.17) shows sensitivity to the energy dependence of the J/ψ photoproduction mechanism. There is a strong qualitative difference between the predictions of the models, with the J/ψ-N rescattering peak barely visible in the two-gluon model—in fact, likely to be invisible in light of uncertainties in any experimental search. Quantitatively, the ratio R_Ψ is greater for the three-gluon than the two-gluon mechanism by a factor of ~ 2 at $\theta_{nl} \approx 30°$. Moreover, at $\theta_{nl} \approx 75°$ (near the kinematic limit), the two-gluon mechanism produces a dip in the ratio R_ϕ not present in the three-gluon model.

This dip is due to the factor of $(s - s_{\text{thr.}})$ in $A_{2g}(s)$. When θ_{nl} close to the upper limit, the angle between the outgoing proton and the J/ψ is smaller (see Fig. 3.1), thus making $s_{\gamma p} = m_p^2 + m_\Psi^2 + 2E_pE_\psi - 2\mathbf{p}_p \cdot \mathbf{p}_\Psi$, which enters into $A_{2g}(s)$ in the PWIA, smaller and thus closer to $s_{\text{thr.}}$. This effect is less pronounced when single-rescattering corrections are taken into account because the s that enters into $A_{2g}(s)$ isn't exactly $(p_p + p_\Psi)^2$ for the rescattering diagrams. Moreover, the fact that the rescattering peak is present at θ_{nl} where the PWIA cross section begins to decrease is what makes the J/ψ-N rescattering peak so difficult to see for the two-gluon exchange mechanism; the effect of the rescattering correction does more to lessen the falloff of the cross section with increasing θ_{nl} than to

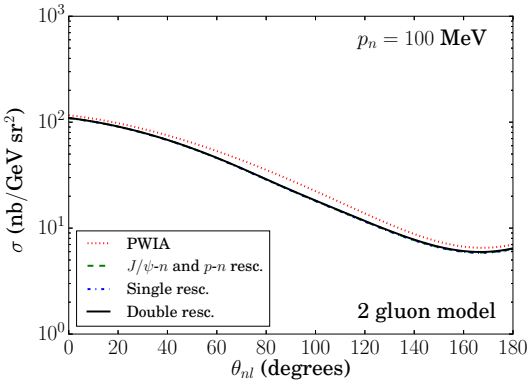

(a) Two-gluon model, $p_n = 100$ MeV

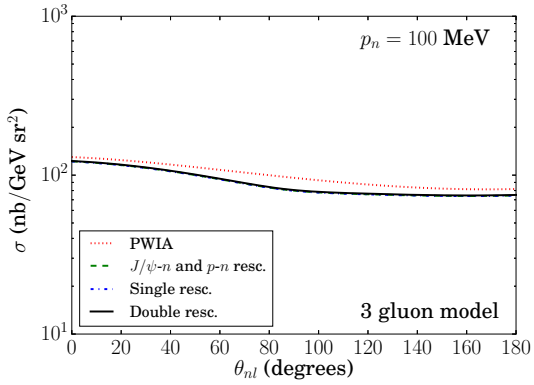

(b) Three-gluon model, $p_n = 100$ MeV

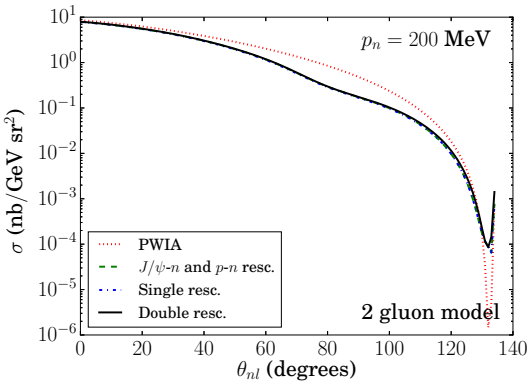

(c) Two-gluon model, $p_n = 200$ MeV

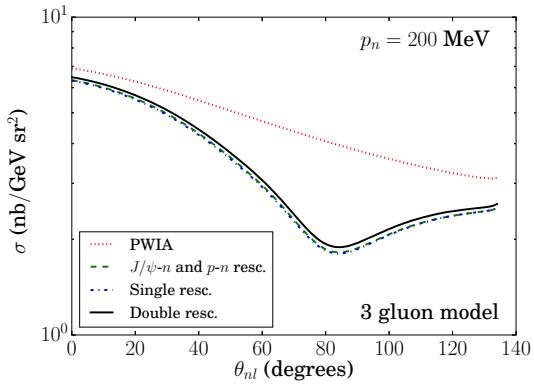

(d) Three-gluon model, $p_n = 200$ MeV

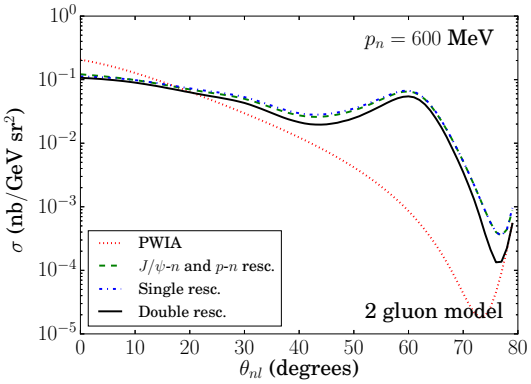

(e) Two-gluon model, $p_n = 600$ MeV

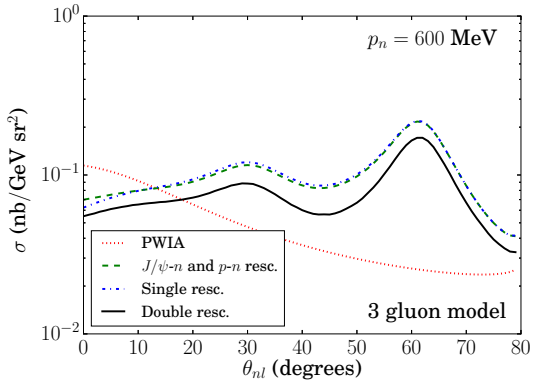

(f) Three-gluon model, $p_n = 600$ MeV

Figure 3.10: Angular dependence of the J/ψ photoproduction cross section at different neutron momenta, for both the two- and three-gluon models of J/ψ photoproduction. These plots consider the contributions due to single and double rescattering against the PWIA. $q_0 = 10$ GeV and $-t = -t_{\text{thr.}} = 2.23$ GeV^2.

produce a peak. This can also be seen in Fig. 3.10, where the absolute differential cross section is given for the two- and three-gluon models.

Ratio of angular distribution of $\gamma d \to J/\psi pn$ (multiple $\sigma_{\Psi N}$)

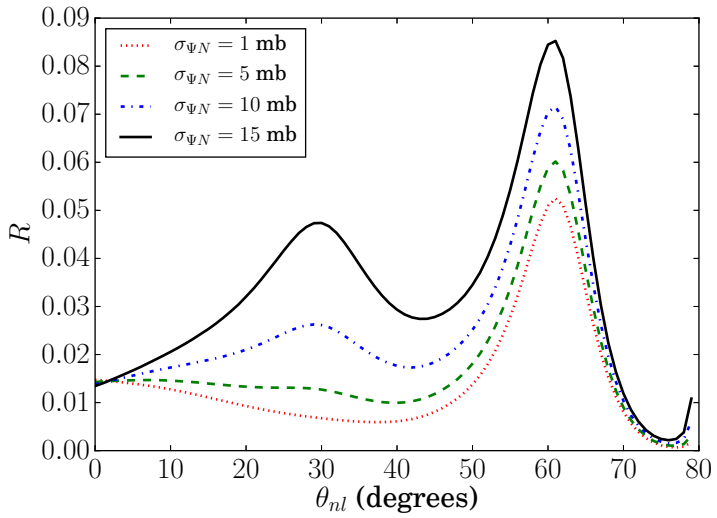

Figure 3.11: Angular dependence of the ratio defined in Eq. (3.90) with different J/ψ-N cross sections, using the two-gluon parameterization of [119]. Estimated at $q_0 = 10$ GeV and $-t = 2.23$ GeV^2. Includes all diagrams.

Despite the largely-invisible peak for the two-gluon model with $\sigma_{\Psi N} = 5$ mb, the rescattering peak may be more prominent if the J/ψ-N cross section is larger, as some models [118] suggest. For this reason, and because it is our intent to study the sensitivity of the breakup reaction (3.17) to the total J/ψ-N cross section, we present in Fig. 3.11 estimates for the ratio R_Ψ with different values of this cross section. The peak does in fact become more prominent with higher J/ψ-N cross sections, and therefore we conclude that near-threshold J/ψ photoproduction accompanied by breakup of the deuteron target can distinguish between different predictions for $\sigma_{\Psi N}$.

3.4.2 Below-threshold J/ψ production

"Below-threshold" production from a deuteron target is possible because the energy threshold for production from a more massive target is smaller. For coherent production, one can find the minimum needed photon energy by substituting m_d for m_p in Eq. (3.88), giving a

production threshold energy of about 5.6 GeV. For incoherent production, accompanied by deuteron breakup, an additional few MeV are needed to break apart the deuteron, but "sub-threshold" production is still possible in the sense that J/ψ can be produced at energies below the threshold for production from a free proton target.

From the perspective of the GEA, in which the J/ψ meson is considered to be produced from one of the deuteron's constituent nucleons, sub-threshold production is possible because the struck nucleon is already in motion prior to being struck. If this nucleon is moving opposite to the incident photon, then the photon has a higher energy—possibly above-threshold—in the nucleon's rest frame. In other words, one must satisfy, in the PWIA, the condition

$$(q + p'_p)^2 > s_{\text{thr.}}. \tag{3.98}$$

One can rewrite Eq. (3.98) in terms of a condition on the magnitude of the proton momentum $|\mathbf{p}'_p|$ needed to allow for J/ψ production to occur, as a function of the photon energy and the initial proton angle. In particular, one has threshold $|\mathrm{p}'_p|$ when

$$M_d^2 + m_N^2 - 2M_d(M_d - E'_p) + 2q_0(E'_p - |\mathrm{p}'_p|) = s_{\text{thr.}}. \tag{3.99}$$

This can be arranged into an equation of the form of Eq. (3.19), the solution of which is explained in Sec. 3.2.1.

A plot of threshold values for $|\mathrm{p}'_p|$ is given in Fig. 3.12, for various proton-photon angles, as a function of the incident photon energy. For all angles, the threshold momentum goes to zero as $q_0 \to E_{\text{thr.}} = 8.2$ GeV, since this is the energy at which J/ψ can be produced from the free proton. For especially small photon energies, such as those close to the from-deuteron production threshold of 5.6 GeV, the threshold momentum becomes extremely large, exceeding 700 MeV, where the applicability of the virtual nucleon approximation is expected to break down. Moreover, the phase space available for J/ψ photoproduction at energies these low is extremely limited, making production at such energies exceedingly unlikely. Accordingly, we examine here sub-threshold energies that are close to threshold, namely $q_0 = 7$ GeV.

Plot of Fermi momentum needed to effect subthreshold J/ψ production

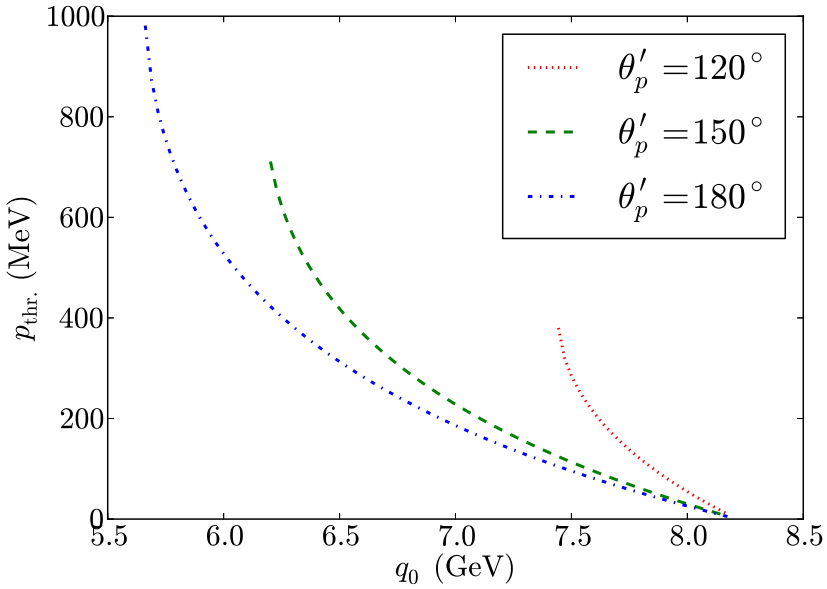

Figure 3.12: The threshold value of the bound proton momentum for J/ψ photoproduction, as a function of photon energy for various proton-photon angles.

At sub-threshold kinematics, final state interactions are expected to be negligible. $\mathcal{M}_{1c}$ is expected to be negligible upon examination of Eq. (3.50), since $-t_{\rm thr.}$ is large and q_0 is small. $\mathcal{M}_{1a}$ and $\mathcal{M}_{1b}$ are also expected to be suppressed, since their pole parts impose the kinematic conditions:

$$p_{nz} = p'_{nz} + \Delta_{1[a/b]}. \tag{3.100}$$

Momentum conservation at the $d \to p + n$ vertex further implies that

$$p_{nz} = -p'_{pz} + \Delta_{1[a/b]} = -|\mathbf{p}'_p| \cos\theta'_p + +\Delta_{1[a/b]}. \tag{3.101}$$

Since $\Delta_{1[a/b]}$ is positive (cf. Eqs. (3.42,3.46)) and $\cos\theta'_p$ is negative for any sub-threshold energy, we have $p_{n,z}$ as a large, positive number. This increases $\Delta_{1[a/b]}$ (which is a monotonically increasing function of p_{nz}), making $\mathcal{M}_{1[a/b]}$ small.

In Fig. 3.13, we present numerical estimates of the sub-threshold J/ψ photoproduction cross section at $q_0 = 7$ GeV, for both the two- and three-gluon exchange mechanisms of

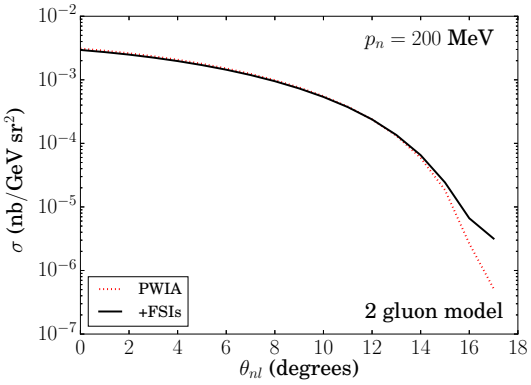

(a) Two-gluon model, $p_n = 200$ MeV

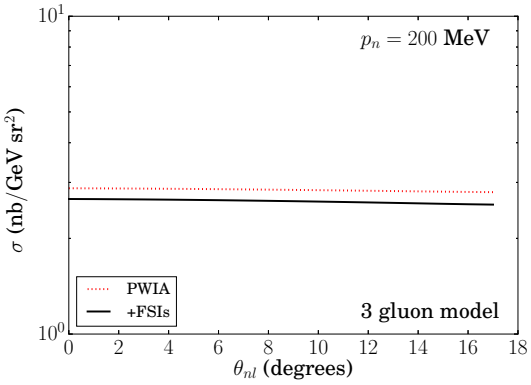

(b) Three-gluon model, $p_n = 200$ MeV

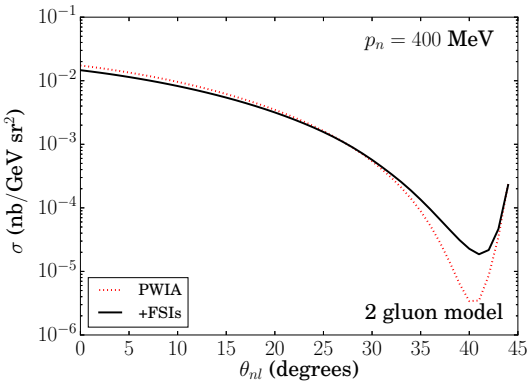

(c) Two-gluon model, $p_n = 400$ MeV

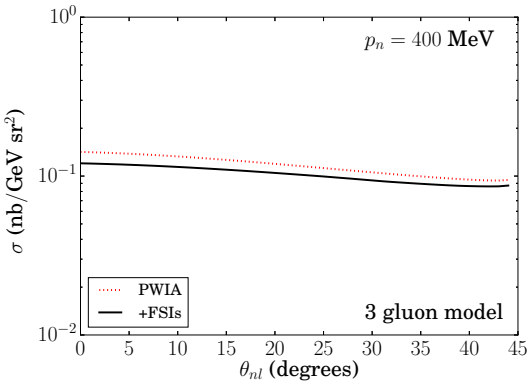

(d) Three-gluon model, $p_n = 400$ MeV

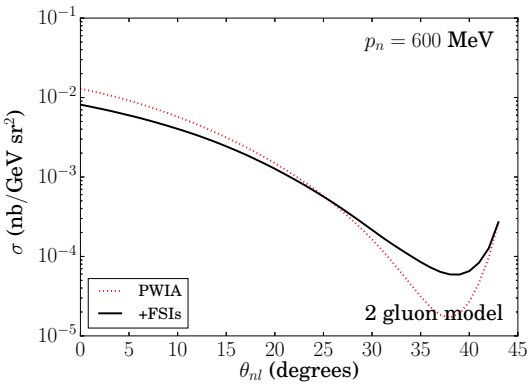

(e) Two-gluon model, $p_n = 600$ MeV

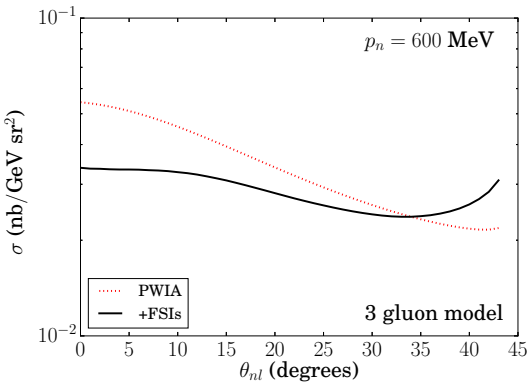

(f) Three-gluon model, $p_n = 600$ MeV

Figure 3.13: Sub-threshold angular dependence of the J/ψ photoproduction cross section at different neutron momenta, for both the two- and three-gluon models of J/ψ photoproduction. These plots consider the contributions due to single and double rescattering against the PWIA. $q_0 = 7$ GeV and $-t = -t_{\text{thr.}} = 2.23$ GeV^2.

Ref. [119]. It can be seen in this figure that FSIs are indeed mostly suppressed at sub-threshold kinematics. One exception is an appreciable increase in the cross section for the two-gluon model at θ_{nl} where the PWIA cross section dips due to $s \sim s_{\text{thr.}}$, but this is due to the PWIA cross section being even more heavily suppressed for the two-gluon model at these kinematics.

Since there is little distortion from FSIs at sub-threshold kinematics, and since these kinematics require high internal momentum within the deuteron, the break-up reaction (3.17) below the from-proton production threshold may prove a fruitful means of probing the high-momentum structure of the deuteron.

3.4.3 Collider-energy J/ψ production

In Sec. 3.3, we saw that (nearly) perfect cancellation between $\mathcal{M}_{1a}$ (Fig. 3.4a) and $\mathcal{M}_{1c}$ (Fig. 3.4c), resulting from anti-symmetry of the deuteron wave function, can occur in specific circumstances. In particular, cancellation between these contributions is expected to occur when the momentum transfers for the sub-reactions $\gamma N \to VN$ and $VN \to VN$ are nearly equal. This does not happen for near-threshold kinematics because of the high $-t_{\text{thr.}}$ entering into the $\gamma N \to VN$ vertex, and because a scenario with two hard (high-t) vertices is exceedingly unlikely. However, as the incident photon energy increases, the minimum value of $-t$ needed to effect photoproduction decreases to zero, meaning at sufficiently high energies, complete cancellation between $\mathcal{M}_{1a}$ and $\mathcal{M}_{1c}$ should occur.

In order to explore this cancellation, we have numerically estimated the cross section for J/ψ photoproduction in the breakup reaction (3.17) at collider energies. Since s is much higher than the models in Ref. [119] were developed at, we parametrize the s dependence of the diffractive scattering amplitude using a leading-order pQCD model from Ref. [123]. In this parametrization, the function $A(s)$ entering into Eq. (3.9) takes the form:

$$A(s) = \mathcal{N}\alpha_s(\mu^2) x G_T(x, \mu^2), , \tag{3.102}$$

where $G_T(x,\mu^2)$ is the gluon structure function of the target at a factorization scale μ^2. After Ref. [123], we take $\mu^2 = \frac{m_\Psi^2}{4}$ and $x = \frac{m_\Psi^2}{s_{\gamma N^*}}$. For parameterizing $G_T(x,\mu^2)$, we used the CJ12 next-to-leading order partonic distribution functions [124], and in Eq. (3.9) we take $\alpha = -0.2$ and $C = 0$ (as done previously), and we use a high-energy value for the slope factor $B = 4.73$ GeV^{-2} found by HERA [125].

Angular distributions of $\gamma d \to J/\psi pn$ at high energies

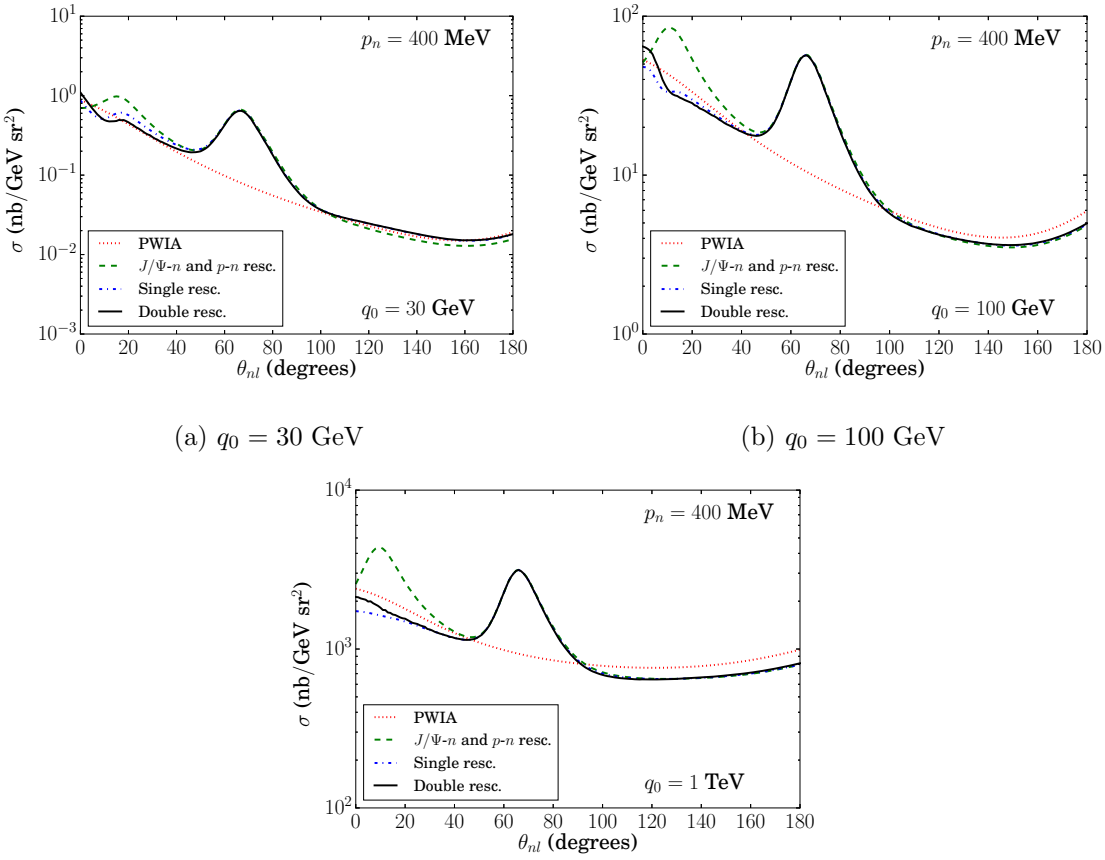

(a) $q_0 = 30$ GeV

(b) $q_0 = 100$ GeV

(c) $q_0 = 1$ TeV

Figure 3.14: Angular dependence of the J/ψ photoproduction cross section at collider energies, given $t = -1.5$ GeV^2 and $p_n = 400$ MeV. Assumes $\sigma_{\Psi N} = 5$ mb.

In Fig. 3.14, we present numerical estimates of the cross section for three increasingly high photon energies: 30 GeV, 100 GeV, and 1 TeV. These results are presented at a more moderate spectator momentum of $p_n = 400$ MeV. The dashed (green) line for each energy estimates the cross section in the absence of contribution from $\mathcal{M}_{1c}$, and produces a J/ψ-

N rescattering peak at $\theta_{nl} \approx 20^\circ$ at all three energies. However, once the contribution from $\mathcal{M}_{1c}$ is taken into account (as in the dash-dotted [blue] and solid [black] lines), nearly complete, if not entirely complete cancellation of the rescattering peak occurs. At 30 GeV, the cancellation is nearly complete, with the rescattering peak contributing only a few percent to the cross section, while at 1 TeV the cancellation is perfect and the J/ψ-N rescattering peak has vanished. At extremely high energies, overall FSI effects are due only to p-n rescattering.

3.5 Summary

Using the virtual nucleon approximation, the cross section for $\gamma + d \to V + p + n$ was calculated in the domain of large momentum transfer (*i.e.*, $-t \geq 1$ GeV^2). This kinematic domain established the applicability of the generalized eikonal approximation, which allowed one of the nucleons to be identified as "struck" by the incident photon, and the other to be a spectator to the $\gamma N \to VN$ sub-reaction. The GEA also allowed for the final state interactions to be calculated as rescatterings of on-mass-shell particles.

The results calculated in this chapter indicate that the $\gamma + d \to V + p + n$ reaction allows information to be extracted regarding $\phi(1020)$-nucleon and J/Ψ-nucleon interactions by the presence of rescattering peaks in the angular distribution of the cross section. At low (near-threshold) energies, there are two peaks in the angular distribution, one due to the proton-neutron rescattering (as seen in previous studies), and the other due th meson-nucleon rescattering; it is this latter peak that allows for the meson-nucleon scattering process to be studied. Most significantly, the size of the meson-nucleon rescattering peak, together with other aspects of the angular distribution, allows for different models of the meson-nucleon interaction to be distinguished, in addition to the overall magnitude of the meson-nucleon total cross section.

Sub-threshold and high-energy extensions of the calculation, however, did not present a meson-nucleon rescattering peak, albeit for different reasons. In the sub-threshold regime, final state interactions were overall suppressed. On the other hand, in the high-energy limit, the contributions of meson production from different nucleons, together with the

antisymmetry of the deuteron wave function, produced a destructive interference which eliminated the J/Ψ-nucleon rescattering peak.

CHAPTER 4

Conclusions

In the preceding chapters, calculations were performed for inclusive and exclusive hard processes involving nuclear targets. These calculations investigated the use of nuclear targets to investigate several elusive aspects of QCD, including both the QCD structure of the nucleus itself, and several currently unknown aspects of photo-hadron production with the use of the nucleus as a micro-laboratory. Overall, it is concluded that the nucleus is a very promising venue for investigating new aspects of QCD.

In Chapter 2, inclusive reactions were studied as a means of elucidating nuclear structure. In particular, cross sections for inclusive dijet production in proton-nucleus collisions were calculated at the operating kinematics of the Large Hadron Collider, with a focus on high-p_T jets. There were two aspects of nuclear structure that these calculations shed light on. Firstly, hard QCD processes (such as dijet production) could be used to further studies of the conventional, nucleonic structure of the nucleus. In particular, QCD processes such as dijet production are sensitive to the presence and strength of two- and three-nucleon short range correlations, which have previously been studied only in low-Q^2, quasi-elastic regime. The high-Q^2 kinematics characteristic of high-p_T jets, however, will allow for SRCs to be seen in the purely inelasic regime. Secondly, hard dijet production is sensitive to the same nuclear modifications of the bound nucleons' parton distributions that have previously been seen in deep inelastic lepton scattering experiments.

The conclusions derived in Chapter 2 were calculated in a framework developed throughout the chapter, which accounted for the latest phenomenology of short range correlations by explicating the light cone fraction distribution (LCFD) of the nucleus, which was defined in analogy to the parton distribution function of a hadron. A model of three-nucleon correlations was developed at length, on the basis of a hypothesis that three-nucleon SRCs arise from a sequence of two-nucleon short range interactions. For nucleons in the mean field, as well as nucleons in both two- and three-nucleon correlations, a convolution formula was derived to calculate the nuclear parton distribution function from the LCFD and the

PDFs of the bound nucleons. A low-Q^2 model of medium modifications was then applied to the nucleons present in two- and three-nucleon correlations, as well as those in the mean field, to account for EMC effect.

A computational algorithm for evolving nPDFs from low Q^2 to the high Q^2 characteristic of high-p_T dijet reactions was created. The optimal parameters were investigated, and the code was then applied to obtain the high-Q^2 nPDFs necessary for the dijet production calculation.

For the dijet production reaction, the applicability of leading order perturbative QCD was successfully established within the relevant kinematic domain, thereby allowing the hard QCD subprocesses contributing to dijet production to be represented as two-parton to two-parton scattering reactions. Within this approximation, the initial kinematics of the partons contained in the initial-state proton and nucleus could be fully determined by measurable jet kinematics, allowing events corresponding to $x_A > 1$ in particular to be selected for. It is such events that most faithfully elucidate the presence of short range correlations. Numerical estimates of cross sections and expected yields for $x_A > 1$ events were given, and calculations were also presented for the $0.6 < x_A < 1$ region—the classical region of the EMC effect—were also given in order to demonstrate the sensitivity of the dijet production reaction to medium modifications.

In Chapter 3, the deuteron was theoretically studied as a micro-laboratory for investigating elusive aspects of exclusive QCD processes that are difficult to study or to accomplish in proton target experiments. In particular, vector meson production from a deuteron target, accompanied by breakup of the target, was investigated as a means of studying both vector meson photoproduction mechanisms, and the interactions between vector mesons and nucleons. It was found that the eikonal regime could be established for this reaction by focusing on knocked-out protons with high final state momentum, thereby allowing clean, unambiguous separation of the sub-reactions contributing to the overall reaction.

Differential cross sections for photoproduction of $\phi(1020)$ and J/ψ in particular were presented, and it was found that two rescattering peaks were present in the predicted angular distributions. This is compatible with previous observations of a single rescattering

peak in deuteron electro-disintegration experiments, known to be due to final state interactions between the proton and neutron. The presence of a second rescattering peak in the photoproduction reaction, due to a final state interaction between the produced vector meson and the spectator nucleon, is new to this reaction, and is the observable that allows meson-nucleon scattering parameters to be investigated. Through the presence and size of the rescattering peak, ϕ photoproduction in the deuteron breakup reaction can distinguish between ϕ-N scattering models that were previously found to be undecidable in non-breakup, coherent production from the deuteron. Additionally, J/ψ photoproduction in this reaction can distinguish between two- and three-gluon exchange models for the J/ψ photoproduction mechanism, and it can gauge the overall strength of J/ψ-N scattering.

The deuteron breakup reaction was studied largely at kinematics that are achievable at Jefferson Lab with the 12 GeV energy upgrade, meaning experimental tests of the predictions contained herein may be possible to achieve in the near future.

Bibliography

[1] J.J. Aubert et al. The ratio of the nucleon structure functions F_2^N for iron and deuterium. *Phys. Lett.*, B123:275, 1983.

[2] Raymond Brock et al. Handbook of perturbative QCD: Version 1.0. *Rev. Mod. Phys.*, 67:157–248, 1995.

[3] K. A. Olive et al. Review of Particle Physics. *Chin. Phys.*, C38:090001, 2014.

[4] J. Gomez, R.G. Arnold, Peter E. Bosted, C.C. Chang, A.T. Katramatou, et al. Measurement of the A-dependence of deep inelastic electron scattering. *Phys. Rev.*, D49:4348–4372, 1994.

[5] P.R. Norton. The EMC effect. *Rept. Prog. Phys.*, 66:1253–1297, 2003.

[6] Simona Malace, David Gaskell, Douglas W. Higinbotham, and Ian Cloet. The Challenge of the EMC Effect: existing data and future directions. *Int. J. Mod. Phys.*, E23:1430013, 2014.

[7] L.B. Weinstein, E. Piasetzky, D.W. Higinbotham, J. Gomez, O. Hen, et al. Short range correlations and the EMC effect. *Phys. Rev. Lett.*, 106:052301, 2011.

[8] K.S. Egiyan et al. Measurement of 2- and 3-nucleon short range correlation probabilities in nuclei. *Phys. Rev. Lett.*, 96:082501, 2006.

[9] L. L. Frankfurt and M. I. Strikman. High-Energy Phenomena, Short Range Nuclear Structure and QCD. *Phys. Rept.*, 76:215–347, 1981.

[10] John C. Collins and Wu-Ki Tung. Calculating Heavy Quark Distributions. *Nucl. Phys.*, B278:934, 1986.

[11] Leonid Frankfurt and Mark Strikman. Photon parton distributions in nuclei and the EMC effect. *Phys. Rev.*, C82:065203, 2010.

[12] Yuri L. Dokshitzer. Calculation of the structure functions for deep inelastic scattering and e+ e- annihilation by perturbation theory in quantum chromodynamics. *Sov. Phys. JETP*, 46:641–653, 1977.

[13] V.N. Gribov and L.N. Lipatov. Deep inelastic e p scattering in perturbation theory. *Sov. J. Nucl. Phys.*, 15:438–450, 1972.

[14] Guido Altarelli and G. Parisi. Asymptotic freedom in parton language. *Nucl. Phys.*, B126:298, 1977.

[15] J. D. Bjorken. Asymptotic Sum Rules at Infinite Momentum. *Phys. Rev.*, 179:1547–1553, 1969.

[16] R. P. Feynman. *Photon-hadron interactions.* 1973.

[17] Yuri V. Kovchegov and Eugene Levin. *Quantum chromodynamics at high energy*, volume 33 of *Cambridge monographs on particle physics, nuclear physics and cosmology*. Cambridge University Press, 2012.

[18] G. Peter Lepage, Stanley J. Brodsky, T. Huang, and P.B. Mackenzie. Hadronic Wave Functions in QCD. In Anton Z. Capri and Abdul N. Kamal, editors, *Particles and Fields 2*, 1982.

[19] J. D. Bjorken and Emmanuel A. Paschos. Inelastic Electron Proton and gamma Proton Scattering, and the Structure of the Nucleon. *Phys. Rev.*, 185:1975–1982, 1969.

[20] E.J. Moniz, I. Sick, R.R. Whitney, J.R. Ficenec, Robert D. Kephart, et al. Nuclear Fermi momenta from quasielastic electron scattering. *Phys.Rev.Lett.*, 26:445–448, 1971.

[21] M. V. Zverev and E. E. Saperstein. On nucleon momentum distribution in nucleus. *Yad. Fiz.*, 43:304–313, 1986.

[22] P. K. A. de Witt Huberts. Proton spectral functions and momentum distributions in nuclei from high resolution (e, e-prime p) experiments. *J. Phys.*, G16:507–544, 1990.

[23] A. E. L Dieperink and P. K. A Huberts. On high resolution (e,e,p) reactions. *Ann. Rev. Nucl. Part. Sci.*, 40:239–284, 1990.

[24] J. J. Kelly. Nucleon knockout by intermediate-energy electrons. *Adv. Nucl. Phys.*, 23:75–294, 1996.

[25] Louk Lapikas. Quasi-elastic electron scattering off nuclei. *Nucl. Phys.*, A553:297c–308c, 1993.

[26] R. Shneor et al. Investigation of proton-proton short-range correlations via the C-12(e, e-prime pp) reaction. *Phys. Rev. Lett.*, 99:072501, 2007.

[27] R. Subedi, R. Shneor, P. Monaghan, B.D. Anderson, K. Aniol, et al. Probing cold dense nuclear matter. *Science*, 320:1476–1478, 2008.

[28] I. Korover, N. Muangma, O. Hen, R. Shneor, V. Sulkosky, et al. Probing the Repulsive Core of the Nucleon-Nucleon Interaction via the 4He(e,e'pN) Triple-Coincidence Reaction. *Phys. Rev. Lett.*, 113:022501, 2014.

[29] E. Piasetzky, M. Sargsian, L. Frankfurt, M. Strikman, and J.W. Watson. Evidence for the strong dominance of proton-neutron correlations in nuclei. *Phys. Rev. Lett.*, 97:162504, 2006.

[30] O. Hen, M. Sargsian, L.B. Weinstein, E. Piasetzky, H. Hakobyan, et al. Momentum sharing in imbalanced Fermi systems. *Science*, 346:614–617, 2014.

[31] Michael McGauley and Misak M. Sargsian. Off-Fermi Shell Nucleons in Superdense Asymmetric Nuclear Matter. 2011.

[32] H. Feldmeier, W. Horiuchi, T. Neff, and Y. Suzuki. Universality of short-range nucleon-nucleon correlations. *Phys. Rev.*, C84:054003, 2011.

[33] Misak M. Sargsian. New Properties of High Momentum Distribution of Nucleons in Asymmetric Nuclei. *Phys. Rev.*, C89:034305, 2014.

[34] L.L. Frankfurt, M.I. Strikman, D.B. Day, and M. Sargsian. Evidence for short range correlations from high Q**2 (e, e-prime) reactions. *Phys. Rev.*, C48:2451–2461, 1993.

[35] K.S. Egiyan et al. Observation of nuclear scaling in the A(e, e-prime) reaction at x(B) greater than 1. *Phys. Rev.*, C68:014313, 2003.

[36] N. Fomin, J. Arrington, R. Asaturyan, F. Benmokhtar, W. Boeglin, et al. New measurements of high-momentum nucleons and short-range structures in nuclei. *Phys. Rev. Lett.*, 108:092502, 2012.

[37] M. Lacombe, B. Loiseau, J.M. Richard, R. Vinh Mau, J. Cote, et al. Parametrization of the Paris n n Potential. *Phys.Rev.*, C21:861–873, 1980.

[38] Yu.D. Bayukov, V.I. Efremenko, S. Frankel, W. Frati, M. Gazzaly, et al. Backward Production of Protons in Nuclear Reactions With 400-GeV Protons. *Phys.Rev.*, C20:764–772, 1979.

[39] James P. Vary. Quark Distributions in Nuclei: Results From Lepton Probes. *Nucl. Phys.*, A418:195C, 1984.

[40] D. Day. Inclusive Electron Scattering at High Q^2 in the Region $1 < x < 3$. *Nucl. Phys.*, A478:397C–406C, 1988.

[41] D. B. Day et al. Inclusive electron nucleus scattering at high momentum transfer. *Phys. Rev.*, C48:1849–1863, 1993.

[42] L. L. Frankfurt and M. I. Strikman. Hard Nuclear Processes and Microscopic Nuclear Structure. *Phys. Rept.*, 160:235–427, 1988.

[43] D.W. Higinbotham, J. Gomez, and E. Piasetzky. Nuclear Scaling and the EMC Effect. 2010.

[44] M.M. Sargsian, T.V. Abrahamyan, M.I. Strikman, and L.L. Frankfurt. Exclusive electro-disintegration of He-3 at high Q2. II. Decay function formalism. *Phys. Rev.*, C71:044615, 2005.

[45] Douglas W. Higinbotham and Or Hen. Comment on "Measurement of 2- and 3-nucleon short range correlation probabilities in nuclei". 2014.

[46] A. Bodek, Martin Breidenbach, D.L. Dubin, J.E. Elias, Jerome I. Friedman, et al. Experimental Studies of the Neutron and Proton Electromagnetic Structure Functions. *Phys.Rev.*, D20:1471–1552, 1979.

[47] A. Bodek and J.L. Ritchie. Fermi Motion Effects in Deep Inelastic Lepton Scattering from Nuclear Targets. *Phys.Rev.*, D23:1070, 1981.

[48] A. Bodek and J.L. Ritchie. Further Studies of Fermi Motion Effects in Lepton Scattering from Nuclear Targets. *Phys.Rev.*, D24:1400, 1981.

[49] R.G. Arnold, Peter E. Bosted, C.C. Chang, J. Gomez, A.T. Katramatou, et al. Measurements of the a-Dependence of Deep Inelastic electron Scattering from Nuclei. *Phys. Rev. Lett.*, 52:727, 1984.

[50] J. J. Aubert et al. Measurements of the nucleon structure functions $F2_n$ in deep inelastic muon scattering from deuterium and comparison with those from hydrogen and iron. *Nucl. Phys.*, B293:740, 1987.

[51] A. Bodek et al. Electron Scattering from Nuclear Targets and Quark Distributions in Nuclei. *Phys. Rev. Lett.*, 50:1431, 1983.

[52] A. Bodek et al. A Comparison of the Deep Inelastic Structure Functions of Deuterium and Aluminum Nuclei. *Phys. Rev. Lett.*, 51:534, 1983.

[53] G. Bari et al. A Measurement of Nuclear Effects in Deep Inelastic Muon Scattering on Deuterium, Nitrogen and Iron Targets. *Phys. Lett.*, B163:282, 1985.

[54] A. C. Benvenuti et al. Nuclear Effects in Deep Inelastic Muon Scattering on Deuterium and Iron Targets. *Phys. Lett.*, B189:483, 1987.

[55] J. Ashman et al. Measurement of the Ratios of Deep Inelastic Muon - Nucleus Cross-Sections on Various Nuclei Compared to Deuterium. *Phys. Lett.*, B202:603, 1988.

[56] J. Ashman et al. A Measurement of the ratio of the nucleon structure function in copper and deuterium. *Z. Phys.*, C57:211–218, 1993.

[57] P. Amaudruz et al. Precision measurement of the structure function ratios F2 (He) / F2 (D), F2 (C) / F2 (D) and F2 (Ca) / F2 (D). *Z. Phys.*, C51:387–394, 1991.

[58] P. Amaudruz et al. Precision measurement of structure function ratios for Li-6, C-12 and Ca-40. *Z. Phys.*, C53:73–78, 1992.

[59] P. Amaudruz et al. Measurements of R(d) - R(p) and R(Ca) - R(C) in deep inelastic muon scattering. *Phys. Lett.*, B294:120–126, 1992.

[60] P. Amaudruz et al. A Reevaluation of the nuclear structure function ratios for D, He, Li-6, C and Ca. *Nucl. Phys.*, B441:3–11, 1995.

[61] K. Ackerstaff et al. Nuclear effects on R = sigma(L) / sigma(T) in deep inelastic scattering. *Phys. Lett.*, B475:386–394, 2000. [Erratum: Phys. Lett.B567,339(2003)].

[62] J. Seely, A. Daniel, D. Gaskell, J. Arrington, N. Fomin, et al. New measurements of the EMC effect in very light nuclei. *Phys.Rev.Lett.*, 103:202301, 2009.

[63] K. A. Griffioen et al. Measurement of the EMC Effect in the Deuteron. *Phys. Rev.*, C92(1):015211, 2015.

[64] Gerald A. Miller and Jason Robert Smith. Return of the EMC effect. *Phys. Rev.*, C65:015211, 2002.

[65] Jason Robert Smith and Gerald A. Miller. Return of the EMC effect: Finite nuclei. *Phys. Rev.*, C65:055206, 2002.

[66] Klaus Rith. Present Status of the EMC effect. 2014.

[67] L.L. Frankfurt and M.I. Strikman. Point-like configurations in hadrons and nuclei and deep inelastic reactions with leptons: EMC and EMC-like effects. *Nucl. Phys.*, B250:143–176, 1985.

[68] Sergey A. Kulagin, G. Piller, and W. Weise. Shadowing, binding and off-shell effects in nuclear deep inelastic scattering. *Phys.Rev.*, C50:1154–1169, 1994.

[69] W. Melnitchouk, M. Sargsian, and M.I. Strikman. Probing the origin of the EMC effect via tagged structure functions of the deuteron. *Z. Phys.*, A359:99–109, 1997.

[70] Leonid Frankfurt and Mark Strikman. QCD and QED dynamics in the EMC effect. *Int.J.Mod.Phys.*, E21:1230002, 2012.

[71] H. Honkanen, M. Strikman, and V. Guzey. Modeling nuclear parton distribution functions. 2013.

[72] L. Frankfurt, V. Guzey, and M. Strikman. Leading Twist Nuclear Shadowing Phenomena in Hard Processes with Nuclei. *Phys.Rept.*, 512:255–393, 2012.

[73] K. G. Wilson and John B. Kogut. The Renormalization group and the epsilon expansion. *Phys. Rept.*, 12:75–200, 1974.

[74] G. Curci, W. Furmanski, and R. Petronzio. Evolution of Parton Densities Beyond Leading Order: The Nonsinglet Case. *Nucl. Phys.*, B175:27, 1980.

[75] W. Furmanski and R. Petronzio. Singlet Parton Densities Beyond Leading Order. *Phys. Lett.*, B97:437, 1980.

[76] R. Keith Ellis, W. James Stirling, and B. R. Webber. *QCD and collider physics*, volume 8. 1996.

[77] M. Miyama and S. Kumano. Numerical solution of Q**2 evolution equations in a brute force method. *Comput. Phys. Commun.*, 94:185–215, 1996.

[78] Jun Gao, Marco Guzzi, Joey Huston, Hung-Liang Lai, Zhao Li, et al. CT10 next-to-next-to-leading order global analysis of QCD. *Phys. Rev.*, D89(3):033009, 2014.

[79] Otto Nachtmann. Positivity constraints for anomalous dimensions. *Nucl. Phys.*, B63:237–247, 1973.

[80] Ingo Schienbein et al. A Review of Target Mass Corrections. *J. Phys.*, G35:053101, 2008.

[81] John Collins. *Foundations of perturbative QCD*. 2011.

[82] B. L. Combridge, J. Kripfganz, and J. Ranft. Hadron Production at Large Transverse Momentum and QCD. *Phys. Lett.*, B70:234, 1977.

[83] R. Keith Ellis and J.C. Sexton. QCD Radiative Corrections to Parton Parton Scattering. *Nucl. Phys.*, B269:445, 1986.

[84] Georges Aad et al. Measurement of inclusive jet and dijet production in pp collisions at $\sqrt{s} = 7$ TeV using the ATLAS detector. *Phys. Rev.*, D86:014022, 2012.

[85] L. L. Frankfurt, M. M. Sargsian, and M. I. Strikman. Feynman graphs and Gribov-Glauber approach to high-energy knockout processes. *Phys. Rev.*, C56:1124–1137, 1997.

[86] Misak M. Sargsian. Selected topics in high energy semiexclusive electronuclear reactions. *Int. J. Mod. Phys.*, E10:405–458, 2001.

[87] J. M. Laget. The Electro-disintegration of few body systems revisited. *Phys. Lett.*, B609:49–56, 2005.

[88] J. M. Laget. Rescattering in meson photoproduction from few body systems. *Phys. Rev.*, C73:044003, 2006.

[89] Sabine Jeschonnek and J. W. Van Orden. A New calculation for D(e, e-prime p)n at GeV energies. *Phys. Rev.*, C78:014007, 2008.

[90] Misak M. Sargsian. Large Q**2 Electrodisintegration of the Deuteron in Virtual Nucleon Approximation. *Phys. Rev.*, C82:014612, 2010.

[91] K. S. Egiyan et al. Experimental study of exclusive H-2(e,e-prime p)n reaction mechanisms at high Q**2. *Phys. Rev. Lett.*, 98:262502, 2007.

[92] W. U. Boeglin et al. Probing the high momentum component of the deuteron at high Q^2. *Phys. Rev. Lett.*, 107:262501, 2011.

[93] L. Frankfurt, W. Koepf, J. Mutzbauer, G. Piller, M. Sargsian, et al. Coherent photoproduction and leptoproduction of vector mesons from deuterium. *Nucl. Phys.*, A622:511–537, 1997.

[94] Claudio Ciofi degli Atti, L. P. Kaptari, and D. Treleani. On the effects of the final state interaction in the electrodisintegration of the deuteron at intermediate-energies and high-energies. *Phys. Rev.*, C63:044601, 2001.

[95] C. Ciofi degli Atti and L. P. Kaptari. Calculations of the exclusive processes H-2(e, e-prime p)n, He-3(e, e-prime p)H-2 and He-3(e, e-prime p)(pn) within a generalized Glauber approach. *Phys. Rev.*, C71:024005, 2005.

[96] T. Mibe et al. First measurement of coherent phi-meson photoproduction on deuteron at low energies. *Phys. Rev.*, C76:052202, 2007.

[97] A. O. Barut. *The theory of the scattering matrix*. 1967.

[98] T. H. Bauer, R. D. Spital, D. R. Yennie, and F. M. Pipkin. The Hadronic Properties of the Photon in High-Energy Interactions. *Rev. Mod. Phys.*, 50:261, 1978.

[99] Jeffrey R. Forshaw and D. A. Ross. *Quantum chromodynamics and the pomeron*, volume 9. 1997.

[100] V. N. Gribov. Interaction of gamma quanta and electrons with nuclei at high-energies. *Sov. Phys. JETP*, 30:709–717, 1970. [Zh. Eksp. Teor. Fiz.57,1306(1969)].

[101] L. Bertocchi. Graphs and glauber. *Nuovo Cim.*, A11:45–62, 1972.

[102] L. L. Frankfurt, W. R. Greenberg, G. A. Miller, M. M. Sargsian, and M. I. Strikman. Color transparency effects in electron deuteron interactions at intermediate Q**2. *Z.Phys.*, A352:97–113, 1995.

[103] R. J. Glauber and G. Matthiae. High-energy scattering of protons by nuclei. *Nucl. Phys.*, B21:135–157, 1970.

[104] R. Blankenbecler and L. F. Cook. Bound states and dispersion relations. *Phys. Rev.*, 119:1745–1752, Sep 1960.

[105] Richard A. Arndt, Igor I. Strakovsky, and Ron L. Workman. Nucleon nucleon elastic scattering to 3 GeV. *Phys. Rev.*, C62:034005, 2000.

[106] J. Beringer et al. Review of Particle Physics (RPP). *Phys. Rev.*, D86:010001, 2012.

[107] T. Ishikawa, D.S. Ahn, J. K. Ahn, H. Akimune, W. C. Chang, et al. phi photoproduction from Li, C, Al, and Cu nuclei at E(gamma) = 1.5-GeV to 2.4-GeV. *Phys. Lett.*, B608:215–222, 2005.

[108] M. H. Wood et al. Absorption of the ω and ϕ Mesons in Nuclei. *Phys. Rev. Lett.*, 105:112301, 2010.

[109] X. Qian, W. Chen, H. Gao, K. Hicks, K. Kramer, et al. Near-threshold Photoproduction of Phi Mesons from Deuterium. *Phys. Lett.*, B696:338–342, 2011.

[110] J. J. Sakurai. *Currents and Mesons*. 1969.

[111] Alexander Sibirtsev, Hans-Werner Hammer, Ulf-G. Meissner, and Anthony William Thomas. phi-meson photoproduction from nuclei. *Eur. Phys. J.*, A29:209–220, 2006.

[112] X. Qian et al. The Extraction of phi-N total cross section from d(gamma,pK+ K-)n. *Phys. Lett.*, B680:417–422, 2009.

[113] W. C. Chang et al. Measurement of the incoherent $\gamma d \to \phi pn$ photoproduction near threshold. *Phys. Lett.*, B684:6–10, 2010.

[114] Jozef Dudek, Rolf Ent, Rouven Essig, K. S. Kumar, Curtis Meyer, et al. Physics Opportunities with the 12 GeV Upgrade at Jefferson Lab. *Eur.Phys.J.*, A48:187, 2012.

[115] B. Knapp, Won-Yong Lee, P. Leung, S. D. Smith, A. Wijangco, et al. Photoproduction of Narrow Resonances. *Phys. Rev. Lett.*, 34:1040, 1975.

[116] Robert L. Anderson, W. Ash, D. Gustavson, T. Reichelt, D. Ritson, et al. A Measurement of the a-Dependence of psi Photoproduction. *Phys. Rev. Lett.*, 38:263, 1977.

[117] D. Kharzeev and H. Satz. Quarkonium interactions in hadronic matter. *Phys. Lett.*, B334:155–162, 1994.

[118] A. Sibirtsev and M. B. Voloshin. The Interaction of slow J/psi and psi' with nucleons. *Phys. Rev.*, D71:076005, 2005.

[119] S. J. Brodsky, E. Chudakov, P. Hoyer, and J. M. Laget. Photoproduction of charm near threshold. *Phys. Lett.*, B498:23–28, 2001.

[120] U. Camerini, J. G. Learned, R. Prepost, Cherrill M. Spencer, D. E. Wiser, et al. Photoproduction of the psi Particles. *Phys. Rev. Lett.*, 35:483, 1975.

[121] Leonid Frankfurt and Mark Strikman. Two gluon form-factor of the nucleon and J / psi photoproduction. *Phys. Rev.*, D66:031502, 2002.

[122] B. Gittelman, K. M. Hanson, D. Larson, E. Loh, A. Silverman, et al. Photoproduction of the psi (3100) Meson at 11-GeV. *Phys. Rev. Lett.*, 35:1616, 1975.

[123] V. Rebyakova, M. Strikman, and M. Zhalov. Coherent rho and J/psi photoproduction in ultraperipheral processes with electromagnetic dissociation of heavy ions at RHIC and LHC. *Phys. Lett.*, B710:647–653, 2012.

[124] J. F. Owens, A. Accardi, and W. Melnitchouk. Global parton distributions with nuclear and finite-Q^2 corrections. 2012.

[125] C. Adloff et al. Elastic photoproduction of J / psi and Upsilon mesons at HERA. *Phys. Lett.*, B483:23–35, 2000.

VITA

ADAM FREESE

2006 - 2009	B.S., Physics Rensselaer Polytechnic Institute Troy, New York
2010 - 2016	Ph.D., Physics Florida International University Miami, Florida

SELECTED PUBLICATIONS AND PRESENTATIONS

1. Adam Freese and Misak Sargsian, *QCD evolution of superfast quarks*, arXiv:1511.06044 [hep-ph] (2015)

2. Adam Freese, *Nuclear parton distributions in theory*, invited seminar presented at Brookhaven National Laboratory, February 26, 2015.

3. Adam Freese, Misak Sargsian, and Mark Strikman, *Probing superfast quarks in nuclei through dijet production at the LHC*, European Journal of Physics C**75**, 534 (2015)

4. Adam Freese, *Dijet production at large x as a probe of superfast quarks in nuclei*, talk presented at LHC Forward Physics and Diffraction WG meeting, Kansas City, MO, September 2014.

5. Adam Freese and Misak Sargsian, *Probing vector mesons in deuteron breakup reactions*, Physical Review C**88**, 044604 (2013)